Electronic Properties of Transition Metal Doped Silicon Clusters

vorgelegt von
Diplom-Physiker
Jochen Rittmann
aus Duisburg

von der Fakultät II - Mathematik und Naturwissenschaften
der Technischen Universität Berlin
zur Erlangung des akademischen Grades

Doktor der Naturwissenschaften
- Dr. rer. nat. -

genehmigte Dissertation

Promotionsausschuss:

Vorsitzender: Prof. Dr. Mario Dähne

Berichter: Prof. Dr. Thomas Möller

Berichter: Prof. Dr. Bernd von Issendorff

Tag der wissenschaftlichen Aussprache: 20.09.2011

Berlin 2011

D 83

Abstract

The interaction of a transition metal atom with a silicon cluster is investigated to understand the stabilizing effect responsible for silicon cage formation in transition metal doped silicon clusters. The analysis was done using VUV spectroscopy and element specific x-ray spectroscopy. Partial ion yield analysis allows observing resonant excitation and direct photoionization channels separately. First experimental indications for the predicted high symmetry [1, 2] of VSi_{16}^+ are found. In addition, studies on different transition metal dopant atoms in this specific silicon cage show that deviation from electronic shell closure seems to affect the silicon cage more strongly than the local electronic structure at the transition metal dopant. Furthermore, the size of transition metal doped silicon clusters shows a strong influence on the localization of electrons and position of valence levels. The latter is studied using a novel analysis method based on the combination of VUV and x-ray spectroscopy. Determination of the HOMO-LUMO gap for a wide range of cluster sizes show good agreement with theoretical predictions. An enhanced HOMO-LUMO gap of $(1.9 \pm 0.2)\,\text{eV}$ is observed in case of the highly symmetric VSi_{16}^+, which can be understood in terms of a spherical potential model [1, 3].

Kurzfassung

In dieser Arbeit wird die Wechselwirkung zwischen einem Übergangsmetallatom und einem Siliziumcluster untersucht. Die Untersuchungsmethoden beinhalten VUV Spektroskopie und elementspezifische Röntgenspektroskopie. Durch die Analyse der partiellen Ionenausbeute können die resonante Anregung und die direkte Photoionisation eines Clusters getrennt betrachtet werden. Erstmalig werden experimentelle Indizien für die vorhergesagte hohe Symmetrie von VSi_{16}^+ [1, 2] gezeigt. Untersuchungen an diesem Siliziumkäfig mit Titan und Chrom als Dotieratom zeigen, dass die Dotierung einen größeren Einfluss auf die Struktur des Käfigs hat als auf die lokale elektronische Struktur des Übergangsmetallatoms. Des Weiteren konnte die größenabhängige Änderung der Lokalisierung von Valenzelektronen näher bestimmt werden. Der in einem erstmalig eingesetzten Verfahren bestimmte Abstand von dem höchsten besetzten und dem niedrigsten unbesetzten Molekülorbital (*HOMO-LUMO gap*) in Abhängigkeit der Clustergröße zeigt eine gute Übereinstimmung mit theoretischen Berechnungen desselben. Eine besondere Stellung hat hierbei das hochsymmetrische VSi_{16}^+ mit einem gemessenen *HOMO-LUMO gap* von $(1.9 \pm 0.2)\,\text{eV}$.

Contents

Introduction

Atomic clusters are ideal systems to analyze fundamental properties of matter on a microscopic scale. They can be tailored in size and composition to address a specific question. Systematic manipulation of one or more properties of a free cluster, as for example its size, allows to monitor the response of the whole system and therefore to determine the microscopic origin of electronic structure, magnetism, and reactivity or other features on a highly defined unperturbed system. Transition metal doped silicon clusters are therefore the ideal system to analyze the interaction between a semiconducting material and a metal. Like metal doping drastically changes the properties of a semiconducting bulk, silicon clusters show a complete change in their geometry and stability upon interaction with a transition metal atom [2, 4]. While a stabilization of the silicon cluster through the metal atom was observed experimentally for specific transition metal doped silicon clusters [5], theoretical results showed that highly symmetric silicon cage structures were formed around the metal atom [2, 6]. The high symmetry of certain sizes and compositions of systems is predicted to result in a high degeneracy of electronic levels, thus allowing further stabilization by potential electronic shell closure and high HOMO-LUMO gaps. This interesting stabilizing interaction of transition metal atoms on silicon clusters gave rise to many theoretical publications on this topic, predicting that the optimal cage structures occur if sixteen silicon atoms encapsulate a Sc^-, Ti, or V^+ atom [1, 2]. On the other hand, experimental studies analyzing the binding mechanism and electronic structure responsible for the reshaping of the silicon cluster are sparse. No experiment has been performed so far to determine the geometric structure of the silicon cages.

In order to understand the interaction and binding mechanism between the transition metal and the silicon cluster, experimental techniques probing global properties of the cluster are of limited use. The role of either the metal or the silicon cage in this interaction has to be probed separately with an element specific method. The method best suited is x-ray spectroscopy, which is therefore applied in this thesis. This element specific method allows to analyze the electronic struc-

ture of a transition metal doped silicon cluster locally either at the silicon cage or at the transition metal center. In addition, size selection is mandatory, as only certain clusters sizes and compositions are predicted to show highly symmetric structures and enhanced stability. Therefore x-ray spectroscopy is used in combination with mass selection of cationic transition metal doped silicon clusters in the gas phase, thus allowing to probe the influence of different cage geometries on the local electronic structure at the transition metal of clusters free of any external perturbation. Furthermore, interchanging the transition metal dopant in equal sized silicon cages allows to study the influence of different electronic configurations of the whole system on its stability and cage symmetry. These studies require *in situ* sample preparation and mass selection, which allows to generate only small quantities of a highly defined system. Using x-ray spectroscopy on these small quantities of size selected clusters in the gas phase requires a high photon flux over a wide energy range, including transition metal as well as silicon absorption edges, only available at third generation synchrotron radiation facilities. Presently, such element specific studies on size selected clusters can only be performed with our experimental setup at BESSY II.

Chapter 1

Theoretical Background of X-ray Absorption Spectroscopy

The following section introduces the theoretical background of x-ray absorption spectroscopy (XAS), which is needed for a profound understanding of the experimental results. First, the absorption process is discussed in section 1.1, which is further distinguished between two absorption channels, the direct photo ionization (cf. sect. 1.1.1) and the resonant x-ray absorption (cf. sect. 1.1.2). The following sections discuss the application of XAS in case of gas phase particles (cf. sect 1.1.3) as well as relaxation channels of the particle upon absorption of a x-ray photon (cf. sect. 1.1.4). A special focus is set on Auger decay. The last sections will briefly discuss density functional theory (DFT, cf. sect. 1.2).

1.1 X-Ray Absorption

X-ray absorption spectroscopy is a powerful tool to investigate electronic properties of a material. Due to the characteristic binding energy of electrons in each element, it is an element specific probe. Hence, it is especially well suited to investigate compound materials.

In general the intensity after absorption of electromagnetic waves in the medium follows the Lambert-Beer law

$$I(d) = I_0 \cdot e^{-\mu \cdot d}, \tag{1.1}$$

where d is the traversed distance into the medium, I_0 the initial intensity and μ an energy dependent absorption coefficient. The absorption coefficient is dominated by the unoccupied density of bound and continuum states and transition

matrix elements into these. Hence, conclusions of the electronic properties can be made with the knowledge of the absorption coefficients photon energy dependence. Electronic excitation of a medium can be explained in terms of basic atomic processes as direct photo ionization and resonant photo ionization. In general, a photon can be absorbed, if it has the same energy as the difference between the electronic initial and final state of the medium and if the transition is allowed with respect to the dipole transition selection rules.

1.1.1 Direct Photo Ionization

Direct photo ionization is a process, where an electron is transfered from a bound state into the continuum by the energy gained through absorption of a photon. This process takes place if the photon energy is sufficient to overcome the ion-
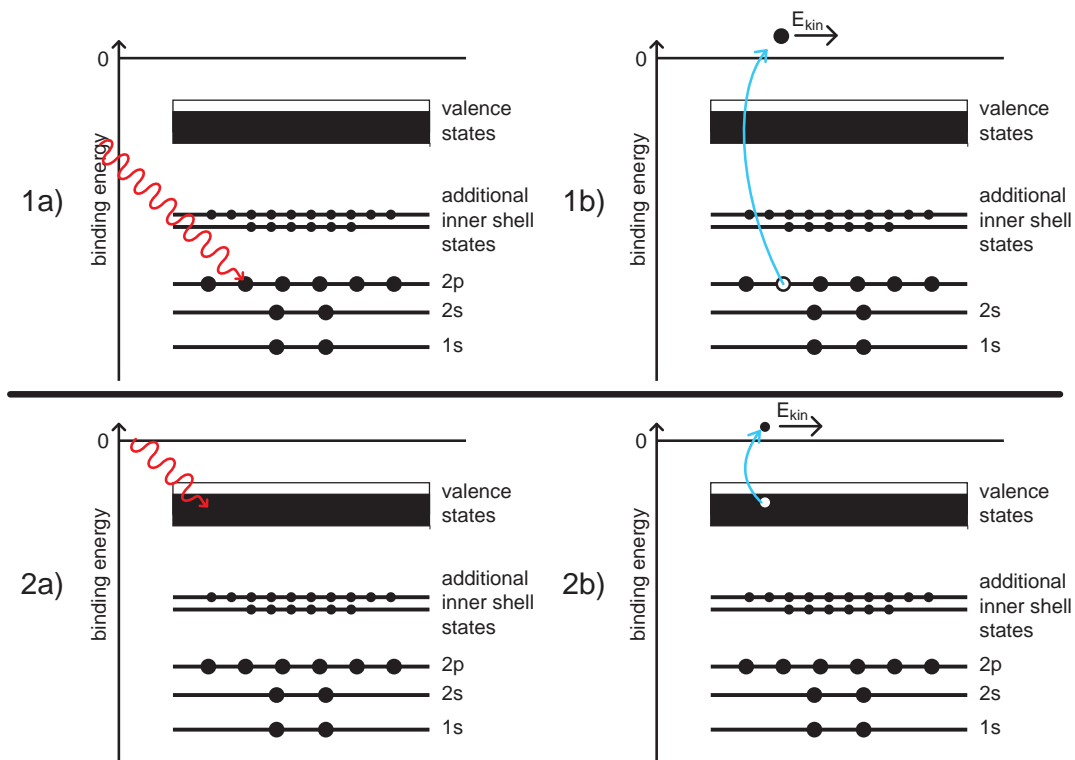
Figure 1.1: Schematic of direct photo ionization of 1) valence and 2) core states. a) A photon with sufficient energy is absorbed, b) an electron is transferred from its bound state to the vacuum level. One negative charge is missing from the particle. In the case of the core state excitation, the cluster is additionally in a highly excited state (1b).

ization threshold of the atom or the work function of the bulk respectively. A general description of the binding energy Φ is given by Einstein's equation (1.2) for bulk material, which includes both, valence electrons and the tighter bound

inner shell electrons [7],

$$h\nu = E_{\text{kin}} + \Phi, \tag{1.2}$$

with Planck's constant h, the photon frequency ν and the electron kinetic energy E_{kin} in the continuum. At a given photon energy, the kinetic energy of the electron reveals the binding energy of the electron and is measured in photo electron spectroscopy or x-ray photo electron spectroscopy. For atoms and molecules, the charge energy has to be taken into account to obtain the right binding energy of the electron. In a classical picture, the photo electron has to be removed from a charged sphere of the radius r. The charge energy is needed to separate the electrons charge from the spheres charge to an infinite distance and scales with r^{-1} [8].

If the initial state of a particle is the cationic ground state, the particle is left in a doubly charged state after direct photo ionization and, if core electrons where involved, a highly excited state (cf. fig. 1.1). The absorption at a specific energy is given by the photo ionization cross section σ. It can be pictured as the effective area a particle exposes to the incoming photons and has the unit [barn], which is equal to 100 fm^2. Calculated cross sections for the direct photo ionization are shown in figure 1.2 for some transition metals, which are used as dopant material in the experiments performed in this thesis [9].
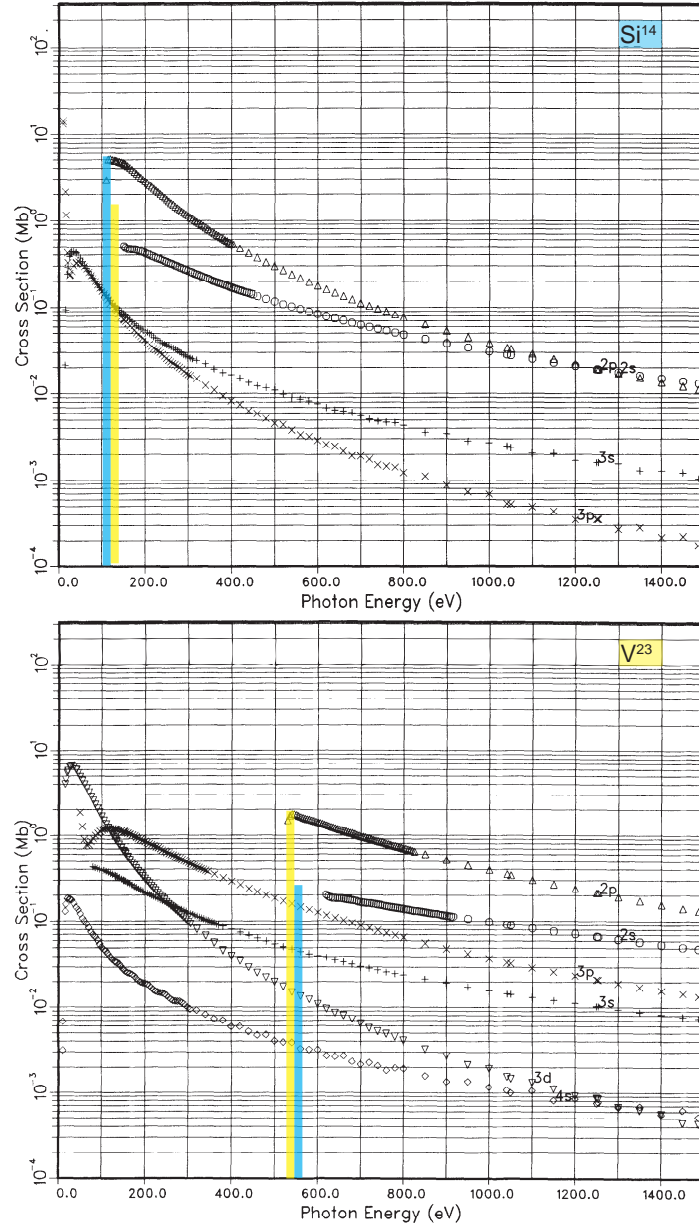
Figure 1.2: Calculated direct photo ionization cross section of vanadium and silicon in the energy range of 0 eV to 1500 eV [9]. The partial contribution of different electronic shells is shown. For binary vanadium-silicon clusters, the contribution of absorption of the two components can be estimated. The vanadium 2p edges contribution at energies of about 526 eV is very high (1.5 Mbarn, blue bar) compared to silicon (0.3 Mbarn, yellow bar). On the other hand, at the silicon 2p edge at about 108 eV the contribution of vanadium (0.8 Mbarn, blue bar) is negliable compared to silicon (5 Mbarn, yellow bar). In resonant x-ray absorption, the vanadium 2p-3d or the silicon 2p-3d resonance will further increase this effect.

1.1.2   Resonant X-ray Absorption

Unlike probing the occupied electronic states of a medium via direct photo ionization, resonant X-ray absorption probes the unoccupied electronic states by photon induced transitions between occupied and unoccupied electronic bound states. The probability of this excitation can be calculated with Fermi's golden rule [10]

$$w(\varphi_i, \alpha_f) = \frac{2\pi}{\hbar} \, |< \alpha_f, E_f \mid W \mid \varphi_i >|^2 \, \rho(\alpha_f, E_f) \cdot \delta(E_i, E_f, \hbar\omega) \qquad (1.3)$$

with the mediums initial state φ_i and final states α_f, the density of bound final states $\rho(\alpha_f, E_f)$, and the transition matrix element W. The final states α_f are in this general case energetically close (degenerate) states, which are all reachable with the same photon energy. Transitions only take place, if the photon energy is equal to the energy difference of the final and the initial state $\hbar\omega = E_f - E_i$. In a one electron picture, the probability depends strongly on the overlap of the wave functions of the electronic states and the selection rule for dipole transitions, allowing only transitions for $\Delta l = l_f - l_i = \pm 1$ and $\Delta m = m_f - m_i = \pm 1$, with the quantum number of the angular momentum l and the magnetic quantum number m. The 3d orbitals are very compact, resulting in a strong overlap with the 2p wave function. This leads to a large oscillator strength for the 2p to 3d transition. In an one electron picture with an initial $3d^n$ state and a final state $2p^5 3d^{n+1}$, the transition of 2p electrons into empty states of the particle probes the empty density of states (unoccupied DOS). The core hole lifts the degeneracy of $j = 3/2$ and $j = 1/2$ states of the spin orbit coupled 2p states, resulting in a 2p spin orbit splitting. The 2p spin-orbit splitting due to the core hole in the final state will result in two spin orbit split transitions into the DOS, separated by the $2p_{1/2}$ and $2p_{3/2}$ core hole energy difference and with the statistical intensity ratio 2:1 due to $2p_{1/2}$ and $2p_{3/2}$ electron occupation. This simple theoretical approach is however not suited for a description of the spectra of 3d transition metals obtained by experiments [11,12]. Even for transition metal atoms, the 2:1 ratio is almost never reached. This is partially due to the fact that for transition metals no pure Russel-Saunders coupling (l-s coupling) is present, nor can the coupling be completely treated as j-j coupling. This complicates theoretical calculations. In addition, multiplet effects originating in the interaction of the core hole in the final state and the 3d electrons have to be considered [12–14].

1.1.3 XAS on Particles in the Gas Phase

In case of dilute samples, measurements of the absorption coefficient in the x-ray regime can prove challenging due to a low absorption cross section. If large quantities are available the target density can be increased by merged beam alignment. For particles only available in small quantities XAS is very challenging. Low particle densities may result, if particles are produced in situ in relatively small quantities, and if the yield is additionally lowered by experimental conditions as in the following case by size selection during the experiment. Also challenging is XAS on charged particles, lowering their density due to coulombic repulsion and the resulting charge density limit, if not trapped in a suited potential. Measuring the absorption in transmission is nearly impossible for such mediums. If a x-ray photon flux as achieved at synchrotron facilities is available and target density can be experimentally accumulated within the interaction zone with the x-rays (cf. sect. 3.5), measuring the x-ray absorption becomes possible. A transmission measurement is still not feasible, as the photon flux is high and absorption of the accumulated medium still fairly low in the x-ray regime. A very low absorption signal would have to be measured at a high background signal if the absorption of the x-ray beam within the medium is measured behind the interaction region. The absorption can be measured with some restrictions by secondary processes following absorption. One is spectroscopy of the fluorescence upon relaxation of a particle after x-ray excitation. Another method is ion yield spectroscopy, measuring a change of a parent systems charge or size as a function of excitation energy. If core holes are generated upon x-ray absorption, relaxation via Auger decays may lead to multiple charges on the cluster, which ion yield is a measure of the x-ray absorption. In addition, the energy deposited in the system in the form of vibrational excitations is likely to result in fragmentation of the particle. In this case the total ion yield of all non-parent particles is a good measure for the x-ray absorption, since a higher absorbance will result in a higher particle fragment ion yield. In fluorescence and ion yield spectroscopy, the signal is similar but not exactly equal to the x-ray absorption of the gas phase particles. In case of ion yield spectroscopy, which is the method of choice in the framework of this thesis, the similarities and differences are discussed below.

After photon induced generation of a core hole and subsequent Auger decay, the particle may fragment into more than one daughter ion (cf. sect. 1.1.4), which is detected in partial ion yield spectroscopy. The partial ion yield exhibits the same lines as the absorption spectrum for transition metals (cf. sect. 1.1.4), but

not the same intensity distribution. Fragmentation of a particle in which multiple charged are generated due to subsequent Auger decays may lead to more than one product ion, hence more than one absorption signal may be detected. For the particles of interest in this thesis, transition metal doped silicon clusters, the complex relaxation process is simplified by the fact that fluorescence can be neglected due to the low probability of this relaxation channel [15] for the 2p core hole relaxation of 3d metals and silicon alike. The relative probability for Auger
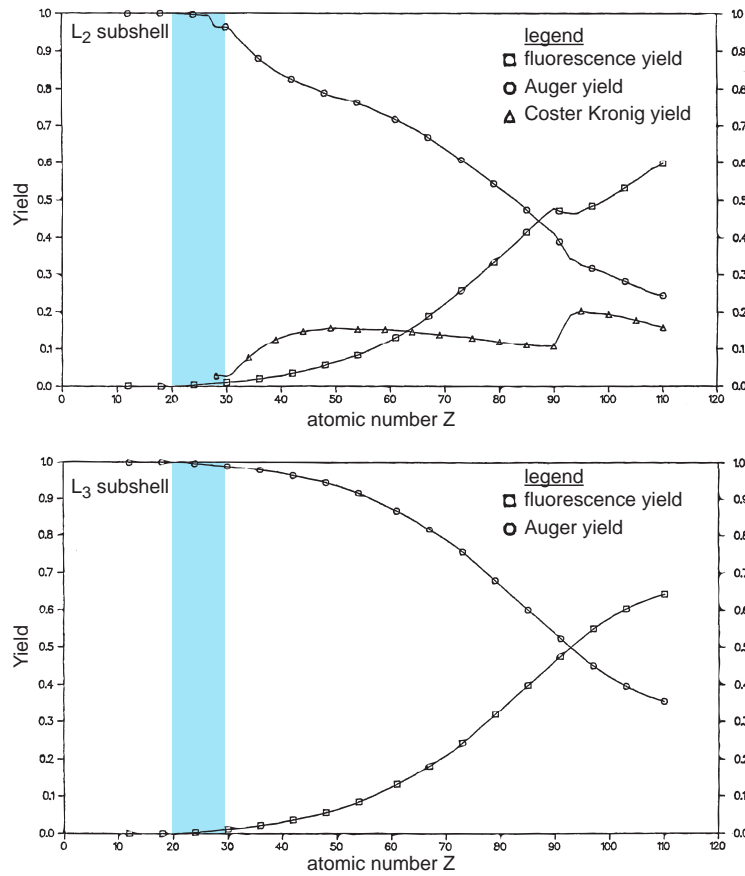
Figure 1.3: Relative probability of the decay channels of $2p^{3/2}$ (L_3) and $2p^{1/2}$ (L_2) core holes. Auger decay ($\square$), flourescence ($\bigcirc$) and Coster-Kronig ($\triangle$) decay. For the atomic numbers relevant in this thesis (^{14}Si, ^{21}Sc, ^{22}Ti, ^{23}V, ^{24}Cr, ^{25}Mn, ^{27}Co, and ^{32}Ge) decay of 2p core holes via fluorescence can be neglected. From [15].

and fluorescent decay as a function of atomic number is shown in figure 1.3. A further simplification is achieved by regarding only fragments of the ion yield that contain a transition metal atom. Since only one transition metal atom is available per transition metal doped silicon cluster analyzed in this work, only one fragment holding the transition metal atom will be seen after absorption of a photon. The experimental procedure to get an absorption spectrum is discussed in detail in section 3.9.

1.1.4 Auger Decay

A particle in a core excited state can relax into energetically lower lying states by transferring an electron to the empty core state. The energy can either be emitted by a fluorescence photon or transferred to an other electron, if the energy gained is sufficient for a transfer of the electron into a continuum state (cf. fig 1.4). The latter process is classified into Auger, Coster-Kroning and Super Coster-Kroning decay, depending on the electronic states involved in the electrons inner atomic transition and the leaving electrons initial state. A detailed classification is given in [16] and elsewhere. For the following analysis this detailed classification is not necessary. If the system after an Auger decay is still excited, multiple Auger
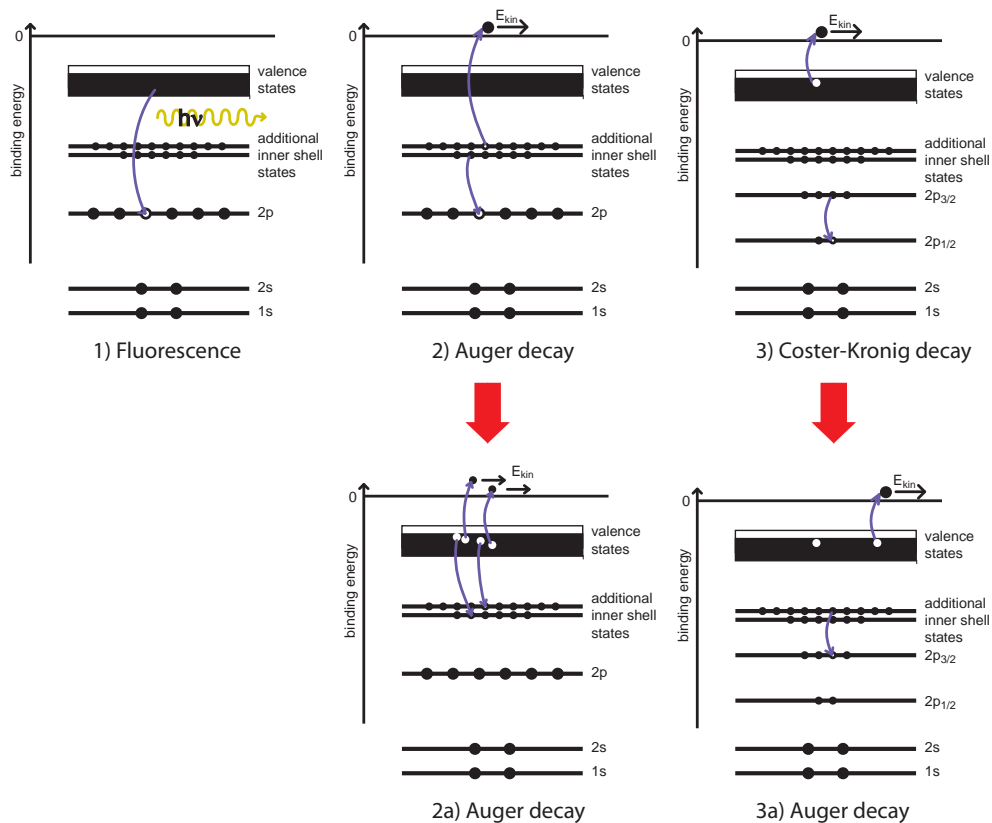
Figure 1.4: Schematic of core hole relaxation channels. 1) Fluorescence: The core hole relaxes via transition of an electron. The excess energy is emitted as a photon. 2) Auger decay. The core hole is filled by an electron, the excess energy is transferred to an other electron leaving the system. 2a) If the electrons participating in a first Auger decay are core electrons themselves, cascading Auger decay is possible. 3) Coster-Kronig decay: Like 2), but the relaxing electron is on the same electronic subshell as the hole. This process is faster than normal Auger decay due to the large overlap of the participating wave functions. The excess energy is normally smaller due to the same subshell restriction. 3a) Subsequent Auger decay, usually following Coster-Kronig decay. Due to the same subshell restriction for Coster Kronig decay, an inner shell core hole is always present.

processes may occur. For particles consisting of more than one atom the charge

present after multiple Auger decays can lead to fragmentation due to Coulomb repulsion of charges on the particles atoms.

1.2   Density Functional Theory Calculations

In the course of this work Density Functional Theory (DFT) calculations are performed on transition metal doped silicon clusters [17, 18] to obtain information on the binding energy of silicon core level electrons in dependence on the average coordination of silicon atoms and valence electron delocalization (chemical shift) in the cluster. The binding energies are compared to binding energies experimentally obtained via partial ion yield studies (cf. sect. 7.2.2). In the following, the concept of DFT is explained. A more detailed view on DFT is found in [18].

DFT is a theory first applied to bulk materials [18]. Due to the large number of electrons, rather than calculating every wave function, calculations are based on the density of the electrons. This simplifies the wave function having 3N variables (N electrons in a three dimensional space) to a problem with just three dimensions [18]. The density functional theory is based on two mathematical theorems by Kohn, Sham and Hohenberg, the first of which states *that the full many-particle ground state is a unique functional of [the electron density] n(r).* [19]. There is a bijective correlation between the ground state wave function and the electron density of a system. The second theorem defines the functional of the first theorem closer: *The electron density that minimizes the energy of the overall functional is the true electron density corresponding to the full solution of the Schrödinger equation.* [18–20]. Therefore, if the true functional is known, the electron density can be obtained by variational principal. An useful way to describe the energy functional is [18]

$$E[\{\Psi_i\}] = E[\{\Psi_i\}] + E_{\mathrm{XC}}[\{\Psi_i\}], \qquad (1.4)$$

with Ψ_i the single electron wave function, $E[\{\Psi_i\}]$ the known contributions to the energy functional and $E_{\mathrm{XC}}[\{\Psi_i\}]$ the exchange correlation functional. While the existence of the exchange correlation functional $E_{\mathrm{XC}}[\{\Psi_i\}]$ can be proved, the form of the functional is unknown. $E_{\mathrm{XC}}[\{\Psi_i\}]$ incorporates all contributing to the energy that is unknown. The known parts are the electrons kinetic energy, coulomb interactions between the electrons and nuclei, the electron electron interaction and the interaction between different nuclei [18]. The wave functions Ψ_i are not free chosen, but are picked from a certain basis set of wave functions.

A rule of thumb is that a larger basis set will result in a better description of
the electronic states of a system. Kohn and Sham showed that finding the right
electron density involves solving a set of equations which involve only a single
electron [18, 20]. These pseudo one-electron Kohn-Sham equations are of the
form

$$[-\frac{\hbar}{2m}\nabla^2 + V(r) + V_{\mathrm{H}} + V_{\mathrm{xc}}]\Psi_i(r) = \epsilon_i \Psi_i(r) \ , \tag{1.5}$$

with the $V(r)$ summed potential of all nuclei, V_{H} the Hartree potential and
V_{xc} the potential describing the exchange and correlation contribution. The
main difference to the Schroedinger equation known from Hartree-Fock calcula-
tions [21, 22] is the Hartree potential V_{H} is no longer a summation over all pairs
of electrons, but rather the interaction of the single electron with the density of
all electrons. The exchange and correlation contribution is also a functional of
the electron density. Since it is in generally not known, several different approx-
imations are used two of which are the local density approximation (LDA) or a
generalized gradient approximation (GGA). A more detailed discussion of these
approximations is found elsewhere [18].

The challenge of DFT theory is that in order to solve the Kohn-Sham equa-
tions (1.5) one needs the Hartree potential. The Hartree potential is provided by
the electron density (in zeroth approximation the linear combination of atomic
orbitals), which on the other hand is given by the single electron wave functions
obtained by solving the Kohn-Sham equations (1.5). This recursion problem can
be solved in an iterative way similar to Hartree-Fock theory [21].

1. Guess a first electron density $n(r)$.

2. Solve Kohn-Sham equations to find the single particle wave function $\Psi_i(r)$.

3. Calculate a new electron density $n^{\mathrm{new}}(r)$ from the obtained single particle
   wave function $\Psi_i(r)$.

4. Compare $E_{\mathrm{xc}}^{\mathrm{new}}[\{\Psi_i\}]$ to $E_{\mathrm{xc}}[\{\Psi_i\}]$ proportional to $n(r)$ and $n^{\mathrm{new}}(r)$. If the
   total energies are the same, the ground state energy is found and therefore
   also the ground state electron density. If the energies densities differ, update
   the starting electron density and start again at 2.

Chapter 2

State of the Art of Studies on Transition Metal Doped Silicon Clusters

Transition metal doped silicon clusters analyzed in this thesis consist of one transition metal and $n = 6-19$ silicon atoms. These nano sized doped semiconductors can yield interesting properties like cage structures with symmetric geometries, high stability and low reactivity as well as a energy gab between the highest occupied molecular orbital and the lowest unoccupied molecular orbital (HOMO-LUMO gap) in the visible range, all depending on their size and composition. In this section the current state of research is presented, divided into sections about the structure, stability, reactivity and HOMO-LUMO gap, followed by a short outlook on potential future applications.

In the following sections the state of the art of experimental and theoretical results concerning transition metal doped silicon clusters is discussed. In order to introduce transition metal doped silicon clusters, first the geometric structure is discussed in section 2.1. After an idea how these systems may look like is established, experimental results corresponding directly to the geometry are shown: The reactivity of transition metal doped silicon clusters (cf. sect. 2.2). As it is directly linked to geometry, predictions of the structure can be obtained also experimentally with reactivity experiments.

The current state of research about the electronic structure of transition metal doped silicon clusters is discussed in detail in section 2.3. The last section 2.4 shows current progress on the research of cluster assembled materials from doped silicon clusters, featuring visions of future applications.

13

2.1 Geometric Structures of Transition Metal Doped Silicon Clusters

The presence of one transition metal atom leads to the formation of a cage structure, which is known for pure carbon clusters like C_{60} [23], but not found to be stable at for pure silicon clusters [24, 25]. The reason for the different behavior is a different hybridization behavior of the valence band, which is sp^3 for bulk silicon in contrast to either sp^2 (graphite) or sp^3 (diamond) hybridization for bulk carbon [26, 27]. Although the electron configuration of the valence states is similar with $2s^2 2p^2$ in carbon and $3s^2 3p^2$ in silicon since both elements are semiconductors located in the fourth main group of the periodic table, different hybridization is present due to a different overlap of s and p orbitals. Therefore pure silicon forms more compact structures. Calculated structures for pure silicon clusters [28, 29] and transition metal doped silicon clusters [28–32] are shown in figure 2.1. Since geometries are mainly calculated for neutral or anionic systems, in this case it is chosen to compare geometries of neutral silicon clusters and transition metal doped silicon clusters which have an larger overlap of calculated geometries in literature. In the few cases cationic geometries are found for both species, a similar trend is observed. Geometries from different authors vary, since finding the global minimum cannot be ensured. The assumption to have found the energetically lowest geometry is made, if after a long sampling time no lower lying isomer is found. In the pioneering experiments of Beck [4, 5] formation of transition metal doped silicon clusters was observed in a laser vaporization supersonic expansion apparatus. In the mass spectra, a high abundance of certain cluster sizes of transition metal doped silicon clusters was observed indicating a high stability of these clusters [4, 5, 33–35]. Formation of cage structures was supposed and corroborated by theoretical studies on the structure of MSi_n clusters [2] as well as photodissociation experiments [36], photoelectron spectroscopy [37], and analysis of the vibrational spectra obtained via infra-red multi photon dissociation [38]. The incorporation of a transition metal atom into the silicon cage is shown nicely with reactivity experiments monitoring the reactivity of the doped silicon clusters with H_2O molecules [33] or the formation of Argon - MSi_n cluster complexes [39] (cf. sect. 2.2). Clusters showing a low reactivity have a closed silicon shell and are referred to as endohedral MSi_n clusters. A high reactivity indicates a incomplete encapsulation of the transition metal. These cluster sizes are called exohedral MSi_n clusters. Theoretical calculations of MSi_n cluster geometries confirm the incorporation of the metal atom into the silicon cluster, if a
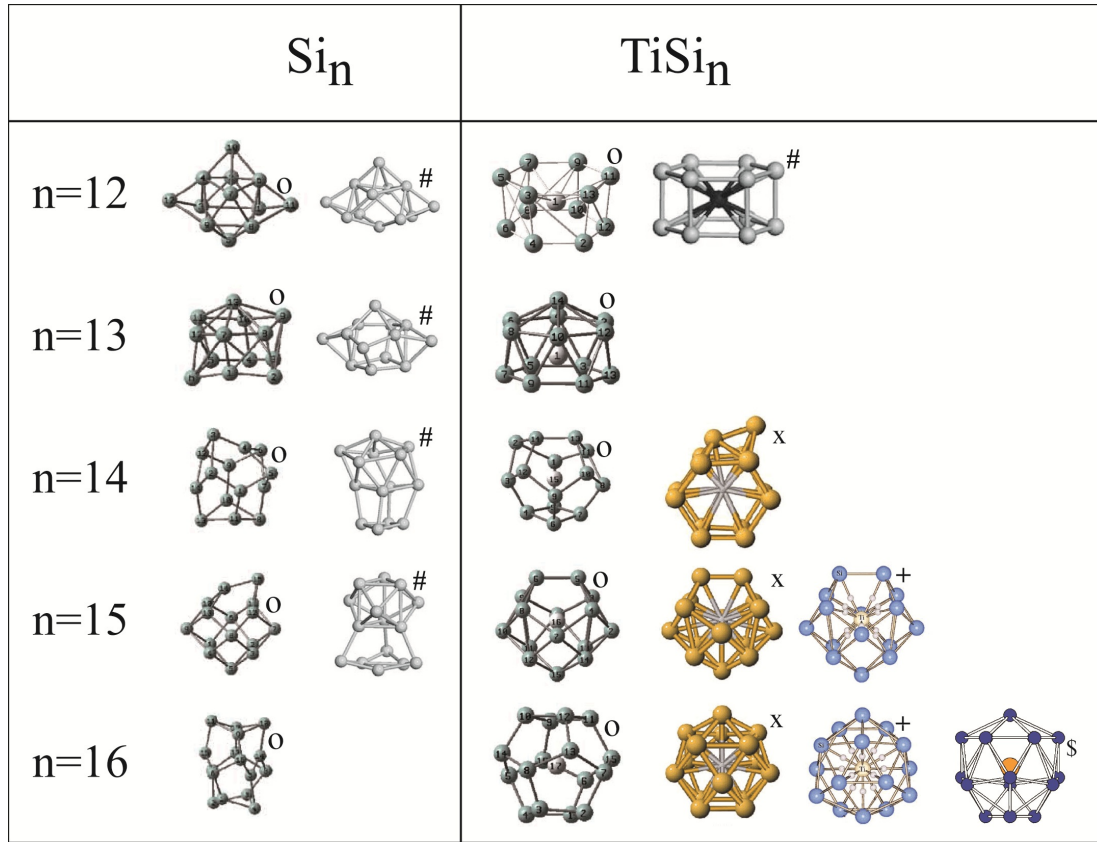
Figure 2.1: Calculated Structures of the energetic lowest geometries of neutral Si_n and $TiSi_n$
clusters. While pure silicon clusters form compact structures, in the $TiSi_n$ size regime from
$n = 12$ to $n = 16$ the Ti atom can be seen to be always in the center. Geometries from different
authors vary, since finding the global geometric minimum cannot be ensured. The data is taken
from various works: o [28], # [29], x [32], + [31], and \$ [30].

Cluster	Energy of second lowest isomer	Energy of third lowest isomer
VSi_{14}^+	0.08 eV [1]	0.14 eV [1]
VSi_{15}^+	0.47 eV [1]	0.69 eV [1]
VSi_{16}^+	0.040 eV [32]| 0.01 eV [1]	1.007 eV [32] | 0.25 eV [1]
VSi_{17}^+	0.11 eV [1]	0.25 eV [1]
VSi_{18}^+	0.04 eV [1]	0.44 eV [1]
VGe_{16}	0.117 eV [32]	0.982 eV [32]

Table 2.1: Energy of calculated geometric structures of transition metal doped silicon clusters
and VGe_{16}^+ with respect to the lowest energy [1, 32].

critical number of silicon atoms depending on the dopant atom is reached. Highly
symmetric geometries are found by theory for some of the transition metal doped
silicon clusters [1, 2, 6, 29, 31, 32, 40–47]. Especially symmetric MSi_n clusters are
the cationic VSi_{16}^+ and the isoelectronic neutral $TiSi_{16}$ and anionic $ScSi_{16}^-$. The
cationic VGe_{16}^+ is not strictly isoelectronic but isovalent, having the same number
of valence electrons. These geometric magic clusters have also an electronic shell

closure, as will be discussed in section 2.3. In addition, calculations showed most structures have few isomers at liquid nitrogen temperature (cf. tab. 2.1). The structure of these highly symmetric $MSi_{16}^{-/0/+}$ clusters is a Frank-Kaspar polyhedron [48] with an almost spherical structure in a T_d symmetry [1, 6]. The metal atom in the center is surrounded by 16 Si atoms located in two closely spaced shells, with four Si atoms in the first shell forming a tetrahedron.

Apart from reactivity experiments, indicating if and at which cluster size the transition metal is incorporated in a MSi_n cluster, structure determination is feasible via the vibrational spectrum of a cluster [38]. The vibrational spectrum of a MSi_n^+ cluster is obtained by infrared multi photon dissociation (IR-MPD) of the argon atom from a $MSi_n^+ \cdot Ar$ complex. Photon energy dependent absorption of an infrared photon heat up the cluster and triggers the dissociation of the argon atom. The rare gas atom is mainly a spectator, being loosely bound to the MSi_n^+ cluster. Because of the low bond strenght, the clusters original geometry is maintained. The absorption cross section is proportional to the depletion of the signal of $MSi_n^+ \cdot Ar$ clusters, measured via mass spectroscopy. The resulting experimental spectrum can be compared to theoretical vibrational spectra of possible geometric structures. Since the vibrational spectrum depends strongly on geometry, a good assignment of a geometry to the experimentally observed vibrational spectrum is possible. This method produces excellent results for MSi_n^+ cluster sizes up to $n = 8$. However, it becomes more challenging with increasing cluster size, as the number of vibrational resonances increase and unique assignment is more difficult. Furthermore, for endohedral cluster sizes the formation of $MSi_n^+ \cdot Ar$ complexes is heavily reduced (cf. sect. 2.2), which renders this method almost impossible to use for endohedral transition metal doped silicon clusters. Unfortunately, cluster sizes for which results on the geometry of MSi_n^+ are presented from IR-MPD do not overlap with the cluster sizes analyzed within this thesis.

2.2 Reactivity of Transition Metal Doped Silicon Clusters

The reactivity of MSi_n clusters depends strongly on the composition of a MSi_n cluster. It is as well a function of the dopant M as a function of the number of silicon atoms n, as shown in several experiments [33, 39, 49]. Reactivity is strongly correlated to the total encapsulation of the metal atom with silicon atoms. Ex-

periments [33,39,49] do not only show the exohedral to endohedral transition, but
also lead to important information about the possible behavior in a low vacuum
environment of few 10^{-2} mbar.

Probing the reactivity of clusters via the formation of cluster - rare gas complexes
has first been established for metal clusters [50]. Experiments on the formation
of Ar + MSi_n^+ → $MSi_n^+ \cdot Ar$ complexes [39] showed that complexes are exclusively
formed for exohedral cluster sizes. Additional experimental data on pure silicon
clusters showed no complex formation with argon atoms occurs for as low cluster
temperatures as 80 K. It is therefore concluded that the argon atom exclusively
binds to the metal atom in MSi_n clusters. The metal atom acts as a reactive
center, polarizing the argon atom. Thereby, a van-der-Waals bond is formed be-
tween the metal atom in the MSi_n cluster and the argon atom. The strength
of the bond between the metal and the argon atom can be extrapolated to the
bond strength at 0 K by temperature dependent measurements of the efficiency of
$MSi_n^+ \cdot Ar$ formation. These measurements are done in the temperature range be-
tween 80 K and 300 K [39]. The bond is shown to be weak, with binding energies
between 0.12 eV to 0.16 eV. Because of this weak binding, the clusters original
geometry is maintained, which is a great advantage of this experimental method.
Furthermore, a cluster size dependent strength of the bond is observed, with the
strength of the van-der-Waals bond being inverse proportional to the cluster size.
The better the metal atom is accessible, the higher the binding energy of the
van-der-Waals bond between the MSi_n^+ cluster and the argon atom. This corrob-
orates the conclusion of the argon atom binding exclusively to the reactive metal
center of the MSi_n^+ cluster.

Experiments with gases other than rare gas showed similar results in the de-
termination of the exohedral to endohedral transition of MSi_n^+ clusters [33, 49].
Reactions with H_2O is as unfavored for pure silicon clusters as for endohedral
doped silicon clusters of a similar size [33]. In contrast to argon adsorption, in
case of H_2O vapor a decrease of line intensity in mass spectrum of presumably
exohedral MSi_n^+ clusters is seen, while no new lines, corresponding to new formed
$MSi_n^+ \cdot H_2O$ complexes are observed [33]. In addition, no other lines increase in
intensity, as for example pure Si^+ clusters. This would indicate fragmentation
takes place and $MSi_n + H_2O$ fragments to $H_2OMSi_{n-x}^{0/+} + Si_x^{+/0}$. In a more recent
work [49], charge state dependence of the reaction process is observed. While the
cationic MSi_n^+ reaction toward H_2O is now reported to form $MSi_n^+ \cdot H_2O$ complexes,
neutral MSi_n clusters tend to form $MSi_n^+ \cdot H_2O$ as well as $MSi_n^+ \cdot O$ complexes. The
anionic species MSi_n^- is reported to exclusively form $MSi_n \cdot O^-$ complexes. As

mainly the metal is the reactive center of the $\mathrm{MSi}_n^{+/0/-}$ cluster, a metal (M) to ligand (H_2O) charge transfer in case of MSi_n^- is supposed to explain the charge state dependent reaction process. The excess charge on the cluster is transferred to the H_2O molecule, which leads to H-O bond dissociation.

A charge dependency is also observed in the exohedral to endohedral transition of $\mathrm{MSi}_n^{+/0/-}$ clusters for equal transition metal dopands M. While the cationic species features the transition at larger cluster sizes n, the anionic species always shows the lowest cluster sizes n for endohedral to exohedral transitions in $\mathrm{MSi}_n^{+/0/-}$. Neutral MSi_n exibit the exohedral to endohedral transition at intermediate cluster sizes n. It is suggested that the silicon cage of the anionic species is larger, covering the metal atom with a higher efficiency, while the cationic cluster has a smaller sized silicon cage, which needs more silicon atoms to effectively incorporate the metallic reactive center atom.

The experiments done in the framework of this thesis include a reactivity analysis of MSi_n^+ clusters exposed to O_2. The results are discussed in chapter 5 with respect to the experiments described above .

2.3 Electronic Structure of Transition Metal Doped Silicon Clusters

The electronic structure of transition metal doped silicon clusters has been calculated for a large number of neutral and anionic clusters, mostly focusing on the valence electrons involved in the binding process [1, 6, 29–31, 42–44, 51, 52]. Photoelectron spectroscopy studies of the valence band [33, 35, 37, 51, 53] are mostly restricted to anions due to laser photon energy limitations. The measurements can be reproduced by DFT calculations, which makes comparison with theory possible. On the other hand, studies on cationic clusters are sparse at the moment [1, 31, 43]. Nevertheless, calculated valence states are available [1], giving information about the HOMO-LUMO gap. HOMO-LUMO gaps of about $2\,\mathrm{eV}$ have been calculated for certain $\mathrm{MSi}_n^{+/0/-}$ cluster sizes that show a very high stability evident by a high abundance in mass spectra.

A silicon cluster can be stabilized by incorporation of a transition metal atom, as can be seen from the calculated binding energy difference of the two species [31]:

$$E_b = E(\mathrm{Si}_n) + E(\mathrm{M}) - E(\mathrm{MSi}_n) \tag{2.1}$$

Explanations for the stability are given in form of two different theoretical ap-

16-I
Sc⁻: 0.00, 1.91, 1
Ti : 0.00, 2.09, 1
V⁺: 0.01, 2.25, 2

16-II
Sc⁻: 0.02, 2.12, 2
Ti : 0 .03, 2.17,2
V⁺: 0 .00, 2.25, 1

16-III
Sc⁻: 0.03, 1.81, 3
Ti : 0.25, 2.01, 3

16-IV
Sc⁻:0.14, 1.04, 4
Ti : 0.40, 1 .32, 4
V⁺: 0 .50, 1.50, 3

16-V
Sc⁻: 1.23, 0.74, 9
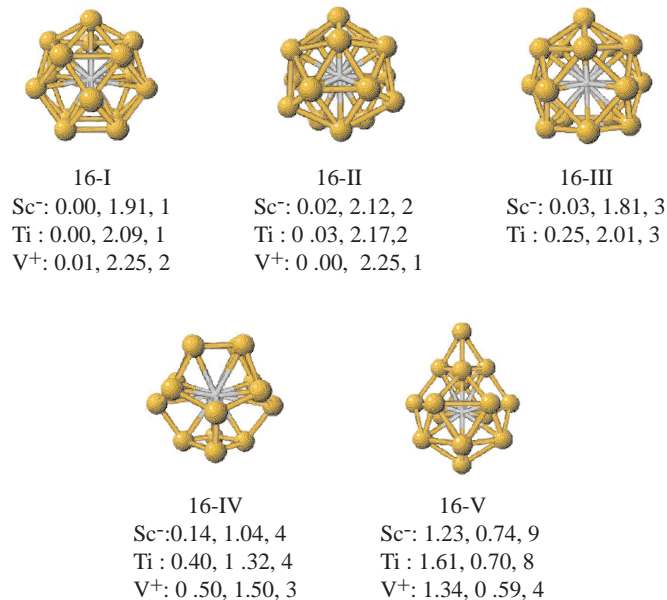Ti : 1.61, 0.70, 8
V⁺: 1.34, 0 .59, 4

Figure 2.2: Calculations of the equilibrium structures of MSi_n clusters ($M=V^+,Ti,Sc^-$) given by structural relaxation using DFT. Given below each structure the energy difference (eV) with respect to the energetically lowest lying geometry, the calculated HOMO-LUMO gap (eV) as well as the ordinal number of the isomer [1]. Note that despite the clusters being isoelectronic, the lowest geometry for the vanadium doped cationic cluster (16-I) differs from the titanium doped neutral and scandium doped anionic silicon cluster (16-II). The third isomer for the later ones is not found for the vanadium doped silicon cluster at all.

proaches. The first one is a simple shell model [54,55] also used for alkali clusters resulting in a jellium model based electron counting rule [31,42]. The theoretical approach suggests that bonding between silicon atoms of the silicon cage needs three of the four valence electrons of the silicon atom, and the remaining valence electron is dedicated to the silicon transition metal bond. The valence electrons dedicated to bonds of the empty silicon cage and the valence electrons responsible for the empty cage to transition metal binding are treated as two different systems. The main interest lies in the binding mechanism of the empty silicon cage to the transition metal. It is suggested [31] that the valence electrons of the transition metal core and the contribution of one valence electron from each silicon atom of the silicon cage can be treated as a free electron gas within the boundaries of the empty silicon cage. In the jellium potential of the cage structure, a shell closure is achieved at 18 and 20 electrons (cf. fig. 2.3), which results in enhanced stability if achieved. Next to other MSi_n clusters, $ScSi_{16}^-$, $TiSi_{16}$ or VSi_{16}^+ fit the requirements. Each of the 16 silicon atoms contributes one electron ($16 \times e^-$) and four valence electrons are present in the scandium anion, neutral

titanium atom or vanadium cation. Therefore a shell closure of 20 electrons and the configuration $1s^2 1p^6 1d^{10} 2s^2$ is achieved (cf. fig. 2.3), thus explaining the high stability of the isoelectronic VSi_{16}^+, $ScSi_{16}^-$ and $TiSi_{16}$. It should be noted that the states this model was originally designed for spherical metal clusters and quantum numbers follow nuclear physics convention and are not to be mistaken with atomic quantum numbers [55].
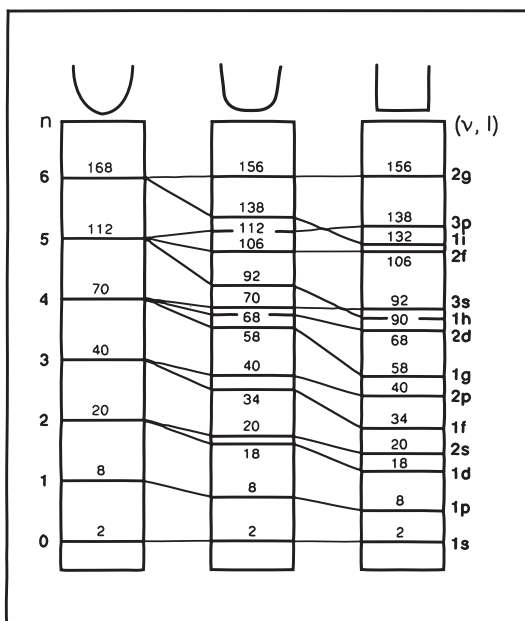

Figure 2.3: Energy levels of a three dimensional spherical (left), square-well (right) and intermediate potential (middle). The quantum numbers follow nuclear physics convention. The total electron occupation is stated at each energy level [55].

The second approach mainly explains the remarkable stability of VSi_{16}^+ [1]. The results of the complete DFT analysis of the geometry of the isoelectronic $ScSi_{16}^-$, $TiSi_{16}$, and VSi_{16}^+ revealed a slightly different geometric ground state structure in case of the vanadium doped cluster despite the same electronic configuration, as is shown in figure 2.2. The high stability of VSi_{16}^+ is also observable in the calculated binding energy difference to $ScSi_{16}^-$ and $TiSi_{16}$ (cf. equation (2.1) [1]), as well as in gain of stability relative to the neighboring MSi_n clusters with $n = \pm 1$, called second difference in the clusters energy [1]

$$\Delta_2 E_n(MSi_n) = E(MSi_{n+1}) + E(MSi_{n-1}) - 2 \cdot E(MSi_n). \qquad (2.2)$$

The binding energy as well as the clusters second energy difference are depicted in figure 2.4. The energetically lowest geometry 16-II (cf. fig.2.2) of VSi_{16}^+ is a Frank-Kasper polyhedron in tetrahedral symmetry T_d with the silicon atoms

arranged in two closely spaced shells with 4 and 12 silicon atoms respectively [1].
The energetically near lying geometry 16-I is nearly identical with 16-II, but with
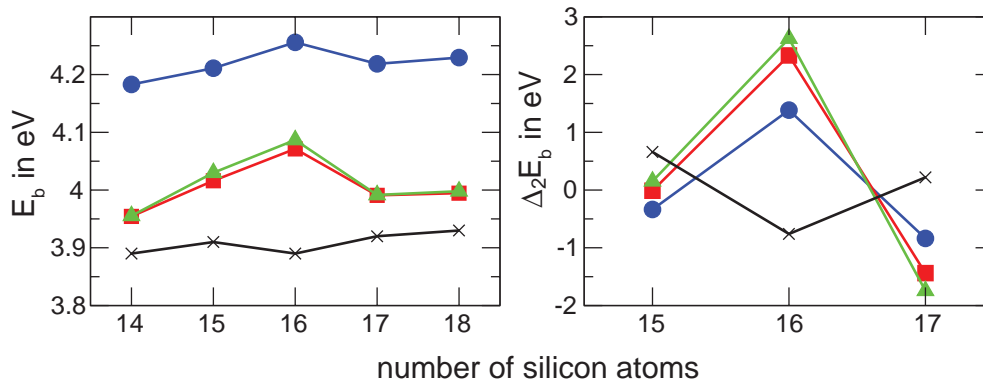a slight distortion, with the triangle along the threefold axis rotated by 30°. Due

Figure 2.4: Calculated binding energy E_b(left) and second difference in binding energy (right)
for M=(Sc$^-$, Ti, and V$^+$; $\bigcirc$, $\square$ and $\triangle$ respectively) doped MSi$_n$ clusters (cf. equation (2.1)
and (2.2)). Pure Si$_n$ clusters are shown as crosses. The line is only a guide to the eye [1].

to the nearly spherical geometry and the fact that the electronic charge distri-
bution of a perfect tetrahedral molecule behaves approximately like a spherical
distribution, DFT calculations of the valence DOS can be done in the framework
of a spherical potential model. Calculations on the density of states in this poten-
tial of the lowest VSi$_{16}^+$ isomer, the tetrahedral Frank-Kasper polyhedron 16-II,
are presented in figure 2.5. This DOS of the cluster represents the electronic
structure of the valence states. It should be noted that the quantum numbers
shown are not atomic quantum numbers. Due to the nearly spherical shape of the
potential, the angular momentum l is a good quantum number [1,3]. Furthermore
distinction of orbitals is given by the quantum number N, which corresponds to
the number of radial nodes plus one of the respective orbital. Therefore, the DOS
obtained by DFT calculations (cf. fig. 2.5 a) can be grouped into valence orbitals
according to spherical potential quantum numbers l (angular momentum) and N
(radial quantum number), $N\,l$ =(1s,1p,1d,1f,2s,...) [1]. The σ orbitals ($1\,l$) have
no radial nodes and are mainly located at the silicon cage [3]. The π orbitals
($2\,l$) have a radial node and therefore intensity in the center of the cluster [3].
Therefore, the bonding among the silicon atoms in the empty spherical cage is
mediated by σ orbitals without radial notes (1s,1p,1d,1f,1g). Bonding of the cage
to the transition metal dopant on the other hand has to be done by the π or-
bitals, since only these orbitals overlap with the metal atom in the center of the
cage (cf. fig. 2.5 b), for which the quantum numbers are again denoted in atomic
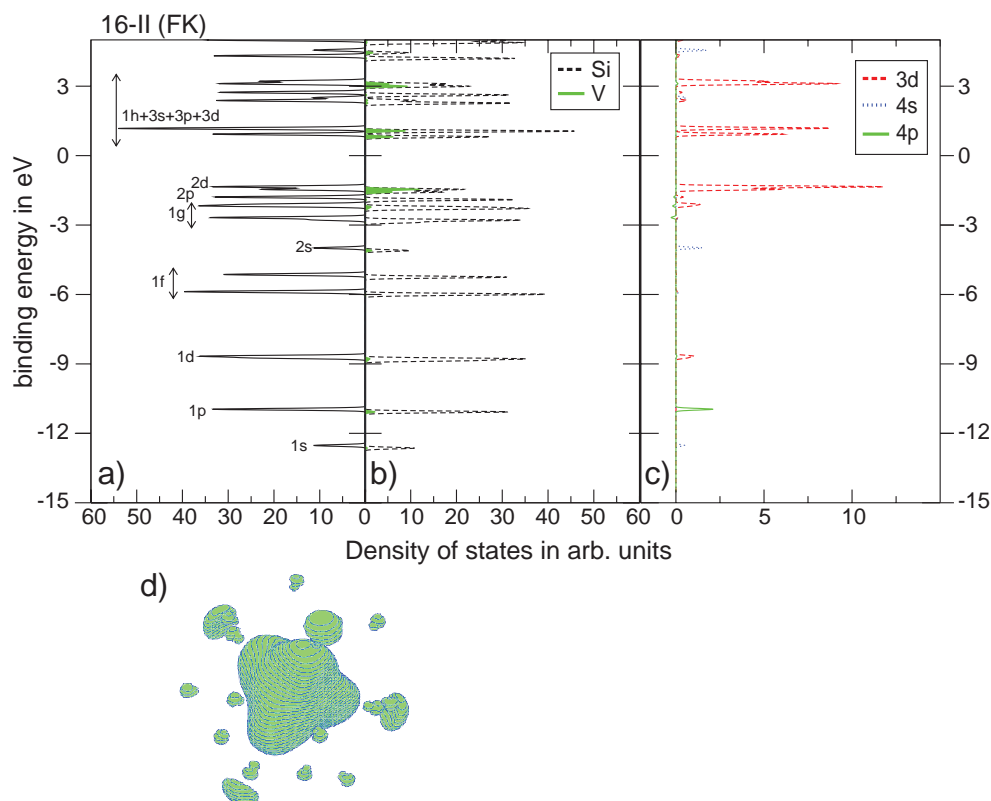
Figure 2.5: DFT calculation according to the spherical potential model of the DOS of the tetrahedral 16-II Frank-Kasper geometry (cf. fig. 2.2). a) The density of states with the quantum numbers according to the spherical potential model. The splitting of states is due to the T_d symmetry of the structure. b) The projected DOS of vanadium and c) the orbital projected DOS [1]. In the lower panel d) isosurface of the electron distribution, showing the tetrahedral symmetry [32].

quantum numbers[1]. These orbitals hybridize with the metals 3d orbitals if they have the same angular momentum character [1, 3, 56]. Therefore, the cage 2s and 2d orbitals can hybridize with the metal 4s and 3d orbitals. These hybrid orbitals form the HOMO bonding orbital of the cluster. Since the orbitals degeneracy is lifted due to the T_d symmetry, hybridization is also possible, if the orbital splitting of the energy level has the same components, which are for tetrahedral symmetry [1]:

---

[1]When describing orbitals in the following sections a mixing of the nuclear and the atomic convention is inevitable. When core level states of atoms are described, this is done exclusively in atomic notation. When describing orbitals of the transition metal atom of a MSi_n^+ cluster, again the atomic notation applies. Valence states of the whole system however are denoted in the nuclear notation often used for spherical potentials in cluster physics [1, 3, 6].

s (a_1)

p (t_2)

d $(e + t_2)$

f $(a_2 + t_1 + t_2)$

g $(a_1 + e + t_1 + t_2)$

h $(e + t_1 + 2\,t_2)$

i $(a_1 + a_2 + e + t_1 + 2\,t_2)$

The splitting of states due to T_d symmetry causing the degeneracy of states
present in a perfect spherical potential to be lifted, is clearly observable in fig-
ure 2.5 b, showing the DOS projected to the transition metal states [1]. The
former transition metal 3d state features now three energetically distinguishable
contributions, which contribute to different hybrid states. While one part of the
metals 3d states hybridizes with the cage 2d states to an bonding orbital, the
other two parts contribute to unoccupied silicon cage states. Due to the energeti-
cally equal position and equal components e and t_2, the metal 3d and silicon cage
1h orbitals can hybridize [1, 3] and form the antibonding LUMO of the cluster.
Furthermore, the unoccupied orbitals 3d and 3s of the cage can hybridize with
the transition metal unoccupied 4s and 3d states forming additional antibonding
orbitals.

The total electron count to fill the valence states of the cluster is 68 ($1s^2$, $1p^6$,
$1d^{10}$, $1f^{14}$, $2s^2$, $1g^{18}$, $2p^6$, and $2d^{10}$), which results in a shell closure of the last
filled 2d shell. Since 64 valence electrons are provided by the sixteen silicon atoms
($16 \cdot 4 = 64$) the silicon cage needs four more electrons for the shell closure. The
empty cage can therefore be seen as tetravalent [57]. The four additional valence
electrons are provided by the vanadium cation V^+ ($5 - 1$), closing the 2d shell of
the cluster with a total number of 68 ($16 \cdot 4 + 5 - 1$) electrons. Since the cages 2d
states can be seen as the binding orbitals between the transition metal dopant and
the empty silicon cage [57, 58], the vanadium is stripped of its valence electrons,
which are now responsible for the binding between transition metal and empty
silicon cage. This leaves the vanadium dopant in a formal $3d^0$ configuration.

Apart from the high binding energy relative to the larger and smaller VSi_n^+ cluster
sizes, the calculated VSi_{16}^+ HOMO-LUMO gap of 2.25 eV also exceeds the ones
of the neighboring VSi_n^+ clusters, being 0.84 eV and 1.06 eV for VSi_{17}^+ and VSi_{15}^+
respectively (cf. fig. 2.2 and 2.6). The gap of VSi_{16}^+ can be seen in the DOS
(cf. fig. 2.5) between the HOMO, labeled as 2d, and the LUMO states, which
have a 1h, 3s, 3d, and 3p character. Since 68 valence electrons are needed to fill

the valence states of the cluster up to the 2d shell ($1s^2$, $1p^6$, $1d^{10}$, $1f^{14}$, $2s^2$, $1g^{18}$, $2p^6$, and $2d^{10}$), the shell closure of the last filled 2d shell is achieved for VSi_{16}^+, as discussed above [1].
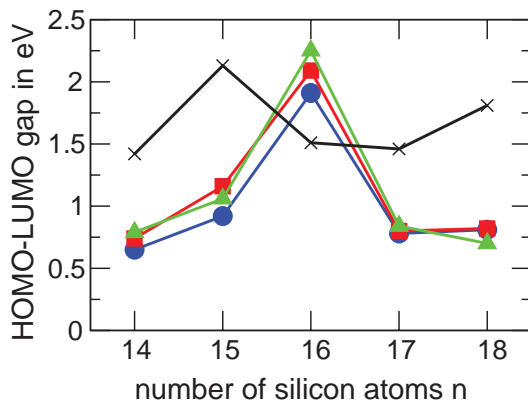

Figure 2.6: Calculated HOMO-LUMO gaps for Sc^-, Ti, and V^+ doped Si_n clusters (circles, squares and triangles respectively). The HOMO-LUMO gap of pure Si_n clusters is shown by the crosses [1].

Very recently, theoretical studies on the influence of the electron count in MSi_{16}^+, M=(Ti,V,Cr) clusters were performed [57]. This analysis was mainly triggered by results obtained within this thesis [58]. In section 6.3.1 it is shown that $TiSi_{16}^+$, VSi_{16}^+, and $CrSi_{16}^+$ show very similar fingerprints in their x-ray absorption spectra. $TiSi_{16}^+$ and $CrSi_{16}^+$ seem to mimic the spectrum of VSi_{16}^+, for which special properties like an electronic shell closure and high geometric symmetry are discussed above.

In case of VSi_{16}^+ the same geometric structure known from other studies [1] is obtained. It is shown that the geometries of $TiSi_{16}^+$ and $CrSi_{16}^+$ are similar to FK polyhedron of VSi_{16}^+. While VSi_{16}^+ exhibited the silicon atoms of the cage in two closely packed shells of 4 and 12 atoms respectively, the geometric degeneracies of the two shells are lifted in case of $TiSi_{16}^+$ and $CrSi_{16}^+$ [57]. Despite the slightly different structure, the geometric differences of the three different clusters are reported to be rather small and have insignificant effect on the electronic density of states [57]. To stress the importance of the cage structure influence on the density of states over the electron count in the different systems, the authors chose to calculate the DOS for different dopant atoms Ti, V, and Cr in the geometry of the ideal VSi_{16}^+ Frank-Kaspar polyhedral structure. The density of states found in all three cases [57] is similar to the one found before [1] and described above and shown in figure 2.5. However, due to the different number of valence electrons of Ti,V, and Cr, the occupancy of the DOS of the Frank-Kasper polyhedron 16-II

differs. While VSi_{16}^+ has a shell closure of the clusters 2p orbital, resulting in a high HOMO-LUMO gap as described above [1], for $CrSi_{16}^+$ and $TiSi_{16}^+$ open shell configurations are present. The 69 valence electrons present for $CrSi_{16}^+$ result in a single occupied molecular 1h orbital, whereas the 67 valence electrons of $TiSi_{16}^+$ show a single unoccupied state in the cluster 2d orbital. Because a similar DOS is maintained in VSi_{16}^+ with a closed electronic shell on the one hand, and $CrSi_{16}^+$ and Ti_{16}^+ on the other hand despite the open shell character, it is suggested that an electronic shell closure plays a minor role in the stability of MSi_{16}^+ clusters.

Furthermore, in order to test the assumption of the formal local d^0 configuration of the vanadium atom in VSi_{16}^+, the radial electron density distribution of VSi_{16}^+ is compared to the radial electron density distribution of $V^{5+}+Si_{16}^{4-}$. It is shown that a strong deviation is found especially a the dopant position. In fact, a neutral dopant in a singly positive charged silicon cage $V^0+Si_{16}^+$ is found to fit the radial electron density distribution of VSi_{16}^+ best. Further investigations of $TiSi_{16}^+$, VSi_{16}^+, and $CrSi_{16}^+$ indicate the dopant contributes each time one electron more to the 2d and 1h states of the cluster, while on the other hand, the number of electrons assigned to the silicon cage stays mainly the same [57]. This discrepancy is explained with an "adapting degree of metal-silicon hybridization" compensating the different total valence electron numbers in $TiSi_{16}^+$, VSi_{16}^+, and $CrSi_{16}^+$ [57]. The adaption of the metal-silicon hybridization is present for the clusters 2d and 1h valence state simultaneously, therefore compensating for either a missing electron for a 2d shell closure ($TiSi_{16}^+$) or an excess electron for a shell closure, located in the next higher state ($CrSi_{16}^+$) [57].

These promising results of the upcoming publication [57] are expected to start a new discussion on how doped silicon clusters may be treated theoretically.

2.4 Cluster Assembled Materials

In the past, considerations about using clusters as building blocks for new materials, in which the cluster properties can be utilized have caused a wide discussion. Transition metal doped silicon clusters are promising candidates for such a material [2, 40, 59–61]. Due to their low reactivity and high stability they are expected not to form a doped silicon solid, but to remain in their spherical shape and interact like solid made of noble gas atoms. However, there is an ongoing debate in theoretical groups, recently enriched by calculations of a drastically decreasing band gap upon the formation of aggregates [61]. Experimental investigations are therefore crucial to gain additional insights.

Since silicon is a semiconducting material, electron transport should occur in these materials. This brings up the question, if electro luminescence is possible, which would highly profit from size and composition of the nanoparticle adjustable band gap. Looking at the properties of these clusters in the gas phase is a very early but nonetheless important first step in the investigation of these clusters.

Chapter 3

Experimental Setup

The experimantal setup used to analyze the electronic structure of transition metal doped silicon clusters is shown in figure 3.1. The main idea is to measure the x-ray absorption of the clusters by means of ion yield spectroscopy. Clusters generated in a magnetron sputtering source are mass filtered and stored in a linear ion trap. Upon irradiation with monochromatic x-rays collinear to the trap axis the clusters fragment. After pulsed extraction from the trap, the ion yield of the fragments is measured as a function of photon energy.

The fundamental parts of the setup are a magnetron sputtering cluster source where the clusters are produced (cf. section 3.1). In the ion guide clusters are lead to the mass filter. The ion guide is also used as a collision / reaction cell, where different gases are introduced to the clusters (cf. section 3.2). The quadrupole mass filter is important for size selected analysis of the clusters (cf. section 3.3). The clusters can be illuminated with x-rays in a quadrupole ion trap which accumulates a sufficiently high target density for interaction with synchrotron radiation (cf. section 3.5). The detection of clusters and photo induced fragments can be conducted in a time-of-flight mass spectrometer with a reflector (cf. section 3.7). After a detailed discussion of each part, the data acquisition will be discussed (cf. section 3.9).
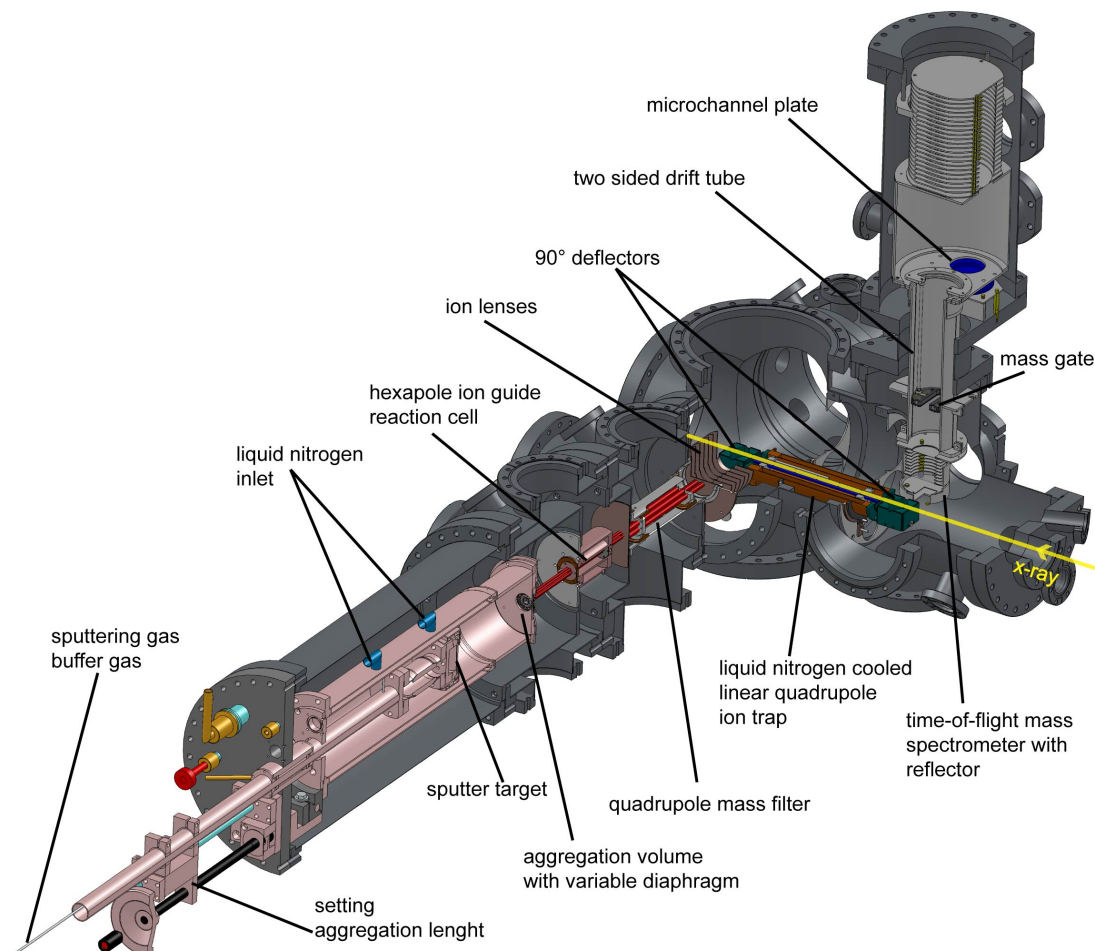
Figure 3.1: Experimental setup. From left to right: Clusters produced in the liquid nitrogen cooled aggregation volume of the magnetron sputtering source are led by a hexapole ion guide to the mass filter. The hexapole ion guide can also be used as a reaction cell by introducing gas through a leak valve. After mass selection, the clusters are stored in an ion trap. Upon irradiation with x-ray photons, the clusters fragment. The photon energy dependent ion yield of the fragments is analyzed in the TOFMS.

3.1 Cluster Source

The cluster source is a standard magnetron sputtering source from von Issendorff group [62]. This kind of cluster source is convenient for producing a broad cluster size distribution of charged as well as neutral clusters in a continuous cluster beam. In the source atoms are sputtered off a target material by high energetic argon ions produced in a direct current (dc) plasma discharge. The magnetron sputtering head is mounted in a double walled aggregation tube cooled by liquid nitrogen. The magnetron head houses the sputter target, which is located in a magnetic field produced by permanent magnets. The field lines cross the target two times, as one pole of the magnet is located behind the target forming a ring

and the other one is behind the target in the middle (cf. fig.3.2). Between the

gas inlet

N

S

N

· He atom
· Ar atom
· Ar⁺ ion
· Si atom
· metal atom

metal sputter target
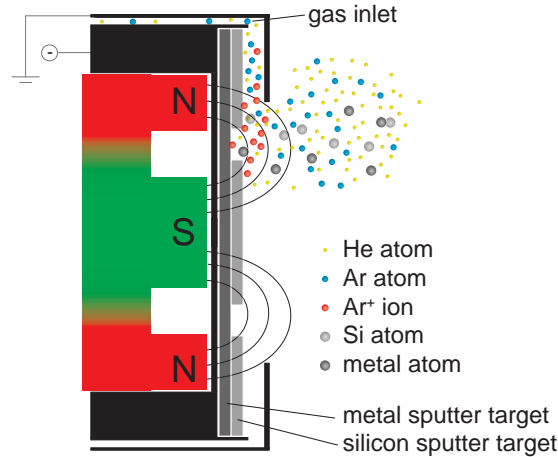silicon sputter target

Figure 3.2: Schematic view of the magnetron head of the cluster source. The target material is located in a magnetic field crossing the target. The sputtering gas is led to the target from the side and is ionized in a dc potential between the target and the front metal of the sputtering head. In case of transition metal doped silicon clusters, the sputtering target consists of two separate targets. The metal target is located behind the silicon target. Sputtering with argon ions of the metal is achieved via holes in the silicon target.

disc shaped target and a ring shaped anode an argon and helium gas mixture is introduced. The gas is ionized by the permanent plasma discharge and the ions are accelerated towards the target material. The magnetic field enhances ionization efficiency of the gas by prolonging the way of the electrons produced in the ionization process toward the anode. The target material is sputtered mainly by argon ions.

If heterogeneous clusters are produced, the target usually consists of two different materials, which are co-sputtered. In case of transition metal doped silicon clusters, the silicon target is located in front of the transition metal target. Sputtering of the transition metal is achieved through holes in the silicon target, as shown in figure 3.2. Since dc sputtering is used, the silicon target has to be conductive to avoid charging of the silicon surface. A charged surface would inhibit further sputtering, as the potential between the target and the ring anode would break down. Therefore, silicon targets used for the production of pure silicon clusters and transition metal doped silicon clusters are mildly boron doped to introduce conductivity to the silicon target.

Cluster growth is initially triggered by forming dimer seeds. If not sputtered off the target material as a dimer, these seeds are formed by three body collisions (cf. fig. 3.3). The pressure inside the aggregation tube, mainly influenced by the amount of helium in the gas mixture, is as high as 10^{-1} mbar to 1 mbar. This rel-

atively high pressure for vacuum applications increases the aggregation efficiency. A high pressure and a low temperature, provided by liquid nitrogen cooled tube walls, increase the probability of three body collisions. The cooling slows down the atoms enhancing the collision duration whereas a higher pressure increases the collision rate [63]. If the cluster seed is formed, cluster growth proceeds by
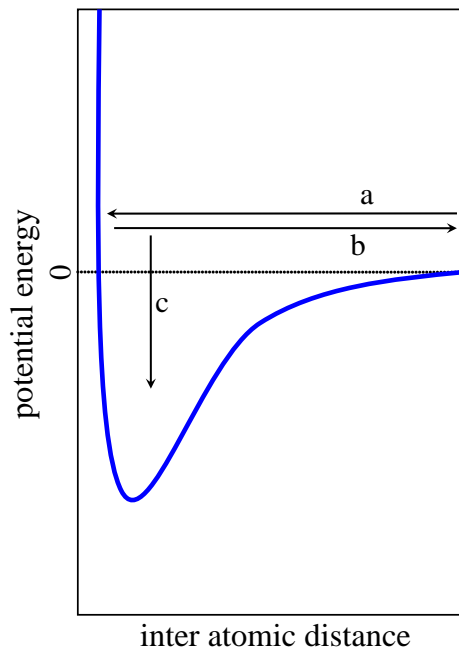

Figure 3.3: Schematic of the process of three body collisions. Clusters can only form, if a cluster seed in the form of a dimer is present. The dimer forms by means of three body collisions, with a third participant taking the kinetic energy out of the system. The collision has to take place when the participants are within the binding potential of the dimer. (a) collision partner approaches, (b) collision between two atoms, collision partner is deflected, (c) three body collision has taken place, the collision partners energy was transferred to a third collision participant.

successive addition of new atoms. The excess binding energy is carried away by the cold helium buffer gas.

The growth process allows reorganization of the geometric structure of the clusters, as every new bound atom heats up the cluster by the amount of the binding energy. This energy is slowly taken from the cluster by collisions with the buffer gas, giving the cluster time to reorganize to the energetically preferred geometry. This tempering of the clusters analyzed in this thesis therefore leads to energetically low lying geometric structures [1, 26, 28, 31, 32, 38, 43]. The temperature of the clusters is about 120 K when leaving the source. It can be expected that only a few isomers are populated at the analyzed cluster sizes and temperature.

The cluster size distribution can be controlled by various factors: The power of

the electric discharge, the aggregation length, the mixture ratio of the helium buffer and argon sputtering gas, the flow speed of the gas mixture and the gas pressure inside the aggregation tube. A typically used power setting of the discharge is about 10 to 20 W for transition metal doped silicon clusters. Tuning power and amount of argon determines the provided material for cluster growth. The aggregation length can be controlled by shifting the position of the magnetron head inside the aggregation tube. The aggregation length and the gas flow velocity affects the time a cluster accumulates material. The aggregation length is adjustable by a linear vacuum feed through. The composition of the gas mixture is controlled by two gas flow controllers. The amount of argon, which is usually about 80 sccm, adjusts the free target material available whereas the helium flow, which is usually about 500 sccm, mainly influences the speed of the gas and, in combination with a variable diaphragm at the exit of the cluster source, the gas pressure.

Due to the complexity of the parameter space tuning the cluster source for a designated cluster distribution requires a lot of experience in its operation. Three body collisions are, for example important for initial cluster growth, but if only sparse target material is present in the aggregation tube and the rate of three body collisions is high, cluster growth and final cluster size is diminished by the large number of competing cluster seeds.

Exiting the source through the variable diaphragm, the clusters can be accelerated into the next stage, the hexapole ion guide, by a tunable potential applied to the diaphragm. The potential of the diaphragm is mainly effective on charged clusters after leaving the cluster source, where a lower buffer gas pressure is present. While still in the aggregation tube, the cluster trajectory determined by the gas stream, the potential of the diaphragm is of minor importance.

3.2 Hexapole Ion Guide / Reaction Cell

The linear hexapole ion guide transfers the charged clusters from the cluster source to the mass filter via two differential pumping stages (cf. fig. 3.1). A radio frequency (rf) potential is applied to the two sets of electrodes of the hexapole, resulting in a radial confining potential keeping cluster ions on axis. The phase shift between the rf potential of each pair is 180°. The cluster entrance side of the ion guide is located in the sources chamber, where the base pressure is about 10^{-2} mbar. The chamber ends with a 3 mm aperture within the ion guide, which works as a differential pumping stage. The middle part of the ion guide behind

this aperture is mounted in a metal housing and ends with a second aperture. The volume has an inlet for gas or water vapor and is used as a reaction cell. Chemical reactions can be studied by introducing various gases to the cluster beam at this stage. Furthermore, by reactions with oxygen doubly doped clusters, partly overlapping with lines of singly doped clusters in the mass spectrum, can be discriminated from the beam (cf. chap. 5). Usage of this chemical etching technique is crucial to discriminate multiple doped clusters from the experiment, thus simplifying subsequent mass selection. In the cluster size region of interest ($n = 1 - 18$) the silicon shell of doubly transition metal doped silicon clusters $M_2Si_n^+$ is not completely closed around the metal atoms, in contrast to singly transition metal doped silicon clusters MSi_n^+. The oxygen pressure present inside the reaction cell p_r can be adjusted with a leak valve. The actual pressure inside the reaction cell is not measured directly and has to be calculated with knowledge of the pressure in the vacuum chamber p_v, the throughput S of the vacuum pump, and the leak rate q_{rv} [64] of oxygen through the reaction cells aperture to the vacuum chamber. The chamber's pressure in dependence of the leak rate and vacuum pump throughput is

$$p_v = \frac{q_{rv}}{S}, \text{ with}$$

$$q_{rv} = \sqrt{\frac{k_B T}{2\pi M_{mol}}} \left(1 + \frac{3}{8}\frac{l}{r}\Phi_K(\lambda)\right)^{-1} \quad 2\pi r^2(p_r - p_v)$$

$$\lambda = \frac{l}{r}$$

$$\Rightarrow p_r = \frac{\left(1 + \frac{3}{8}\frac{l}{r}\Phi_K(\lambda)\right)p_v S}{2\pi r^2 \sqrt{\frac{k_B T}{2\pi M_{mol}}}} + p_v, \tag{3.1}$$

with the Temperature T, the molar mass of the respective gas molecule or atom M_{mol}, the length l and radius r of the exit aperture. The correction factor $\Phi_K(\lambda)$ is given in [64] on page 112. For the present geometry of $l = 1\,\text{mm}$ and $r = 1.5\,\text{mm}$ the correction factor is $\Phi_K(^2\!/\!_3) \approx 1.31$. However, the pressure in the vacuum chamber measured with a cold cathode gauge is inaccurate. The calibration of the gauge is with respect to air and not only oxygen. The resulting error is neglected.

Furthermore, the reaction cell double walled housing can be cooled by liquid nitrogen or heated with a thermocoax heating element. A thermocouple junction is used to monitor the temperature of the hexapole housing. Chemical reactions can therefore be measured as a function of cluster temperature. However, the

reaction measurements of transition metal doped silicon clusters are conducted at room temperature of the hexapole. Therefore temperature dependent experiments are not discussed in the following.

After the second aperture the last part of the ion guide is located within a second vacuum chamber. In this chamber the base pressure is lowered to 10^{-5} mbar. The ion guide ends in front of the entrance aperture of the quadrupole mass filter.

By means of the adjustable rf voltage and frequency as well as an adjustable direct potential for all six electrodes and a adjustable potential for both the apertures, the transmission of the ion guide can be tuned to transmit a designated cluster size distribution. These are additional parameters to the cluster sources parameters, used to obtain a high cluster abundance.

3.3   Mass Filter

The linear rf mass filter [65] is build like a linear quadrupole ion guide with an entrance and exit aperture. The rf potential, which is again phase shifted by 180 degrees for neighboring electrodes, has the amplitude U_{rf}. The static potential U_{static} is equal for all four electrodes. In case of mass filtering, an additional potential is applied to the electrodes, which is positive for one of the pairs U_+ and negative U_- for the other pair. The total potential for each pair of electrodes, U_1 and U_2 can therefore be written as

$$U_1 = U_{\text{static}} + U_+ + U_{\text{rf}} \sin \omega t \tag{3.2}$$

$$U_2 = U_{\text{static}} + U_- + U_{\text{rf}} \cos \omega t, \tag{3.3}$$

with the rf frequency ω and the time t. The trajectory of charged particles within the electric field 3.3 of the mass filter is given by Mathieus differential equations:

$$\frac{d^2x}{d\tau^2} + (a_2 + 2q_2 \cdot \cos(2\tau)x = 0 \tag{3.4}$$

$$\frac{d^2z}{d\tau^2} - (a_2 + 2q_2 \cdot \cos(2\tau)z = 0, \text{ with} \tag{3.5}$$

$$a_2 = \frac{4qU_\pm}{mr_0^2\omega^2} \tag{3.6}$$

$$q_2 = \frac{2qU_{\text{rf}}}{mr_0^2\omega^2} \tag{3.7}$$

$$\tau = \frac{1}{2} \cdot \omega t \tag{3.8}$$

In these equations m is the mass of the particle and r_0 the radius of the quadrupole rods. The solution for stable trajectories through such an electric field given by equations (3.4) to (3.8) can be illustrated in the form of a triangle (cf. fig. 3.4) as a function of a_2 and q_2. The denotation of parameters a_2 and q_2 is the historically established [66]. It can be seen that the ratio $a_2/q_2 = 2U_\pm/U_{\rm rf}$ depends only on the amplitude of the rf signal and the asymmetric part $U\pm$ of the static potential. A fixed ratio in the (a_2, q_2) parameter space is a straight line through the origin and with a slope $2U_\pm/U_{\rm rf}$. For the specific values $a_2 = 0.237$ and $q_2 = 0.706$ the line crosses but the tip of the triangle. These values describe infinite mass resolution of the mass filter. Leaving the ratio $2U_\pm/U_{\rm rf}$ unchanged but varying the amplitude of the two potentials will select the mass to charge ratio of the transmitted particle along the working line. The trajectories of particles not in
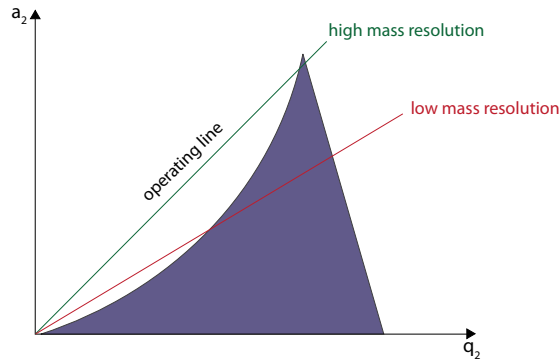

Figure 3.4: Visualization of the solution space of Matthieus differential equations. working parameters are shown as a straight line with the slope $2U_\pm/U_{\rm rf}$. The length of the line - triangle intersection resembles the set mass resolution of the mass filter, with the line crossing but the tip of the triangle for infinite mass resolution [67].

this mass to charge ratio regime are not stable and will build up high oscillation amplitudes until they finally leave the mass filter vertically or hit the mass filters rods. Mass resolution can be reduced if necessary by choosing a flatter slope of the line. The maximum mass resolution achieved also depends on the number of rf oscillations the passing particle will encounter. If it encounters only a few, the vertical oscillation of the particle might not build up high enough for the cluster to hit the filters rods. The kinetic energy of the clusters can be set by the potentials at the entrance and exit aperture as well as the potential $U_{\rm static}$.

Before the middle of 2010 all measurements were made with a home build mass filter with a mass resolution of $m/\Delta m \approx 50$. For later experiments a commercial mass filter[1] with a mass resolution as high as $m/\Delta m = 4000$ was available.

---

[1]Extrel GP-203 Quadrupol mass filter, http://www.extrel.com/ (June 2011)

3.4 Ion Lenses and First 90° Deflector

Adjacent to the rf mass filter the charged particles pass an ion lens system and a ninety degree deflector, which is followed by the ion trap entrance aperture. An ion lens system has the same impact on ions that normal lenses have on light. It consists of one or more apertures with a static potential. In this setup six apertures are used to focus the ions onto the entrance aperture of the ion trap behind the 90° deflector to increase particle density for the experiment. Because of the 90° deflector, the cluster ion flight direction leaves the straight path that connected the cluster source and the entrance of the deflector. The clusters are guided by a static potential. The deflector prevents neutral clusters that could have gotten up to this point along a straight line, from entering the ion trap.

3.5 Ion Trap

Since photon flux at synchrotron radiation facilities is limited to $10^{12}\,\mathrm{photons/s}$ to $10^{13}\,\mathrm{photons/s} \times 0.1\%$ bandwidth at $100\,\mathrm{mA}$ Ring current and absorption cross section at the transition metal L-edges is as low as $10\,\mathrm{Mbarn}$, it is necessary to accumulate high target density to gain a x-ray absorption signal. For spectroscopy on bulk materials this is achievable, but measurements of size selected clusters in the gas phase are challenging (cf. sect. 1.1.3). In order to reach a high target density compared with a normal ion beam a cluster source can produce, a linear ion trap (Paul trap) is used. By means of a linear ion trap, a density of charged particles up to a maximum of $5 \times 10^8\,\mathrm{cm}^{-3}$ can be reached [68].

The ion trap is about 20 cm long and build like a quadrupole ion guide with an entrance and an exit aperture. Charged particles are radially trapped by the rf potential. The particles enter the trap through the entrance aperture, the potential of which is just high enough for the particles to enter, as shown in fig. 3.5. The particles are slowed down by collisions with helium, which introduced into the trap as a buffer gas at about $4 \times 10^{-4}\,\mathrm{mbar}$ partial pressure[2], and are reflected at the exit apertures potential. The decrease of kinetic energy of the particles inside the ion trap prevents the particles from leaving the trap at the entrance aperture after being reflected at the exit aperture. The static potential inside the trap is a superposition of a static potential of the four quadrupole electrodes and

---

[2]Calculated by the usually set helium partial pressure in the vacuum chamber of $5 \times 10^{-6}\,\mathrm{mbar}$ with equation (3.1) with the presumption that the pressure gauge is showing the right pressure.
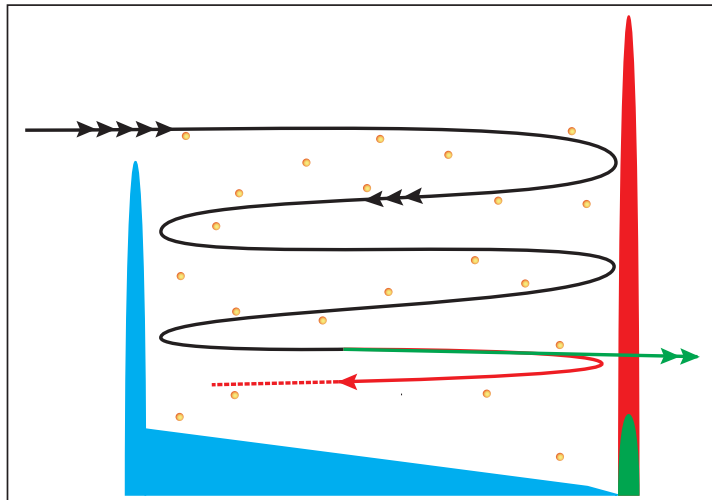
Figure 3.5: Schematic of the ion traps gradient potential and the entrance and exit apertures trapping potential. Static potentials are shown in blue. Clusters enter the trap and are reflected at the exit apertures potential (red) and slowed down via collisions with the helium buffer gas, visualized as yellow circles. Upon extraction, the exit apertures potential is lowered (green) for the clusters to leave the trap. Radial trapping is achieved via a quadrupole rf potential (not shown).

the potential of triangle shaped side electrodes positioned between the electrodes. The triangle creates an effective linear potential, which pushes the particles toward the exit aperture. Ion bunches can be extracted from the trap by lowering the potential of the exit aperture (cf. fig. 3.6).

The helium buffer gas also thermalizes the clusters, since the double walled housing of the ion trap is cooled by liquid nitrogen.Therefore rf heating has a negligible influence on the clusters temperature. The particles will remain in a low lying geometry until excitation with x-rays takes place. X-ray absorption of the accumulated particles is achieved by aligning the trap parallel to the x-ray beam, with the focus of the beam in the middle of the ion trap. Upon absorbing a x-ray photon, the particle will fragment or emerge multiply charged (cf. section 1.1 for more details). The rf amplitude is set in a way that product ions and parent particles are stored at the same time. By the pulsed potential of the exit aperture, a part of the fragments and parent particles are extracted from the ion trap towards the second 90° bender and adjacent mass analysis.

3.6   Second 90° Bender and Ion Lenses

After pulsed extraction from the ion trap, the particles are led trough a second 90° bender and focused into the first acceleration region of the time-of-flight

mass spectrometer (TOFMS). Focusing is necessary to increase particle yield of the beam, which is divergent after the extraction, as well as to increase mass spectrometer resolution, which depends on the spatial spread of the beam. In principle the time-of-flight mass spectrometer could be installed behind the exit of the trap. This way, however, the x-ray beam would pass through the first acceleration region ionizing the chambers residual gas inside this region resulting in an unwanted residual gas signal in the time-of-flight spectrum. However, more important and disturbing would be the additional signal of helium buffer gas from the ion trap. The helium buffer gas ionized in the ion trap will show up heavily in the time-of-flight spectrum limiting the maximum allowed amplification of the mass spectrometers micro channel plate (MCP).

In our setup the ions extracted from the ion trap disperse with respect to their masses while traversing the distance from the ion trap to the mass spectrometer. This is due to the same kinetic energy of the clusters gained in the extraction potential of the ion trap, which results in a mass dependent velocity of the ions. Therefore different ion masses arrive at the extraction region of the time-of-flight mass spectrometer with a mass dependent delay. The mass range analyzed can be selected by tuning the time delay between the pulsed extraction from the ion trap and the extraction pulse of the first acceleration region of the mass spectrometer (cf. fig. 3.6).

Measurements of only a designated mass range of x-ray induced daughter ions and cropping the huge amount of helium ions created by direct photo ionization and parent particles from the magnetron source, enables the full use of the amplification range of the micro channel plate. The parent particle is nonetheless visible in the mass spectra because of a constant parent cluster current from overflow of the trap. Obtaining the total mass range fragment ions are visible in, may require several runs at different timing delays of the trap - TOFMS pulses.
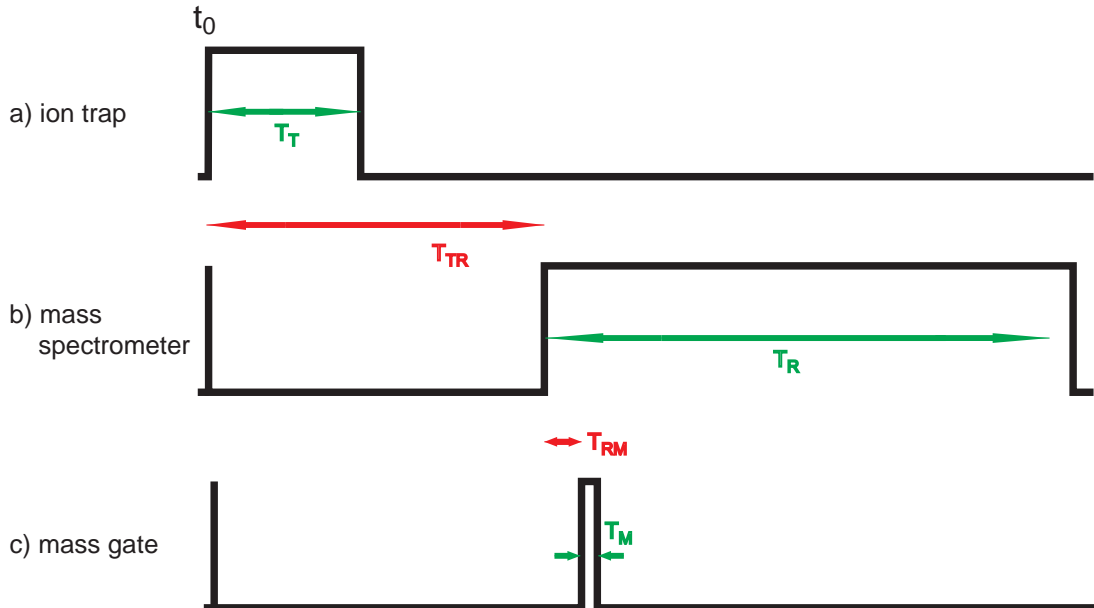
Figure 3.6: Sequence of the experiments pulsed potentials. All pulses are with respect to the initial trigger t_0. a) extraction of an ion bunch from the ion trap. The duration of the pulse T_T is variable and in the range between $1\,\mu$s and $10\,\mu$s. b) Extraction pulse of the TOFMS. The pulse starts with a delay T_{TR} with respect to the start of the ion traps extraction pulse. The delay selects the mass region of interest (see text) and has typically values between $10\,\mu$s and $50\,\mu$s. The TOFMS pulse duration is with $200\,\mu$s longer than the typical time of flight of the ions in the spectrometer, to prevent new ions leaking out of the ion trap to enter the spectrometer. c) Mass gate pulse deflecting a mass range inside the spectrometer that should not reach the MCP detector. With the delay T_{RM} the mass is chosen. The length of the pulse T_M is short with about $0.5\,\mu$s to only influence the designated mass.

3.7 Mass Spectrometer

The time-of-flight mass spectrometer [69] is the last stage of the experimental setup. The mass of particles can be measured with this kind of device. It is based on the dispersion of particles with different masses which hold the same kinetic energy while flying a defined path length. The time of flight can be re-calculated to a corresponding mass to charge ratio of the particle. The initial time is the start of the extraction pulse (cf. fig. 3.6), accelerating the particles perpendicular to the propagation direction in the prior stages (cf. fig. 3.1). In the following, the time-of-flight mass spectrometer will be explained in detail, since it was designed and built in the context of this thesis.

During a preceding diploma thesis [70] a two staged Wiley-McLaren TOFMS [69] was built, which was designed in connection with an experimental setup for XAS of neutral transition metal clusters [71]. Due to a low spatial distribution of the x-ray induced daughter ions in these experiments, the mass resolution was $m/\Delta m = 600$. This mass resolution was sufficient for the past experiment.

In the first version of the current experimental setup (cf. sect. 3.10), this two staged TOFMS was integrated. In the following experiments with ions, having a larger spatial spread in the initial position in the TOFMS, mass resolution dropped to $m/\Delta m = 200$. Since there was a high demand for particle recognition by their isotopic pattern to distinguish between undoped, singly and multiple doped silicon clusters, a new mass spectrometer was designed, featuring a reflector [72, 73] as well as a longer flight path thus increasing mass resolution to a maximum of $m/\Delta m = 1800$. In a second step, a mass gate was introduced to the mass spectrometer to discriminate transmission of a certain mass. This is mainly used for monitoring fragments of water clusters without the huge yield of argon ions lying in the same mass region as the H_2O fragments and originating from the vacuum chambers residual gas. Since argon is usually used for venting the vacuum chamber, it is very dominant in the residual gas composition.

3.7.1 Basic Principles

While the dispersion of charged particles can be achieved even in a simple gradient field, the introduction of a gradient free region after this field gives the possibility of space focusing particles with different starting points in space. The space spread distribution of particles will nonetheless have the same flight time for equal masses. A sketch of the principle of a one staged linear TOFMS is shown in figure 3.7. Particles starting behind a certain reference plane will leave the first stage (electrode to grid) into the field free region later than the reference particles, but due to their longer path through the field with a higher velocity, thus catching up with them somewhere in the field free region. This length is known as the spatial focus of the TOFMS. Introducing a third stage, a second acceleration stage, gives the possibility to choose the position of the spatial focus by adjusting the ratio of the two acceleration potentials. An additional reflector can improve mass resolution by extending the flight distance, thus increasing the dispersion of the masses, as well a making velocity focusing possible. Velocity focusing can focus particles with an initial velocity distribution parallel to the spectrometers axis. The velocity component perpendicular to the spectrometers axis does not have any influence on the spectrometers resolution.

When designing a TOFMS, the first step is to calculate the time-of-flight of a particle with the mass m and the charge z, with the spectrometers dimensions as variables. The starting position is given relative to a designated plane in the
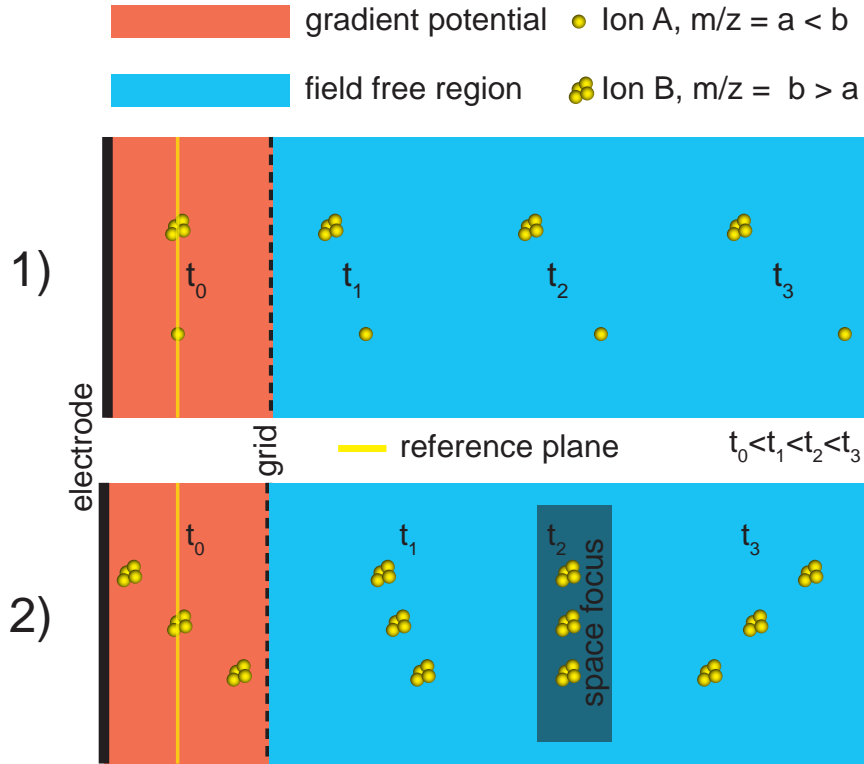
Figure 3.7: Principle of a time of flight mass spectrometer. 1) Ions with different masses disperse after acceleration in an electric field. 2) Ions starting left (right) of the reference plane gather a higher (lower) velocity due to a prolonged (shortened) path length through the electric field. The position in the field free region, where faster ions having a longer distance to fly in the acceleration region and slower ions having a shorter distance to travel, are at the same time at the same plane, is known as the spatial focus of the mass spectrometer. The detector is normally placed here.

middle of the first acceleration stage perpendicular to the spectrometer axis. The main idea is to eliminate all terms in the time-of-flight depending on the starting position of the clusters. The spectrometer dimensions and potentials are parameters of the equations. The solution space for this parameters are possible values for the new design. A review of this rather long equations is given in literature [69, 73, 74].

As can be seen from figure 3.8 particles need a forward energy to reach the MCP. Since this energy is not well defined due to its dependence on trapping parameters, the first part of the drift cylinder is segmented into two half cylinders, between which a deflecting potential can be applied. This allows an adjustment of the clusters kinetic energy in forward direction, perpendicular to the time-of-flight relevant spectrometer axis. This adjustment is necessary for the clusters to pass the first part of the drift region and renders the often used tilted reflector to change the trajectory of the particles unnecessary. The dimensions and poten-
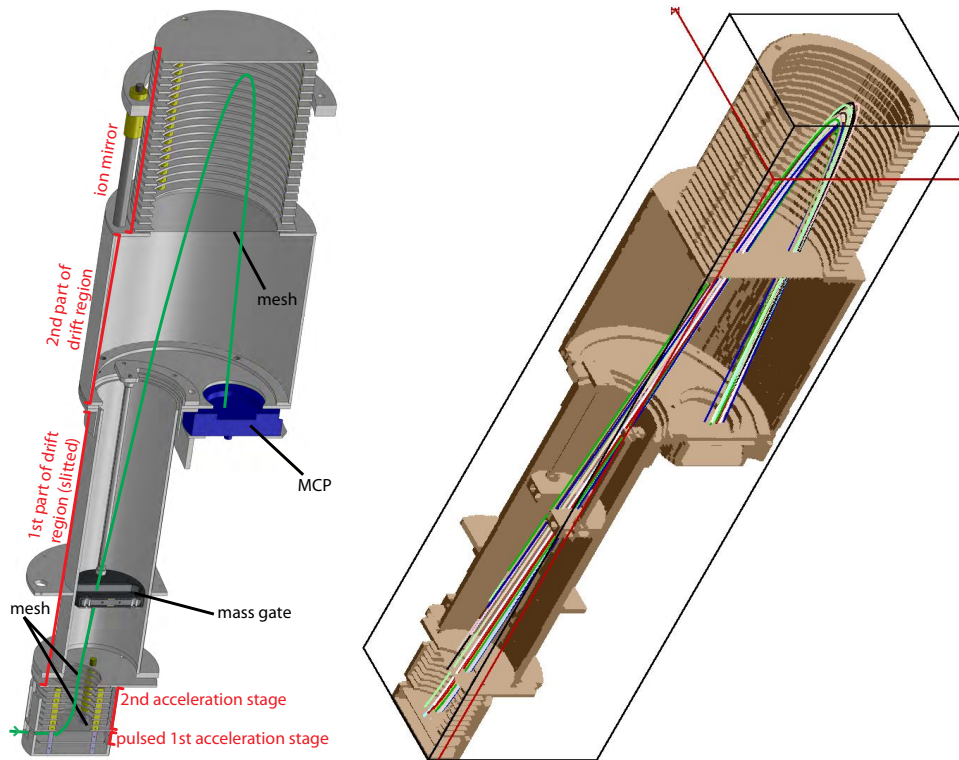
Figure 3.8: left: Blueprint of the TOFMS with flight path (green) of the particles
right: Simulated spectrometer with the same dimensions. The flight path of the particles was
calculated using Simion$^{©}$ [75].

tials predicted by the calculation do not always show the highest mass resolution
in the experiment. This can be due to distorted potentials and interference of
potentials of different stages of the mass spectrometer. It is therefore mandatory
to simulate the setup in order to preview the operability of the designated geom-
etry, especially because of the unusual approach of adjusting the particles kinetic
energy perpendicular to the spectrometer axis. The results of the simulation are
subject of the next section.

3.7.2 Simulation of the Particles Flight Path

Simulations of a preliminary design of a experimental setup can help to find
challenges not observed before. Therefore a simulation of the designed setup is
recommended after having calculated the potentials for ion lenses, guides, traps
or mass spectrometers. In the simulation electric field penetration and distorted
electric fields can be identified and the design can be refined accordingly.

The software SimIon$^{©}$ [75] was used to simulate the TOFMS. This program
package is used to calculate the trajectories of charged particles in electric and
magnetic fields for a given configuration of electrodes. The simulation software
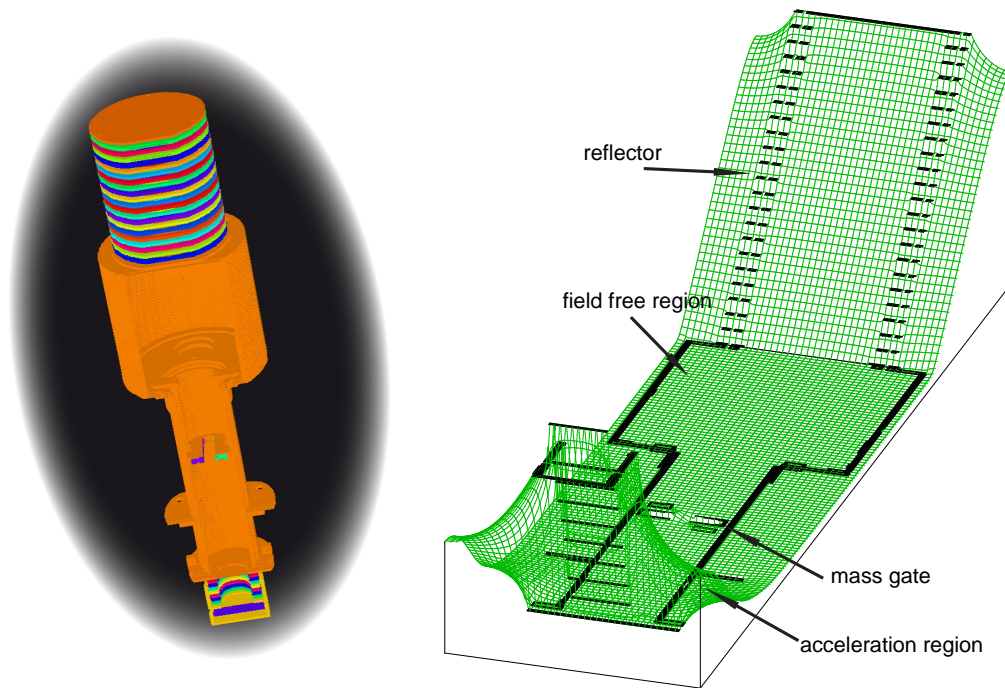
Figure 3.9: Left: Sectional view of the spectrometer in SimIon©. Different potential surfaces are shown in different colors. Right: Potential distribution inside the spectrometer. The potential is visualized by the green grid. Solid elements of the spectrometer are colored black.

calculates the trajectory of particles in the electric field given by superposition of all contributions of all electrodes after adjusting the user given potentials. An illustration of the spectrometers 3d model used for simulations is given in the left panel of figure 3.9. The color coded potentials show a momentary picture as the deflection of the particles in the mass gate is switched on, which only occurs when the mass to be discriminated passes the mass gate. The right panel of figure 3.9 shows the potential surface along the spectrometers axis, represented by the green grid. Simulation are helpful to show weak points in the design as insufficient electrical shielding of the flight path. Although the simulation shows that potentials given by theory do not necessarily give the best mass resolution for the given geometry, the potentials found in the simulation are similar to the potentials calculated. For the experimental setup it is helpful to adjust the potentials by setting the potentials from the simulation as initial values.

The right panel of figure 3.8 shows the flight path of particles through the spectrometer. This simulation of the particles flight path is used to evaluate the kinetic energy perpendicular to the spectrometer axis a particle needs to reach the MCP. The potential difference between the two segments of the first part of the drift cylinder is set to zero and only the forward energy of the particles is analyzed. The simulated value for the particles kinetic energy is about 15 eV,

which can be given to them before entering the spectrometer or in the slit part of the drift tube. However, in the latter case the kinetic energy given to the particles has to be slightly higher because they have less time to cover the distance to the MCP.

3.8 Synchrotron Facility

The source of the x-ray beam used for the experiment is the synchrotron facility BESSY II of the Helmholtz-Zentrum für Materialien und Energie GmbH (HZB) in Berlin, Germany. It is a third generation synchrotron radiation facility optimized for the soft x-ray energy regime. In this chapter, the basic principles of synchrotron generated x-ray radiation is explained, starting with the actual synchrotron and the storage ring with undulators[3]. In a second section the three beam lines will be discussed, at which the experiments on transition metal doped silicon clusters were performed.

3.8.1 Basic Principles of Synchrotron Radiation

Synchrotron radiation was first seen in 1947 at the General Electric Synchrotron [76]. It is generated by transversally accelerated charged particles like electrons or positrons with relativistic velocities [77]. The acceleration is a change in the particles kinetic energy or direction of flight due to a electric or magnetic force influencing the charged particle. At synchrotron radiation facilities the magnetic force constrains the particle on a curved path via Lorentz force. The angular distribution of the emitted photons of charged particles with a relativistic velocity is mainly collinear to the velocity due to relativistic effects in contrast to a toroidal emission perpendicular to their acceleration, as seen in figure 3.10. The emitted power of a charged particle [78,79] with the charge q, the mass m and the kinetic energy E on a curved trajectory with the radius r is

$$P_S = \frac{cq^2 E^4}{6\pi\epsilon_0 r^2 (mc^2)^4}. \tag{3.9}$$

As can be seen in equation (3.9), emitted power is inversely proportional to the mass of the particle, making protons and heavier particles unsuitable for x-ray generation. Electrons and positrons however are the best candidates for

---

[3]lat. undula - small wave (Electrons passing an undulator are forced on a multiple curved trajectory.)
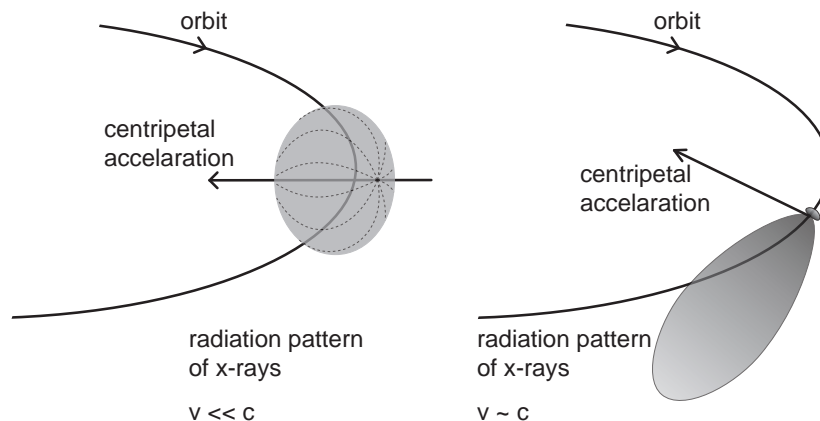
Figure 3.10: Illustration of the characteristic angular distribution of the radiation emitted by relativistic (left) and non-relativistic (right) charged particles on a curved trajectory. While non-relativistic particles emit radiation with a toroidal distribution perpendicular to the accelerating force, the emission of a relativistic particle shows a heavy distortion of the toroid when observed from the laboratory system. Due to the relativistic velocity of the charge, the main emission direction is collinear to the direction of motion.

x-ray generation. Since electrons can be easily produced by thermionic cathodes, positrons have to be made by pair production and are therefore not feasible for large scale production.

3.8.2 Electron Source and Microtron

At the synchrotron storage ring facility BESSY II electrons are produced by a thermionic cathode and accelerated to a kinetic energy of about 2 MeV. This acceleration is achieved in several devices, the first of which is a linear accelerator endowing the electrons with a kinetic energy of 70 keV. In the adjacent static magnetic field of a microtron the electrons are further accelerated in a microwave resonator and forced on a curved trajectory. Only electrons phase matching the alternating electric field are accelerated in the microwave resonator. By this, electrons are grouped into so called electron bunches, small packets of electrons with a distinct lateral separation.

As kinetic energy of the electrons increases with every passing through the microwave resonator, the radius of their trajectory in the magnetic field is increased due to a balance between Lorentz and centrifugal force. When the designated radius equivalent to a kinetic energy of about 50 MeV is reached, the electron bunches are kicked out of their orbit by a magnetic field into the synchrotron ring.

The entire accelerator as well as the storage ring are in a ultra high vacuum

environment with a base pressure of 10^{-10} mbar to avoid electron losses due to collisions with residual gas atoms.

3.8.3 Synchrotron

The term synchrotron has its origin in the fact that a fixed orbit of the electron bunches is achieved during acceleration by increasing magnetic bending fields synchronized with the increase in the electrons kinetic energy, due to acceleration in a microwave resonator. A curved orbit has the advantage of electrons passing through a microwave resonator multiple times, thus lowering the number of microwave resonators needed to highly accelerate the electrons in contrast to linear accelerators. By passing through the resonator multiple times the electrons gain a final kinetic energy of about $1.7\,$GeV before being transferred from the synchrotrons orbit into the storage ring.

3.8.4 Storage Ring and Undulators

In the storage ring the electrons are in a stable orbit inside a vacuum tube with a base pressure of 10^{-10} mbar. Besides the dipole bender magnets other components are present to stabilize the electron orbit: Multiple quadrupole magnetic fields lower the radial extension of the electron bunches driven apart by electrostatic repulsion whereas sextupole magnetic fields are needed to stabilize the orbit after the influence of the quadrupole fields. In straight parts of the storage ring, undulators[4] are introduced generating the x-rays. The few dipole magnet beam lines are not discussed in detail, because they are not used within the frame of this thesis. An undulator mainly consists of a sequence of alternating magnetic dipole fields produced by permanent magnets which are arranged in two large blocks with a variable distance allowing to adjust the strength of the magnetic field. An illustration of an undulator is given in the left panel of figure 3.11. The trajectories of electrons passing through such a structure are bent multiple times. This results in the emission of radiation in the direction of flight. Up to this point undulators are in appearance similar to wigglers. The difference between wigglers and undulators is the amplitude of the modulations, which is smaller for undulators resulting in a higher overlap of the emitted radiation and finally interference of the emitted beams. Due to this, undulator radiation has a much

---

[4]In general, an electron optical instrument in straight parts of the storage ring is called *insertion device* or ID.
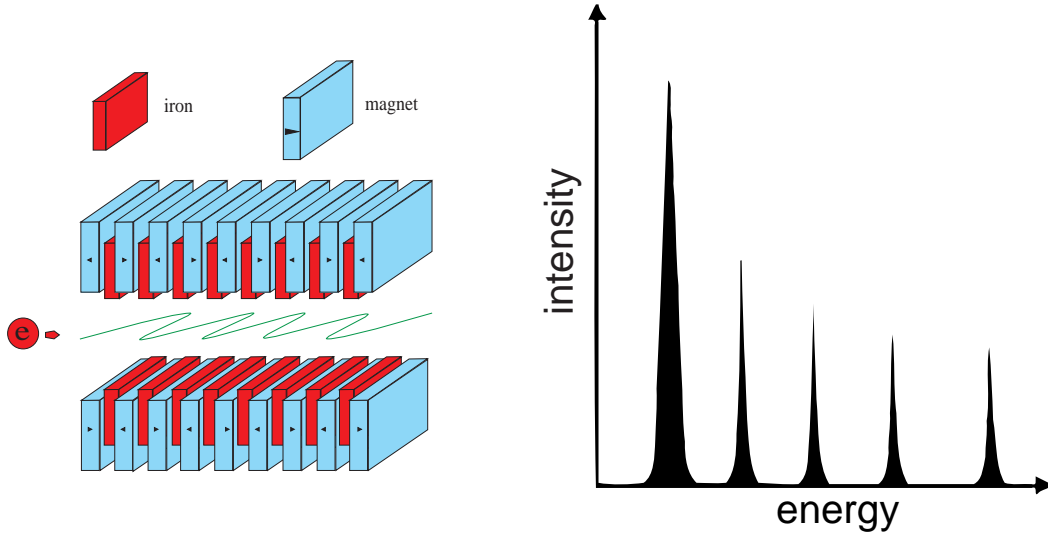
Figure 3.11: Left: Illustration of an undulator. The magnets are periodically arranged, bending the trajectory of a passing electron multiple times. The emitted photon energy distribution is shown on the right.
Right: Energy distribution of x-rays generated by an undulator. Due to interference of light emitted at each period of the magnetic structure, the distribution shows a narrow line and its higher harmonics. HZB©

higher brilliance[5] than wiggler radiation. The distinction between undulators and wigglers is not well defined, but can be made with respect to the undulator or wiggler parameter

$$K = \frac{e}{2\pi m_e c}\lambda_U \cdot B_0, \tag{3.10}$$

with the charge e and mass m_e of an electron, the speed of light c, the magnetic field of the undulator B_0 and the length of one period of the adjacent pair of antipodal permanent magnets λ_U. The deflection of the electrons d can be approximated with the help of the K parameter to be $d = \pm K/\gamma$, with $\gamma = \sqrt{1 - v^2/c^2}^{-1}$, and the velocity of the electron v. For $K = 1$ the deflection of the electrons is in good agreement with the normal angle of the x-ray beam $1/\gamma$, and the light emitted by electrons of this deflection can show interference effects. Therefore devices with $K = 1$ are defined as undulators. In the experiment the main difference between wigglers and undulators is their characteristic photon energy spectrum. While the spectrum of a wiggler is continuous and resembles the spectrum of a bending magnet with a higher photon flux, the spectrum of an undulator shows a discrete energy peak with additional peaks at higher harmonics. The wavelength of the n$^{\text{th}}$ harmonic λ_n is given by the length of the periods λ_u, the velocity of the

---

[5]Brilliance B is a measure often used to express a x-ray sources performance. It is defined as $[B] = \frac{\text{photons}}{\text{s mm}^2 \text{ mrad}^2 \text{ 0.1\%bandwidth}}$.

electrons and the undulator parameter K containing the magnetic field. Within the labeling of an undulator the length of the periods λ_u is given, for example 49 mm for a U49. The wavelengths of the various harmonics are stated in the following equation, also known as undulator equation

$$\lambda_n = \frac{\lambda_u}{2n\gamma^2}(1 + \frac{K^2}{2} + \gamma^2\Gamma_x^2 + \gamma^2\Theta_y^2). \tag{3.11}$$

Γ_x and Θ_y are angles with respect to electrons main flight direction and the undulators harmonic $n \in \mathbb{N}$, n uneven.

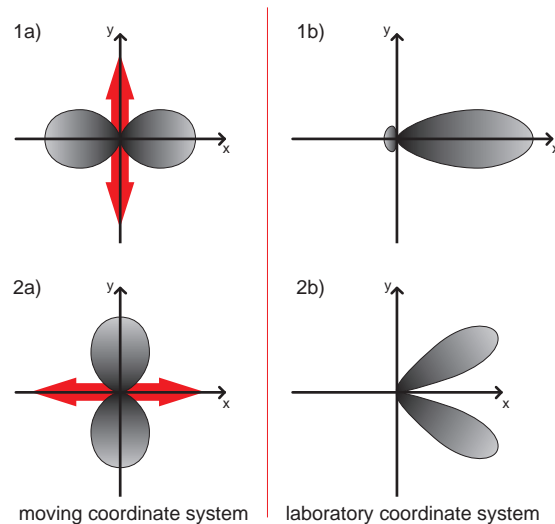Even undulator harmonics are also present, but these are not generated by the

Figure 3.12: Illustration of the angular radiation emission distribution of odd and even undulator harmonics. The angular distribution of the radiation of a vertical oscillating charge with relativistic velocity results in odd undulator harmonics. Figure 1a) shows the angular distribution from the moving reference system, 1b) shows the same angular distribution from the laboratory system. Even undulator harmonics are a result of longitudinal oscillations of relativistic electrons. Figure 2a) shows the angular distribution of the radiation emitted, as seen from the moving reference system, figure 2b) shows the same distribution seen from the laboratory system. It can be seen that odd undulator harmonics show intensity on the plane of electron propagation, whereas even harmonics only show intensity off this plane.

vertical oscillation but rather a longitudal oscillation also caused by the electrons pathway in the magnetic fields, and can therefore only be detected off axis. Due to the relativistic velocity of the electrons the x-ray directional characteristic is for both types of harmonics shifted to have the greatest fraction in the main drift direction, as is shown in figure 3.12. In the right panel of figure 3.11 the undulator harmonics are shown.

3.8.5 Beamlines U49/2-PGM1, U125/2-SGM, and U125/2-NIM

The bandwidth provided by undulator harmonics is still to high to get satisfying results in energy dependent x-ray absorption measurements. Therefore a beam line transferring the x-rays from the undulator in the ring to an experimental station is equipped with a monochromator to further increase energy resolution of the x-ray beam. During an energy scan, the monochromator sets the energy and the undulator gap corresponding to the magnetic field B_0 is adjusted to shift the center of energy of the undulator harmonic to be maximal for this energy. The three beamlines used for analysis of the electronic structure of transition metal doped silicon clusters are chosen to cover energies of certain absorption edges of interest of these systems. Table 3.1 gives an overview of the energy range of the beamline and the corresponding absorption edge analyzed of the cluster.

Beam line	Energy range	Analyzed absorption
U49/2-PGM1	80 eV to 900 eV	Transition metal 2p edge
U125/2-SGM	30 eV to 400 eV	Silicon 2p edge
U125/2-NIM	5 eV to 30 eV	Valence band

Table 3.1: Overview of the energy range of beam lines used in the experiments and corresponding absorption edges probed to analyze the electronic structure of transition metal doped silicon clusters.

3.9 Data Acquisition

In order to measure the x-ray absorption of particles in the ion trap, photon energy dependent ion yield spectra are measured. A detailed discussion of the correlation between x-ray absorption and ion yield spectroscopy is given in chapter 1. In this section the data acquisition of ion yield spectroscopy with the earlier specified setup is discussed. Understanding the energy dependent yield of daughter ions upon irradiation of parent particles with x-rays is essential and explained in section.

The time scale of the experimental operating sequence can be separated into two different scales, a slow one executed once every energy step in the order of seconds and a fast one, the data acquisition of ion yield spectra, which is done repetitively within microseconds. A pictogram of the measurement cycle for a complete photon energy scan of the ion yield is given in figure 3.13.

For each energy point measured, the initial position of the experiment is the
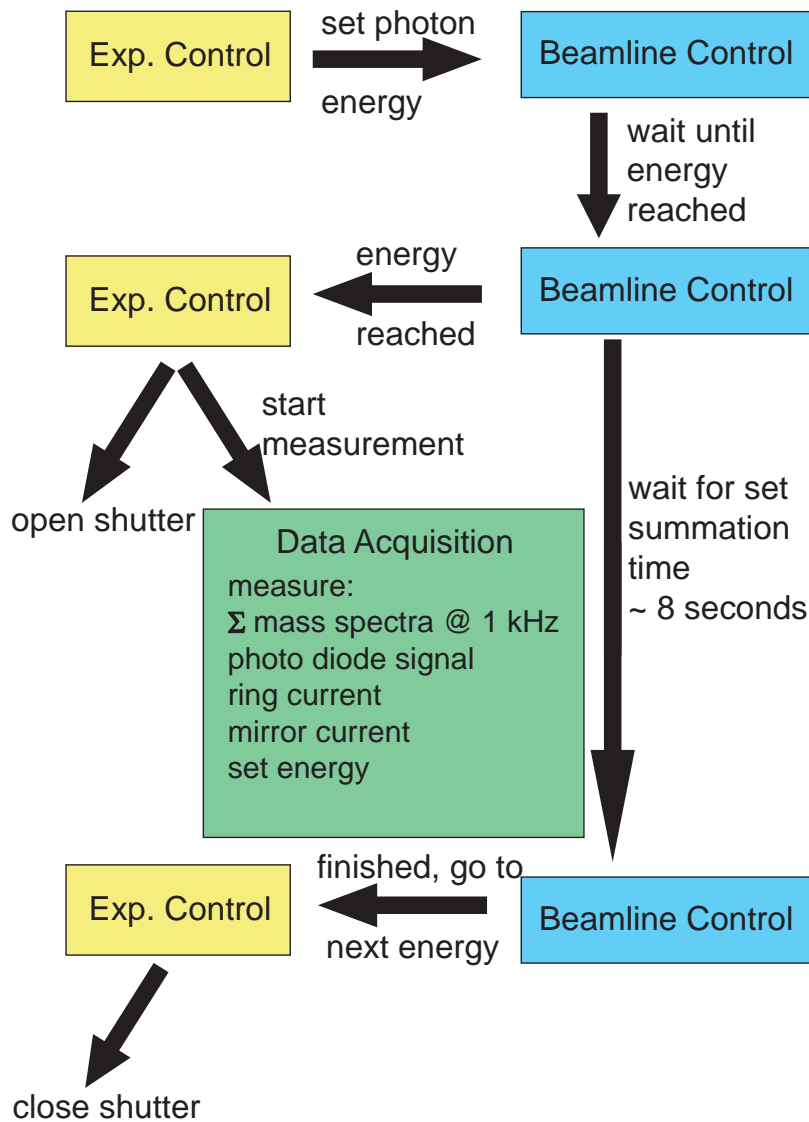
Figure 3.13: Illustration of the measurement process. The measurement is commenced by the Experimental Control, giving signals to the beam line control, the Data Acquisition and the x-ray shutter control. A detailed description of the measurement process is given in the text.

light being shut by a shutter, and the ion trap filled with parent cationic particles. On the slow time scale the following steps are executed: The experiment control signals the beam line control, controlling monochromator and undulator movement, to set the first photon energy of the scan. Upon reaching the designated energy a signal is given to the shutter control to open the shutter, illuminating the parent particles in the trap, and a gate signal is given to the measurement control to begin the fast time scale measurement. It then waits for a set time to integrate repetitively measurements of the daughter ion yield. The measurement time per energy step is normally set to about 8 seconds. When complete, the gate

signal is withdrawn, the shutter closes again and the monochromator and undulator approaches the next energy step of the scan, repeating the whole process there. The closed shutter during monochromator movement defines the energy of the measurement and avoids undefined photon energies to be present in the ion trap during movement. In order to avoid daughter ions being stored in the trap during the movement of the undulator from one energy to the next, the ion trap is emptied by switching of the confining electric quadrupole field. This happens for about 100 ms at the same moment the shutter closes. However, due to electrical interferences disrupting the switch-off signal, in some cases the trap was switched off shortly during measurements, resulting in a decreased daughter ion yield signal for this point. This dropped points are cared for as explained in section 4.2.1. In measurements made after 2009, the ion trap is not switched off anymore between energy points. By this time experimental experience allowed tuning the trapping parameters in such a way that daughter ions completely vanish from the trap on the time scale of the undulator and monochromator movement.

Some of the fast time scale processes (green box in figure 3.13) take place continuously, others only if the gate signal controlled by the experiment control system is set. The process taking place continuously is the pulsed extraction of daughter ions and parent particles from the ion trap. Timing of this process is achieved via a delay generator[6] running at a constant frequency usually set to be about 1 kHz[7]. The delay between the pulsed extraction of the ion trap and the extraction of ions in the first acceleration stage of the time-of-flight mass spectrometer is also controlled by the delay generator. The extraction pulse of the mass spectrometer is simultaneously the trigger pulse of the data acquisition device (cf. 3.10), which measures the time-of flight mass spectra. The spectra are only saved, if the gate signal of the photon energy controlling system is set, indicating the monochromator to have reached the designated photon energy and staying there for the set integration time. The data acquisition integrates a total amount of N mass spectra, with $N = (T - 0.1\,\text{s}) \cdot \nu^{-1}$ with the integration time T and the repetition rate ν. The decrease of integration time by a tenth of a second is to assure finishing of N integrations before the gate pulse is withdrawn again.

During each scan additional information tuple are taken, which include the photon flux at this energy measured by a photo diode, the synchrotron ring current,

---

[6]For most measurements a SRS DG 535 was used. For a short period in 2009 the timing was made by a Quantum Composers 9835 which has more options and channels but had some rebooting issues.

[7]For the first version of the experiment data acquisition limited the frequency to be 50 Hz (cf. 3.10)

the photon induced current on the monochromator grid as well as information only available for some beam lines like undulator gap, energy resolution or the positions of various apertures. This is not done by the same computer used for taking ion yield spectra, but is as part of the data acquisition also shown in the green box in figure 3.13. For analysis only two values are essential, which are the photon energy and the associate photon flux. The ring current is used to review the consistency of the photon fluxes of different measurements, the other values available are important to help analyze experimental difficulties if measurements show a low quality.

3.10 Time Line of Major Setup Modifications

October 2007 First revision of the setup with home-build mass filter with a mass resolution of $^m/\Delta m = 30$ and linear time of flight mass spectrometer previously used in an other experiment [70] with a mass resolution $^m/\Delta m = 200$. For data acquisition a LeCroy LC564A 1 GHz Oscilloscope was used with internal average function which ran at 50 Hz, limiting the experiments repetition rate.

April 2008 Data acquisition revised by taking mass spectra with an Aquiris$^©$ PCI Computer card. The repetition rate is now adjustable up to a frequency of 2 kHz, limited by flight times and ion trap extraction efficiency depending on the repetition rate. The quality of the spectra is increased due to better statistics for equal measurements periods.

July 2008 Hexapole ion guide equipped with a solid metal housing to perform reactivity experiments on the clusters. The clusters can be exposed to various gas types, led to the hexapole via a fine leak valve.

May 2009 The time-of-flight mass spectrometer is exchanged for a new home-build mass spectrometer with a longer ion path and a reflector. The detection mass resolution is increased to $^m/\Delta m = 1500$, making cluster cation identification and selection easier by their now clearly visible isotopic pattern.

June 2010 Home-build mass filter exchanged with a commercial EXTREL$^©$ mass filter with a mass resolution up to $^m/\Delta m = 4000$. The separation of different cluster sizes as well as the clusters transmission during selec-

tive mode was greatly improved. Selection of MSi_n^+ nearly overlapping with Si_{n+2}^+ is now possible.

December 2010 Experimental control, previously done by BESSY II EMP program linked to a Labview$^©$ program, is fully implemented in Labview$^©$.

Chapter 4

Data Analysis

Data analysis is the key part of each experimental analysis. In the following chapter, data analysis for the data obtained with the cluster experiment is explained in detail. To start with, section 4.1 shows how the mass to charge ratio is extracted from time of flight spectra. The way total and partial ion yield spectra are obtained from time of flight spectra is discussed in section 4.2. The ion yield spectra are of the main interest within this thesis, since the ion yield at a certain photon energy is directly linked to the x-ray absorption of the clusters, as discussed in section 1.1.3. The analysis scheme presented is used for excitation measurements at the transition metal 2p edge, the silicon 2p edge, and the valence band alike.

4.1 Mass Calibration

Mass calibration is an essential part of the data analysis and recording. The intensity of lines recorded with the time-of-flight mass spectrometer has to be assigned to a certain mass to charge ratio. In a first step, time-of-flight spectra of residual gas in the chamber ionized by synchroton radiation are taken. The position of the lines can be assigned to certain residual gas ions and fitted with a fit function $m(t) \approx a + b \cdot t^2$, with a, b as free parameters. The calibration can be tested using other lines in the residual gas mass spectrum. If all clusters of a wide distribution show up in the right place, the calibration is saved for further assignment. If experimental parameters in the mass spectrometer are changed, for example potentials of the spectrometer, the calibration has to be redone. The mass calibration found can be double checked with the isotopic pattern of a certain cluster. Due to the combination of atoms with a specific isotopic pattern,
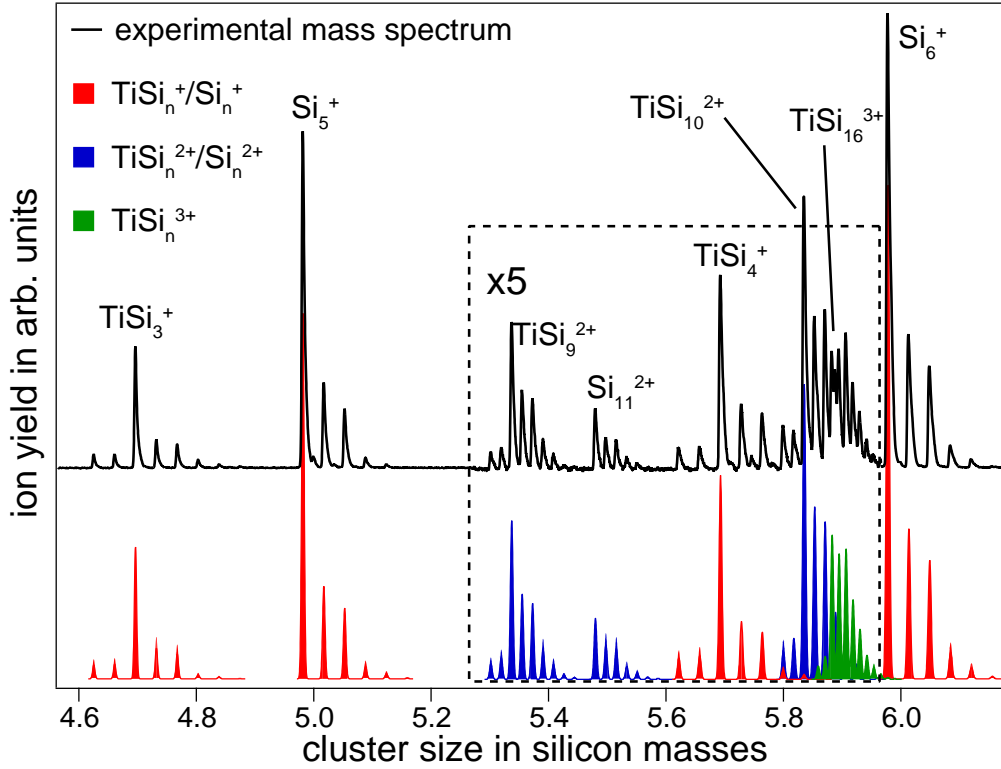
Figure 4.1: Close view of a mass spectrum containing Si_n^+ and $TiSi_n^{k+}$ product ions generated from $TiSi_{16}^+$ parent cluster. For better statistics, the spectrum is the sum of all mass spectra taken in an energy scan from 96 eV to 111 eV. The resolution of the mass spectrometer is sufficient to observe the isotopic pattern of a certain cluster. For comparison, calculated isotopic patterns are shown [80,81]. Different charge states k of the calculated isotopic patterns are color coded (red curves (k=1), blue curves (k=2) and green curves (k=3)). The mass calibration can therefore be double checked by comparison of calculated and experimentally observed isotopic pattern of a certain cluster size.

each cluster or molecule features its own isotopic distribution. This fingerprint can be seen in the mass spectra taken with the time-of-flight mass spectrometer. The mass resolution is sufficient to observe the isotopic pattern for all cluster of interest within this thesis. An example of the isotopic pattern obtained in experiment and the respective calculated isotopic pattern, calculated with [80,81] is shown in figure 4.1.

4.2   Ion Yield Spectra and Photon Flux Normalization

In almost every chapter of this thesis, ion yield spectra are shown. Therefore it is crucial to understand how the spectra are obtained and processed. The partial ion yield of a photo induced product ion at a specific photon energy is directly
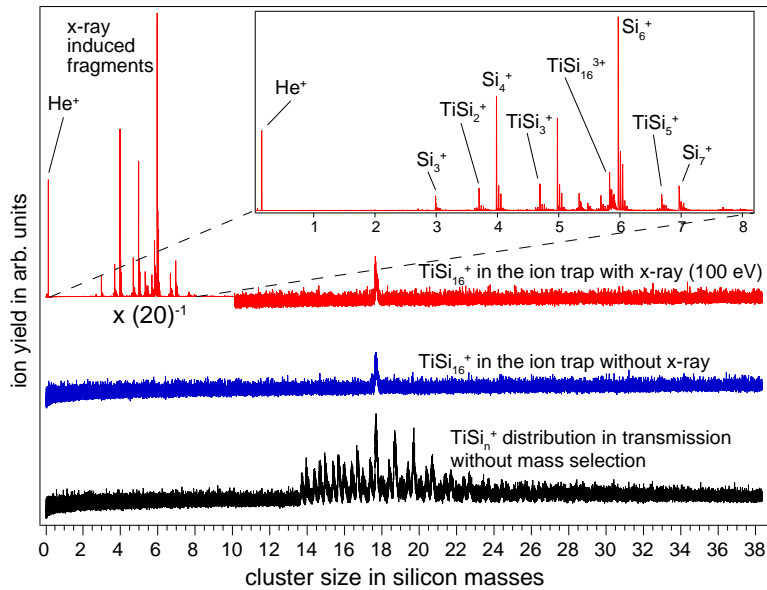
Figure 4.2: Example of mass spectra taken with (topmost (red) spectrum) and without (middle (blue) spectrum) x-ray photons irradiating the clusters. The $TiSi_{16}^{+}$ is mass selected and can be seen at a position of about 17.7 silicon masses. The photo induced product ions (red spectrum) are shown scaled to 5% due to their high signal intensity with respect to the parent cluster. The high abundance is due to ion trap parameters, which are set to efficiently trap product ions. The inset on top shows a more detailed view of product ions, with mass peaks labeled according to the product ion size and composition. The bottom spectrum (black) shows the cluster size distribution without mass selection as obtained from the magnetron cluster source.

obtained from the mass spectra taken at subsequent photon energies. Before measuring the photon energy dependent ion yield it is mandatory to check if a product ion visible in the mass spectrum is really photo induced. This is done repetitively between energy scans by taking one mass spectrum with the x-ray shutter closed and one with irradiated clusters. An example of these two spectra is shown in figure 4.2.

To obtain a partial ion yield (PIY) spectrum normalized to the photon flux, the photon energy E_i, photon flux Φ_i and mass spectrum M_i are needed. Each photo induced product ion is analyzed separately in order to distinguish between various possible fragmentation channels. Product ion classification is done with a LabView© tool [82] and transferred to an analysis program written in the programming language of IgorPro©. A PIY spectrum for a certain product ion is obtained by integrating over all lines belonging to the isotopologues of this ion excluding the background signal between the lines to obtain better signal to noise ratio. Furthermore, the background signal being up to 10% of the total signal height is substracted from each mass spectrum setting the baseline to zero, mandatory for subsequent normalization with respect to the photon flux. Mul-

tiple lines dependent on product ion composition can occur due to isotopes of atoms. The combinations of these show a specific isotopic pattern, as discussed above (cf. fig. 4.1). The ion yield Y_i at a given energy E_i is given by

$$Y_i = \sum_{\text{All lines of fragment}} \int_{a_i}^{b_i} M_i \, dm, \qquad (4.1)$$

with a_i, b_i the left and right foot point of the line respectively and dm the detectors resolution of the calculated mass axis depending on the time resolution. The time resolution ultimately depends on the sampling rate of the data acquisition, which is usually 2 Gs.

The photon flux can be calculated from the current of the GaAsP photo diode I_i and the quantum efficiency curve. Since the calibration curve has much less points than the normal scan range used, interpolation is mandatory to get the electron yield for all photon energies, resulting in a interpolated calibration curve A_i. The photon flux of step i of the measurement is calculated by the following equation

$$\Phi_i = \frac{I_i \cdot 6.24 \cdot 10^{18} [\text{e/s}]}{A_i \, [\text{e/Photon}]} [\text{Photon/s}]. \qquad (4.2)$$

In order to get a PIY spectrum normalized to the flux $Y_{i,\text{norm}}$ but still considering the quality of the spectrum the following equation is used to normalize each mass spectrum

$$Y_{i,\text{norm}} = \frac{M_i}{\Phi_i} \frac{\sum_{i=0}^{N} \Phi_i}{N}, \qquad (4.3)$$

with the number of data points of the scan N. By this normalization, the overall intensity of a spectrum is maintained.

Note that the relative intensity of ion yields of different product ions may vary, and not all product ions are necessarily recorded. Therefore, the total ion yield of a cluster is not determined due to the data acquisition method discussed in section 3.5. However, if all PIY spectra recorded for a parent cluster show an equal energy dependence, the total ion yield spectrum is presumably very similar to the sum of PIY spectra. However, different product ion's yield may show different PIY spectra, making an analysis of partial ion yield spectra mandatory for each parent cluster. Figure 4.3 visualizes how PIY spectra are obtained.
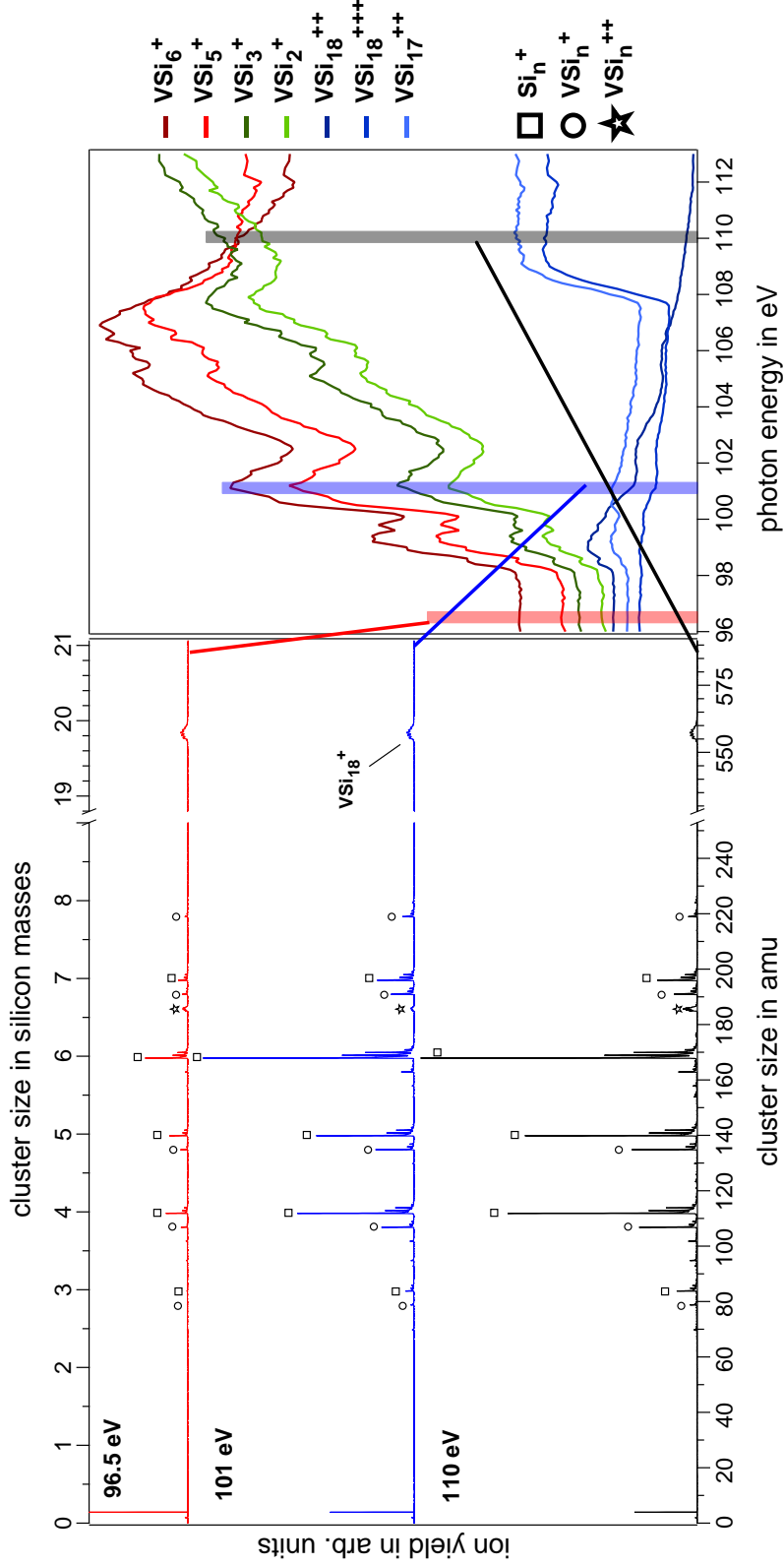
Figure 4.3: Demonstration of how ion yield spectra are obtained. Left: Mass spectra taken at three different photon energies. The partial ion yield of pure and mixed singly product ions is a function of photon energy. Mixed product ions VSi_n^+ can be seen left of pure Si_{n+2}^+. The mass axis is intersected to show the ion yield of the MSi_n^+ parent cluster. Right: Partial ion yield spectra of VSi_{18}^+. The mass spectra at the respective energies are shown in the right panel and are colored according to the colored bars in the energy dependent ion yield spectra. The trend of a partial ion yield depends on size, composition and charge state of a product ion.

The left panel of figure 4.3 shows the respective mass spectra at different excitation energies. The ion yield intensity of a certain product ion at a given energies is obtained by integration of the product ion's lines in the respective mass spectrum according to equations 4.1 and 4.3. In the right panel PIY spectra of different product ions are shown. Excitation energies for which mass spectra are shown in the right panel are marked according to the color of the respective mass spectrum. Different energy dependences of PIY spectra of certain product ions can be observed. Hence in case of this ion yield, the total ion yield of the parent ion cannot be determined, as relative intensities between PIY spectra are not known, as mentioned above.

Photon Flux Normalization in the VUV Range

Due to a poor performance and calibration curve of the photo diode in the low energy range from 4 eV to 40 eV, normalization of spectra taken at the NIM beam line does not show good results. The normalized spectra only show the spectral signature of the calculated photon flux curve, as can be seen in figure 4.4. The
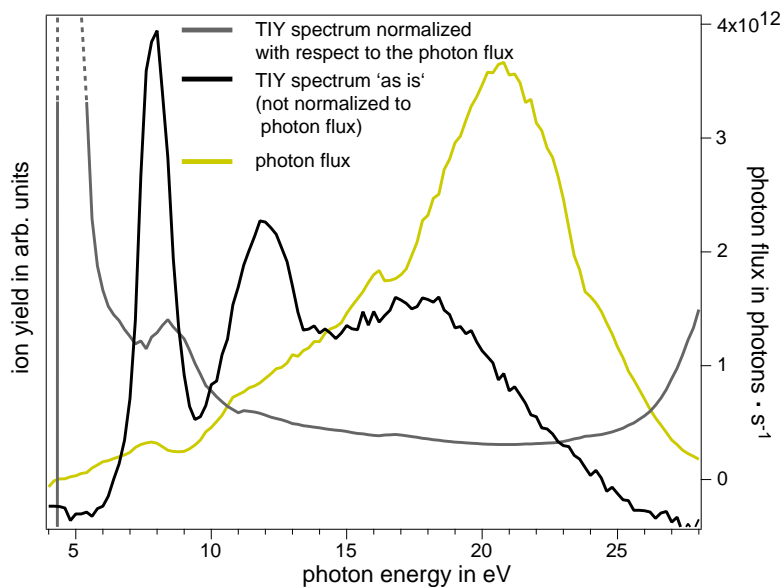

Figure 4.4: Spectrum of the photon flux obtained by the photo diode current (cf. equation 4.2, The normalized ion yield spectrum (cf. equation 4.3 and the spectrum of the respective raw data. The spectrum calibrated with respect to the photon flux is mainly dominated by photon flux features. The high intensities at low energies are not physically reasonable. This is due to the low photon energy range not inside the photo diode specifications. Ion yield spectra obtained in this energy regime are therefore shown without photon flux normalization.

raw spectra however show sensible features not to be associated with features of the photon flux. Therefore, spectra in the photon energy range between 4 eV and

40 eV are shown 'as is' in the whole thesis.

4.2.1 Handling of Dropped Points in Ion Yield Spectra

In some cases ion yield spectra show dropped points, at which the intensity is very low. This is due to electric interferences in the ion trap, switching it off for a short time during measurements as explained in section 3.9. How these points are treated in order to maintain the spectrum despite some dropped points is explained in the following.

The ion yield Y_i^A of the dropped points energy E_i^A in an energy scan A is calculated by its neighboring points with

$$Y_i = \frac{1}{2}(Y_{i-1} + Y_{i+1}), \tag{4.4}$$

if some preconditions are fulfilled. It is only made, if a second spectrum B, with $E_i^A = E_i^B$ is available showing the same trend in the rest of the spectrum and having no dropped point at the same energy E_i^B. A second spectrum is always taken to analyze reproducibility. Furthermore, in the second spectrum the ion yield Y_i^B has to be in between the two points Y_{i-1}^B, Y_{i+1}^B in such a way, that the ion yield in the vicinity of the dropped point in energy scan A resembles the one in B.

If all preconditions are fulfilled, the new calculated point will nevertheless contribute only a maximum of 50% to the ion yields shown in this thesis, since for better statistics energy scans of the same parent cluster are summed, as explained above. Else, the whole spectrum is discard.

4.2.2 Derivatives of Ion Yield Spectra

In some cases, derived ion yield spectra show additional information not at first visible in within the normal ion yield spectrum. Due to the discrete values of the spectrum, derivatives can be obtained by different means. In the following a method is used supported by IgorPro$^{©}$ calculating the derivative D_i of a certain value Y_i at the energy point E_i by the neighboring points with

$$D_i = \frac{Y_{i+1} - Y_{i-1}}{E_{i-1} - E_{i+1}}. \tag{4.5}$$

Derivatives of partial ion yield spectra showing a direct photo ionization edge are in good agreements with data expected from XPS studies as is explained in section 7.2.1.

Chapter 5

Reactivity of Doped Silicon Clusters

Reactivity experiments on MSi_n clusters give valuable information about the geometry of these clusters. It is known from literature, that reactivity of MSi_n clusters is reduced if the metal atom is completely encapsulated by the silicon [33, 39]. The cluster sizes for the exohedral - endohedral transition, known for $Ti_{1,2}Si_n^+$, $V_{1,2}Si_n^+$, and $Cr_{1,2}Si_n^+$ [33, 39] are confirmed by the studies presented.

In this chapter, the results of reaction experiments performed in the framework of this thesis on transition metal doped silicon cluster cations are presented and compared to existing data (cf. sect. 2.2 and [33, 39, 49]). The first section 5.1 shows a detailed analysis of reactivity experiments conducted in the reaction cell (cf. sect. 3.2) of the experimental setup. Exemplarily reactivity of vanadium doped silicon cluster cations is shown to show how transition metal doped silicon clusters react upon oxygen exposure and what results are obtained in the analysis. The influence of experimental conditions like the partial oxygen pressure on the reaction is thoroughly discussed. In the second section 5.2 the exohedral to endohedral transition (cf. sect. 2.1) of scandium, titanium, vanadium, chromium and manganese doped silicon clusters are presented. The final section 5.3 briefly states the importance of the chemical etching technique for experiments on size selected transition metal doped silicon clusters.
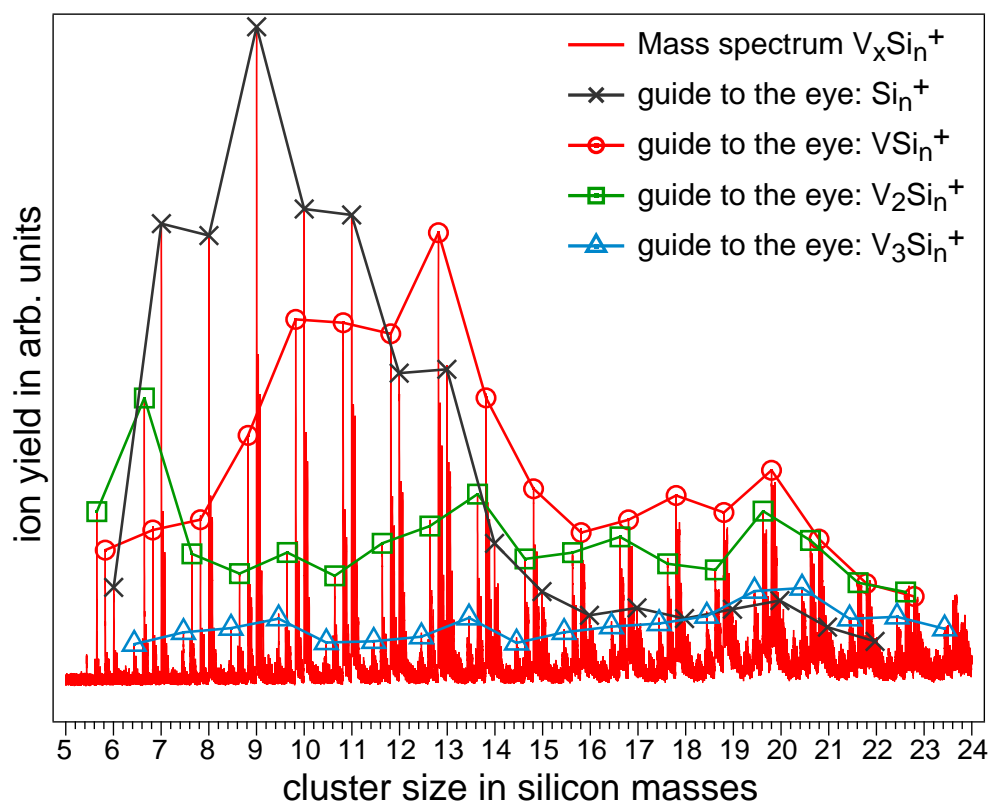
Figure 5.1: Mass spectrum of $V_xSi_n^+$ and Si_n^+ clusters as produced by the cluster source. Pure (black ×), singly (red ○), doubly (green □) and triply (blue △) doped silicon clusters. Markers are set on top of the most intensive line of the respectivly doped species. Connecting lines are guides to the eye. The abundance of differently doped species varies with cluster size. While in the lower size regime pure silicon exhibit the most intense lines, for larger clusters the singly doped species dominates the spectrum.

5.1 Reactivity of Vanadium Doped Silicon Clusters

In this section, a detailed description is given of how the exohedral to endohedral transition of MSi_n^+ clusters is obtained from the data. The results obtained for additional MSi_n^+ (M=Sc,V,Ti,Cr) cations are given in section 5.2.

The mass distribution of $M_xSi_n^+$ clusters produced in the magnetron sputtering source can be changed by oxidation in the hexapole collision cell. In figure 5.2, two mass spectra of clusters obtained without mass filtering or trapping in the ion trap are shown. The red spectrum shows the cluster size distribution as produced by the magnetron source, with pure silicon clusters, singly and multiply vanadium doped silicon clusters. The blue spectrum shows the mass distribution after exposure to oxygen in the reaction cell. The blue spectrum is inverted and the mass axis is split for better comparison of the relevant mass ranges
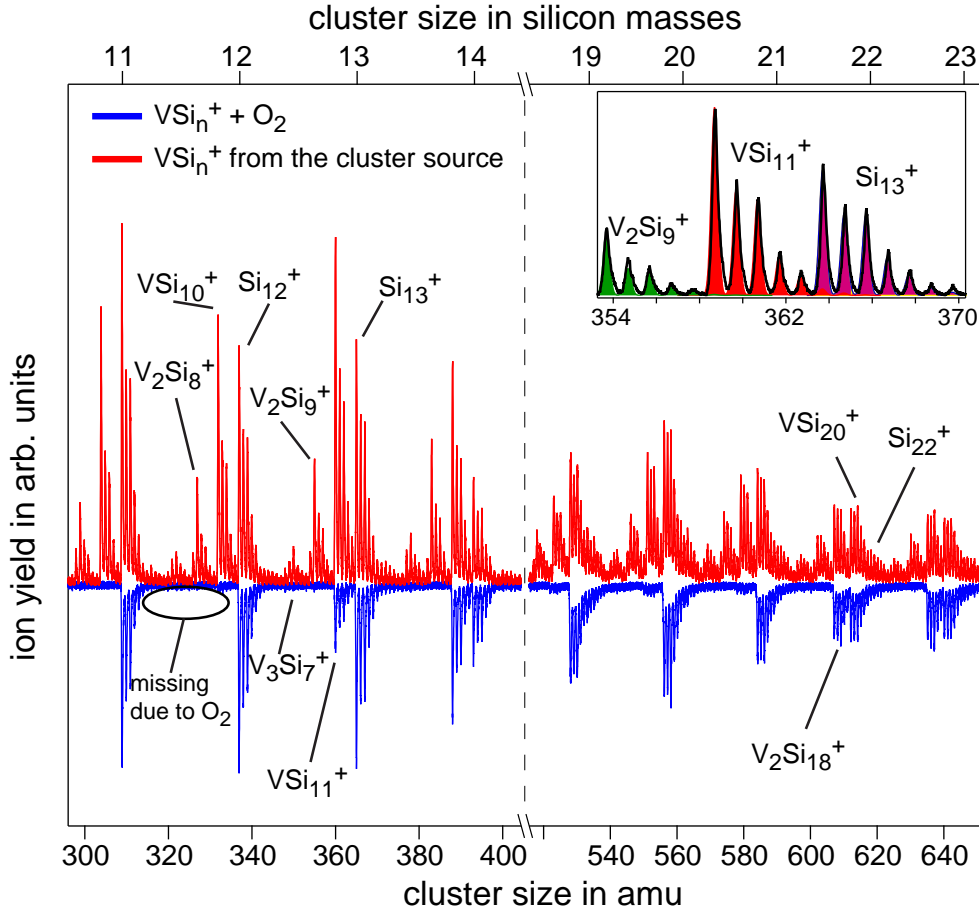
Figure 5.2: Mass spectrum of $V_xSi_n^+$ and Si_n^+ clusters. The red spectrum shows the cluster distribution delivered by the cluster source (cf. fig. 5.1), the blue spectrum shows the same distribution after reaction with oxygen, inserted into the reaction cell at 7.7×10^{-3} mbar pressure (cf. fig. 3.1). For better comparison the blue spectrum is inverted. The horizontal axis is intersected and shows two mass ranges. In the first range from 300 amu to 400 amu the transition between endohedral and exohedral cluster sizes for VSi_n^+ can be observed and in the second mass range form 520 amu to 640 amu the respective transition for $V^2Si_n^+$. The inset shows that clusters in experimental mass spectra (black line) can be distinguished by their calculated isotopic pattern (solid colors) [80, 81]

exohedral to endohedral transition of cluster geometries occur. As can be seen in figure 5.2, some clusters present in the mass spectrum without reaction gas (red curve) are absent in the mass spectrum upon oxygen exposure (blue curve). Clusters with active reaction centers (namely the transition metal) react with the oxygen and fragment, whereas clusters showing up in the red as well as blue spectrum remain unchanged upon oxygen exposure. Possible fragments $VO^{+/0}$ and other small fragments are not observed in the mass spectrum in figure 5.2 because ion guide, mass filter and ion trap[1] parameters are set to transmit larger

---

[1]The mass filter and the ion trap are used as normal ion guides. No filtering or trapping of the clusters is done.

masses for this measurement. With these parameters, small masses do not reach the spectrometer. However, when setting parameters to show smaller cluster sizes while maintaining all experimental parameters of the cluster source and the reaction cell, still no fragments are observed. It is assumed that this is due to disadvantegeous transmission parameters. It is possible that due to the high pressure in the reaction cell, small fragment clusters are deflected from the cluster beam and therefore do not reach the mass spectrometer. Although the fragments cannot be observed directly, in other measurements it was observed that exohedral clusters stored in the ion trap for a few seconds will fragment to very small final fragment sizes VO^+ and $VSiO^+$ upon oxidization by the chambers residual gas. In the following the evaluation of the spectra shown in figure 5.2 is explained exemplarily. In the cluster size region between Si_{12}^+ and Si_{13}^+ the singly vanadium doped silicon cluster VSi_{11}^+, the doubly doped $V_2Si_9^+$, and the triply doped $V_3Si_7^+$ can be seen in the red spectrum, which are therefore abundant in the cluster beam when the clusters are not exposed to oxygen. Upon oxygen exposure the mass distribution changes and $V_2Si_9^+$ and $V_3Si_7^+$ are not visible anymore. VSi_{11}^+ on the other hand is still to be observed, but at a lower intensity. Comparing this decrease with the loss in intensity of the pure silicon cluster Si_{13}^+, which is inert towards oxygen, suggests that a part of the VSi_{11}^+ clusters is oxidized and another is stable against oxygen. The intensity drop in VSi_{12}^+ upon oxygen exposure is far less, which suggests that the stability of VSi_{12}^+ is enhanced compared to VSi_{11}^+. To get a quantitative value to compare the stability of a cluster towards fragmentation upon a chemical reaction, the relative stability S is introduced. The relative stability towards reactions with oxygen molecules is defined as

$$S(V_xSi_n^+) = I(V_xSi_n^+ + O_2)/I(V_xSi_n^+), \qquad (5.1)$$

with the integral over all lines $I(V_xSi_n^+ + O_2)$ corresponding to the blue and $I(V_xSi_n^+)$ to the red spectrum. The results for singly and doubly vanadium doped silicon clusters $V_xSi_n^+$ exposed to different partial oxygen pressures is given in figure 5.3. Triply vanadium doped silicon clusters are not shown, since they are not stable in the size range analyzed.

5.1.1 Stability of Singly Vanadium Doped Silicon Clusters VSi_n^+

The stability S of VSi_n^+ is shown in figure 5.3. Cluster sizes up to n=10 show a very low stability for high and medium partial oxygen pressures 1.4×10^{-2} mbar and 7.7×10^{-3} mbar. The rise in stability at low oxygen partial pressures of 4.6×10^{-3} mbar is discussed later on. It can be seen that the transition from exohedral structures to endohedral structures is not at a certain cluster size, but that VSi_{11}^+ seems to be at an intermediate stage in between reactive exohedral or inert endohedral cluster sizes. Although VSi_{11}^+ appears stable in the mass spectrum (cf. fig. 5.3) compared to smaller vanadium doped silicon clusters cations, the stability of VSi_{11}^+ is low compared to VSi_n^+ ($n > 11$), as can be seen in figure 5.3. This might be explained with the presence of two or more isomers of VSi_{11}^+. If one of the isomers is exohedral and one other is endohedral, this is expected to have the effect on the stability S, which is observed in figure 5.3. The decrease in intensity in figure 5.2 is due to fragmentation of exohedral isomers, while endohedral isomers are responsible for the remaining intensity. A huge increase in stability S compared to VSi_{11}^+ is observed for VSi_{12}^+, which is considered the first endohedral cluster in literature [33, 39], meaning that most of the isomers of VSi_{12}^+ are endohedral. However, results of resonant x-ray absorption at the transition metals $L_{3,2}$ edge exhibiting a drastic change in the spectral fingerprint upon exohedral to endohedral transition. This suggests that VSi_{11}^+ is the smallest endohedral cluster (cf. sect. 6.2).

Therefore, VSi_{11}^+ is shown as the smallest endohedral cluster in figure 5.5, since its stability is not as low as the stability of smaller singly vanadium doped silicon cluster sizes. Apart from the trend of exohedral having a low and endohedral clusters having a high stability, one cluster size shows an exceptional behavior, namely VSi_{16}^+. As stated in section 2.3, calculations on VSi_{16}^+ attest a high symmetry of the geometric structure as well as an electronic shell closure with a band gap larger $2\,\mathrm{eV}$ [1]. This cluster is therefore expected to have an exceptional stability, as observed in mass spectra of clusters produced in a laser evaporation cluster source [33, 39]. In reactivity experiments with H_2O [33, 83] as well as adsorption of Ar [33, 39, 83], VSi_{16}^+ behavior does not differ from the neighboring doped silicon cluster cations. In the presented reactivity experiments however, VSi_{16}^+ shows a higher stability S than the neighboring VSi_{15}^+ and VSi_{17}^+ clusters, as can be seen in figure 5.3. An explanation for this behavior differing from the adsorption experiment could be that VSi_{16}^+ intensity is increased in the

experiments presented due to predominant fragmentation of $V_2Si_n^+$, $n > 16$ clusters towards VSi_{16}^+. The question remains, why this behavior was not observed in reactions with water molecules. Fact is that the experimental data presented confirms the high stability for VSi_{16}^+ proposed by theoretical calculations as well as experimental data (cf. sect. 2.1 and 2.3).

5.1.2 Stability of Doubly Vanadium Doped Silicon Clusters $V_2Si_n^+$

Doubly vanadium doped silicon clusters need more silicon atoms to be endohedral, due to the larger surface of the two metal atoms to be encapsulated compared to only one metal atom. The larger number of silicon atoms and the high abundance of doubly doped silicon clusters after the exohedral-endohedral transition proves that the two metal atoms are in the center of a silicon cage in energetically low lying geometries of these clusters. The other possible option would have been the doubly doped silicon clusters adopting the geometry of singly doped clusters, with the second metal atom arranged at the surface of the structure. In figure 5.2 the doubly doped $V_2Si_{18}^+$ cluster can be seen to emerge beside VSi_{20}^+ at the lower mass side of Si_{22}^+. Note that the pure silicon cluster is not pronounced and blends with lines of the prominent VSi_{20}^+. In contrast to the singly doped exohedral - endohedral transition with VSi_{11}^+ showing a pejorative stability as discussed above, between the stability S of exohedral $V_2Si_{17}^+$ and endohedral $V_2Si_{18}^+$ a sharp distinction is observed (cf. fig. 5.3). Triply doped clusters (not shown) exhibit no exohedral to endohedral transition in the size range analyzed.

5.1.3 Pressure Dependence of the Stability S

As is discussed more detailed in section 5.3, the selective etching technique via oxygen exposure of the clusters is used to support size selection of singly transition metal doped endohedral cluster cations. To gain optimal conditions, it is essential to know at which oxygen pressure in the reaction cell the undesired clusters are most efficiently discriminated. For very high pressures exohedral clusters are discriminated after all, but simultaneously the intensity of endohedral clusters decreases due to a reduced transmission of the ion guide. If the collision rate with oxygen molecules is too high, clusters are scattered out of the cluster beam. This
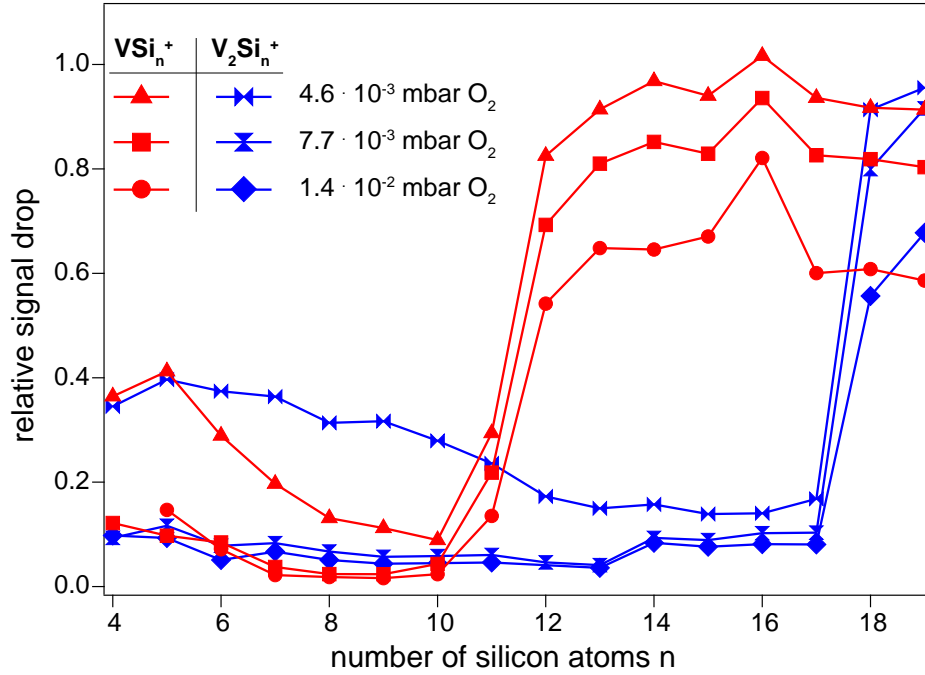
Figure 5.3: Relative stability against oxygen induced fragmentation $S(\mathrm{V}_x\mathrm{Si}_n^+)$, ($x \in [1,2]$; $n \in [4,19]$). Singly (red) and doubly (blue) doped silicon cluster stability is shown for three different partial oxygen pressures in the reaction cell ($\bigcirc$ 1.4×10^{-2} mbar, $\square$ 7.7×10^{-3} mbar, and $\triangle$ 4.6×10^{-3} mbar). The drastic increase in stability, visible for all partial pressures, is linked to an total encapsulation of the metal atom by silicon atoms. The smallest of these endohedral clusters are found at $n = 12$ for singly and $n = 18$ for doubly vanadium doped silicon cluster cations. The stability $S(\mathrm{VSi}_{16}^+)$ of the VSi_{16}^+ is exceptional high (see text and sect. 2).

is demonstrated in figure 5.4, showing the relative stability S as a function of the partial oxygen pressure in the ion guide for VSi_{12}^+ and $\mathrm{V}_2\mathrm{Si}_{18}^+$. This cluster sizes are chosen exemplary for all endohedral clusters, as both are the first endohedral clusters of the respective doped species which show the same stability as their larger cluster sizes. The pressure dependence of other cluster sizes is shown exemplarily for three different pressures in figure 5.3. The oxygen pressure the clusters are exposed to is not measured directly, but can be calculated by the known pressure in the vacuum chamber with equation (3.1), as explained in section 3.2. It can be seen that effective elimination of exohedral clusters is achieved for 1.4×10^{-2} mbar and 7.7×10^{-3} mbar, as exohedral cluster intensity is nearly zero. At an oxygen pressure of 4.6×10^{-3} mbar a residual intensity remains for singly doped as well as doubly doped exohedral silicon clusters. Either some exohedral clusters pass the reaction cell without a collision with oxygen or that multiple doped exohedral silicon clusters $\mathrm{M}_y\mathrm{Si}_n^+$ fragmented upon oxydization into a smaller exohedral cluster $\mathrm{M}_{y-1}\mathrm{Si}_{n-x}^+ + \mathrm{VO} + \mathrm{Si}_x$. To eliminate these fragments,
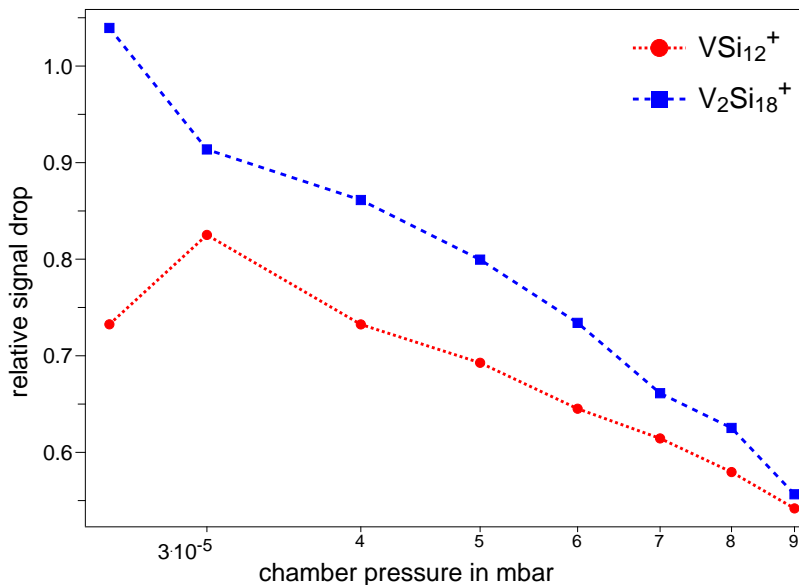
Figure 5.4: Stability $S(\mathrm{VSi}_{12}^+)$ and $S(\mathrm{V_2Si}_{18}^+)$ of endohedral singly and doubly doped vanadium silicon cluster cation as a function of the partial oxygen pressure in the reaction cell of the ion guide. The apparent decrease of stability is due to scattering of clusters from the cluster beam by oxygen molecules.

further reactions with oxygen are necessary. Collision rates with oxygen molecules therefore have to be increased. Since the exposure time depends on the velocity of the clusters and therefore on ion guide potentials (cf. sect. 3.2), the number of collisions with oxygen of a cluster cannot be determined precisely. The pressure has to be adjusted to full discrimination of exohedral clusters experimentally. It is also possible to tune ion guide parameters or to use the ion guide as an ion trap by applying a pulsed extraction at the exit aperture thus prolonging dwell time of the clusters.

5.2 Exohedral-Endohedral Transition of Sc, Ti, V, Cr, and Mn Doped Silicon Clusters

The transition between exohedral clusters and endohedral clusters can be experimentally determined via reactivity experiments, as described in the prior section for vanadium doped silicon clusters. Further analysis of scandium, titanium, chromium, and manganese as dopant of the silicon cluster are executed equivalently. The results are shown in figure 5.5, showing the smallest endohedral MSi_n^+ cluster size observed. Obviously, the number of silicon atoms needed to encapsulate the metal atom depends on the respective transition metal. Since the atomic number of $^{21}\mathrm{Sc}$, $^{22}\mathrm{Ti}$, $^{23}\mathrm{V}$, $^{24}\mathrm{Cr}$, and $^{25}\mathrm{Mn}$ increases along the groups of the peri-

MSi_n^+ Dopant Atom M	Smallest Endohedral Cluster Size in silicon atoms in number of silicon atoms n		
	n^*	$n°$	$n^\#$
Sc	17	-	16
Ti	13	13	13
V	12	12	11 (see caption)
Cr	-	11	11
Mn	-	-	11
Co	-	8	(8)

Table 5.1: Experimental values for the exohedral-endohedral transition of Sc, Ti, V, Cr, Mn and Co doped silicon cluster cations (n^* [49], $n°$ [39], $n^\#$ this work). The value for MSi_n^+ exohedral-endohedral transition observed by means of the spectral fingerprint in TIY spectra at the transition metal 2p edge is given brackets (cf. sect. 6.2). VSi_{11}^+ shows a partial stability towards oxygen exposure, which leads to the suggestion that multiple isomers are populated at least one of which can be characterized as endohedral (see text).

odic table, the higher charge of the nucleus contracts the 3d and 4s orbitals due to coulombic interaction, decreasing the effective radius of the atom [84–86]. A clear correlation between atomic radii and minimal number of silicon atoms to encapsulate the transition metal can be seen in figure 5.5. For comparison, in table 5.1 the exohedral-endohedral transition found in literature is given.
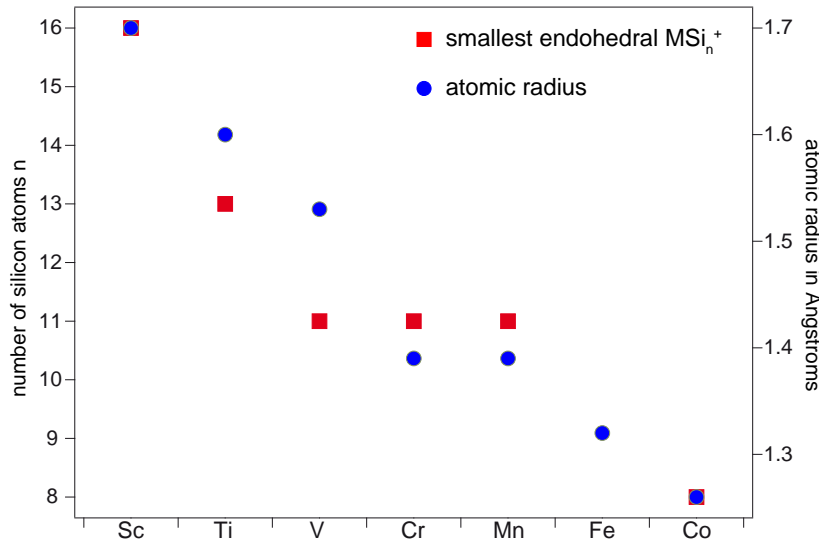

Figure 5.5: Exohedral-endohedral transition of Sc, Ti, V, Cr, and Mn doped silicon cluster cations. The number of silicon atoms of the smallest endohedral cluster observed is shown on the left side axis. A decrease in the number of silicon atoms needed to encapsulate the transition metal can be seen along the 3d series. This is due to a decrease in the atomic radius [86] with increasing atomic number along a period of the periodic table. The numeric values and values found in literature are compared in table 5.1.

5.3 Application of Selective Etching

Experimentally, the selective chemical etching of exohedral clusters simplifies mass selection of singly doped MSi_n^+ clusters by discriminating multiply doped species in a specific size regime from the cluster beam (cf. sect. 2.2 and 3.2). In case of small singly doped endohedral cluster sizes, the lines of different doped species in the mass spectrum can be separated by mass filtering. The lines of larger MSi_n^+ clusters ($n \approx 12$) begin to mix due to the isotopic pattern of silicon (cf. fig 5.1). Above a critical size doubly doped clusters become endohedral and etching can no longer be used to discriminate doubly doped clusters from the beam. Hence the mass filter has to be operated in high resolution mode, drastically reducing transmission. This can be avoided if chemical etching is applied to assist mass selection.

The results on chemical reactions presented above show that chemical etching is well suited to improve experimental conditions in x-ray absorption studies on size selected transition metal doped silicon clusters.

Chapter 6

Ion Yield Spectroscopy at the Transition Metal Dopant 2p Edge

In this chapter the results of x-ray absorption spectroscopy at the transition metal dopant 2p edge of a MSi_n^+ cluster are presented [58]. It is known that x-ray absorption spectroscopy is very sensitive to the local unoccupied density of states (cf. sect. 1.1). It is therefore perfectly suited to reveal silicon cage induced changes in the local electronic configuration of the transition metal dopant. The influence is analyzed for different numbers of silicon atoms, which therefore gives the opportunity to monitor possible differences in the electronic structure of MSi_n^+ clusters between endohedral and exohedral species. In addition, different transition metals are used as dopants to analyze changes in the electronic structure between equal sized MSi_n^+ clusters. Furthermore, the influence of the cage structure on the metal dopant is not only analyzed by interchanging the dopant, but also via substitution of silicon by germanium.

The absorption of MSi_n^+ clusters at the metal $L_{3,2}$ edge is measured via ion yield spectroscopy as discussed in chapter 4. In order to evaluate and classify information gained via partial ion yield spectra it is mandatory to analyze the partial ion yields of different product ions first, as discussed in chapter 4. This is done in form of an excursion in the beginning of this chapter. The experimental results are presented in section (6.2) in which the influence of an open silicon cage in contrast to a closed cage on the local density of states at the metal atom is analyzed. The VSi_{16}^+ high symmetry and electronic shell closure are the central theme of the following section 6.3.1, which shows that apparently $TiSi_{16}^+$ and $CrSi_{16}^+$ have a similar local electronic structure at the respective metal atom. The influence of similar cage materials silicon and germanium having a similar elec-

tronic configuration on the electronic structure of VX_n^+ (X=Si,Ge) is presented in section 6.3.2.

6.1 Excursion: Evaluation of Ion Yield Spectroscopy at the Metal $L_{3,2}$ Edge

Analysis of the TIY spectrum is straight forward, as all partial ion yield (PIY) spectra exhibit the same features with similar intensity despite their dissimilar composition, as shown in figure 6.1 (cf. sect. 4.2). In the left panel of figure 6.1 a mass spectrum with two product ions of $TiSi_{16}^+$ are shown, a pure silicon fragment and the titanium cation. These are the main fragmentation channels which show in the mass spectrum as they have the highest abundance upon absorption at the metal $L_{3,2}$ edges. The mass spectrum shown in figure 6.1 is the sum of all mass spectra obtained in an energy scan at the titanium $L_{3,2}$ edge. The summed spectrum is only used to gain better visualization of the occurring photon induced fragments by an increased statistics. The fragments can be identified by their isotopic pattern in comparison with the calculated isotopic pattern of Si_2^+ (blue) and Ti^+ (red) [80, 81]. The respective partial ion yields displayed in the right panel are colored accordingly. In case of the transition metal $L_{3,2}$ absorption analyzed within this chapter, these product ions are considered to be in good agreement with the total ion yield. In the following the sum of partial ion yield spectra is therefore referred to as total ion yield (black curve in the left panel of figure 6.1), in contrast to the analysis done at the silicon $L_{3,2}$ edge or the analysis in the VUV range in chapter 7 and 8. In the energy range of the transition metal $L_{3,2}$ edges, silicon does not have absorption edges, but does only show a monotonic decreasing background ion yield background signal with low intensity due to silicon L edge absorption. However, the silicon L edges is at an energy of about $100\,eV$($L_{3,2}$) and $150\,eV$ (L_1) [9, 87] and therefore the silicon absorption in the transition metal $L_{3,2}$ edge energy regime of about $400\,eV$ (Sc) to $800\,eV$ (Co) [9, 88, 89] can be neglected. All silicon fragments analyzed show a non monotonically decreasing energy dependence in their partial ion yield spectra. Therefore they have to be products of a transition metal doped silicon cluster, which fragmented upon metal $L_{3,2}$ edge absorption and can be included in the analysis of metal $L_{3,2}$ edge absorption.
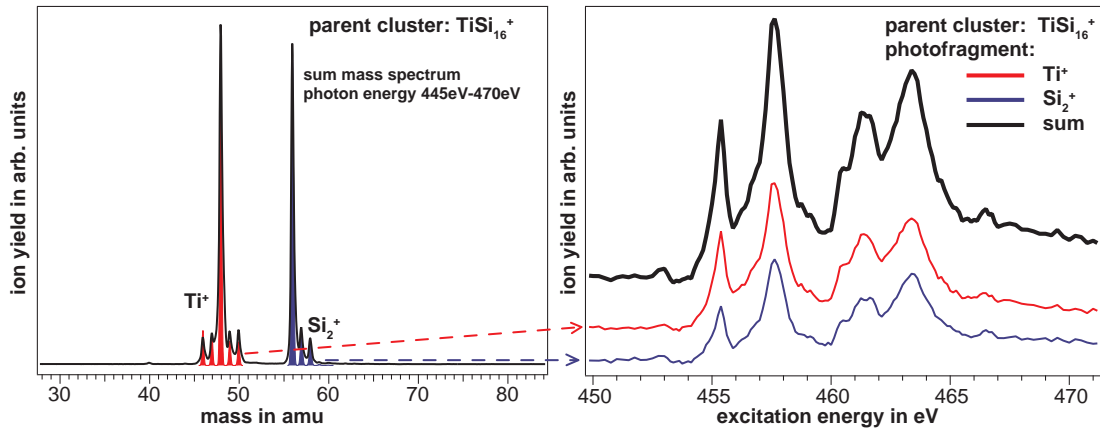
Figure 6.1: Left: Most intense product ions generated by excitation at the titanium $L_{3,2}$ edge of $TiSi_{16}^+$. The lines show the isotopic pattern of Ti^+ and Si_2^+, which are underlaid with the calculated isotopic pattern (solid red (Ti^+) and blue (Si_2^+) curve) [80, 81]. To gain better statistics for comparison of the isotopic pattern, the mass spectrum is the sum of all mass spectra obtained in an energy scan at the titanium $L_{3,2}$ edge.

Right: Partial ion yield (PIY) of each daughter ion colored according to the isotopic pattern in the left panel. Both PIY show the same energy dependence, although the daughter ions differ in composition. This shows that for $L_{3,2}$ absorption, the PIY is in good agreement with the total ion yield (see text).

6.2 Experimental Results and General Discussion

In this section the TIY spectra of $ScSi_n^+$, $TiSi_n^+$, VSi_n^+, and $CrSi_n^+$ as well as $MnSi_n^+$ and $CoSi_n^+$ (cf. fig. 6.4 to 6.9) are discussed. Along the 3d transition metal dopants M of MSi_n^+ clusters valence occupancies are increased by one additional valence electron when keeping the number of silicon atoms constant, as can also be seen by the electron configuration of the dopant metals given in figure 6.2. The sequence of figures 6.4 to 6.9 of TIY spectra is chosen in respect of their dopant's atomic number. A section of the periodic table showing dopant materials is shown in figure 6.2. In each figure the TIY spectra are sorted with respect to the number of silicon atoms of MSi_n^+ from bottom to top, as indicated by the number of silicon atoms given on the vertical axis. Each TIY spectrum of a MSi_n^+ cluster is normalized to equal height of the highest intensity to obtain better comparability. The red-blue bar at the right side of each graph denotes the exohedral (red) or endohedral (blue) character of a MSi_n^+ cluster. The transition from exohedral to endohedral cluster is investigated via reactivity experiments, for which results are shown in chapter 5. All spectra show two distinct groups of lines displayed in figure 6.3, corresponding in first approximation to transitions of $2p_{3/2}$ and $2p_{1/2}$ electrons into dipole accessible s- and d-like local unoccupied
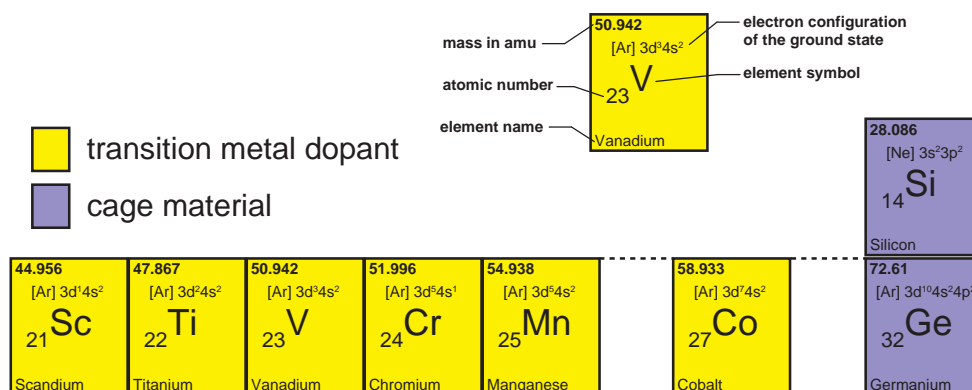
Figure 6.2: Section of the periodic table showing the transition metal dopants as well as cage materials used in the experiments presented. In general, figures showing TIY spectra of transition metal doped clusters are sorted with respect to the transition metal dopant position in the periodic table.
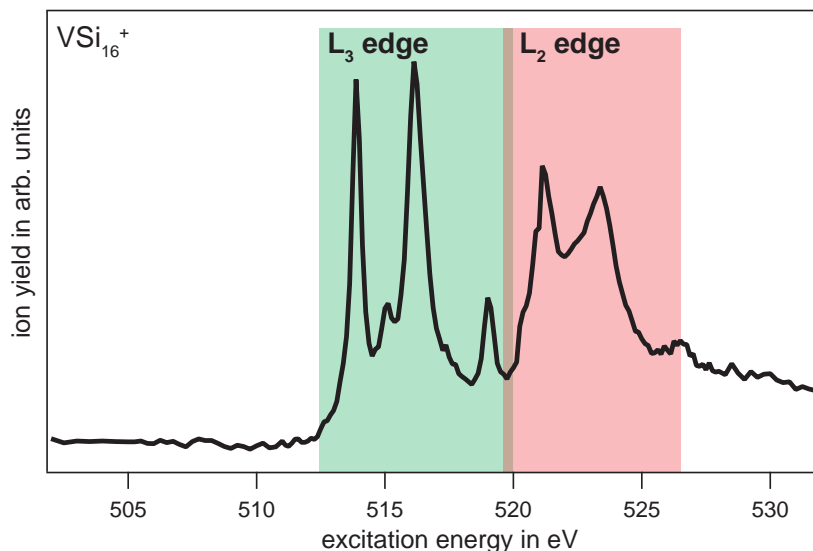

Figure 6.3: Contribution of the $2p_{3/2}$ and $2p_{1/2}$ (green region) and L_2 edge (red region) to a TIY spectrum shown at the example of VSi_{16}^+. Due to multiplet and crystal field effect [22], the contribution can not be exactly specified. This is schematically indicated by the overlap of both regions.

states at the metal atom (L_3 and L_2 edge respectively). The contributions of L_3 and L_2 to the spectrum are shown exemplarily for the TIY spectrum of VSi_{16}^+ by a green and red marked area respectively. It should be noted that this assignment is only an approximate label. A determination of whether a line corresponds to a $2p_{3/2}$ or $2p_{1/2}$ transition is challenging. Due to multiplet effects [22] the number of underlying lines of $2p_{3/2}$ and $2p_{1/2}$ transitions is spread over a large energy region. Since an energetic overlap of the L_3 or L_2 contributions to the spectrum can not be neglected especially for early 3d transition metals with a low spin-orbit splitting, a clear assignment of a peak of the TIY spectrum to a certain

$2p_{3/2}$ or $2p_{1/2}$ transitions is challenging (cf. fig. 6.3). In case of the late transition metals, the spin orbit splitting is higher than the widening of the L_3 and L_2 lines, which makes a good distinction between $2p_{3/2}$ and $2p_{1/2}$ transitions easier, as can be seen in figure 6.8 and 6.9. However, in order to simplify discussion the energetic lower lying lines are considered to belong to the $2p_{3/2}$ (L_3), the energetically higher lines to the $2p_{1/2}$ (L_2) transitions. The overall shape of the $L_{3,2}$ lines in figures 6.4 to 6.9 changes as a function of cluster size for each transition metal dopant. The spectra presented in figure 6.4 to 6.9 show a gradual change of the spectra with cluster size in both the exohedral and the endohedral cluster size regime. A general shift of the weightened mean intensity towards higher binding energies is observed for all MSi_n^+ (M=Sc,Ti,V,Cr,Mn,Co). This is due to a lower screening of the core potential in the initial state of the resonant excitation process. The energy difference between an initial state of the cluster Ψ_i and a final state Ψ_f corresponds to the excitation energy of resonant excitation $E(\Psi_i) - E(\Psi_f) = E_{res}$. A lowering of the initial states energy leads to a shift of resonant transition energy differences to higher energies. Screening in the initial state corresponds to a screening of the atomic core potential by the valence electrons, thus lowering the 2p binding energy. In this case, screening becomes less effective due to an incresing delocalization of valence electrons with cluster size. Obviously, delocalization is further increased at the cluster size n for which MSi_n^+ becomes endohedral. In addition, the electronic structure of the unoccupied density of states seems to change abruptly upon the transition from exohedral to endohedral cluster sizes, resulting not only in an energetic shift but also in a strong change in the spectral fingerprint. In general, the TIY spectra of the exohedral MSi_n^+ cluster in figures 6.4 to 6.9 show one broad line for the L_3 edge, which shows minor structure in some cases. In contrast to this, endohedral cluster sizes exhibit two or more features in their L_3 edge. This change in the spectral fingerprint is best seen for features marked (A) and (B) in figures 6.6 to 6.9. While this feature is less prominent in exohedral cluster sizes, its intensity is highly increased upon the exohedral to endohedral transition. It is supposed that feature (A) belongs to a state that forms when the transition metal is completely encapsulated in the silicon cage. This state therefore might form due to a full hybridization of the metal states with the silicon states, which is obviously favored due to a higher coordination of the metal atom. A similar reason might explain the growing of the line marked (B), which also seems to be linked to a closed silicon shell around the metal atom. It might result from a hybridization upon the total encapsulation of the transition metal by the silicon atoms. The markers

(A) and (B) are therefore set in figures 6.6 to 6.9 to observe the development
of the marked line for each dopant material at the smallest endohedral cluster
size to the largest cluster size measured of the particular dopant material M of
MSi_n^+ clusters. Feature (A) is assigned to the L_3 edge, since it shifts only slightly
compared to the increasing spin orbit splitting from about $3\,eV$ in the spectra of
VSi_n^+ to about $5\,eV$ in the spectra of $CoSi_n^+$ behind the middle of the L_3 edge.
Although both marked lines show upon the exhohedral to endohedral transition
of a MSi_n^+ species, the supposed corresponding formation of hybrid states seems
to be sensitive to different properties of a closed silicon shell. Feature (A) shows
in case of $CrSi_n^+$ only faint and in case of $CoSi_n^+$ at a one silicon atom larger cluster
size than (B). In case of $ScSi_n^+$ it does not show at all, which is explained later
on. On the other hand (B) shows accurately at each exohedral to endohedral
transition of MSi_n^+ clusters, but is not very pronounced for cluster sizes MSi_n^+
($n \geq 17$). It is assumed that while a single silicon shell around the metal atom
promotes formation of the corresponding states, silicon atoms in a second shell
showing from (n=17) (cf. fig. 6.10) inhibit this hybridization. In the following
the exohedral to endohedral transition of MSi_n^+ clusters identified with iscelp of
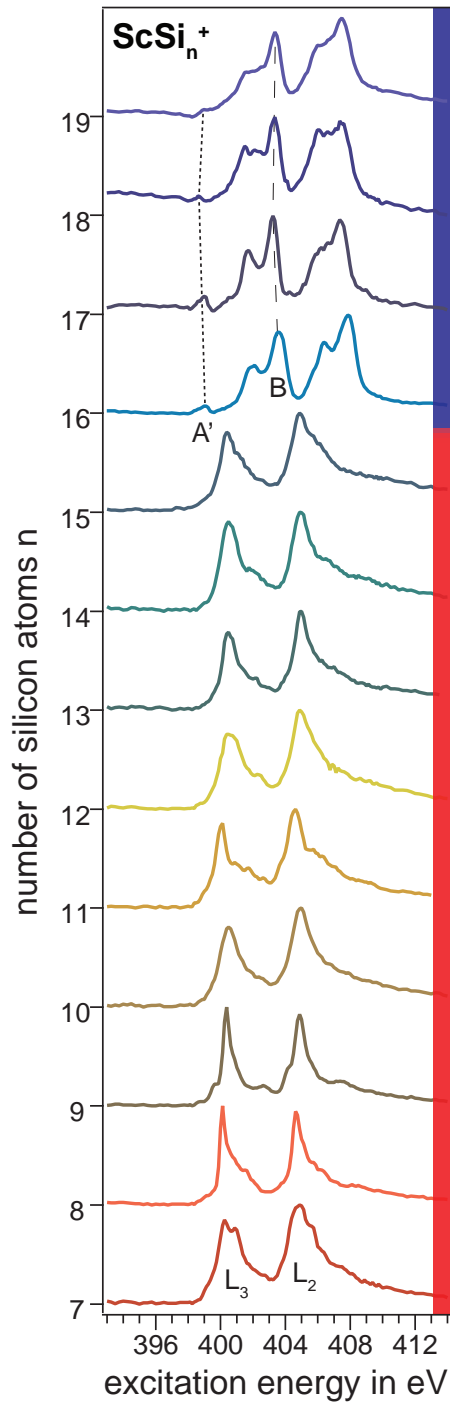lines (A) and (B) are discussed in detail.

Figure 6.4: Total ion yield spectra of $ScSi_n^+$. The cluster size n is given on the vertical axis. The red-blue bar on the right side shows the exohedral-endohedral transition. MSi_n^+ clusters in the red region are exohedral while clusters in the blue region are endohedral. The endohedral-exohedral transition results in a drastic change in the fingerprint of the spectra as a function of cluster size, which can be observed well in case of features (A') and (B') (see text).
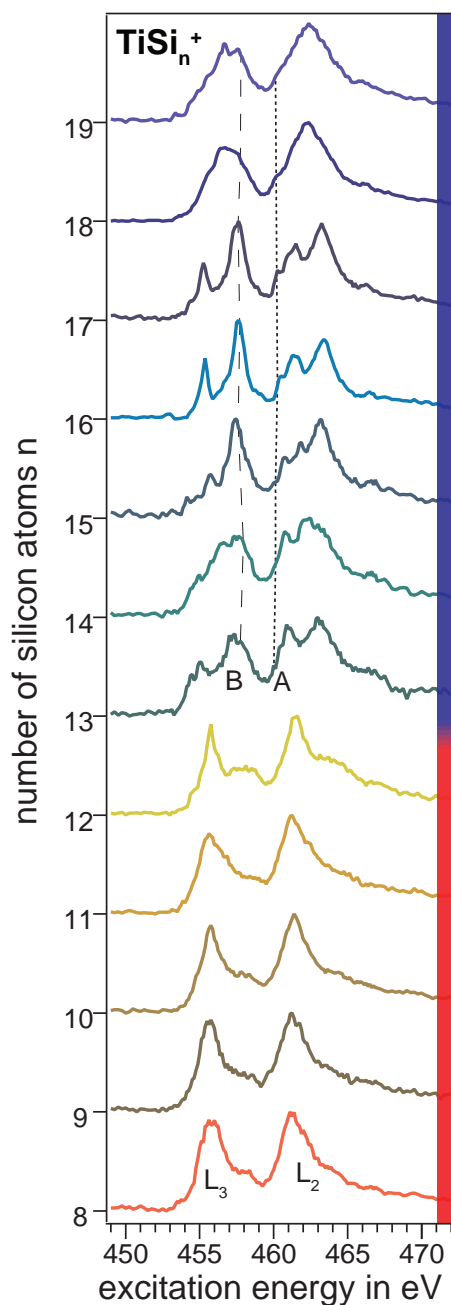
Figure 6.5: Total ion yield spectra of $TiSi_n^+$. The cluster size n is given on the vertical axis. The red-blue bar on the right side shows the exohedral-endohedral transition. MSi_n^+ clusters in the red region are exohedral while clusters in the blue region are endohedral. The endohedral-exohedral transition results in a drastic change in the fingerprint of the spectra as a function of cluster size, which can be observed well in case of features (A) and (B) (see text).
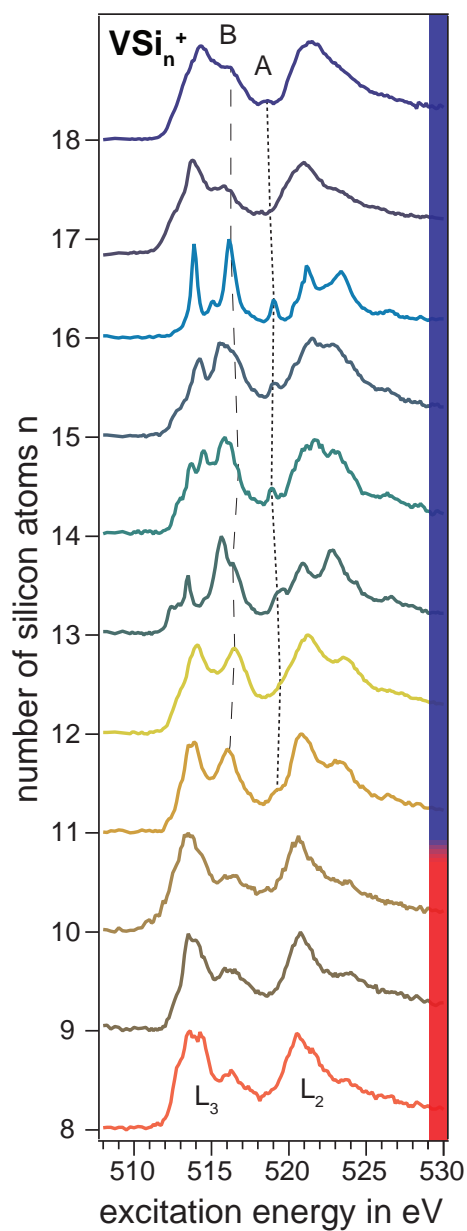
Figure 6.6: Combined ion yield spectra of VSi_n^+. Same description as in fig. 6.5.
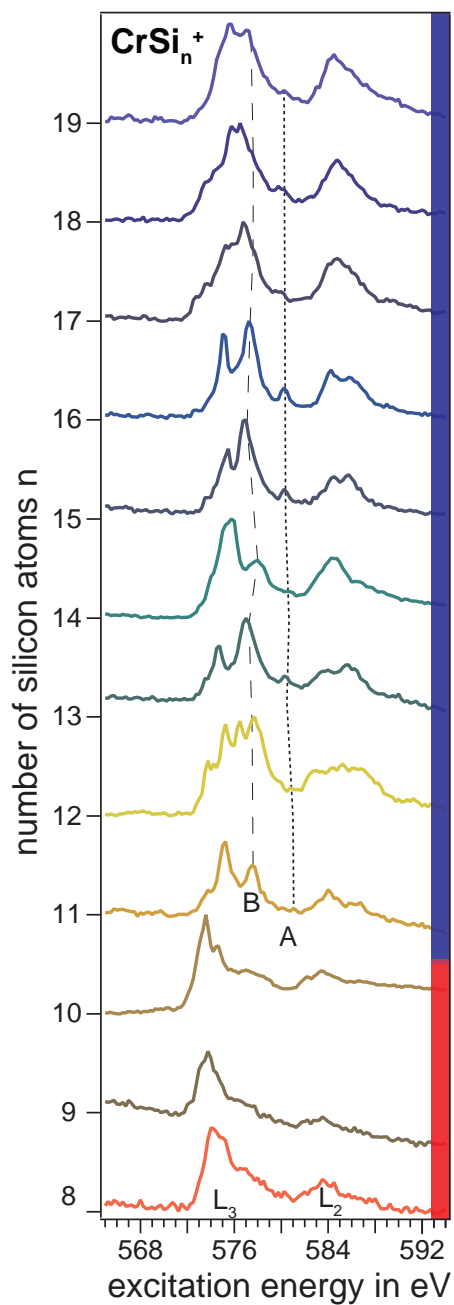
Figure 6.7: Combined ion yield spectra of $CrSi_n^+$. Same description as in fig. 6.5.
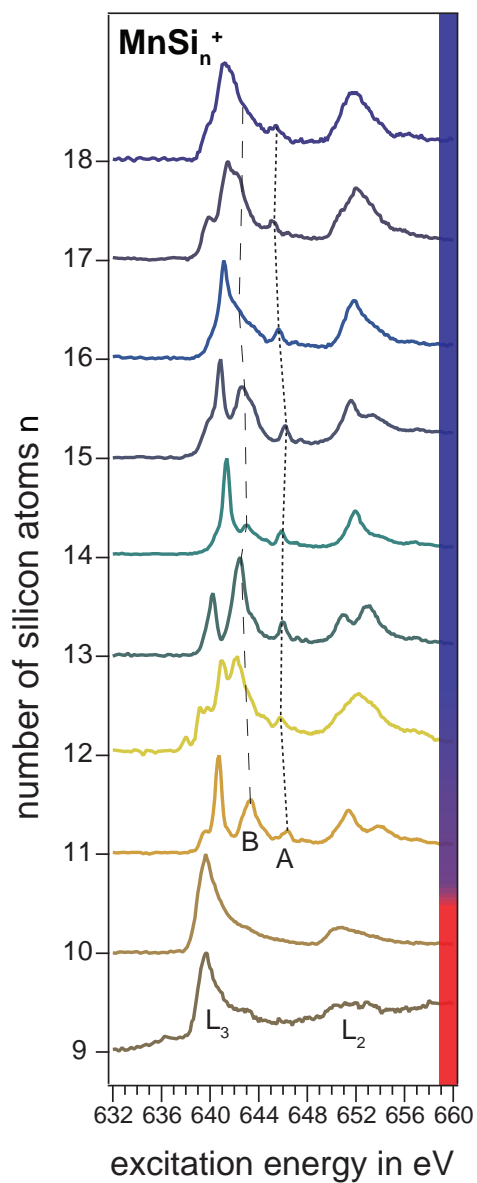
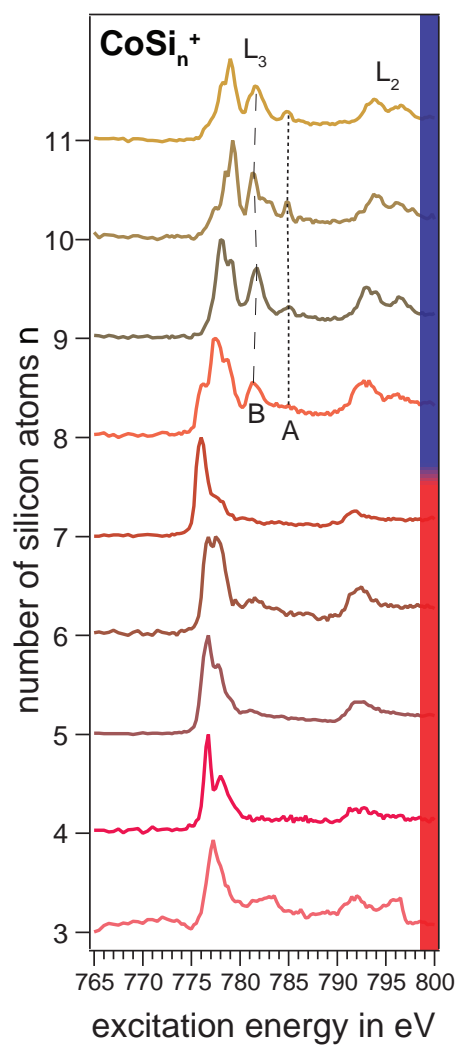**Figure 6.8:** Combined ion yield spectra of MnSi$_n^+$. Same description as in fig. 6.5.

Figure 6.9: Combined ion yield spectra of CoSi$_n^+$. Same description as in fig. 6.5.

Exohedral-Endohedral Transition in ScSi$_n^+$

In case of ScSi$_n^+$ clusters, the line marked (A) in the spectra of other MSi$_n^+$ clusters and the corresponding hybrid state is supposed to be overshadowed by the lines of the L$_2$ edge due to the low spin orbit splitting. However, another line shows at the low energetic side of the L$_3$ edge, which is due to a similar intensity to line (A) in other spectra named (A'). Although (A') cannot correspond to the same hybrid state as (A) due to the different electronic position, it is assumed that a similar hybridization takes place.

Despite this, the L$_3$ edge splits into two pronounced in lines the second of which is marked (B) in agreement with other transition metals. It seems that a drastic reallocation of the valence electrons take place, which may be due to the formation of hybrid states. In addition, the shift in energy of the mean intensity weight of the TIY spectrum due to a higher delocalization of valence electrons is much larger than in other MSi$_n^+$ clusters analyzed. Since this relatively large change in the spectral fingerprint does not only coincides with the exohedral-endohedral transition but are also measured in different beam times, these spectra are also discussed in section A.1. However, as no distortion of the partial ion yield by the experiment has become obvious, this spectra are included in the general discussion.

Exohedral-Endohedral Transition in TiSi$_n^+$

The endohedral-exohedral transition of TiSi$_n^+$ clusters can be observed in a growth of feature (B), which is assumed to correspond to a hybrid state only present in the endohedral cluster (cf. fig. 6.5). A similar state is responsible for feature (A), which is only merely recognizable as it is obscured by the L$_2$ edge contribution to the spectrum. Nonetheless, the cluster size at which the transition occurs is in good agreement with results obtained in reactivity experiments (cf. sect. 5.2).

Exohedral-Endohedral Transition in VSi$_n^+$

In case of vanadium doped silicon clusters the drastic change of the spectral fingerprint visible in feature (A) as well as (B) is observed at the transition between VSi$_{10}^+$ - VSi$_{11}^+$ (cf. fig. 6.6) in agreement with the exohedral-endohedral transition as a result of reactivity experiments (cf. chapter 5). Although comparison with the relative reactivity in figure 5.3 reveals the transition to be between $n = 10$ and $n = 11$, a much higher stability is observed for $n = 12$. This is explained in

chapter 5 with the coexistence of endohedral and exohedral low energetic geometric isomers for this cluster size. However, as indicators (A) and (B) of endohedral behavior in TIY spectra at the vanadium $L_{3,2}$ edge also show up at an cluster size $n = 11$, this size is taken as the smallest endohedral cluster. In literature, the exohedral-endohedral transition is marked at VSi_{12}^+ in reactivity experiments with water vapor [33, 49]. However this is no contradiction, as the authors took the value at a point where no reactivity is observed rather than the first drop in reactivity. Therefore the values are in good agreement with our observations. The same applies for experiments determining the exohedral-endohedral transition via argon adsorption [39]. Additional information is given in the discussion of reactivity experiments on MSi_n^+ clusters in chapter 5.

Exohedral-Endohedral Transition in $CrSi_n^+$

Although feature (A) and (B) both seem to be sensitive on the exohedral-endohedral transition and therefore both are suggested to correspond to states formed only in endohedral clusters, in the TIY spectra of $CrSi_n^+$ feature (A) is barely visible at the respective cluster size (cf. fig. 6.7). However, feature (B) is very prominent in the TIY of the first endohedral cluster size $CrSi_{11}^+$, in agreement with reactivity experiments performed in the framework of this thesis (cf. sect. 5.2) and literature [39]. Since feature (A) and (B) do not show with similar prominence, it is suggested that formation of the respective hybrid states has a different sensitivity on the degree of encapsulation of the transition metal by the silicon atoms.

Exohedral-Endohedral Transition in $MnSi_n^+$

In the TIY spectra presented in figure 6.8, the exohedral-endohedral transition between $MnSi_{10}^+$ and $MnSi_{11}^+$ known from reactivity experiments (cf. tab. 5.1) does again coincide with a change in the spectral fingerprint (cf. fig. 6.8). However, it shows that for some cluster sizes (n=14,16,18) feature (B) which is supposed to correspond to a hybrid state only present in endohedral clusters is only barely visible, whereas feature (A) which is assumed to belong to a similar state can be seen throughout all endohedral clusters. A possible explanation could be that this particular hybrid state is almost completely occupied for these cluster sizes. The reason why this is only observed in $MnSi_{14,16,18}^+$ and not in corresponding cluster sizes of other doped species is not yet understood, but it is expected that a detailed analysis of the geometric structure of $MnSi_{14,16,18}^+$ and comparison of

these to other $MSi^+_{14,16,18}$ clusters might help to understand the underlying effect. At the moment, no structures of cationic manganese doped silicon clusters are available in literature to compare to the structures of other doped species (cf. fig. 6.10).

Exohedral-Endohedral Transition in $CoSi^+_n$

Since for the cobalt doped species no data from reactivity experiments of our group or literature is available, the change in its spectral fingerprint visible in feature (B) between the cluster sizes $CoSi^+_7$ and $CoSi^+_8$ can be regarded as the transition size (cf. fig. 6.9). The same value is also found in literature via Argon adsorption [39]. Similar to $CrSi^+_n$, feature (A) is to be seen clearly only at the next larger cluster size. Again, this may be due to a different sensitivity of hybrid state formation towards the coordination of the metal atom.
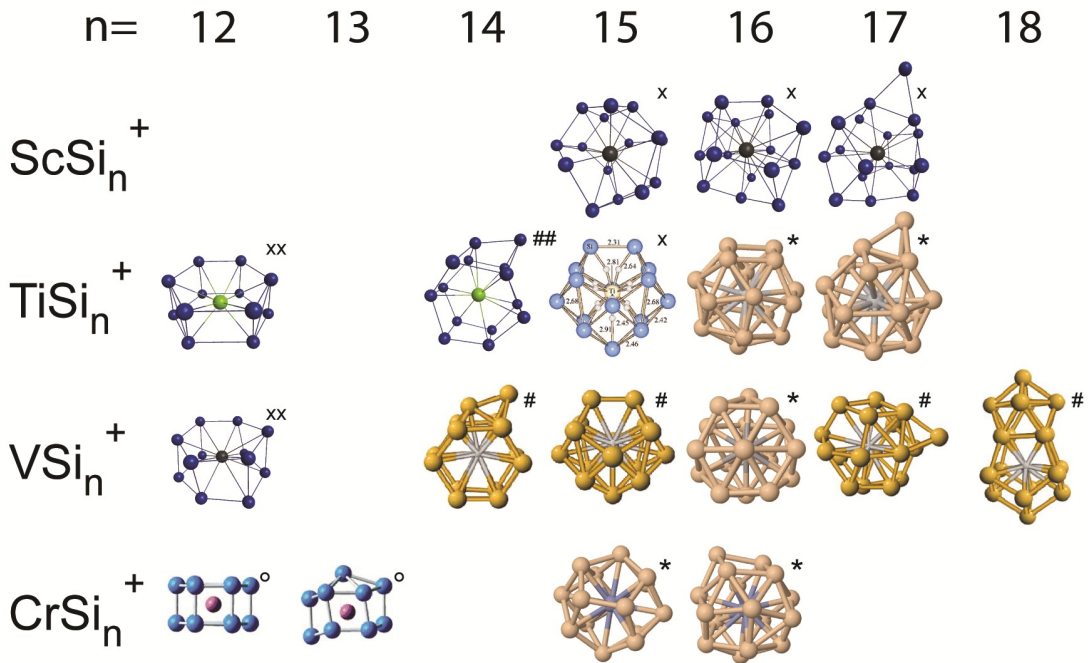
Figure 6.10: Calculated structures of cationic transition metal doped silicon clusters. The coordination of silicon atoms of the VSi^+_{16} Frank-Caspar polyhedron explains the high degeneracy of states suggested by the ion yield spectrum (cf. fig. 6.6). The geometries of $TiSi^+_{16}$ and $CrSi^+_{16}$ with one additional/missing electron in the valence DOS occupancy of the system are similar to VSi^+_{16}. Both geometries are distorted FK polyhedrons. x [31], $*$ [32], $\#$ [1], and o [90]. Ion geometries xx and $\#\#$ relaxed from neutral structures x [31] and $\#$ [1].

6.3 Detailed Analysis of Selected Transition Metal Doped Silicon Clusters

The central theme of section 6.3.1 are selected cluster sizes showing an exceptional behavior in figures 6.5 to 6.7. In the first section, the highly symmetric VSi_{16}^+ is discussed and compared to dopant materials at neighboring positions in the periodic table (cf. fig. 6.2) in equal sized silicon cages, $TiSi_{16}^+$ and $CrSi_{16}^+$. VSi_{16}^+ is very interesting because of its high stability and low reactivity, observed in experiments [39,49]. In addition, a theoretical model exists, explaining the observed properties by means of a spherical potential model [1]. $TiSi_{16}^+$ and $CrSi_{16}^+$ are integrated into the chapter, since their TIY spectra at the metal $L_{3,2}$ edge exhibits the same spectral fingerprint as VSi_{16}^+, indicating a similar local electronic density of states of the unoccupied valence density of states.

This section is followed by section 6.3.2, comparing different cage materials. It analyzes the possibility of interchanging the silicon cage with an element of similar electronic configuration, germanium.

6.3.1 Highly Symmetric VSi_{16}^+ and Equal Sized $TiSi_{16}^+$ and $CrSi_{16}^+$

Among the endohedral MSi_n^+ clusters analyzed, one cluster size exhibits outstanding features, VSi_{16}^+ shown in figure 6.6. VSi_{16}^+ is known to have a highly symmetric, nearly spherical geometry of a Frank-Kaspar polyhedron (cf. sect. 2.3). Due to its high symmetry [1,32,57] and high stability [39,49] indicating a high HOMO-LUMO gap [1,31] it is also extensively analyzed by theory [1,32,57] and experiments [39,49,58,91] alike. The results on the metal $L_{3,2}$ edge excitation presented in the following are therefore compared to existing theoretical results. Parts of the following section have been published in [58]. In the 2p x-ray absorption spectrum of the transition metal dopant, VSi_{16}^+ shows very sharp lines. Surprisingly, a very similar spectral fingerprint is also found in the spectra of $TiSi_{16}^+$ and $CrSi_{16}^+$. The spectra are presented in figure 6.11. For better comparison, the spectra of $TiSi_{16}^+$, VSi_{16}^+, and $CrSi_{16}^+$ are plotted in figure 6.11 aligned with respect to the first peak of their L_3 edge, arbitrary set to an energy of 0 eV. The figure also shows the TIY spectra of monomer cations of the MSi_n^+ clusters respective dopant material, which are also aligned with respect to the first peak of their L_3 edge. In order to compare a MSi_{16}^+ cluster with the respective transition metal ion, a relative shift between both TIY spectra is present, since the ion's absorption spectrum
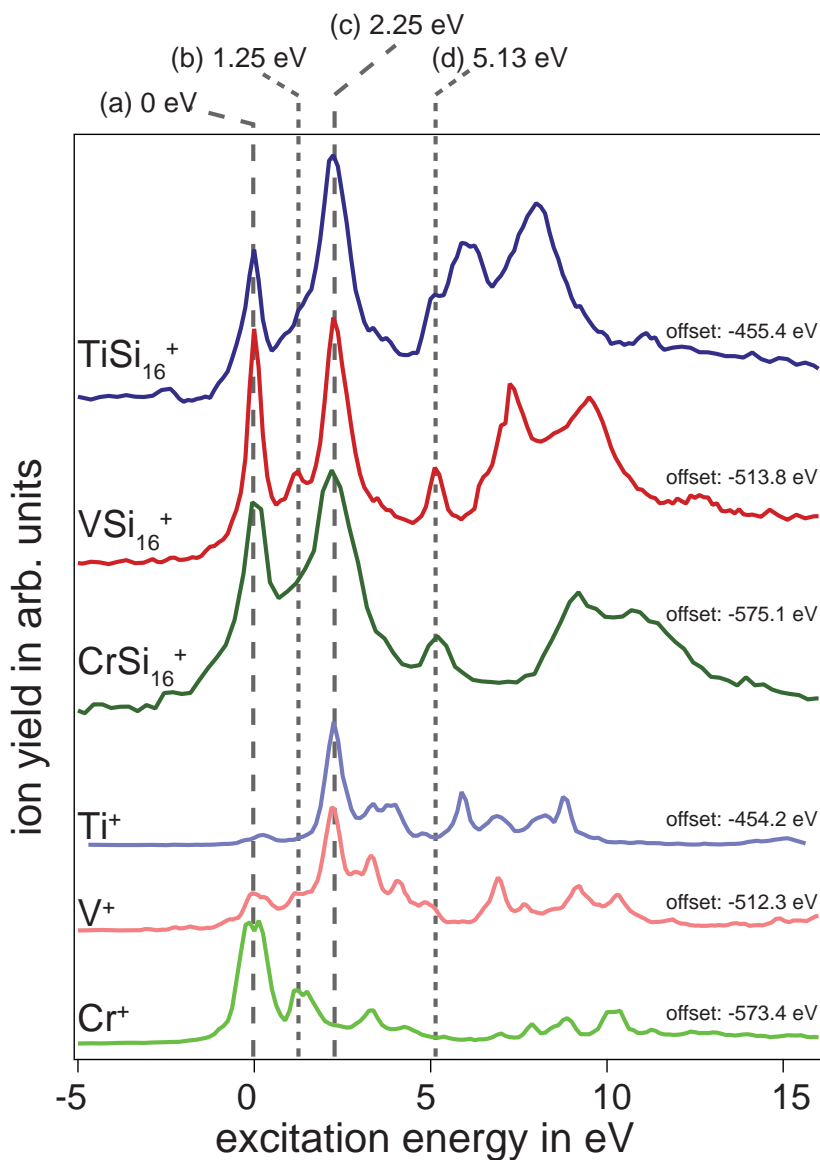
Figure 6.11: Ion yield spectra of the highly symmetric VSi_{16}^+. The spectrum exhibits sharp features. Its fingerprint is also found for $TiSi_{16}^+$ and $CrSi_{16}^+$. For comparison, the spectra are aligned with respect to their first peak, set arbitrarily to $0\,eV$. The energy each spectrum is shifted for alignment is given on the right side above each spectrum. Below the TIY spectrum of the doped silicon cluster, the respective cationic monomer are shown, which are also aligned with respect to its first peak. The marked features (a), (b), (c), and (d) can be assigned to transitions into certain states of the cluster, as shown in figure 6.12 and explained in detail in the text.

is found at about $1.2\,\text{eV}$ to $1.7\,\text{eV}$ lower photon energies. The lower excitation energy of the ions can be explained with a higher screening of the core potential in the ion's initial state due to a higher localization of atomic 3d valence electrons. Thus the 2p binding energy is decreased. In the cluster a delocalization of the former metal's valence electrons is energetically preferred. Therefore, the screening of the metals core potential is decreased. The absolute shift used for alignment is given on the right side above each TIY spectrum.

Apart from the shift of the L_2 line due to a increasing spin orbit splitting with atomic number of the dopant, all three spectra of transition metal doped silicon clusters exhibit equal features. This is notable, as the spectra of the pure metal dopant monomers, shown underneath each MSi_{16}^+ spectrum do not show such resemblance when compared to each other. The cations exhibit differences in their resonant 2p x-ray absorption due to their different 3d occupancy. Since XAS is very sensible to the local electronic configuration, differences in the TIY spectra is exactly what would be expected. The high resemblance of the TIY spectra of TiSi_{16}^+, VSi_{16}^+, and CrSi_{16}^+ shows that the three clusters have a very similar local electronic structure at the metal dopant, which is obviously not the case for the respective cationic monomers (cf. fig. 6.11). The local electronic structure inside the silicon cage is therefore dominated by the silicon cage. In the following the features appearing in the L_3 edge are discussed, which are marked in figure 6.11 by vertical lines.

The first (a) and third (c) line are coarse dashed and mark the most prominent features, while the second (b) and fourth (d) fine dashed line mark features of minor prominence. All lines mark features that are at the same relative positions for all three dopant elements. This indicates that these lines belong to the L_3 edge, as their position is not affected by the spin orbit splitting. Since the lines are reproduced in all three MSi_{16}^+, M=(Ti,V,Cr) spectra, the local electronic configuration has to be similar for the different transition metal dopant atoms (cf. sect. 2.3). Since the electronic configuration at the metal atom is influenced by the symmetry of its electronic environment, XAS is also sensitive on this symmetry. This allows to evaluate the degree of symmetry for the silicon cage. To understand the resemblance of the three TIY spectra, in the following the shape of VSi_{16}^+ spectra will be discussed within the spherical shell model [1]. After this it is discussed, if the resemblance of the TIY spectra of TiSi_{16}^+ and CrSi_{16}^+ is also understandable within this theoretical description.

Comparison with the valence DOS of VSi_{16}^+ FK-polyhedron [1] reveals an explanation for the fingerprint. The DOS is displayed in figure 6.12 as a simplified
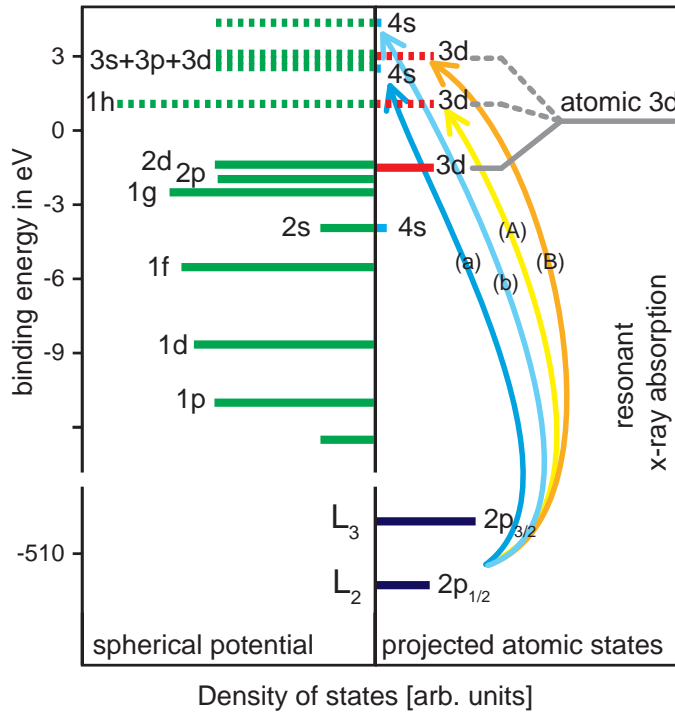
Figure 6.12: Simplified view of the DOS of VSi_{16}^+, shown in figure 2.5. In the left panel orbitals are denoted in spherical potential convention, while in the right panel orbitals of the transition metal atom are denoted in atomic convention. The HOMO-LUMO gap is visible between the clusters 2d and 1h orbital. The transition metals 3d orbitals hybridized with the silicon cages 2d and 1h orbitals due to their same angular momentum character [1]. The transitions marked (a), (c), (b), and (d) correspond to the features marked by lines in fig. 6.11. A comprehensive explanation is given in the text.

graphic of the calculated DOS [1] already known from figure 2.5). The DOS (left side in fig. 6.12) of VSi_{16}^+ and the DOS projected to the atomic states of the vanadium atom (right side in fig. 6.12) shows a splitting of the metal 3d orbital. In the theoretical approach, the DOS states are denominated with respect to their radial character N and their angular momentum l, Nl =(1s,1p,1d,1f,2s,...) according to harmonic oscillator notation [1,3]. The 1l orbitals, also called σ orbitals, have no radial nodes and are mainly located at the silicon cage [3]. The 2l orbitals, also called π orbitals, have a radial node and therefore intensity in the center of the cluster [3]. Therefore, the bonding among the silicon atoms in the empty spherical cage is mediated by σ orbitals without radial notes (1s,1p,1d,1f,1g) and 1h is also a state of the empty cage structure. Bonding of the cage to the transition metal dopant on the other hand has to involve π orbitals, since only these orbitals overlap with the metal atom in the center of the cage. An exception to this rule is the 1h orbital, which also mixes with the transition metals atomic 3d orbital[1].

---

[1]It should be noted that in the description atomic orbitals are denoted in atomic convention, while states of the silicon cage follow spherical potential notation originally known from nuclear

Why this is possible is explained below. The π orbitals hybridize with the metal atomic 3d orbital if they have the same angular momentum character. Therefore, the cage 2s and 2d orbitals can hybridize with the metal 4s and 3d orbitals. These hybrid orbitals form the HOMO bonding orbital of the cluster. Since the orbitals degeneracy is lifted due to the T_d symmetry, mixing is also possible, if the orbital splitting of the former degenerate energy level has the same components, which are for tetrahedral symmetry [1,3]:

s (a_1) $\rightarrow$ Mixing of: V atomic 3s + Si cage 4s

p (t_2)

d $(e + t_2)$ $\rightarrow$ Mixing of: V atomic 3d + Si cage 2d,

                                           V atomic 3d + Si cage 3d

f $(a_2 + t_1 + t_2)$

g $(a_1 + e + t_1 + t_2)$

h $(e + t_1 + 2\,t_2)$ $\rightarrow$ Mixing of V atomic 3d + Si cage 1h

Due to the energetically equal position (cf. fig. 6.12) and equal components e and t_2, the metal 3d and silicon cage 1h orbitals can also hybridize [1,3] and form the LUMO of the cluster. Furthermore, the unoccupied orbitals 3d and 3s of the cage can hybridize with the metal's atomic unoccupied 4s and 3d states forming additional orbitals, as shown in figure 6.12. In the resonant absorption process, transitions of atomic 2p core electrons into orbitals with a 3d,4s character are dipole allowed. Since the vanadium 2p core hole generated by resonant x-ray absorption is located at the vanadium atom, and the metal 3d states have major contributions to the silicon cage's narrowly grouped unoccupied 1h and 3d states, the two prominent lines (a) and (c) of the L$_3$ edge of VSi$_{16}^+$ in figure 6.11 can be explained with transitions into these hybrid orbitals, as shown by the yellow and orange arrows in figure 6.12. The non-distinctive lines (b) and (d) therefore correspond to transitions into the clusters unoccupied 3s and 4s orbitals, as indicated by the light blue and dark blue arrows in figure 6.12. The explanation of the shape of the spectrum of VSi$_{16}^+$ mentioned above is close to another model, which could help to gain additional knowledge of the local unoccupied DOS at the metal dopant. This is the crystal field splitting model used to explain the x-ray absorption spectra of transition metal ions in compounds [58,92]. According to this model, the transition metal in the center of the silicon cage is in a tetrahedral site of the tetravalent silicon cage contributing its valence electrons

---

physics [1,56].

to bonding orbitals, analog to octahedral symmetry discussed in [92]. In case of vanadium, this would lead to an effective local $3d^0$ configuration, with the atomic 3d orbital split into e and t_2 due to the tetrahedral symmetry of the silicon cage environment. The spherical potential of the empty silicon cage would have with the additional four valence electrons of V^+ a shell closure of its 2d state with 68 electrons. A preliminary calculation [93] of the configuration $3d^0$ in tetrahedral symmetry is shown in the upper panel of figure 6.13. The similarities of
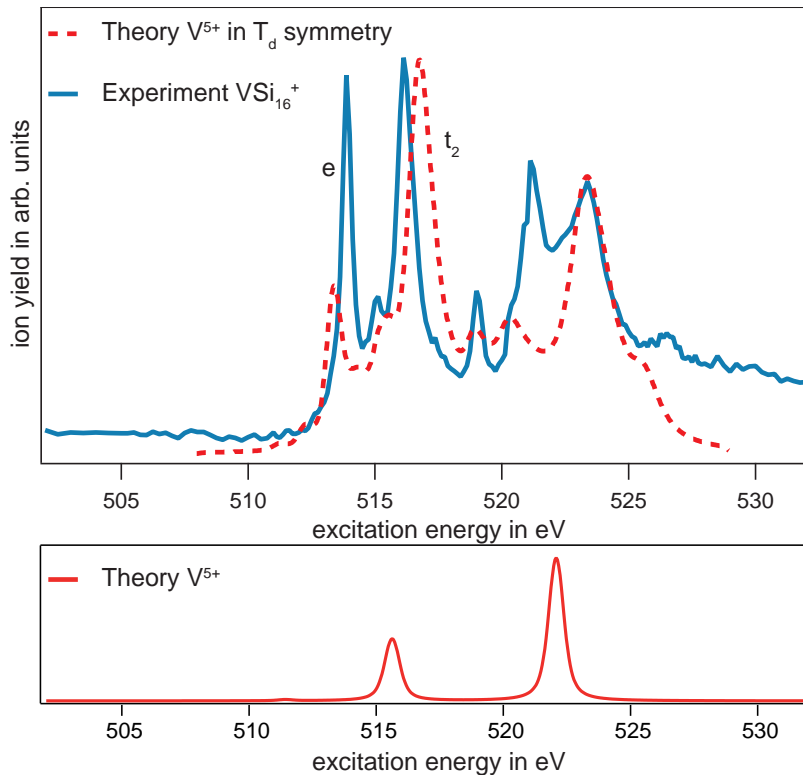
Figure 6.13: HF calculation of a V^{5+} in a tetrahedral crystal field. A resemblance between the experimental x-ray absorption spectrum at the vanadium 2p edge and the calculated spectrum can be observed. The calculated spectrum is shifted in energy to match the experimental spectrum. Calculations by [93].
Lower panel: HF calculation of V^{5+} without crystal field. The energy axis is arbitrarily shifted for better comparison with the upper panel.

experimental and theoretical data mainly visible in the first peak corroborate the assumption of a local $3d^0$ configuration. The splitting into e and t_2 of the atomic 3d state corresponds to the two contributions of the L_3 edge. It is clearly an effect of inclusion of the tetrahedral symmetry in the calculation [93] as can be seen in comparison with a HF calculation of the single V^{5+} cation displayed in the lower panel of figure 6.13.

The agreement between the theoretical calculations and the experimental findings is not good enough to clearly verify the assumptions. On the other hand,

one would not expect a total charge transfer leading to a complete local d^0 configuration at the metal atom. This can be seen in the DFT calculations of the DOS of the spherical silicon cage in figure 6.12. The projection of the silicon cages states on the atomic 3d state of vanadium shows that the lower part of the e and t_2 split 3d state has an electron occupation.

The opposite to the complete charge transfer approach, resulting in the local $3d^0$ configuration at the transition metal dopant of the doped silicon cluster [1, 58], recent theoretical results [57] suggested that the transition metal V is in a local neutral state, leaving the silicon cage Si_{16} in a singly charged state in VSi_{16}^+ (cf. sect. 2.3). Since this new theoretical approach not only focuses on VSi_{16}^+ but also explains the resemblance of its TIY spectrum with the TIY spectra of $TiSi_{16}^+$ and $CrSi_{16}^+$. Therefore it is discussed in the next section.

Comparison of Similar TIY Spectra of VSi_{16}^+, $TiSi_{16}^+$, and $CrSi_{16}^+$

The similar fingerprints in the TIY spectra of VSi_{16}^+, $TiSi_{16}^+$, and $CrSi_{16}^+$ are discussed in the following. The discussion will start with the total charge transfer approach, discussed above [93]. Then, a explanation within the framework of the spherical potential model [1, 3, 58] is discussed. At the end of this section a very recent theoretical approach concentrating on the resemblance in the transition metal $L_{3,2}$ edge's TIY spectra of VSi_{16}^+, $TiSi_{16}^+$, and $CrSi_{16}^+$ is presented [57].

In the first approach, a total charge transfer of the transition metal dopant's 3d and 4s valence electrons to the silicon cage is suggested. If this would happen not only for VSi_{16}^+, but would also occur in case of $TiSi_{16}^+$ and $CrSi_{16}^+$, the local electronic state of the transition metal dopant would in all three cases be a local $3d^0$ configuration. Since a x-ray absorption spectrum is mainly dominated by the local unoccupied density of states, the spectra of VSi_{16}^+, $TiSi_{16}^+$, and $CrSi_{16}^+$ should look alike, showing all the fingerprint of a local $3d^0$ configuration in tetrahedral symmetry.

The resemblance in spectral fingerprint of $TiSi_{16}^+$ and $CrSi_{16}^+$ might also be explained within the spherical shell model [1, 58]. $TiSi_{16}^+$ and $CrSi_{16}^+$ have an additional or missing electron respectively, and a 68 electron shell closure of the clusters 2d orbital followed by the band gap to the clusters 1h orbital is therefore not achieved. Hence, a $2d^9$ configuration is present for $TiSi_{16}^+$, with most of the clusters 2d orbitals contribution at the silicon cage [1]. The small change in the valence occupancy of the 2d orbital does not effectively influence the x-ray transition, as only a small part of the 2d hole is located at the titanium dopant, as can

be seen in the metal projected density of states shown in figure 2.5. The 2p-3d
transition taking place at the metal atom therefore resembles the transition for
VSi_{16}^+, with a slight broadening of lines due to the Jahn-Teller distortion [94] of
the $TiSi_{16}^+$ geometric structure, which is shown next to the structures of $CrSi_{16}^+$
and the ideal FK polyhedron VSi_{16}^+ in figure 6.10.

The explanation for $CrSi_{16}^+$ holding 69 valence electrons is similar, but with one
additional electron located in the 1h orbital above the HOMO-LUMO gap. The
electron is mainly located at the silicon cage, due to the lack of a radial node
of the 1h orbital and therefore has a negligible influence on the local electronic
structure of the unoccupied DOS. The broadening of the lines with respect to the
spectrum of VSi_{16}^+ visible in figure 6.11 is again due to Jahn-Teller deformation,
which is apparently larger than for $TiSi_{16}^+$ (cf. fig. 6.10).

The recent results on the apparently similar local electronic density of states at
the transition metal of $TiSi_{16}^+$, VSi_{16}^+, and $CrSi_{16}^+$ showing in XAS at the metal
$L_{3,2}$ edges focuses on the electron density in these clusters obtained via DFT cal-
culations [57]. The authors mainly try to explain the stabilization of a Si_{16} cage
by a Ti^+ and Cr^+, and V^+ atom by analyzing the local electron density at the
metal atom. The DOS of these clusters obtained in DFT calculations is equal to
the one shown in the spherical potential model [1]. Therefore the same nomencla-
ture applies for the hybridized cluster states. It is stressed that calculation show
for all three cases the electronic configuration of a neutral transition metal atom
(Ti,V,Cr) in a singly charged silicon cage (Si_{16}^+). Since the number of valence
electrons differs in neutral titanium, vanadium, and chromium atoms as can be
seen by their electronic configuration in figure 6.2, the unoccupied local density
of states differs, which should result in different spectral fingerprints. Therefore,
this model is not suited to describe the similar TIY spectra at the transition
metal $L_{3,2}$ edge found for $TiSi_{16}^+$, VSi_{16}^+, and $CrSi_{16}^+$.

6.3.2 Comparison of Silicon and Germanium Cage Struc-
tures

Analysis of x-ray absorption of transition metal doped silicon clusters for different
cluster sizes (cf. sect. 6.2) yields information about size effects in these clusters.
In addition, interchanging the dopant at equal cluster size, allows observation of
the influence of valence occupancy in MSi_n^+ clusters. The theoretical approaches
of a spherical potential model with electron counting rules (cf. sect. 2.3) and
a spherical shell model (cf. sect. 2.3 and 6.3.1) are based on the geometry of

the encapsulating atoms and the total valence occupancy of the cluster. These models can be tested by interchanging the cage silicon with another element with a similar valence electron structure. If the geometry is maintained and therefore a similar electronic structure is present, the x-ray absorption spectrum should reveal the same fingerprint.

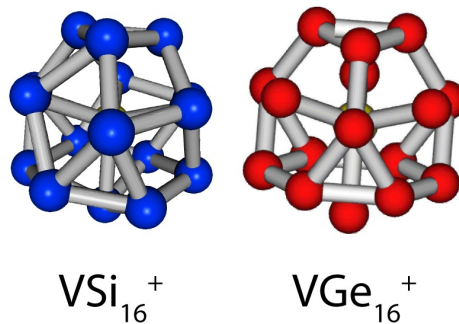Good candidates for silicon replacement are carbon, germanium, tin and lead,

Figure 6.14: Calculated Structures of VSi_{16}^+ and VGe_{16}^+. Both clusters hold the same geometry of the Frank-Kaspar polyhedron [32].

having all a ns^2np^2 configuration due to their position in the 14th group of the periodic table. Since the analysis should include the extensively studied [1, 32, 57, 58, 83] highly symmetric FK polyhedron with vanadium as dopant, tin and lead are not a suitable choice. The high absorption signal of the $M_{4,5}$ (Sn) and $N_{4,5}$ (Pb) edges in the vicinity of the transition metal $L_{3,2}$ edge [89] drowned the vanadium 2p absorption signal. Germanium is therefore chosen as a test system, due to a better sputtering yield than carbon.

Similar studies on the influence of the cage materials Si, Ge, Sn, and Pb are published, which analyzed TiX_{16}^- by means of photoelectron spectroscopy [83]. Comparison with DFT calculations suggests that all TiX_{16}^- clusters have the same geometric ground state, which is a distorted Frank-Kaspar polyhedron similar to the perfect Frank-Kaspar polyhedron found for $TiSi_{16}$ and VSi_{16}^+ [1, 2, 83]. In addition, a high resemblance in the photoelectron spectra of TiX_{16}^- is observed [83], which suggests a similar electronic structure of these clusters. If these results can be translated to the perfect Frank-Kaspar polyhedron geometry of VSi_{16}^+, the results obtained via x-ray absorption at the vanadium $L_{3,2}$ edge should also show similar spectra for VSi_{16}^+ and VGe_{16}^+. This is indeed so, as can be seen in the results presented in figure 6.15. In addition to VX_{16}^+ (X=Si,Ge), the respective spectra for cluster sizes VX_n^+ (n=12-16) are shown.

As can be seen in figure 6.15, the features of the VGe_{16}^+ and VSi_{16}^+ show an astonishing resemblance with only a slight energy shift of 125 meV towards higher
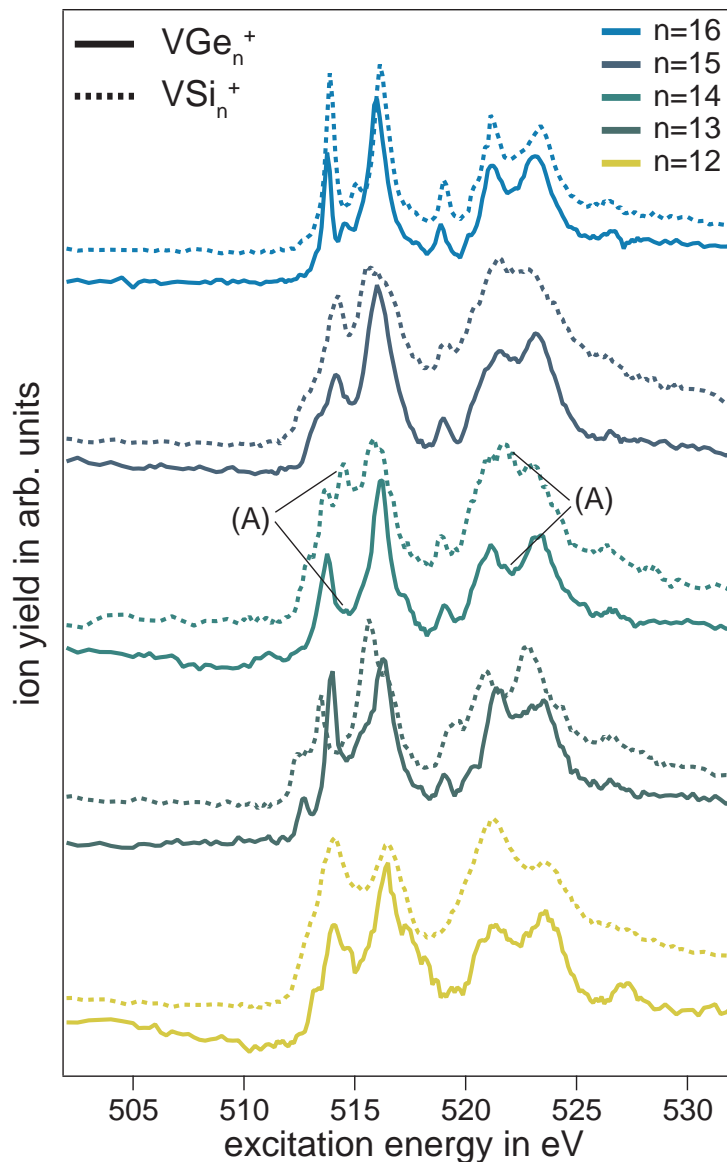
Figure 6.15: TIY spectra of VGe_n^+ clusters (solid line) and VSi_n^+ clusters (dashed line). Equal sized clusters exhibit a similar spectral fingerprint. For the smaller clusters $n \in [12, 14]$, the intensity of the lines varies between the vanadium doped germanium and vanadium doped silicon cation.

photon energies. Since energy calibration of this particular beam line is very good, it might be that this shift in energy is due to the differences in the radius of the cluster the slightly different binding energies of ns^2np^2 valence electrons in silicon and germanium. This may result in a difference in the screening of 2p electrons thus influencing the excitation energy of resonant x-ray absorption. Theoretical calculations confirm equal geometric structure for VGe_{16}^+ and VSi_{16}^+ [32, 83], indicated by the same fingerprint in the x-ray absorption spectra (cf. fig. 6.14 and 6.15).

VSi_{14}^{+}					
Energy	0.00 eV	0.08 eV	0.14 eV	0.18 eV	0.19 eV
HOMO-LUMO gap	0.79 eV	0.55 eV	0.77 eV	0.76 eV	1.15 eV
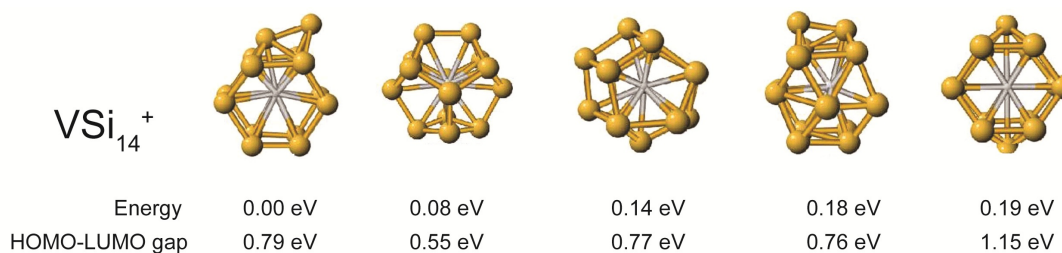
Figure 6.16: Calculated geometries of the five energetically lowest isomers of VSi_{14}^{+} [1].

With decreasing cluster size, the resemblance between VSi_n^{+} and VGe_n^{+} diminishes but is nevertheless strong. All peaks visible in the spectra of VGe_n^{+} are present in the spectrum of VSi_n^{+}, but the intensity differs in some cases drastically. An example is the high intensity of feature (A) visible in the L_3 and L_2 edge of the spectrum of VSi_{14}^{+} in figure 6.15, which is barely visible in the spectrum of VGe_{14}^{+}. This difference in the spectra is assumed to correspond to unlike geometries of these two cluster sizes. It is known that VSi_{14}^{+} has a large number of isomers lying energetically close to the ground state [1], as can be seen in figure 6.16. It is suggested that the ground state of VGe_{14}^{+} is another geometry than the ground state of VSi_{14}^{+}. If the ground state of VGe_{14}^{+} is more like the second or third isomer in figure 6.16, the more spherical structure might explain the lower number of lines visible in the spectrum. Apparently VGe_{14}^{+} has a higher level of degeneracy of valence states than VSi_{14}^{+}. The overall high similarity of the spectra of equal sized endohedral cluster however, substantiates the assumption that a transition metal atom has a similar electronic environment in a silicon shell as in an equal sized germanium shell. Furthermore, the similar spectra of VX_{16}^{+} (X=Si,Ge) indicate a similar local unoccupied density of states in both clusters. This should also be the result of the spherical shell model due to equal geometry and number of valence electrons in both systems. The measurements therefore shows that this model seems to be suited to explain the electronic structure of MSi_{16} clusters in the geometry of a Frank-Kaspar polyhedron.

Chapter 7

Ion Yield Spectroscopy at the Silicon Cage 2p Edge

X-ray absorption studies of MSi_n^+ clusters at the silicon $L_{3,2}$ edge are important to obtain detailed information about the electronic structure of the valence orbitals of these clusters in conjunction with x-ray absorption studies at the transition metal M $L_{3,2}$ edge. While absorption at the metal $L_{3,2}$ edge gives information about the local unoccupied density at the transition metal, studying the absorption of MSi_n^+ at the $L_{3,2}$ edge of silicon offer an insight into the unoccupied density of states at the silicon cage around the transition metal center. Therefore, a full description of the clusters electronic structure can only be reached by combining the results obtained from the respective absorption edges.

The main focus in this context is the electronic structure of the highly stable and symmetric VSi_{16}^+ [1, 57], for which a high degeneracy of the electronic states is found theoretically and which can be described with spherical shell model (cf. sect. 2.3). The high degeneracy of states also shows in the analysis of the transition metal $L_{3,2}$ edge ion yield spectrum. Furthermore, $TiSi_{16}^+$ and $CrSi_{16}^+$ showed similar absorption spectra at the transition metal $L_{3,2}$ edge, which has to be the result of a similar local electronic structure. Since atomic Ti, V and Cr do not share similar electronic configurations (cf. fig. 6.2), the similar local electronic structure at the metal atom has to be an effect of the symmetric silicon cage. This effect can be investigated via absorption spectroscopy at the silicon $L_{3,2}$ edge.

In the following, the results of x-ray absorption spectroscopy at the silicon 2p edge via ion yield spectroscopy are presented. It is shown that analysis of the partial ion yield (PIY) does not only provide information on the unoccupied electronic density of states of the cluster via resonant x-ray absorption (cf. sect. 7.2.1), but

97

also on the 2p binding energy with respect to the vacuum level, since a photon induced daughter ion is identified showing the direct photoionization edge of the silicon 2p orbital (cf. sect. 7.2.2). Furthermore, the possible geometric structure of an MSi_n^+ cluster can be deduced from comparison of DFT calculations to silicon 2p direct photoionization efficiency, as is explained in detail in section 7.2.3. However, it is mandatory to discuss the generation of product ions in the silicon $L_{3,2}$ energy regime first. Unlike the fragmentation pattern of a MSi_n^+ cluster upon excitation at the transition metal $L_{3,2}$ edge for which only few photo fragments are observed and PIY spectra of different photo fragments show the same energy dependence, absorption at the silicon $L_{3,2}$ edge of a MSi_n^+ parent cluster yields multiple photo fragments MSi_x^{k+} ($x < n$) and in addition daughter ions MSi_n^{p+} ($p > 1$) of equal size as the parent ion with different energy dependences in their respective PIY. The differences in PIY spectra of daughter ions and photo fragments [1] can be understood by an analysis of generation channels of the respective ion. These generation channels are equal for all MSi_n^+ parent cluster's daughter ions and photo fragments. The generation and its effect on the PIY spectrum of a respective product ion is discussed exemplarily on the PIY spectra of the parent cluster VSi_{16}^+.

7.1   Effect of the Generation Channel of Product Ions on the PIY Spectra

The PIY of product ions of a MSi_n^+ cluster generated upon photo excitation in silicon $L_{3,2}$ edge energy regime show different energy dependences, which can be understood by analyzing the possible generation channels of the corresponding product ion. Since product ion generation follows a pattern that holds true for all MSi_n^+ parent clusters [2] this pattern is explained for the arbitrarily selected parent cluster VSi_{16}^+, in the next section 7.1. The PIY spectra of VSi_{16}^+ is shown in figure 7.1. Since the analysis described in the following is equal for all parent clusters, the more general term MSi_n^+ is used instead of VSi_{16}^+. In general, different types of PIY spectra can be identified. Therefore, the PIY spectra of product ions generated upon silicon 2p absorption of a MSi_n^+ parent cluster are grouped

---

[1]In the following, the term *daughter ion* refers to ions MSi_n^{p+} ($p > 1$) equal sized to the parent ion, whereas *photo fragments* MSi_x^{k+} ($x < n$) refers to generated ions of a smaller size than the parent ion. The term *product ion* refers to daughter ions and photo fragments alike.

[2]Similar differences in PIY spectra have been observed for pure silicon clusters measured with the same experimental setup [8]. However, in these systems generation channels an corresponding product ions follow a different pattern.
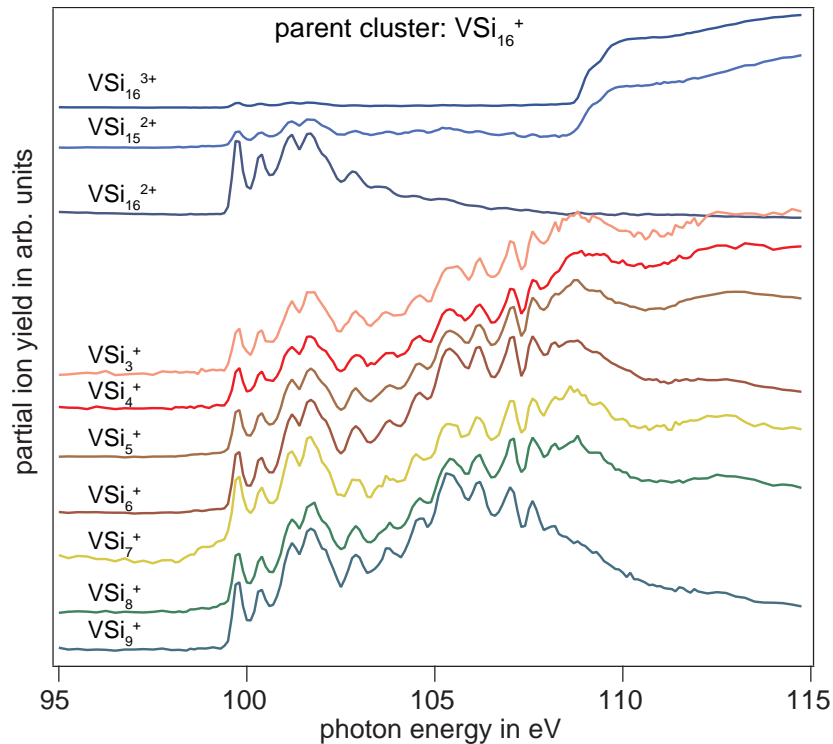
Figure 7.1: Energy dependent partial ion yield spectra of VSi_{16}^+ in the vicinity of the silicon 2p edge. Photo fragments as well as daughter ions show different energy dependences trends. While multiple daughter ions show a resonant tendency in the PIY spectrum, VSi_{16}^{3+} exhibits an edge feature. An explanation is given in fig. 7.2 analyzing possible fragmentation channels.

accordingly. The MSi_n^{2+} daughter ion only has intensity in the first part of the spectrum. In contrast, MSi_{n-1}^{2+} as well as MSi_n^{3+} daughter ions show less features in the low energy region of the spectrum, but a distinct edge feature at photon energies around 110 eV. Mixed metal-silicon fragments MSi_x^+, $(x \in \mathbb{N}, x < n)$ show PIY features in the low energy region rising up in intensity to the energy the edge occurs in the MSi_{n-1}^{2+} and MSi_n^{3+} PIY spectra. At this energy, a minor distinction can be made between mixed fragments, as a different slope in the following PIY intensity is observed depending on the size of the MSi_x^+ ion.

Generation Channel of the Daughter Ion MSi_n^{3+} Showing a Direct Photoionization Edge in its PIY Spectrum

The PIY spectra of the daughter ions MSi_n^{3+} and MSi_{n-1}^{2+} of the parent cluster MSi_n^+ differ strongly from the ion yield of other product ions, as can be seen in figure 7.1, by exhibiting a well pronounced edge feature. MSi_{n-1}^{2+} shows the resonant excitation as well as the edge feature. In order to understand this energy dependence of the PIY spectra, the relaxation channels leading to the respective daughter ions have to be analyzed. A sketch of the suggested main decay channels

for the daughter ions MSi_n^{3+} and MSi_{n-1}^{2+} is shown in figure 7.2. The generation
of the daughter ion showing the direct photoionization edge in figure 7.2 a) starts
with a photoionization of a 2p state and a photoelectron leaving the cluster. The
doubly charged and core excited cluster MSi_n^{2+**} remains. The core hole relaxes
via Auger decay, leaving the cluster triply charged (cf. sect. 1.1.4). Eventually
further relaxation is achieved by emission of a silicon cation due to coulombic re-
pulsion, eventually enhanced by deposited energy heating the cluster. This is the
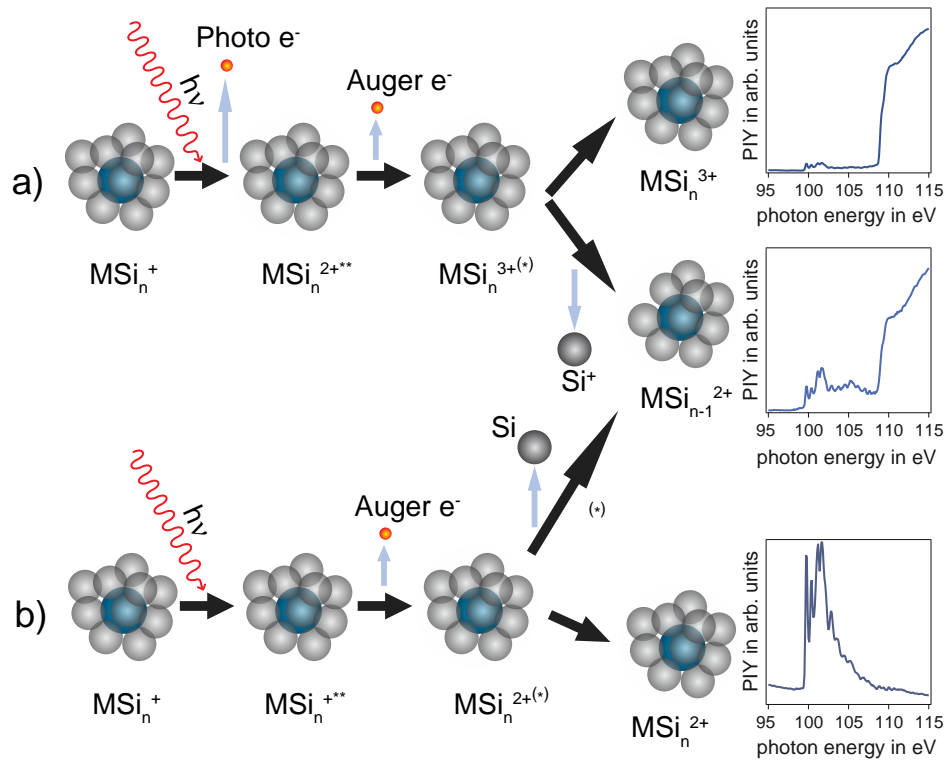
Figure 7.2: Illustration of excitation and decay channels possible to obtain the triply charged
parent cluster, the doubly charged parent cluster and the doubly charged parent cluster missing
one silicon atom / cation. The MSi_n^{3+} daughter ion is primarily reached via a photoionization
in the first step, the MSi_n^{2+} daughter ion via an resonant excitation with only one subsequent
Auger decay. Pure resonant and or edge features visible in the PIY spectra (cf. fig. 7.1) of MSi_n^+
are understood via this relaxation channels. The states involved in Auger decay are shown in
fig. 7.3.

main generation channel of the daughter ion MSi_n^{3+}, since one or two subsequent
Auger decays are unlikely to result in a triply charged cluster, as explained in
the following via DFT calculations on the shown in figure 7.3. DFT Calculations
were done for the cationic ground state. The core hole is not accounted for in
the DFT calculation, but is not expected to drastically change the overall shape
of the orbitals. It could cause an energetic shift of the orbitals, which does not
change the following interpretation. Although the absolute energetic positions
and degeneracy of the states shown in figure 7.3 may vary for different dopant

and numbers of silicon atoms, the following explanation is valid for all doped silicon clusters. Two Auger processes are only possible if after the first one a core
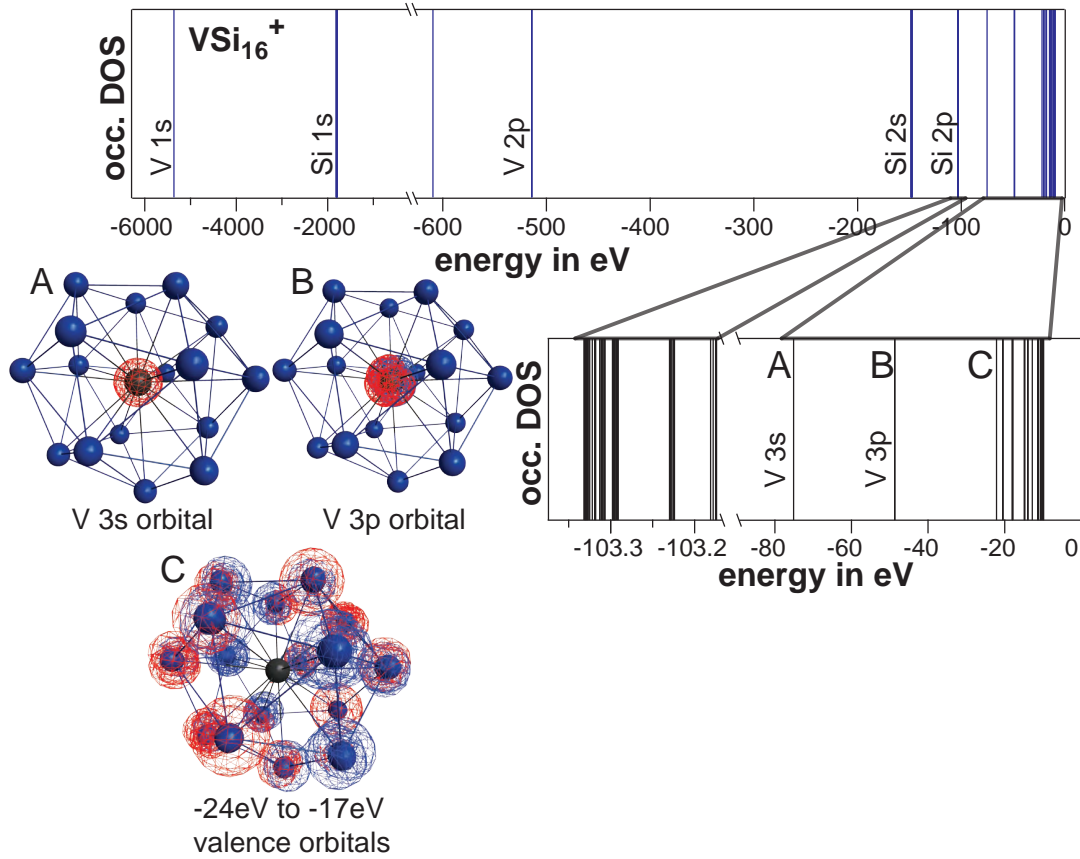

Figure 7.3: Total occupied DOS of VSi$_{16}^+$ obtained via DFT calculations. The isosurface shown for the orbitals at (A) -71 eV and (B) -45 eV (lower panel) are located at the transition metal atom in the center of the cluster. Therefore, the overlap of these two states with a silicon 2p core hole is small, under the assumption that the presence of a core hole do not change the extension of the orbitals. An Auger decay of a 2p core hole involving the states located at the metal center is unfavorable (see text).

hole is still present. In the first step of figure 7.2 a) a core hole is generated in one of the states located around 100 eV. For two Auger processes to happen, the core hole for the second process must have been populated by the emitted Auger electron or the electron filling the first core hole. The Auger electron as well as the electron filling the first core hole mainly come from the states (C) above 25 eV, as the states at about 70 eV (A) and 45 eV (B) (cf. fig. 7.3) are localized at the transition metal atom. The states correspond to the vanadium 3s (A) and 3p (B) states. The filling of a silicon 2p core hole by an electron located at the transition metal is most unlikely. Therefore the only electrons available for the first Auger decay are the electrons at binding energies lower 25 eV (C). However, if an Auger process happens via a transition of a (C) state electron into the silicon 2p core

hole, the new electronic hole in the (C) valence states does not have enough energy for a second Auger process. An intra valence state (C) electronic transition process would only yield about $10\,\text{eV}$, which is too low for an additional Auger process of the already doubly charged (due to the first Auger process) cluster. Therefore direct photoionization is most likely to generate MSi_n^{3+} daughter ions. However, in the PIY spectrum of MSi_n^{3+} showing the direct photoionization edge, small resonant features can be seen at lower excitation energies. Therefore an other process including a resonant excitation also must lead to this daughter ion. There are two additional generation channels possible: Interatomic decay and one Auger decay with an additional electron shake off.

Interatomic Decay Revealed in PIY Spectra of Multiply Charged Product Ions

A further analysis of the PIY spectrum of MSi_n^{3+} shown in figure 7.5 reveals additional information about possible decay channels after silicon 2p core level excitation. In the spectrum of MSi_n^{3+} minor resonant features are visible between (X) and (Y) at about $100\,\text{eV}$, which have to correspond to resonant excitation for energetic considerations, since direct photoionization of the 2p state is only feasible at higher excitation energies (Z). As is discussed above, after resonant excitation Auger decay involving only states of the silicon atom cannot result in a MSi_n^{3+} daughter ion. Although there is little overlap between the metal 3s and 3p orbitals with the silicons 2p orbital as shown in figure 7.3, resonant absorption followed by two successive Auger decays with metal electrons participating has for energetic reasons to be the responsible for the resonant features in the PIY spectrum of MSi_n^{3+}. This proves interatomic decay occurs. The concept of interatomic decay is shown in figure 7.4 in comparison to normal Auger decay. In interatomic decay, not only electronic states located at the atom with the core hole are involved, but also electrons of neighboring atoms may fill the core hole. Therefore, the resulting Auger process involves states located at two different atoms. Hence, this kind of decay channel is denominated *interatomic decay*. In addition, one resonant excitation with a subsequent Auger decay in combination with an electron shake off process may generate two charges on the cluster. In the first process a resonant excitation of a silicon 2p electron into a bound state. The core excited system relaxes by Auger decay. The resulting Auger electron interacts with an other valence electron, which is transferred into the vacuum level by a shake off. Therefore two charges are generated on the system, which
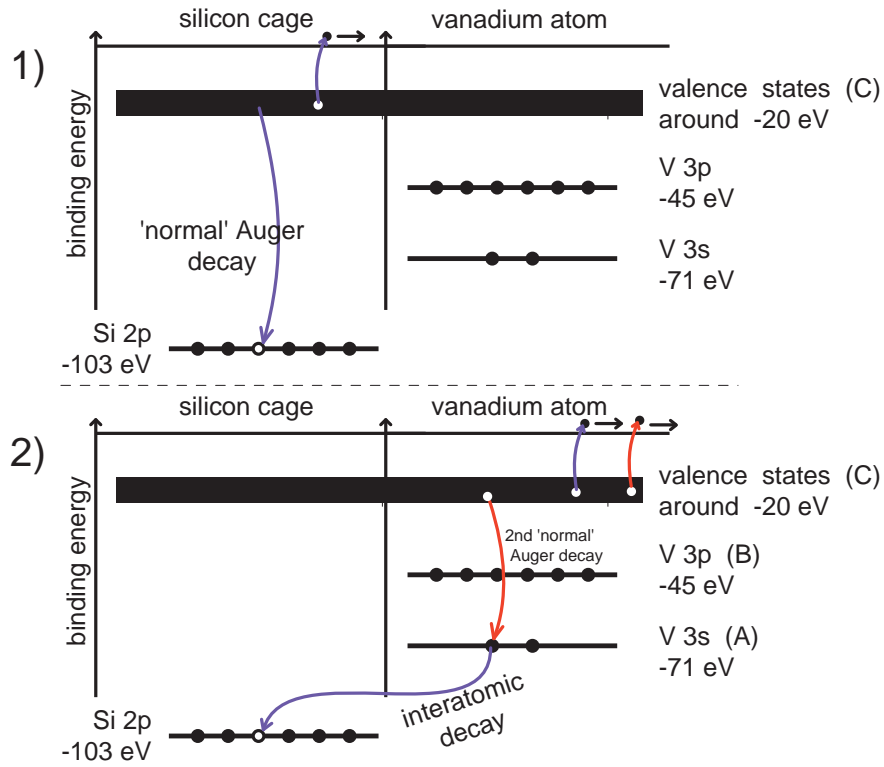
Figure 7.4: Illustration of a normal Auger decay (1), and interatomic decay (2) of a silicon 2p core hole. The density of states of a doped silicon cluster is shown (cf. fig. 7.3) and ordered with respect to the element the state originates from. States localized at a silicon atom of the cage are shown on the left, local states of the transition metal (vanadium) on the right side of each panel. Approximate binding energies correspond to the binding energies found in DFT calculations for VSi_{16}^{+}.

would result in case of MSi_n^+ parent cluster in a MSi_n^{3+} final state.

Generation Channel of the Daughter Ion MSi_n^{2+} Showing the Fingerprint of Resonant Excitation in its PIY Spectrum

The daughter ion MSi_n^{2+} showing only resonant excitations in its partial ion yield spectrum can be explained similar to the triply charged parent cluster. The first process shown in figure 7.2 b) has to be a resonant 2p excitation. An Auger decay involving only silicon states is most likely due to the low overlap of the metal states at about $70\,eV$ (A) and $45\,eV$ (B) and silicon states (cf. fig. 7.3). After this, the possibly remaining holes are located in states with a low binding energy. Therefore the remaining energy is not high enough for a second Auger process. If there is sufficient energy left in MSi_n^{2+}, emission of a neutral silicon atom may lead to MSi_{n-1}^{2+} explaining simultaneous presence of resonant excitation and direct photoionization in the PIY spectrum of MSi_{n-1}^{2+}.

However, not all resonant excitations can be observed in the PIY spectrum of MSi_n^{2+}, as can be seen in figure 7.5. All features of the ion yield spectra presented that show below the direct photoionization energy marked (Z) in figure 7.5 have to correspond to resonant excitations in the first absorption process for energetic considerations. The spectrum of MSi_n^{2+} showing only resonant features, exhibits in comparison with the combined ion yield (CIY) spectrum[3] of singly charged fragment ions MSi_x^+ little resonant excitation features between a photon energy (Y) and the direct photoionization threshold energy (Z). While the PIY spectra of MSi_n^{2+} and the CIY of MSi_x^+ are in good agreement at the low energetic side of the spectrum between the photon energies marked (X) and (Y), the MSi_n^{2+} daughter ion exposes a falling intensity with excitation energy after an excitation energy of about $100\,eV$ (Y) instead of a steadily rising signal intensity observed in the CIY spectrum. This shows that MSi_n^{2+} originates only from the excitation into one low lying unoccupied molecular orbital, since low PIY intensities are observed at higher excitation energies. When exciting into energetically higher unoccupied bound states, either the relaxation of the valence excited intermediate state MSi_n^{2+*} heats the cluster so much that fragmentation occurs or the valence excited intermediate state MSi_n^{2+*} corresponds to a dissociative potential curve. Therefore, mixed VSi_x^+ fragments PIY show a higher intensity in the resonant part of the spectrum from excitation energies (Y) to (Z) than the MSi_n^{2+} daughter ion. However, resonant features can also be seen faintly in the low intensity part from (Y) to (Z) in the PIY spectrum of MSi_n^{2+}. These resonant features may occur if the cluster is thermalized fast enough by the cold helium buffer gas to prevent

---

[3]The CIY is the sum of all singly charged fragment ions MSi_x^+.

fragmentation. In conclusion, the daughter ion generation depends strongly on the final state of the cluster after resonant x-ray excitation.
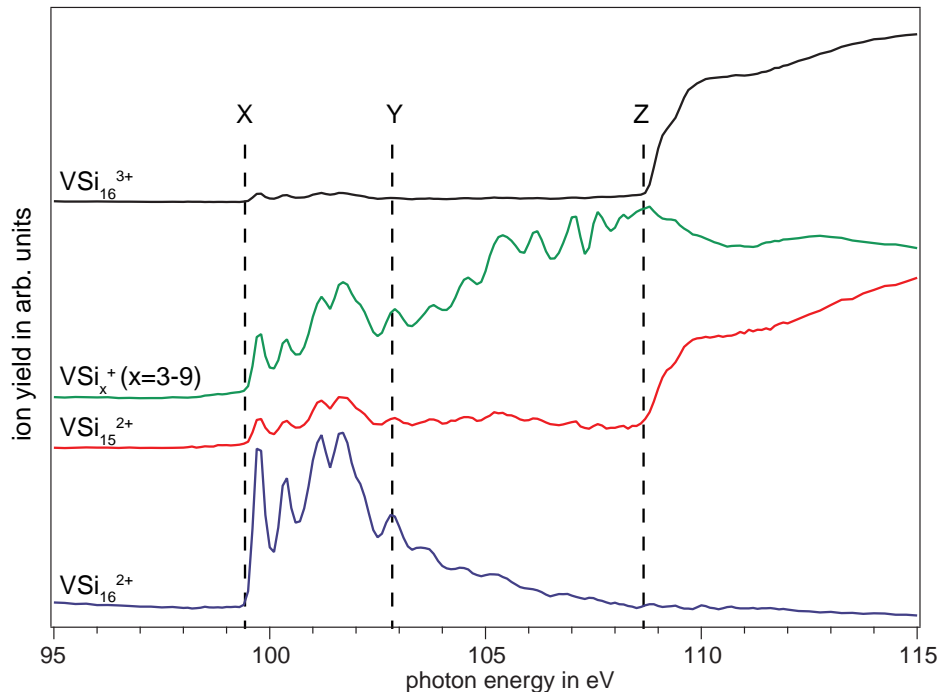

Figure 7.5: Partial ion yield spectra of different daughter ions of VSi_{16}^+. The realization of a direct photoionization edge in the spectrum of VSi_{16}^{3+} as well as only resonant features in the spectrum of VSi_{16}^{3+} is understood via the generation channels of these daughter ions in figure 7.2. The multiply charged daughter ion VSi_{15}^{2+} exhibit and intermediate spectrum of the two former spectra, suggesting the daughter ion generation to be possible via direct photoionization or resonant x-ray absorption.

Generation Channel of the Fragment Ion MSi_{n-1}^{2+} Showing Features of Resonant Excitation and Direct Photoionization in its PIY Spectrum

The MSi_{n-1}^{2+} fragment ion's PIY featuring both, the edge as well as the resonant part shows a much stronger resonant feature than MSi_n^{3+} (cf. fig. 7.5). Two fragmentation pathways lead to this daughter ion, as shown in figure 7.2. The emission of Si^+ from MSi_n^{3+} explains the edge feature in the PIY of MSi_{n-1}^{2+}. The MSi_{n-1}^{2+} clusters are also created by evaporative cooling via emission of a silicon atom from MSi_n^{2+}, explaining the resonant part of the spectrum. Comparison of the resonant features between energy (X) and (Y) in the PIY spectra of MSi_{n-1}^{2+} and MSi_n^{2+} in figure 7.5 shows the cooling effect of the emission of a neutral silicon atom from MSi_n^{2+}. Between the excitation energy (X) and (Y), both spectra show resonant lines, while at higher excitation energies than (Y), the signal of MSi_n^{2+} decreases, meaning that this daughter ions stability is low at this excita-

tion energy, while the PIY of MSi_{n-1}^{2+} shows the fingerprint of resonant excitation at a nearly constant intensity up to the direct photoionization energy (Z), due to stabilization via evaporative cooling.

Generation Channel of Singly Charged Daughter Ions

Mixed singly charged daughter ions show the resonance as well as an increasing intensity with excitation energy in their ion yield spectra. These daughter ions are generated by multiple channels and exhibit therefore features from resonant excitation as well as direct photoionization. Possible decay channels leading to a certain fragment ion are numerous. Comparison of the fragment ions MSi_x^+ of a parent cluster MSi_n^+ does not show many differences in their PIY energy dependence. However, it is seen that PIY intensity is increasing with photon energy. Depositing more energy in the cluster enhances chances of fragmentation, which is expected. The only deviation of PIY spectra observable in figure 7.1 mentioned before shows a different slope of the respective PIY intensity of MSi_x^+ at the direct photoionization energy. This could be an artifact due to storage of cluster in the ion trap prior detection. Since at the direct photoionization energy the total charge of clusters inside the trap is increased by the generation of MSi_n^{3+} and its fragment ions, coulombic repulsion increases and more clusters than before are pushed out of the trap. Obviously smaller fragment ions are affected more by the repulsion than heavier fragments. This may show the trapping efficiency for different ion masses, which depends on experimental conditions like the rf frequency, rf potentials and dc potentials of the ion trap as explained in section 3.5. Another explanation may be that generation channels change upon reaching the direct photoionization threshold, resulting in the observed effect.

Intermediate Conclusion

It has been shown that x-ray spectroscopy via ion yield measurements is not only an element specific method, but in case of transition metal doped silicon clusters as well as pure silicon clusters [8] also sensitive to the excitation channel. Therefore it is known how product ions are generated, which gives the possibility to interpret the the PIY spectra of the respective ions. Furthermore, the knowledge whether the first absorption is direct photoionization or resonant excitation gives the information about the relative energetic distance of the 2p electrons to the first unoccupied state reachable via photoexcitation and an estimate of the 2p

electrons absolute binding energy due to the direct photoionization threshold. In the next section, the results of resonant as well as direct photoexcitation of MSi_n^+ is discussed.

7.2 Resonant Excitation and Photoionization Edges

In the following, the PIY spectra of MSi_n^+ clusters at the silicon $L_{3,2}$ edge are analyzed. Due to the different excitation channels of resonant excitation and direct photoionization visible for certain product ions, this analysis is split into two sections, each focusing on one excitation channel. In the first section 7.2.1 the resonant silicon 2p excitation of MSi_n^+ clusters is discussed and the cluster size dependent energetic threshold of this excitation is presented. An additional focus is laid on the highly symmetric VSi_{16}^+ having an high stability due to an electronic shell closure [1] in comparison with $TiSi_{16}^+$ and $CrSi_{16}^+$, which show a slightly reduced symmetry but lack a closed electronic shell. Since these clusters showed similar local electronic structures at the transition metal center of the clusters by their similar ion yield spectra for excitations at the transition metal $L_{3,2}$ edge, it is of high interest if similar results are obtained for the local electronic structure of the silicon atoms of the cage.

In the second section 7.2.2 the direct silicon 2p photoionization of MSi_n^+ clusters is discussed by the PIY spectra of the respective daughter ion. It is shown that the results are comparable with potential results of photoelectron spectroscopy at the silicon 2p orbital. It is shown that the fingerprint of the 2p state depends on the collective coordination of the silicon atoms of MSi_n^+ clusters, and that comparison with calculated photoelectron spectra therefore gives information about possible geometries a distinct cluster size adopts. Furthermore, the direct photoionization threshold is presented, which gives in combination with the resonant excitation threshold a good estimate for the absolute position of the lowest unoccupied electronic state with respect to the vacuum level. Combining this with results on the position of the lowest occupied state of the cluster yields an experimentally determined HOMO-LUMO gap, which is presented in chapter 9.

7.2.1 Resonant Partial Ion Yield - Excitation Energy and Electron Screening

The resonant excitation of MSi_n^+ clusters is discussed by analyzing the combined ion yield (CIY) of fragment ions mentioned before. The CIY consists of all singly

charged mixed fragment ions MSi_x^+. Pure silicon fragments are excluded since they may descent from pure silicon clusters which may be coexistent in the ion trap due to similar masses of Si_{n+2}^+ and MSi_n^+ with respect to mass filtering limitations (cf. sect. 3.3 and 4.2). If not excluded, this may lead to an interference of the absorption spectrum of the pure silicon cluster and the metal doped cluster of interest. It is chosen to exclude the resonant excitation in the PIY spectrum of MSi_n^{2+} despite the well-defined generation channel proving only resonant excitation to lead to this daughter ion. All information that would be gained can also be extract from the CIY spectrum, which shows even more resonant absorption features.

The direct photoionization energy is known to be above $108\,eV$. Therefore, all spectral features below this energy has to correspond to resonant excitations. Comparison of the CIY of MSi_x^+ and the PIY of MSi_n^{2+} shown before in figure 7.1 exhibits a better visibility of features, especially in the energy range just below the direct photoionization edge, where MSi_n^{2+} has a extremely low intensity as explained above (cf. sect. 7.1). The CIY spectra of MSi_n^+ clusters at the silicon $L_{3/2}$ edge are shown in figure 7.6 and 7.7. The panels are arranged from left to right with respect to the transition metal dopant's position in the periodic table (cf. fig. 6.2) and from top to bottom according to the cluster size. Equal sized clusters with transition metal dopant atoms along the 3d transition metals of the periodic table have a increasing valence electron count due to the increasing 3d occupation of the respective dopant. All CIY spectra of MSi_n^+ clusters shown in figure 7.6 and 7.7 show the same coarse energetic dependence. The general trend shows rising CIY with increasing photon energy. Resonant x-ray absorption features in the CIY spectrum starting at about $98.5\,eV$ are to be seen exclusively up to about $108\,eV$. Above the latter energy fragment ions may also be generated after direct silicon 2p photoionization of the cluster. Furthermore, a drop in intensity is observed at this energy, which is an artifact of the detection method. Upon a massive increase of one product ion[4] the ion yield of other cluster ions decreases due to space charge limitation in the ion trap. These approximate energies of the resonant absorption threshold and the direct photoionization edge are valid for all doped silicon cluster cations presented in figure 7.6 and 7.7.

Before discussing the shape of a particularly interesting CIY of figure 7.6 and 7.7, we will focus on the threshold energy the resonant x-ray absorption, which corresponds to the energetic distance of the initial states energy of the MSi_n^+ cluster in its ground state and the energy the final 2p core-excited state MSi_n^{+*}.

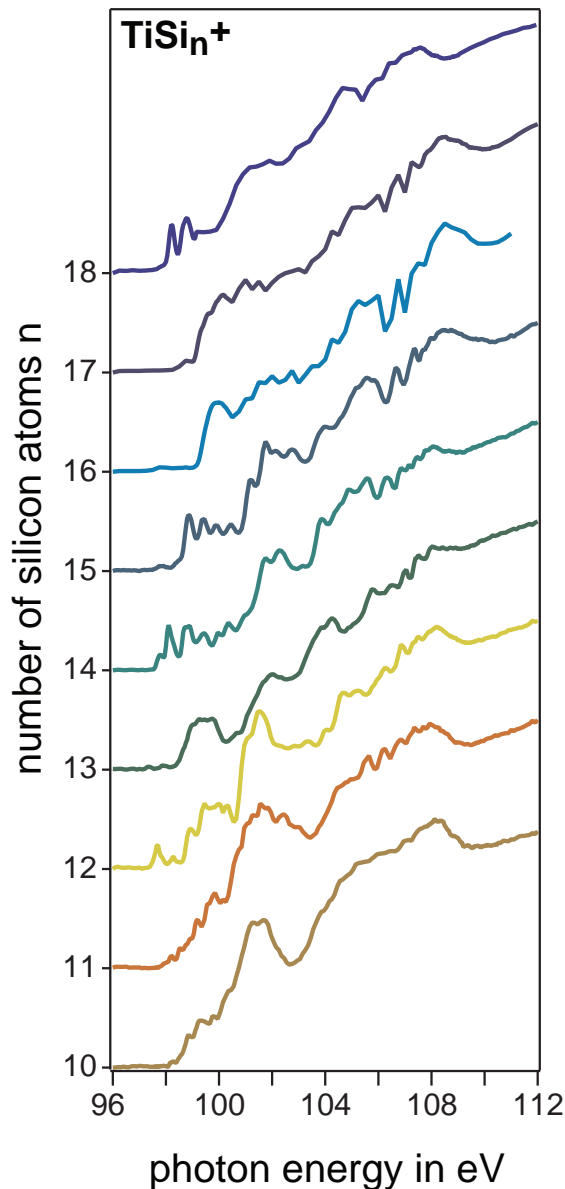[4]In this case generation of MSi_n^{3+} via direct photoionization.

Figure 7.6: Combined ion yield spectra of TiSi_n^+ at the silicon $\text{L}_{3,2}$ edge. The spectra are all normalized for better visualization. Spectral features visible below a photon energy of about 108 eV are exclusively corresponding to resonant 2p excitations (see text).

Resonant Silicon 2p X-Ray Excitation Threshold

As is observed directly, the threshold energy is a function of cluster size in each MSi_n^+ cluster. The observed threshold energies are plotted in figure 7.8 for all MSi_n^+, M=(Sc,Ti,V,Cr) clusters shown in figure 7.6 and 7.7. Since the lowest threshold energy corresponding to a resonant transition of a 2p electron into the lowest unoccupied state is of interest, even very low ion yield intensities are considered as shown in figure 7.8 on the example of the CIY of TiSi_{16}^+. The highest threshold energy of resonant 2p excitation is observed for VSi_{16}^+, with an almost
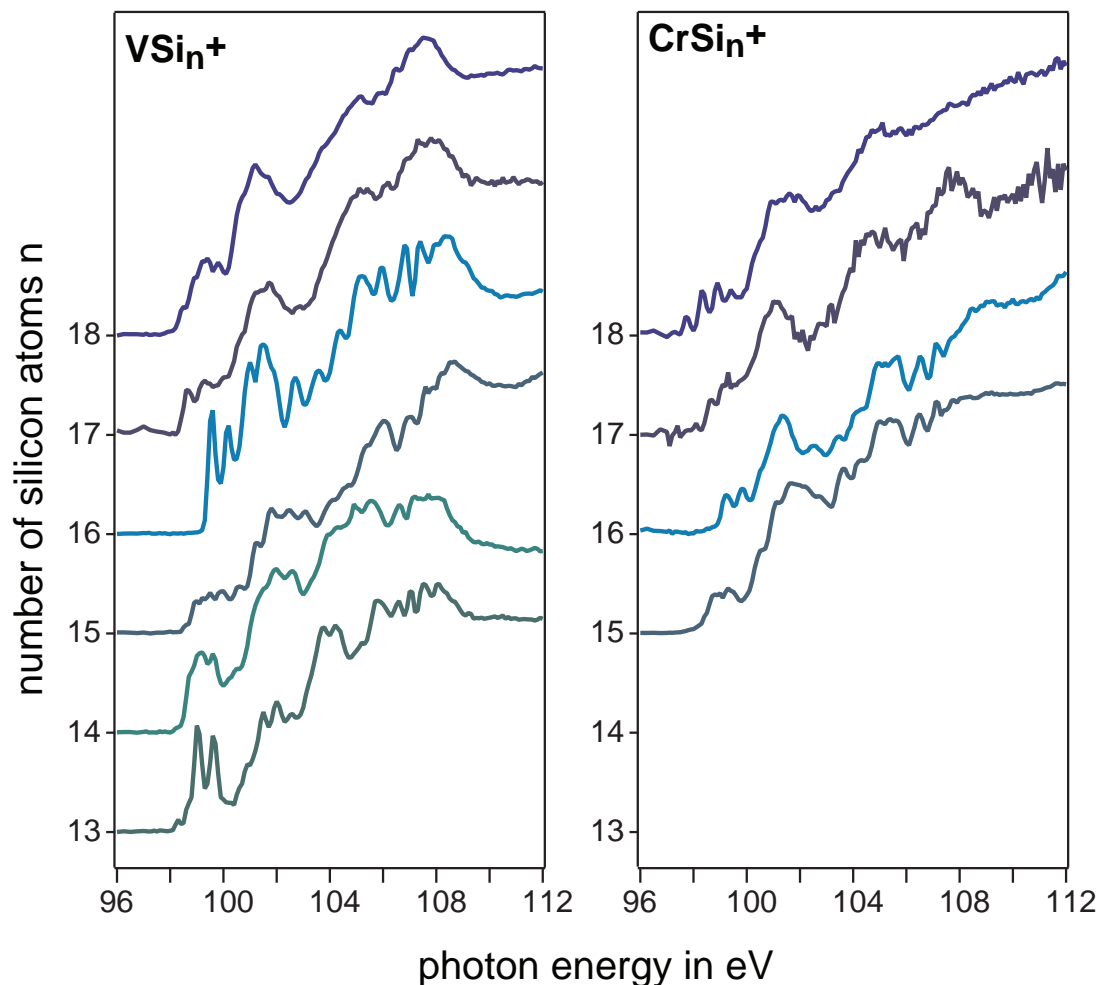
Figure 7.7: Like figure 7.6 but for MSi_n^+, M=(V,Cr). Sharp features in a CIY spectrum point to a high degeneracy of states at the silicon cage and are observed for example in the CIY spectrum of VSi_{16}^+.

1 eV higher value than other vanadium doped cluster sizes. A similar cluster size dependence of the threshold energy is as for VSi_{16}^+ is found in case of $CrSi_n^+$, for which $n = 16$ is very prominent. In contrast to this, the threshold energy of $TiSi_n^+$ clusters in figure 7.8 does not shows a high threshold energy for $n = 16$ but a increased resonance threshold energy for $n = 17$. The succession of the energy threshold of MSi_{16}^+ (M=V,Cr,Ti) is in good agreement with theoretical approach of the spherical shell model [1]. The density of states of a spherical MSi_{16}^+ with tetrahedral symmetry is shown in figure 8.5 in addition to the valence electron count of the three MSi_{16}^+ (M=V,Cr,Ti) clusters for which this model is applied. It is assumed that the density of states is similar for all three clusters, despite a lowered symmetry of the Frank-Kaspar polyhedral geometry [48] due to a Jahn-Teller deformation [94] in $TiSi_{16}^+$ and $CrSi_{16}^+$. Furthermore it is shown that electronic valence states are almost equal in calculations of MSi_{16}^+ (M=V,Cr,Ti)
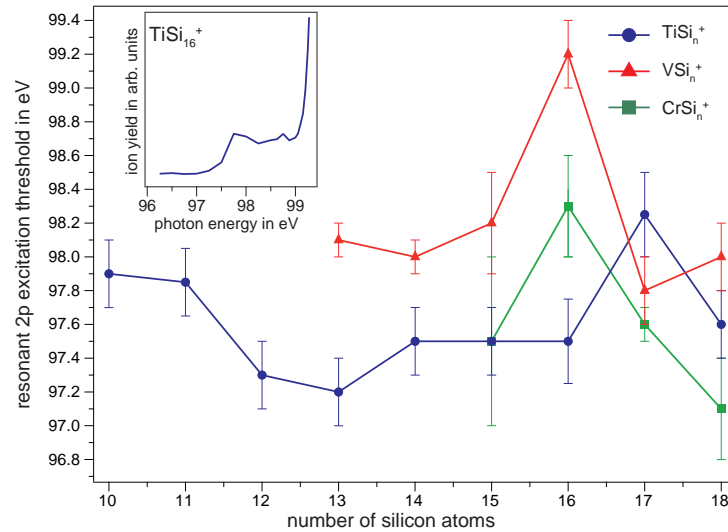
Figure 7.8: Energy threshold for the dipole allowed resonant silicon 2p excitation of MSi_n^+, M=(Sc,Ti,V,Cr) clusters (cf. fig. 7.6 and 7.7). For VSi_{16}^+ a high threshold energy is observed compared to other MSi_n^+ clusters.

Inset: Magnification of the resonant excitation threshold in the ion yield of $TiSi_{16}^+$. A small pre-edge is visible, which is considered in the threshold values of the resonant x-ray absorption. Similar pre-edges are visible in other MSi_n^+ clusters as well.

if equal geometries are assumed [57]. Resonant excitations of silicon 2p electrons into the lowest unoccupied state therefore correspond to transitions to the clusters 1h valence state for VSi_{16}^+ and $CrSi_{16}^+$ and to transition to the clusters 2d valence state for $TiSi_{16}^+$. Therefore the lowest resonant excitation threshold energy should be observed in case of $TiSi_{16}^+$ which is in good agreement with the experimentally obtained threshold. The difference in threshold energy between VSi_{16}^+ and $CrSi_{16}^+$ is due to an increased binding energy of the 1h state in $CrSi_{16}^+$ due to the single electrons occupation, which is also seen in calculations [57]. It may also correspond to a higher degeneracy of valence states due to the Jahn-Teller deformation of the cluster.

The high threshold energies of VSi_{16}^+ and $CrSi_{16}^+$ compared to other cluster sizes with the respective dopant atom can be explained with the concept of screening, as is explained in the following. An increase in threshold energy of resonant x-ray absorption from one cluster to another cluster[5] might give information about the delocalization of valence electrons in the cluster. Since the energy threshold corresponds to the energy difference between the initial state and the final state energy of the cluster $E(\Psi_i) - E(\Psi_f) = E_{thres}$, a lowering of the initial states energy leads to an increased threshold energy. Screening in the initial state corresponds to a screening of the atomic core potential by the valence electrons, thus

---

[5]Either the clusters have different sizes or different dopant atoms.

111

lowering the 2p binding energy. In this case, screening becomes more effective, if the valence electrons are localized at the respective atom. Screening as a final state effect lowers the energy of the final state by screening the core hole thus lowering core hole interaction. This is more effective if the valence electrons are delocalized, which therefore have a higher mobility and can more easily react on a positive charge. Hence, initial state screening and final state screening change the transition threshold energy in opposite directions when seen as a function of valence electron delocalization. If the delocalization of valence electrons is known, it can be determined if the cluster size dependent change in the threshold energy is an initial or final state effect by simply observing if the energy is shifted towards higher or lower energies. In pure silicon clusters it is shown that with increasing cluster size the resonant 2p excitation threshold energy shifts towards higher energies [8]. For these systems, analyzed in the size range Si_n^+ (n=5-92), an increasing delocalization of the valence electrons is assumed. If this is correct, it is shown that the initial state screening is dominating the threshold energy, since only for this process the threshold increases with increasing delocalization of the valence electrons. If it is therefore assumed that initial state screening is dominant for resonant silicon 2p x-ray absorption, then the threshold energy in dependence of the cluster size is an estimate of the delocalization of the valence electrons in a MSi_n^+ cluster. The high resonant excitation threshold energy of VSi_{16}^+ and $CrSi_{16}^+$ therefore indicates a high delocalization of valence electrons in these clusters, which is a reasonable result due to the almost spherical structure. That this high delocalization is not observed in the threshold energy of $TiSi_{16}^+$ is an artifact due to the determination method used. As explained above, even small pre-edges are considered, which is shown for $TiSi_{16}^+$ in figure 7.8. In case of $TiSi_{16}^+$ the silicon 2p electron is transferred into the clusters 2d state (cf. fig. 8.5), which is a special case as this corresponds to a transition into an almost completely occupied state with a high energy gap to the next unoccupied state. If pre-edges are not considered, $TiSi_{16}^+$ shows the highest threshold energy of $TiSi_n^+$ cluster, similar to the equal sized titanium and vanadium doped silicon clusters. However, this last consideration shows that the concept of screening might be problematic in these systems, since the electronic structure of distinct electronic states has to be considered in contrast to small metal clusters with electronic bands [68].

Local Density of States at the Silicon Cage in MSi$_{16}^+$ (M=Ti,V,Cr)

Having shown exceptional high stability in reactivity experiments and exhibited the most distinct lines in resonant absorption studies at the 2p metal edge, VSi$_{16}^+$ shows the most prominent distinct lines in the resonant absorption CIY spectra at the silicon 2p edge as well (cf. fig. 7.6 and 7.7). However, while in similar studies
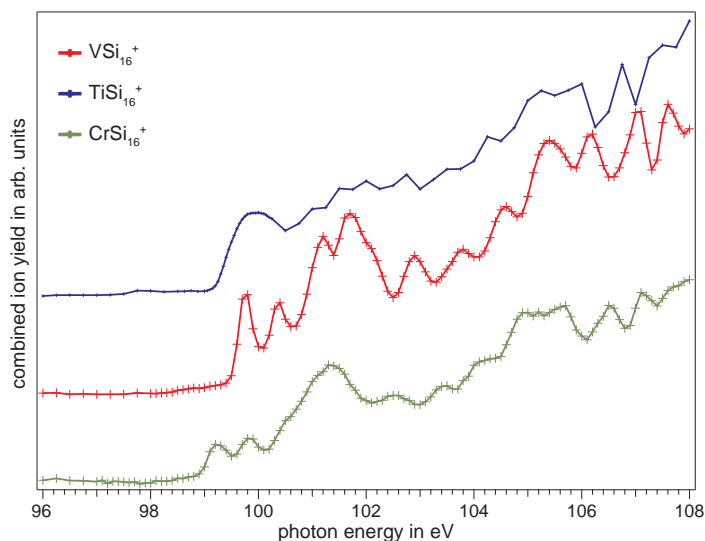

Figure 7.9: Combined ion yield spectra of TiSi$_{16}^+$, VSi$_{16}^+$, and CrSi$_{16}^+$. Despite similar geometries, the spectra show different spectral fingerprints.

at the transition metal L$_{3,2}$ edge the ion yield spectra of CrSi$_{16}^+$ and TiSi$_{16}^+$ mimic the spectral signature of the highly symmetric VSi$_{16}^+$ Frank-Kaspar polyhedron thus indicating a similar local density of states at the transition metal, comparable high similarities are not observed in the resonant absorption at the silicon L$_{3,2}$ edge as can be seen in figure 7.9. The cage causes a similar local electronic structure at the transition metal dopant despite slightly differing geometries of TiSi$_{16}^+$ and CrSi$_{16}^+$ compared to VSi$_{16}^+$ due to Jahn-Teller distortions. However, spectroscopy at the silicon cage atoms is expected to be more sensitive to this distortion. In addition, if a similar local electronic structure is found at the transition metal despite a differing valence electron count of the cluster due to different dopant atoms (cf. fig. 8.5 and 6.2), a different electron occupation is expected at the silicon cage. This may explain differing resonant excitation signatures.

113

7.2.2 Direct Photoionization Efficiency - Chemical Shift of Silicon 2p

The partial ion yield of MSi_n^+ showing the direct photoionoization efficiency is obtained from the daughter ion MSi_n^{3+} as explained in detail in section 7.1 and shown in figure 7.2. Before analyzing MSi_n^{3+} partial ion yields of the respective cluster sizes and explaining how information about isomer geometry is obtained from it, the direct photoionization threshold energy is discussed.

The direct photoionization threshold yields information on the silicon 2p core level binding energy and chemical shifts. The direct photoionization threshold energies of MSi_n^+ (M=Ti,V,Cr) are determined similar to resonant photoexcitation thresholds (cf. sect. 7.2.1) and shown in figure 7.10. Like in the resonant
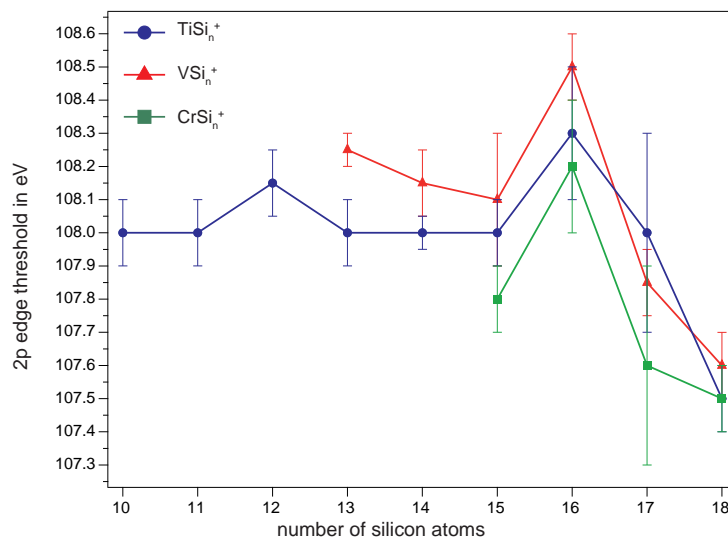
Figure 7.10: Direct photoionization threshold of the silicon 2p state of MSi_n^+, M=(Ti,V,Cr) clusters. Comparison with the trends of the resonant absorption threshold in figure 7.8 shows a similar size dependence.

excitation threshold energies, $CrSi_{16}^+$ and VSi_{16}^+ exhibit the highest direct photoionization threshold energy of the respectively doped clusters. The explanation is the same as given above in case of the resonant threshold energy. If the assumption is true that initial state screening is the dominating effect, a higher delocalization decreases the screening of the core potential by valence electrons and therefore increases the binding energy of 2p electrons (cf. sect. 7.2.1). In case of direct photoionization, this can also be seen for $TiSi_{16}^+$, since the absolute position of the unoccupied density of states is no longer relevant. It only matters how high the degree of delocalization of the valence electrons is. In conclusion, from the direct photoionization threshold energy it can be seen that

the highest degree of valence electron delocalization in MSi_n^+ clusters is found in MSi_{16}^+ (M=Ti,V,Cr), which is due to their nearly spherical and highly symmetric Frank-Kaspar polyhedral geometry.

7.2.3 Silicon 2p Spin Orbit Splitting and Relative Chemical Shift Compared to Geometric Structures

Analysis of the direct photoionization efficiency of MSi_n^+ visible in MSi_n^{3+} partial ion yield spectra in figure 7.11 does not only give information about the photoionization threshold but also on the silicon 2p spin orbit splitting and the relative chemical shift of the silicon 2p binding energy depending on the coordination of the absorbing silicon atom. The form of the photoionization efficiency curve is given by a linear combination of the 2p binding energy of each silicon atom of MSi_n^+ and therefore holds information about each silicon atom's coordination in the cluster [95]. As an simple example, the direct photoionization efficiency curve of VSi_{16}^+ is shown in figure 7.11, for which the form of the PIY spectrum is very simple since all silicon atoms are similar coordinated and therefore only a small relative chemical shift is observed. It can be clearly seen that the photoionization efficiency curve consists of two distinct components, which are identified to belong to the direct photoionization of the spin-orbit split $2p_{3/2}$ and $2p_{1/2}$ orbitals. Experimentally, the respective PIY spectrum integrates over all daughter ions produced by direct photoionization and therefore rises with increasing energy as tighter bound electronic states are reached. A derivative of the photoionization efficiency curve therefore shows the occupation of the probed states. Similar spectra are obtained by photoelectron or x-ray photoelectron spectroscopy. In x-ray photoelectron spectroscopy (XPS) a fixed energy is used to ionize a particle and the kinetic energy of the photoelectrons is determined. The x-ray photoelectron spectrum of a particle shows in first approximation the energy levels and occupation density of states convolved with the experimental resolution. If the excitation energy is higher than the binding energy of the silicon 2p electrons in MSi_n^+, the linear combination of the spin-orbit split 2p states shifted for each silicon atom according to its coordination can be observed. A comparison between the derivative of the direct photoionization efficiency curve and the calculated silicon 2p states should therefore show, if the geometry of the cluster found in theory is a possible isomer observed in the experiment. In the following excursion it is shown how the silicon 2p density of states is obtained via DFT calculations and how it can be compared to the experimental data.
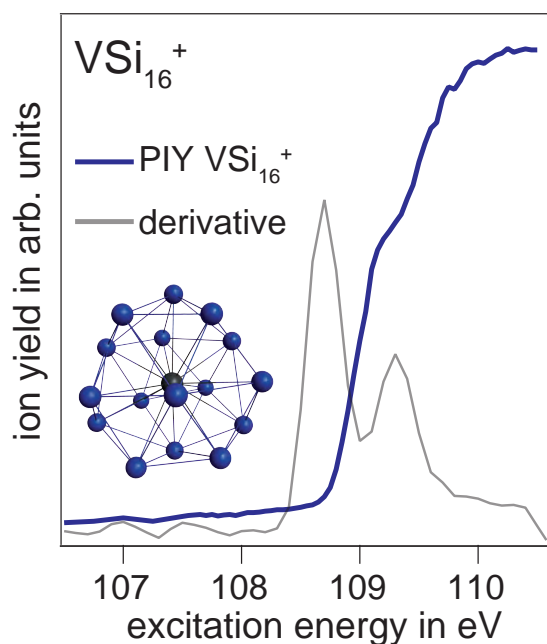
Figure 7.11: Direct silicon 2p photoionization edge visible in the PIY spectrum of the VSi_{16}^{3+} daughter ion. The derivative of the curve is similar to a spectrum obtained via XPS (see text).

Excursion: Density of States Obtained via DFT Calculations - Comparison to Direct Photoionization Edge Spectra

The total density of states of a MSi_n^+ cluster is obtained via DFT calculations using TURBOMOLE[©] program package with B3LYP and TZVP basis set [17, 96]. The results of a DFT calculation give the approximate energetic positions[6] and occupation of the orbitals of a cluster. The states in the vicinity of about -100 eV binding energy correspond to 2p states of the silicon atoms of the cluster, which are shown in figure 7.12. If silicon atoms are in different chemical environments, the orbitals are spread over an energy range of a few tenths of electron volts. This energetic spread of the 2p states is the fingerprint depending on the coordination of silicon atoms and therefore on the cluster's geometry. However, in the density of states obtained via DFT calculations $2p_{1/2}$ and $2p_{3/2}$ states are not spin orbit split since no core hole can be included into normal DFT calculations. Due to the presence of a core hole in the experiment, degeneracy is lifted. In order to introduce the resulting spin orbit splitting in a first approximation to the calculated states, the $j = 1/2$ and $j = 3/2$ states should be shifted to lower or higher en-

---

[6]DFT calculations are known not yield precise absolute energy positions. When compared to experimental results, calculated spectra are shifted to match the experimentally obtained excitation energies. This may result in different energy axis in figures only showing calculations and figures presenting experimental data.
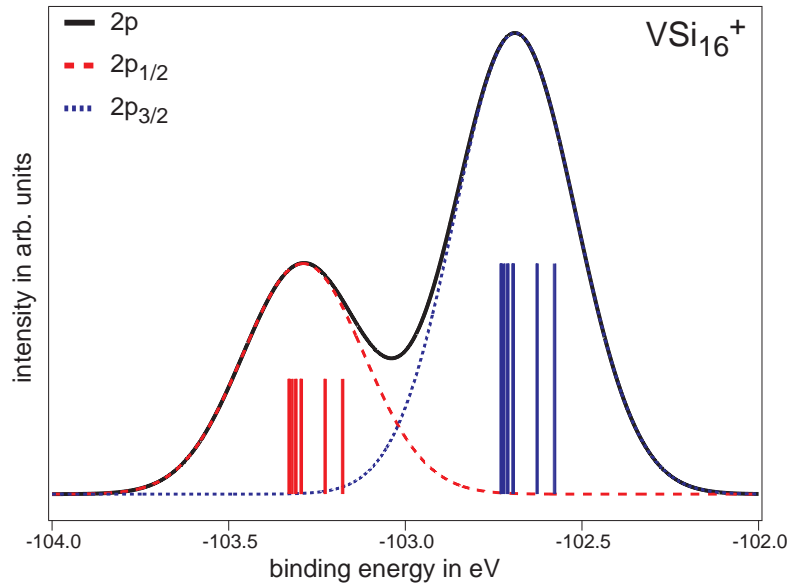
Figure 7.12: DFT calculation of the DOS of VSi_{16}^+. Shown are only the silicon 2p orbitals (blue sticks). The spin orbit splitting is introduced later on, as explained in the text. The red sticks correspond to $2p_{1/2}$ and the blue sticks to $2p_{3/2}$ states. The states are broadened with a Gaussian distribution to match experimental resolution. Binding energies of DFT calculations are known to show no precise absolute values.

ergies respectively by the spin orbit splitting energy. However, DFT calculations do not provide the angular momentum of the states. Since the respective states are degenerate in the calculation the spin orbit split 2p DOS can be simulated in first approximation by copying and shifting the calculated DOS according to the experimental determined spin orbit splitting of $0.6\,\mathrm{eV}$ in bulk silicon [97,98]. Furthermore, the electronic occupation ratio $2p_{3/2}:2p_{1/2} = 2:1$ has to be introduced by relative scaling the two groups accordingly. The blue lines in the left panel of figure 7.12 belong to the $2p_{3/2}$, the red lines to $2p_{1/2}$ states. The height of the lines represents the electronic occupation ratio $2p_{3/2}:2p_{1/2} = 2:1$. To account for experimental resolution and lifetime broadening present in the experimental data, the lines have to be broadened with a Voigt profile, which is a convolution of the resolutions Gaussian distribution and the lifetimes Lorentzian distribution. Since the experimental resolutions FWHM is large compared to lifetime broadening, the pure Gaussian distribution is in good agreement with the Voigt profile. Therefore, each line is broadened with a pure Gaussian profile. All Gaussian profiles of the $2p_{3/2}$ and $2p_{1/2}$ states add up to the equally colored dashed lines in figure 7.12. The black drawn line reflects the sum of the broadened $2p_{3/2}$ and $2p_{1/2}$ contributions. Assuming all transition of electrons into the vacuum level have the same oscillator strength, a photo electron spectrum should show the mirror image of the black distribution in figure 7.12. To simulate this,

the energy axis can be inverted. The result showing in first approximation the photo electron spectrum of a doped silicon cluster is shown in figure 7.13.
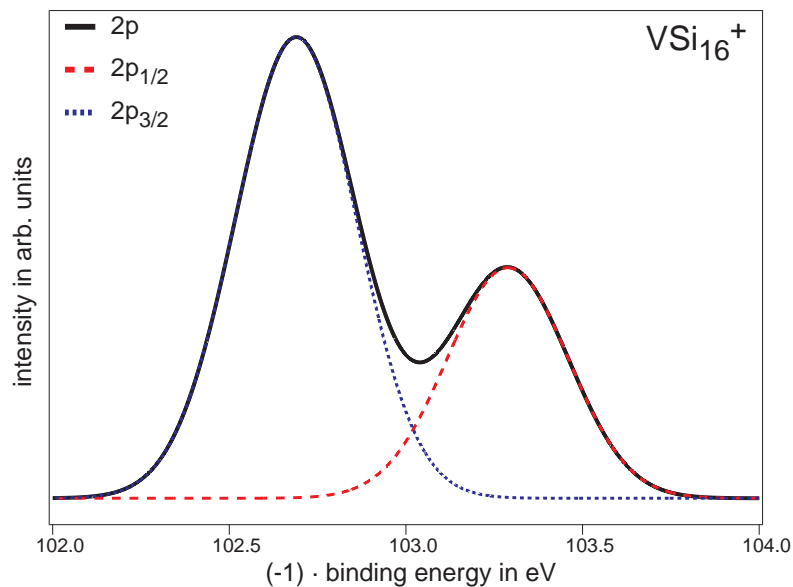
Figure 7.13: First approximation of a photo electron spectrum of VSi_{16}^+ obtained by refining DFT calculation as discussed in the text.

Comparison of Theoretically Obtained Energetically Lowest Isomers to Experimental Data

In the following, direct photoionization efficiency curves of MSi_n^+ (M=Ti,V,Cr) clusters are discussed (cf. fig. 7.14 and 7.15) and compared to calculated spectra obtained as explained in section 7.2.3. A subsequent discussion shows on the example of two cluster sizes MSi_{15}^+ and MSi_{17}^+ that features visible in the derivative spectra of the photoionization efficiency curve can directly be linked to certain atoms of a geometric structure.
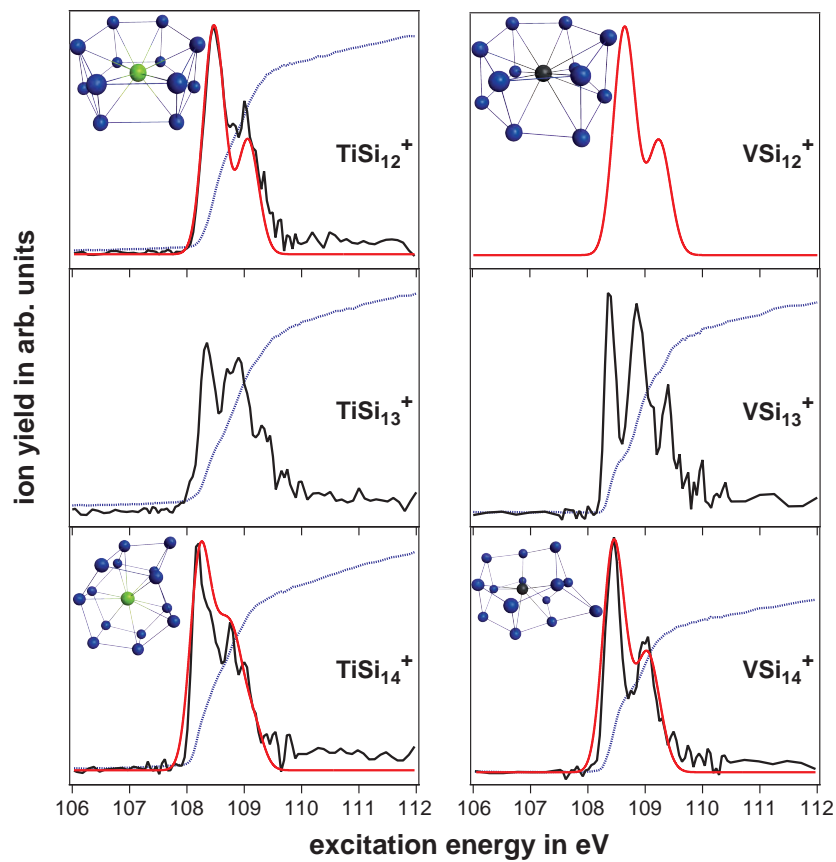
Figure 7.14: Direct photoionization edge of MSi_n^+, (M=Ti,V; $n = 12 - 14$) obtained via PIY spectroscopy (blue curve), derivative of the PIY (black curve) and theoretical results obtained via DFT calculation. The calculated spectra are obtained as explained in section 7.2.3. Geometry files provided by [1, 31]
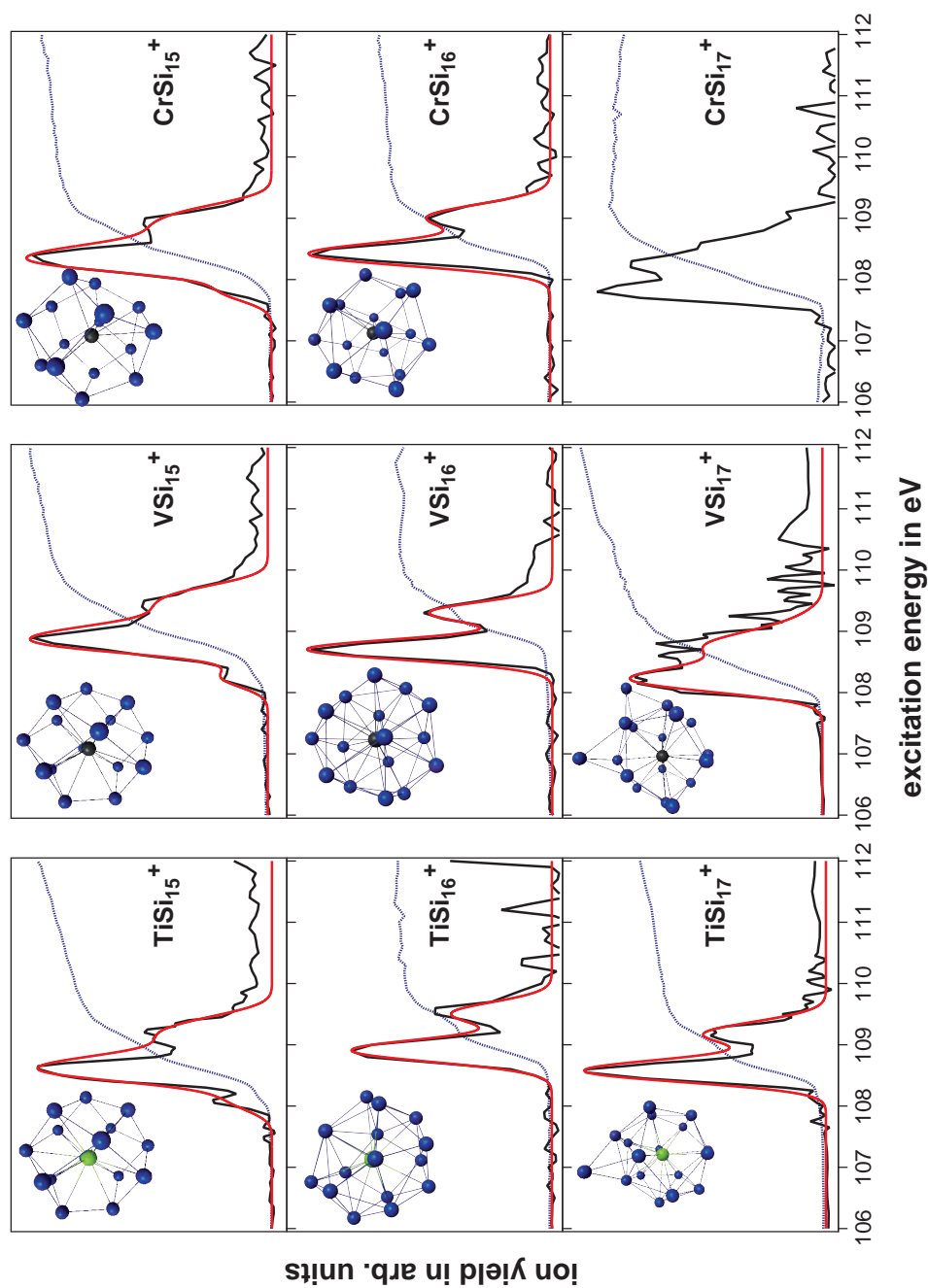
Figure 7.15: Direct photoionization edge of MSi_n^+ MSi_n^+, (M=(Ti,V,Cr; $n = 15 - 18$= obtained via PIY spectroscopy (blue curve), derivative of the PIY (black curve) and theoretical results obtained via DFT calculations (cf. sect. 7.2.3). Geometries provided by [1, 31, 32]

A high overall similarity is observed between the derivative spectra of the experimentally obtained photoionization efficiency curve and calculations corresponding to the energetically lowest isomer found in literature in almost all MSi_n^+ clusters. On first comparison of calculated spectra of MSi_{15}^+ and MSi_{16}^+ it is obvious that although both structures are in first approximation spherical, the calculation is sensitive on the overall different coordination. Although comparison of experimental data is not suited to confirm a certain isomer, it is expected that at least an exclusion of isomers showing an different calculated spectrum is possible [95].

MSi_{12}^+ :The shape of the spectrum of $TiSi_{12}^+$ indicates a high symmetry of the cluster since only two distinct lines are visible corresponding to the spin orbit splitting of silicon 2p. Comparison of the experimental and theoretical data shows an overall similarity of line shape. VSi_{12}^+ calculated data indicate a similar structure to $TiSi_{12}^+$. This indicates that no silicon atoms are in a completely different chemical environment in both MSi_{12}^+.

MSi_{14}^+: Surprisingly, VSi_{14}^+ does not show many lines in the calculated or the experimental spectrum, although calculated structures show a much lower symmetry than MSi_{12}^+ (cf. fig. 7.14). Since both spectra are in good agreement, it is obvious that the silicon atoms are in a similar chemical environment, although the structure DFT calculations of the DOS are done for does not indicate this. It is mainly a heavily distorted structure of VSi_{12}^+, with two silicon atoms on one side. The expectation that these two atoms have a different chemical environment compared to the silicon atoms of the distorted six-fold rings due to a lower coordination and a large distance to the transition metal is not confirmed.

MSi_{15}^+: In figure 7.15, MSi_{15}^+ clusters all show the same trend, with two lines with a high intensity corresponding to the 2p spin orbit split $j = 1/2$ and $j = 3/2$ states. Additionally, a pre-peak is found at the lower energetic side of the peak with the highest intensity. In the spectrum of $CrSi_{15}^+$, this feature is also present in form of a shoulder to the main line. This first low intensity line is very well reproduced by the calculations. Comparison with the calculated 2p states of MSi_{15}^+ reveals the origin of the pre-peak. A few 2p states are separated from the rest at lower binding energies, corresponding to electronic states located at two silicon atoms of the structure, as shown in figure 7.16. The calculated binding energy is shown inverted to positive energies. The two particular silicon atoms are at the same locations in the structure of $TiSi_{15}^+$, VSi_{15}^+, and $CrSi_{15}^+$. However, no

similarity in bond length of these two silicon atoms to the transition metal atom is observed. While the two silicon atoms are closest to the vanadium atom in VSi_{15}^+ , in $CrSi_{15}^+$ they have the largest distance to the chromium atom. In addition, the two silicon atoms behind and below them show almost equal bonding lengths to the chromium center of the cluster. In case of $TiSi_{15}^+$, the two silicon atoms corresponding to the highlighted states in figure 7.16 are the closest and fourth closest to the center atom. The silicon atoms behind and below the left of the silicon atoms with orbitals are the second and third closest. Nonetheless, the screening of the core potential is higher for the silicon atoms orbitals are shown for in figure 7.16. This means that the valence electrons are more localized at these silicon atoms, without showing any tendency regarding their distance to the transition metal atom. The only MSi_{15}^+ cluster missing the low energy peak completely is the $ScSi_{15}^+$, for which no experimental data is available. The structure, being more asymmetric than the equal sized titanium, vanadium, or chromium doped silicon cluster results in a different coordination of each silicon atom and therefore to a more homogeneous energetic splitting of the 2p states, which can be seen in the DOS in figure 7.16. The explanation for the different structures of $TiSi15^+$, $VSi15^+$, and $CrSi15^+$ one the one side and $ScSi15^+$ is the size of the metal atom. Since scandium has a larger atomic radius, a symmetric encapsulation is not possible in contrast to titanium, vanadium and chromium, which show an endohedral structure when surrounded by 15 silicon atoms. The transition metal dependent endohedral-exohedral transition is discussed in section 5.2. An overview over the respective transition values is given in table 5.1 on page 69.

MSi_{16}^+: MSi_{16}^+, M=(Ti,V,Cr) exhibit two well distinct lines in figure 7.15, with VSi_{16}^+ showing the sharpest lines. The narrow lines in the derivative of the direct photoionization PIY spectrum of VSi_{16}^+ are another prove of the highly symmetric structure of this cluster, indicating almost equal coordination for all silicon atoms. A closer look on the calculated energies of the 2p orbitals of VSi_{16}^+ in figure 7.17 exhibits two pairs of close lying lines, which are considered to correspond to the slightly different distances of the silicon atoms from the vanadium atom in the center. The sixteen silicon atoms are located in two closely spaced shells of four on a smaller radius and twelve atoms slightly more distant (cf. sect. 2.1). Orbitals A in figure 7.17 correspond to the tetrahedral arranged four silicon atoms. Therefore, orbitals combined to orbitals B correspond to the twelve silicon atoms on the wider radius, due to electrons count considerations coincide with twelve silicon atoms. The slightly higher coordination of the four silicon atoms seems to
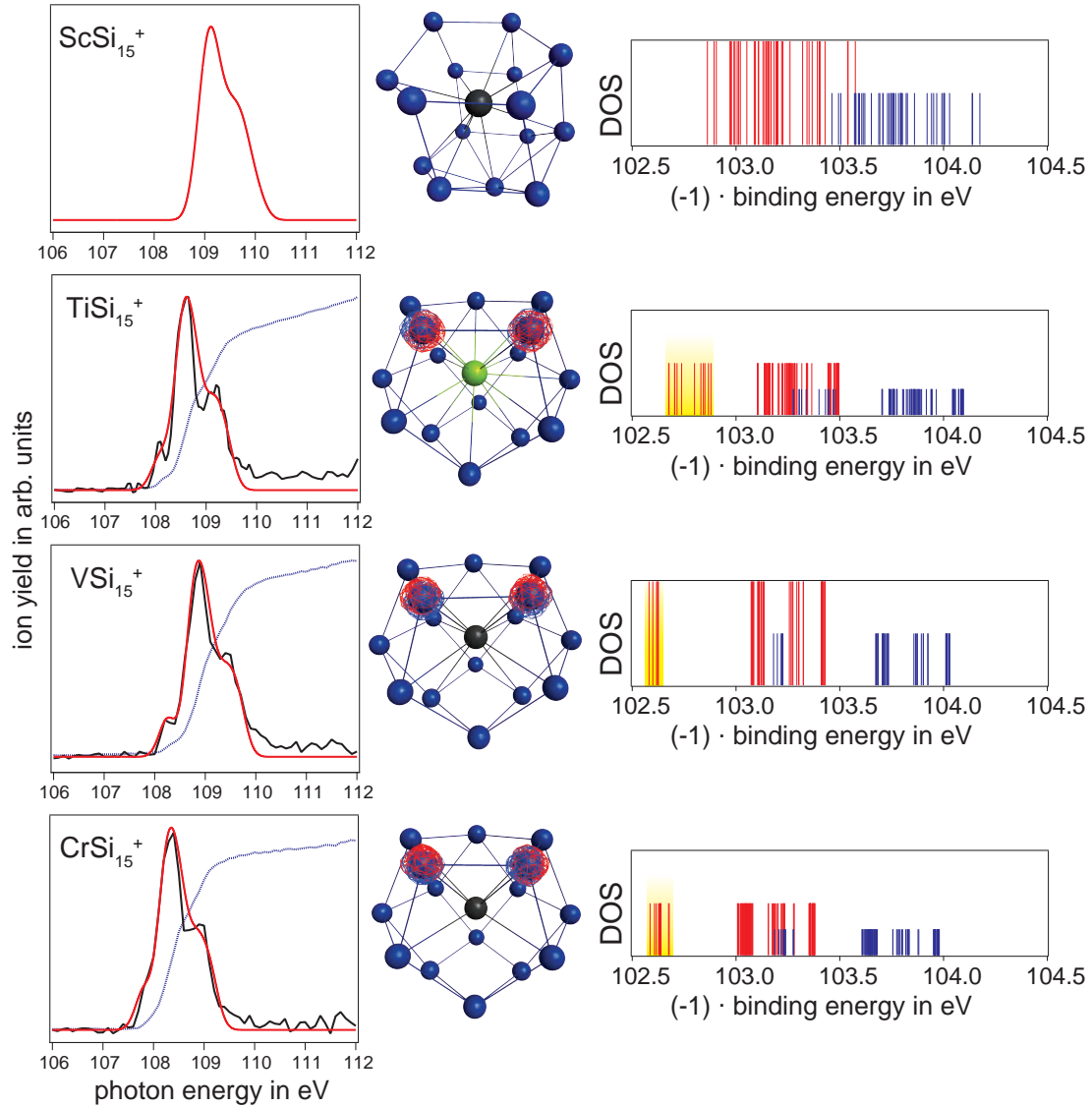
Figure 7.16: Left: Photoionization efficiency spectrum (blue), derived photoionization efficiency (black) and corresponding calculated (red) spectrum of MSi_{15}^+ M=(Sc,Ti,V,Cr). Middle: Geometries of MSi_{15}^+, M=(Ti,V,Cr). The orbitals corresponding to the marked states in the right panel are visualized in the respective geometric structure. Right: Calculated DOS of the binding energy of the 2p states. The binding energy is inverted to positive energies for better comparison with the x-ray absorption spectra.

increase the screening of the core potential, resulting in a lower binding energy of the 2p electrons in the four silicon atoms. The orbitals corresponding to the states of the tetrahedral arranges silicon atoms B are visualized in the inset of figure 7.17, showing the structure of the cluster. The states A' and B' correspond to the spin orbit splitting of 0.6 eV, added after the DFT calculation as explained in section 7.2.3.
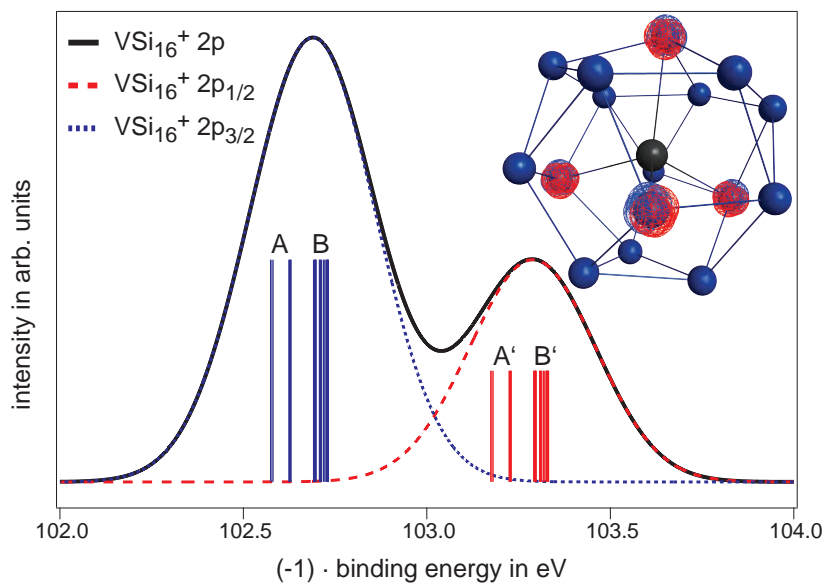
Figure 7.17: DFT calculation of the silicon 2p DOS of VSi_{16}^+. The lines are broadened to fit experimental resolution. The states are divided into two groups (A) and (B). The groups (A') and (B') correspond to the spin orbit split states, introduced after the DFT calculation as explained in section 7.2.3. The 2p states of group (A) correspond to the silicon atoms in tetrahedral geometry, for which orbitals are shown in the structure of the cluster.

MSi_{17}^+: Although the energetically lowest isomer calculated shows a low coordinated silicon atom in the second shell of the structure, which can be seen in figure 7.18, no certain line in the calculated spectra of MSi_{17}^+ or MSi_{17}^+ can be attributed to this atom. It would be expected that due to this outside low coordinated position, the silicon 2p electrons of this atom show a differing chemical shift in the spectrum. The expected distinction is only seen as an line at the high energetic side in the calculated spectrum of $ScSi_{17}^+$, for which no experimental data can be presented. Contrary to the expected high localization of the valence electrons in the outer atom due to the long distance to the rest of the structure, the valence electrons seem to be highly delocalized. This results in a lower screening of the core potential in the initial state and consequently in a higher binding energy of 2p electrons. Again, the respective 2p states of this atom are highlighted and the orbitals visualized at the $ScSi_{17}^+$ structure in figure 7.18. The feature is however not pronounced in the respective spectra of $TiSi_{17}^+$, VSi_{17}^+, and $CrSi_{17}^+$. Surprisingly, the 2p states with the highest binding energy do not belong to the apparently loosely bound silicon atoms, although VSi_{17}^+ shows a separation of some 2p states toward higher binding energies. However, even these states are equally distributed among the clusters silicon atoms. It should be noted that the density of states and the respective direct photoionization spectrum cannot be explained with a careful observation of the geometry alone.
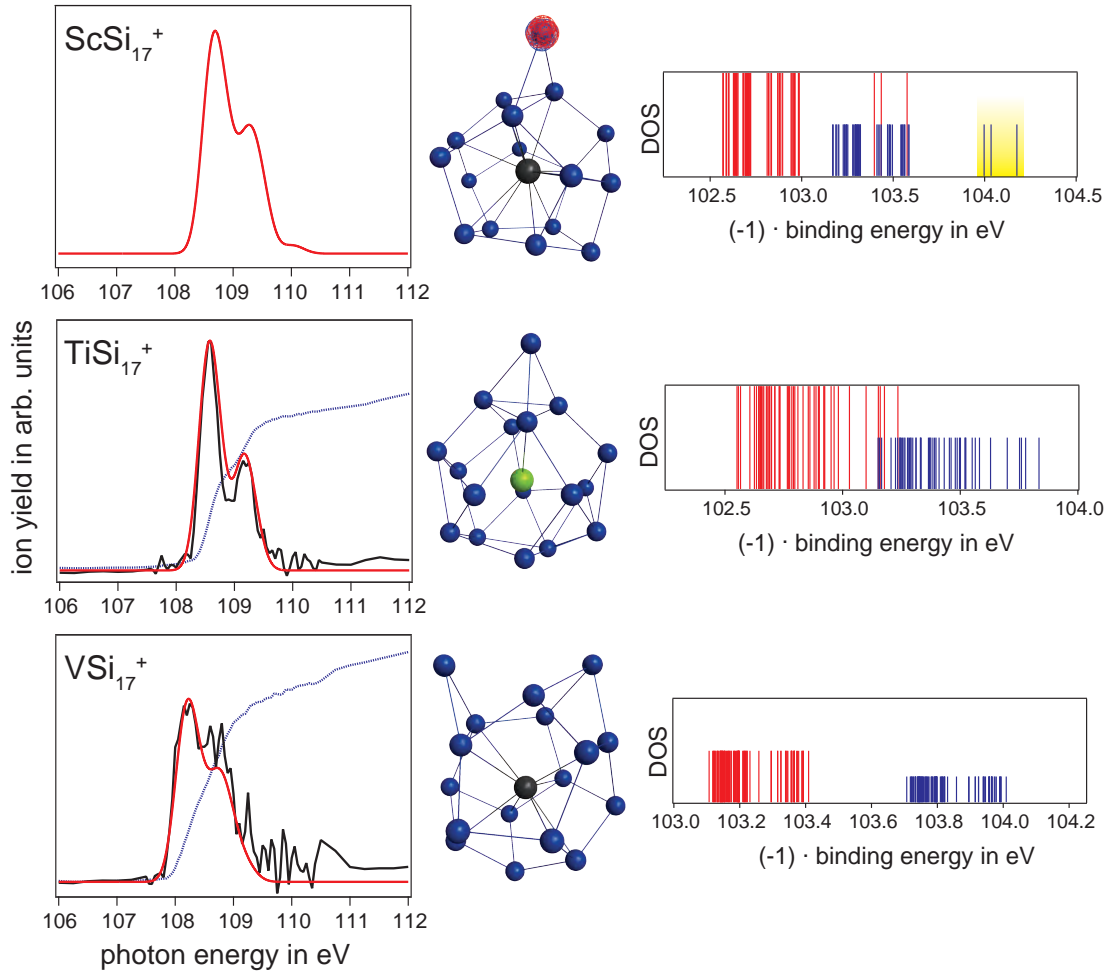
Figure 7.18: Like 7.16 for MSi_{17}^+ M=(Ti,V,Cr).

Conclusion

The results on the energy dependent partial ion yield upon x-ray absorption of the clusters at the silicon $L_{3,2}$ edge presented in this chapter showed that a distinction can be seen between different photo excitation channels probing different electronic states of the cluster. The product ion MSi_n^{3+} is directly linked to direct silicon 2p photoionization whereas resonant silicon 2p excitation into low lying unoccupied states is responsible for the generation of the product ion MSi_n^{2+}. Partial ion yield spectra of fragment ions MSi_x^+ ($x < n$) correspond to transitions into the total unoccupied density of states up to the direct photoionization threshold. It is shown that absorption thresholds and general trends in the partial ion yield spectra of the ideal (M=V) and distorted (M=Ti,Cr) Frank-Kaspar polyhedron MSi_{16}^+ can be explained with the spherical shell model [1]. A measure of the

degree of delocalization of valence electrons is found in the direct photoionization and resonant excitation energy thresholds, showing a high degree of valence electron delocalization in the symmetric closed electronic shell system VSi_{16}^+ in comparison to other VSi_n^+ cluster sizes. Furthermore, comparison of the chemical shift dependent silicon 2p direct photoionization efficiency and calculated spectra using the DFT calculated density of states of a supposed geometry show if the respective isomers found in literature may correspond to the geometry of the cluster observed in the experiment.

Chapter 8

Ion Yield Spectroscopy at the Clusters Valence Orbitals

In addition to ion yield spectroscopy at the silicon $L_{3,2}$ or transition metal $L_{3,2}$ edge, the valence band absorption of transition metal doped silicon clusters is analyzed with photon energies in the vacuum ultraviolet (VUV) regime using ion yield spectroscopy. It is shown that the results of VUV measurements presented in the following yield information about the occupied density of states (DOS) of a MSi_n^+ cluster, which gives in combination with results on the unoccupied DOS information about the HOMO-LUMO gap in MSi_n^+ clusters. Therefore, the measurements are complementary to the x-ray absorption measurements at the silicon $L_{3,2}$ and transition metal $L_{3,2}$ edges, in which the respective local unoccupied DOS is probed. The main interest of these measurements is the electronic valence structure of the highly symmetric VSi_{16}^+, whose electronic shell closure [1] should show in the measurements, and less symmetric $TiSi_{16}^+$ and $CrSi_{16}^+$, whose x-ray absorption spectra at the transition metal $L_{3,2}$ edge is found to mimic the spectra of VSi_{16}^+. Because of this similarity and the sensitivity of x-ray absorption spectroscopy to the unoccupied density of states, it of interest to find out if similarities are also observed in the electronic valence structure.

Analysis of the collected ion yield data in the VUV range is challenging due to much larger number of product ions and fragmentation channels compared to the x-ray absorption studies presented. Therefore, in the first section 8.1 it is discussed how information on the electronic structure of MSi_n^+ cluster can be extracted from partial ion yield spectra. Afterwards, the results obtained are discussed, which yield information on the energetic position of the HOMO via the direct photoionization threshold (cf. sect. 8.2).

127
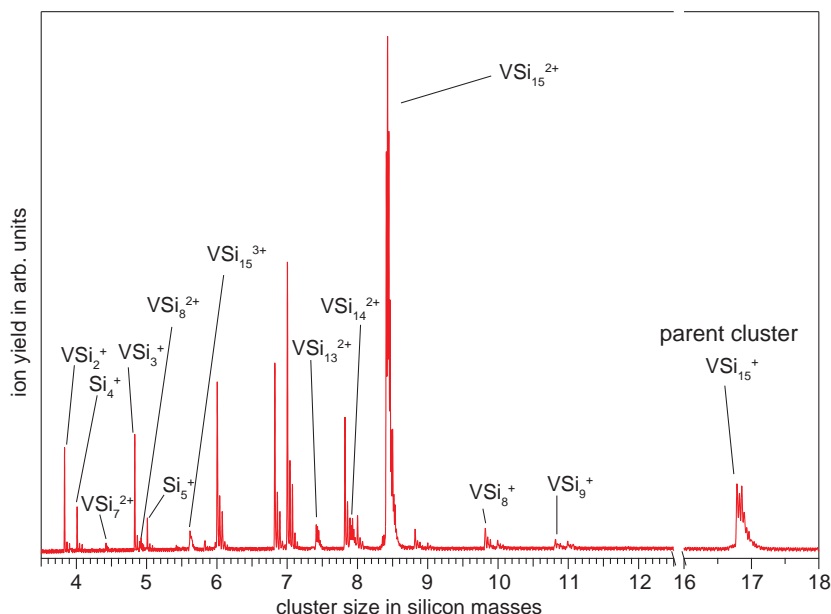
Figure 8.1: Mass spectrum of product ions generated from VSi_{15}^+ in the energy range between 5 eV and 26 eV. For better visibility, the spectrum is smoothed. No product ions are recorded below VSi_2^+ or above Si_{11}^+ (see text).

8.1 Photoionization Efficiency

In the VUV regime daughter ions can be produced via direct photo ionization. Other possible processes responsible for product ion generation can be intra- or inter-band transitions causing vibrations which may lead to fragmentation through evaporative cooling or, if the excitation energy is sufficiently high, Coster-Kronig decay. In addition, potentially existing plasmon resonances of the cluster [99] may generate daughter ions, since plasmon excitation may dissipate the energy to vibrations which again may lead to fragmentation. Analysis of the fragmentation pattern of MSi_n^+ clusters upon VUV excitation reveals an even higher number of daughter ions than is observed in the x-ray absorption process at the silicon $L_{3,2}$ edge, as is shown in figure 8.1. However, the process of daughter ion generation of MSi_n^{2+} is known with high certainty. The threshold energy at which MSi_n^{2+} is generated has to correspond to the direct photoionization threshold of the parent cluster MSi_n^+ for energetic reasons. The lowest energy at which an electron may leave the cluster thus creating a second charge corresponds to the energy difference between the initial state energy $E(MSi_n^+)$ and the final state energy $E(MSi_n^{2+})$. The PIY of MSi_n^{2+} is therefore a measure of the vertical photoionization efficiency. The energetic threshold of this PIY is a good estimate of the sum of binding energy of the valence electrons and charge energy to move the

electron to infinity. Before presenting the results on the direct photoionization in section 8.2, the generation of other daughter ions shown in figure 8.1 is discussed. In contrast to the partial ion yield (PIY) at the silicon L$_{3,2}$ edge grouping of product ions according to similarities in their PIY spectrum is challenging, which is assumed to be due to the multiple fragmentation channels that may lead to a certain product ion. The analysis is complicated since normalization with respect to the photon flux cannot be performed with the available experimental data in this energy range as already described in section 4.2. To ensure consistency of PIY spectra even without photon flux normalization (cf. sect. 4.2), features observed at a certain energy in PIY spectra are checked if they might correspond to features in the photon flux at the respective photon energy. This helps to select only absorption induced features for further analysis.

The reason for the fragmentation pattern and the respective PIY of the product ions is unknown, except in case of the doubly charged parent ion MSi$_n^{2+}$, from whose PIY the direct photoionization threshold can be extracted. Therefore, this chapter will focus on this daughter ion. Nonetheless, a detailed description of other product ion's PIY spectra is available in appendix A.2.

8.2 Direct Photoionization Threshold of MSi$_n^+$ Clusters

The direct photoionization efficiency of a MSi$_n^+$ cluster can be estimated by the PIY of the photo induced daughter ion MSi$_n^{2+}$. The respective PIY spectra for TiSi$_n^+$, VSi$_n^+$, and CrSi$_n^+$ clusters are presented in figure 8.2. The selection of dopant materials was chosen to gain information about the electronic structure at the valence states of MSi$_{16}^+$ (M=Ti,V,Cr) clusters, for which theoretical predictions are possible by means of the spherical shell model (cf. sect. 2), which was already used to explain x-ray absorption spectra of these three clusters at the metal L$_{3,2}$ and silicon L$_{3,2}$ edge in chapters 6 and 7.
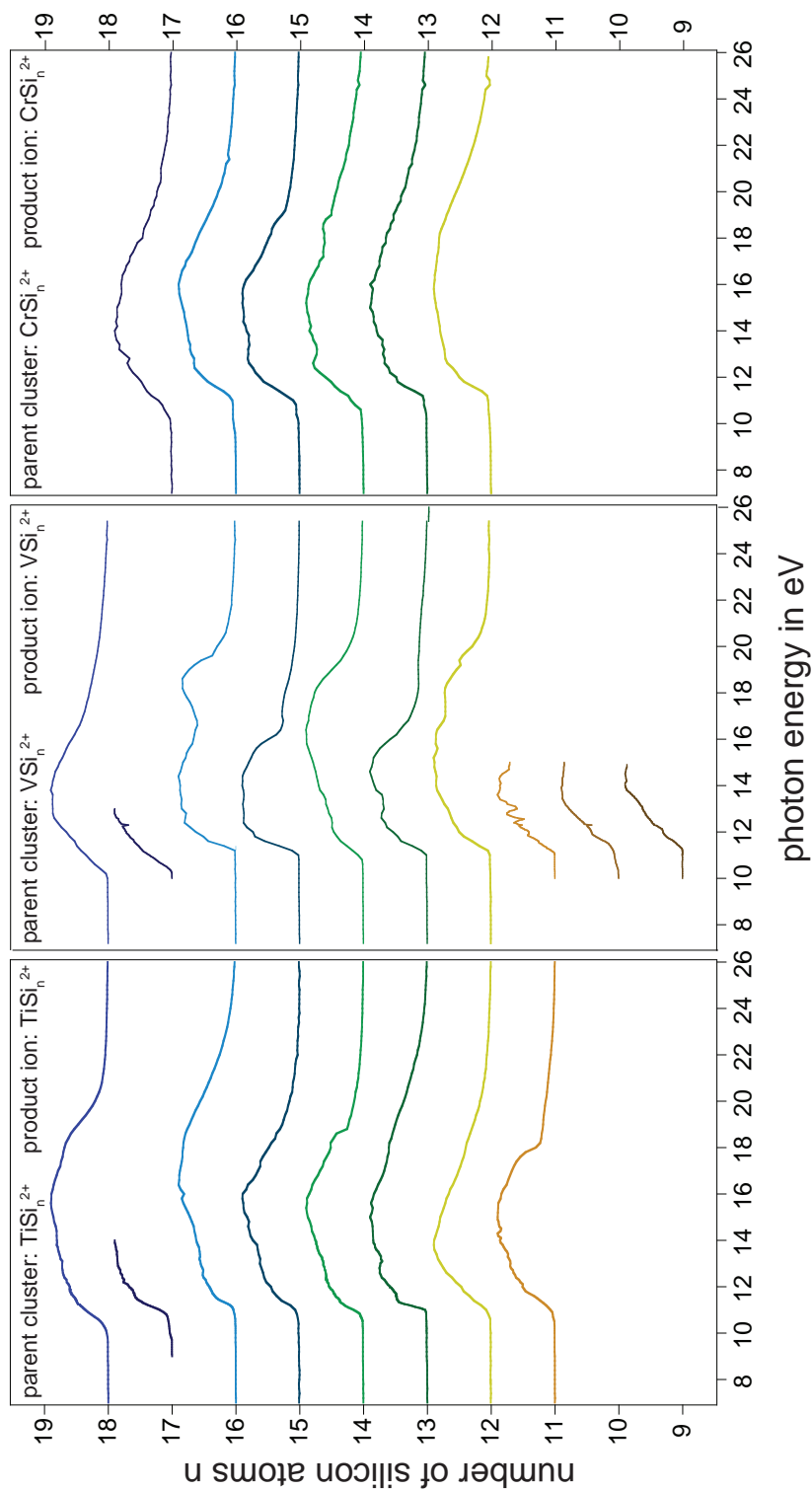
Figure 8.2: Photoionization efficiency spectra of MSi_n^+.

The general trend of the MSi$_n^{2+}$ PIY in figure 8.2 shows a steep rise in intensity and a following decrease to zero with increasing photon energy. Not all PIY spectra are measured over the whole energy range, since the main idea is to determine the direct photoionization threshold. Therefore only the energetic region of the threshold energy was scanned. However, the direct photoionization threshold is not always located at the position of the steep rise in a spectrum but in some cases at a small pre-edge, as is shown in figure 8.3. The graph shows the magnification of the rising edge of the photo efficiency curves of figure 8.3. The pre-edges having a low photoionization efficiency are suggested to correspond to photoionization of electronic states with a low electron occupation. Small pre-edges are visible in the PIY spectra of TiSi$_n^{2+}$ ($n = 10, 11, 13, 17, 18$), VSi$_{11}^{2+}$, and CrSi$_n^{2+}$ ($n = 13, 15, 16$). In the case of CrSi$_{16}^+$ this pre-edge is discussed in chapter 9. The threshold energy of each photo efficiency curve is marked by a red dash. The position of this direct photoionization threshold corresponds to the second ionization potential (2nd IP) of the MSi$_n$ cluster[1], even if ionization efficiency is low.

The IP of MSi$_n^+$ clusters is size dependent, as shown in figure 8.4. In a simple model, the direct photo ionization threshold depends on the binding energy (BE) of the weakest bound electron with respect to the vacuum level and the charge energy, as explained in section 1.1.1. The charge energy depends in a simple metallic sphere linearly on the inverse radius of the cluster $r^{-1} \propto n^{-1/3}$. Although the general decrease in the IP might be observed in figure 8.4 despite the small mass range analyzed, the IP does not only depend on the cluster radius, as can be seen by the non-monotonic trend. This shows the influence of the valence electron BE.

In the following only cluster sizes are discussed, which show a strong derivation from in their IP from other cluster sizes. Of special interest are the MSi$_{16}^+$ clusters in perfect (M=V) or slightly distorted (M=Ti,Cr) Frank-Kaspar polyhedral geometry (cf. fig. 2.2). The spherical shell model [1] introduced in section 2.3 predicted an electronic shell closure in case of VSi$_{16}^+$. The electronic structure of the valence orbitals is shown schematic in figure 8.5. In general, closed electronic shell systems feature a higher binding energy than open electronic shell systems. Therefore, VSi$_{16}^+$ having a shell closure shows an exceptional high IP. In comparison, TiSi$_{16}^+$ shows a lower IP than VSi$_{16}^+$, which is nonetheless higher than the

---

[1]The 1st IP is not measurable within this experiment, as the parent cluster is already singly charged upon production in the cluster source. Since no other ionization potential is discussed within this chapter than the IP corresponding to the initial state MSi$_n^+$ and the final state MSi$_n^{2+}$, in the following only the term IP is used.
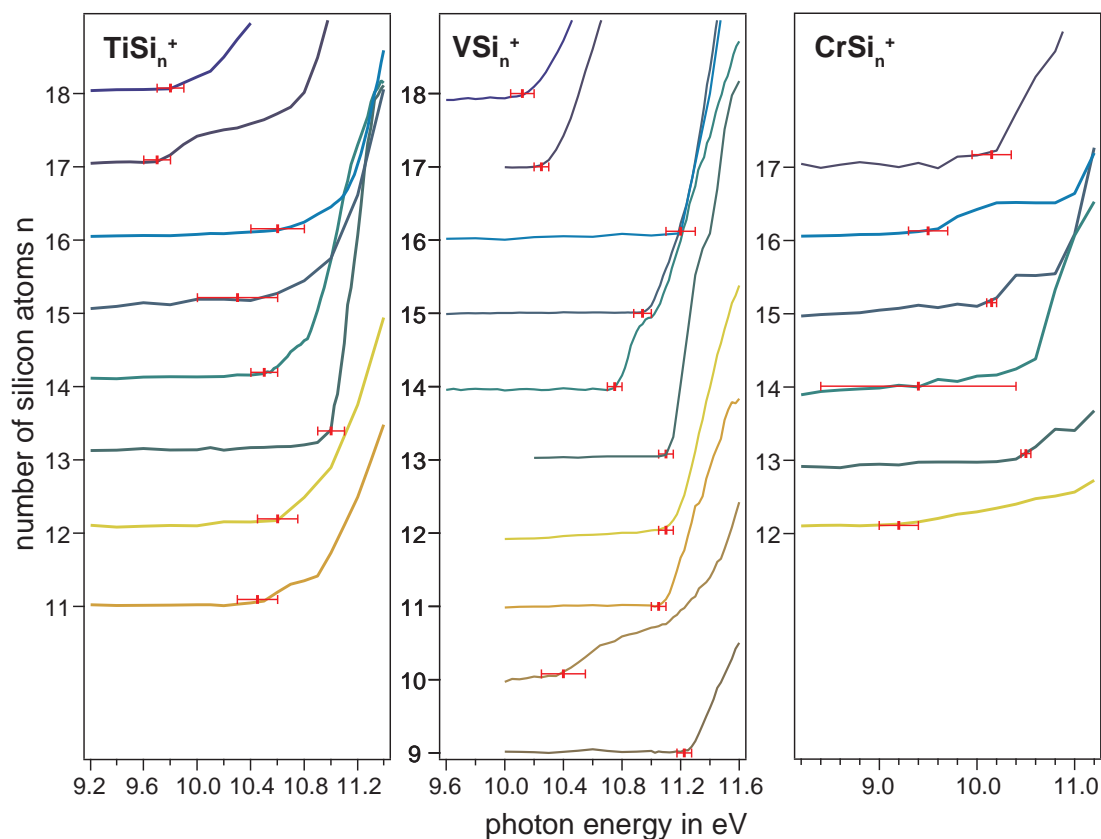
Figure 8.3: Closeup of the MSi_n^+ direct photoionization threshold. The threshold is in some cases not at the steep rise of the photoionization efficiency curve, but at a low intensity pre-edge.

average IP of $TiSi_n^+$ clusters. The lowest IP of MSi_{16}^+ analyzed is found for $CrSi_{16}^+$. The enhanced IP of $TiSi_n^+$ can also be understood by means of the electronic structure provided by the theoretical approach of the spherical shell model. If the electronic structure is assumed to be similar to the electronic structure of VSi_{16}^+, $TiSi_{16}^+$ is missing only one electron towards a shell closure. Similar to the general trend of the IP of atomic elements along a period of the periodic table, the nearer an electronic configuration is towards a shell or sub-shell closure, the higher the IP of the corresponding element. The highest IP of a period is reached at the noble gases, whereas the lowest IP is usually found for alkali elements. Therefore, it is clear that due to the almost completely occupied 2d orbital in terms of the spherical shell model, a high IP should be found for $TiSi_{16}^+$. For $CrSi_n^+$ an explanation in agreement with the spherical shell model also applies. Due to the one electron located in the 1h state, having a low binding energy due to its extreme open shell character with only a single electron occupation of the 1h state, the low IP observed is in good agreement with expectations from comparison with the periodic table. As mentioned above, the low one electron

132
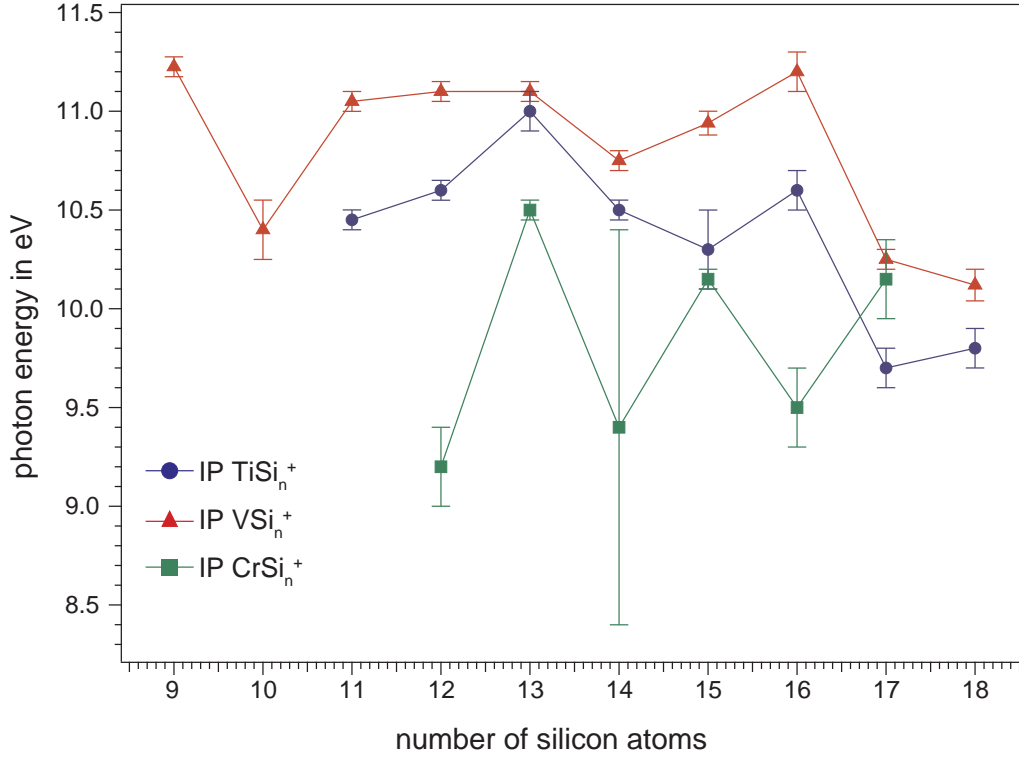
Figure 8.4: Ionization potential (IP) of MSi$_n$, M=(Ti,V,Cr), $n = 9 - 18$ clusters.

occupancy of 1h is also observed in the photoionization efficiency in figure 8.3 and discussed in section 9.3

The neighboring cluster sizes VSi$_{15}^+$ and VSi$_{17}^+$ of VSi$_{16}^+$ have a much lower IP. It is expected that due to their lower geometric symmetry the valence states have a low degeneracy. Therefore, no shell or sub-shell closures can be expected. This is in good agreement with the lower IP compared to the IP of VSi$_{16}^+$. It can be deduced that no electronic shell closure is present in these systems.

A similar size dependence of the IP is found for TiSi$_{15}^+$ TiSi$_{16}^+$ and TiSi$_{17}^+$. In case of CrSi$_{15}^+$ and TiSi$_{17}^+$, higher IP's are found than the one observed for CrSi$_{16}^+$. This indicates that in contrast to CrSi$_{16}^+$ there is not only one low bound valence electron in an otherwise closed shell system, but presumably a partially occupied state. A general comparison of the IP's of VSi$_n^+$ to TiSi$_n^+$ and CrSi$_n^+$ shows that VSi$_n^+$ always has a higher IP than the equal sized titanium or chromium doped silicon cluster. A possible explanation could be that while VSi$_n^+$ always has an even number of valence electrons, all CrSi$_n^+$ and TiSi$_n^+$ have an odd number. Therefore shell or sub-shell closures or even the full occupation of a specific state by two electrons with antiparallel spins can only be achieved in VSi$_n^+$.
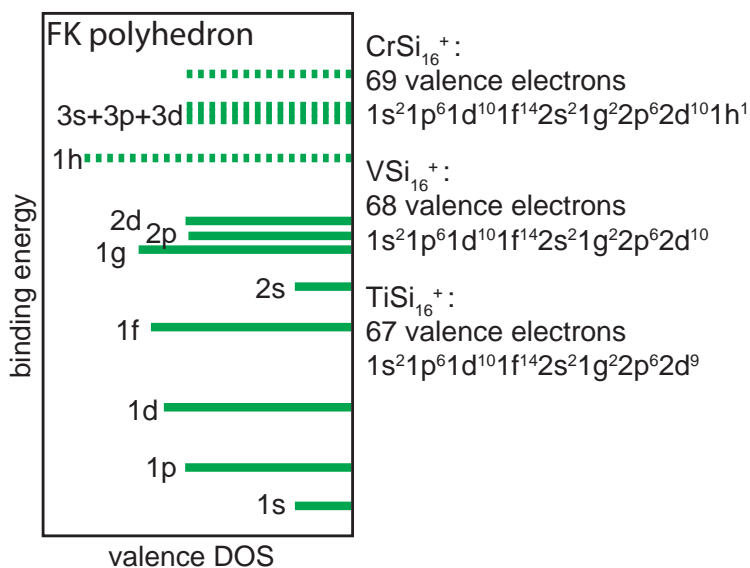
Figure 8.5: Schematic illustration of the valence density of states of the spherical MSi_{16}^+ with tetrahedral symmetry (Frank-Kaspar polyhedron). The states are denominated according to the spherical shell model [1]. On the right side the electronic configuration of MSi_{16}^+ (M=Ti,V,Cr) is given.

Conclusion

It is shown that the direct photoionization potentials of MSi_n^+ clusters can be determined by ion yield spectroscopy in the VUV regime. The ordering scheme of ionization potential values in spherical Frank-Kaspar polyhedron VSi_{16}^+, $TiSi_{16}^+$, and $CrSi_{16}^+$ of 11.2 eV, 10.6 eV, and 9.5 eV respectively can be explained with the spherical shell model [1].

Chapter 9

HOMO-LUMO Gap

The electronic structure of valence states is most interesting in an atom, molecule or cluster, since it mediates bonding, defines the conductivity and absorption in the low energy range where also visible light is found. The energetic gap between the highest occupied molecular orbital and the lowest unoccupied molecular orbital (HOMO-LUMO gap) is a parameter often used in quantum chemistry to describe the electronic structure of a molecule or cluster near the Fermi level. With increasing size of the molecule or cluster, the HOMO-LUMO gap is evolving into the respective bulk parameter, the band gap, which is of the upmost importance in applied semiconductor physics. In order to avoid confusion in the following chapter, the use of the term HOMO-LUMO gap within this thesis is described.

To know what can be understood by the term HOMO-LUMO gap, the band gap and band gap determination is described first. The energetic distance of the band gap is not equal to the excitation energy of an electron from the valence band to next unoccupied state, since these are excitonic states at lower energies (cf. fig. 9.1 1a). Furthermore, the band gap is not present in all materials. In case of bulk metals with partially occupied bands as shown in figure 9.1 1b, no band gap is present. The HOMO-LUMO gap is the energetic distance between the lowest unoccupied molecular orbital and the highest occupied molecular orbital. Historically, this term was used in quantum chemistry for closed shell systems, where it is quite self-explanatory as shown in figure 9.1 2a. In systems with a partially occupied molecular orbital the term HOMO is misleading, as the orbital is also partially unoccupied. In such cases, as shown in figure 9.1 the highest occupied and lowest unoccupied molecular orbitals are degenerate (cf. fig.9.1 1b). Furthermore, it should be noted that unoccupied states can only measured by an electronic transition into them and therefore by occupation. The lowest en-
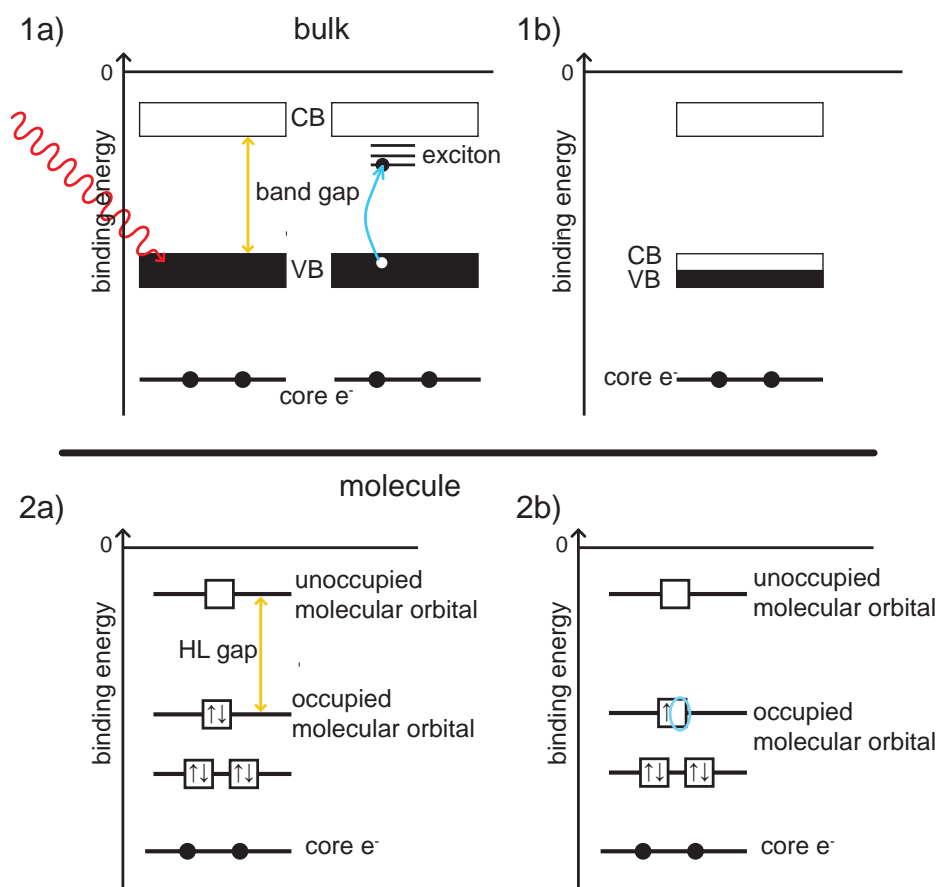
Figure 9.1: Upper panel: Band gap of bulk materials. 1a) The excitation energy for an electron into the next unoccupied state is not equal to the band gap in the initial state of the system due to excitons in the final state. 1b) bulk metal without a band gap.
Lower panel: HOMO-LUMO gap in molecules. 2a) The highest molecular orbital has a closed electronic shell. The energetic distance between the highest occupied and lowest unoccupied molecular orbital in the ground state is shown. 2b) Highest occupied and lowest unoccupied molecular orbital are degenerate. The term HOMO-LUMO gap does not apply.

ergy difference between a molecule in the ground state and a molecule in an excited state is therefore referred to as HOMO-LUMO gap. If energies between an theoretically calculated occupied molecular orbital and an unoccupied molecular orbital are degenerate, the term HOMO-LUMO gap does not apply.

Measuring the HOMO-LUMO gap like a band gap in bulk material by absorption spectroscopy by transmission of light is challenging for the small quantities of size selected transition metal doped silicon clusters in the gas phase, due to a low target density (cf. sect. 1.1.3) and resulting a high transparency. Although optical methods like cavity ring down measurements are especially designed to fit low target densities, only recently direct absorption measurements of size selected clusters accumulated in an ion trap succeeded [100]. In this chapter,

a novel analysis method is introduced to determine the HOMO-LUMO gap of transition metal doped silicon clusters indirectly by ion yield spectroscopy of the x-ray and (vacuum-)ultraviolett photo absorption [91]. It is expected that this method is widely applicable on silicon compounds. First results on pure silicon clusters [8] already showed the capability of this novel method. Comparison of this new method with other methods described in literature to determine the HOMO-LUMO gap showed that an estimate of a HOMO-LUMO gap of neutral MSi_n clusters can be obtained via photo electron spectroscopy at anions of closed electronic shell MSi_n clusters [51, 83], as discussed in section 2. However, of 3d transition metal doped silicon clusters only one HOMO-LUMO gap of the closed electronic shell system $TiSi_{16}$ is available in literature. The obtained HOMO-LUMO gap of about $2\,eV$ is in good agreement with theoretical results of the electronic valence structure of this cluster [1, 57].

Before presenting the results on HOMO-LUMO gaps of MSi_n^+ clusters in section 9.2, the method used to obtain it is explained and the capability as well as limitations are discussed in section 9.1.

9.1 Determination of the HOMO-LUMO Gap by Ion Yield Spectroscopy in the VUV and at the Silicon 2p Edge

The HOMO-LUMO gap is calculated with a Born-Haber cycle of core level and valence photo ionization thresholds and resonant x-ray absorption threshold [91]. To calculate the level spacing, three energy differences are needed, which are shown in figure 2.3. The direct photo ionization threshold energy of the HOMO E_V is obtained via VUV spectroscopy at the valence band. The energy obtained is the sum of the binding energy of the electron occupying the highest energetic level of the DOS and the charge energy (cf. section 1.1.1). A detailed discussion on the results of valence state absorption spectroscopy is given in section 8.2. The direct photo ionization threshold energy E_C is obtained by the threshold of a partial ion yield spectra of a certain daughter ion. In case of transition metal doped silicon cluster cations, this is the PIY of MSi_n^{3+}, as shown in section 7.2. The energetic position of the threshold is equivalent to the binding energy of the silicon 2p level plus the charge energy. The last needed energy, the threshold energy for resonant x-ray absorption E_{XAS}, is obtained as shown in section 7.2.1 by the energy difference of the 2p state to the lowest unoccupied energy level
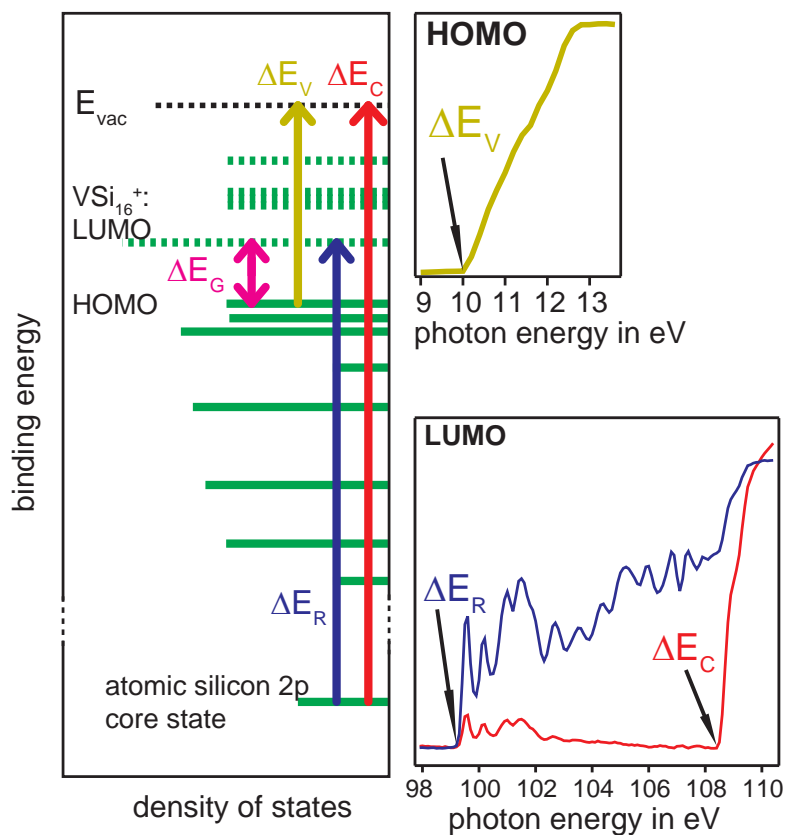
Figure 9.2: Schematic of the method used to determine HOMO-LUMO gap in case of VSi_{16}^{+}. The gap E_G is the result of a Born Haber cycle involving the direct silicon 2p photo ionization threshold E_C, resonant silicon 2p x-ray absorption threshold E_{XAS}, and the valence orbital direct photo ionization threshold E_V. On the left side the respective energies are marked by arrows in the schematic DOS of the cluster [1]. The spectra on the right show ion yield spectra from which the respective threshold energies are obtained.

reachable via dipole allowed transition.

In case of MSi_n^+ clusters, the lowest unoccupied molecular orbital has 4s-3d character [1]. Therefore, transition into this unoccupied state are dipole allowed. Otherwise, the method might result in a underestimated binding energy of the lowest unoccupied energy level reachable, as the observed energy threshold of the resonant 2p transition does not belong to the *lowest* unoccupied level. Even if the transition into the lowest unoccupied energy level is dipole allowed, the energy difference is not exactly the energy difference between the silicon 2p state and the lowest unoccupied energy level of the parent cluster, as the energy is lowered by core hole interaction in the final state. This leads to a systematical overestimation of the binding energy of the lowest unoccupied molecular orbital and finally to an underestimated HOMO-LUMO gap.

The HOMO-LUMO gap E_{G} is calculated by

$$E_{\mathrm{G}} = \underbrace{E_{\mathrm{V}}}_{\text{(highest occupied energy level)}} - \underbrace{(E_{\mathrm{C}} - E_{\mathrm{XAS}})}_{\text{(lowest unocc. energy level)}} \quad . \quad (9.1)$$

relative to the vacuum level

Since the charge energy is present in two values forming a difference, it should
cancel out. However, the core hole interaction is still present and inflicts an
systematic error to the calculated HOMO-LUMO gap. Therefore it should be
kept in mind that the HOMO-LUMO gap obtained with equation (9.1) is expected
to underestimate the "'real"' HOMO-LUMO gap of the cluster.

9.2 HOMO-LUMO Gaps of Transition Metal Doped Silicon Clusters

In this section the results of HOMO-LUMO gap determination of TiSi_n^+, VSi_n^+,
and CrSi_n^+ are presented. First, the HOMO-LUMO gaps of VSi_n^+ are discussed,
with the main focus on VSi_{16}^+, which showed the theoretically predicted highly
symmetric structure and electronic shell closure [1, 31] already in the analysis
of the x-ray absorption at the metal $\mathrm{L}_{3,2}$ and silicon $\mathrm{L}_{3,2}$ edge (cf. chapters 6
and 7) as well as in VUV spectroscopy (cf. chap. 8). Its predicted high stability
and low reactivity is shown by [33, 39, 49] and in chapter 5. All these features
should lead to a high HOMO-LUMO gap with respect to its neighboring cluster
sizes and other dopant metals of the transition metal doped silicon cluster cations.

General Trend of the HOMO-LUMO Gaps of VSi_n^+

The HOMO-LUMO gaps[1] of VSi_n^+ shown in figure 9.3 confirm the theoretical re-
sults stating that VSi_{16}^+ has an increased HOMO-LUMO gap compared to neigh-
boring cluster sizes [1,31]. Starting with VSi_{16}^+, a drastic decrease of the HOMO-
LUMO gap for the neighboring VSi_{15}^+ and VSi_{17}^+ is visible due to an expected open
shell configuration, a lower symmetry and a resulting higher degeneracy of states.
This is also observed in the calculated gap values. In general, the experimental

---

[1]It should be noted that preliminary results of the presented level spacings of VSi_n^+ [8,91] do
also show the same progression as the theoretical determined HOMO-LUMO gaps with cluster
size. However, after a more detailed analysis of the experimental data, the experimental values
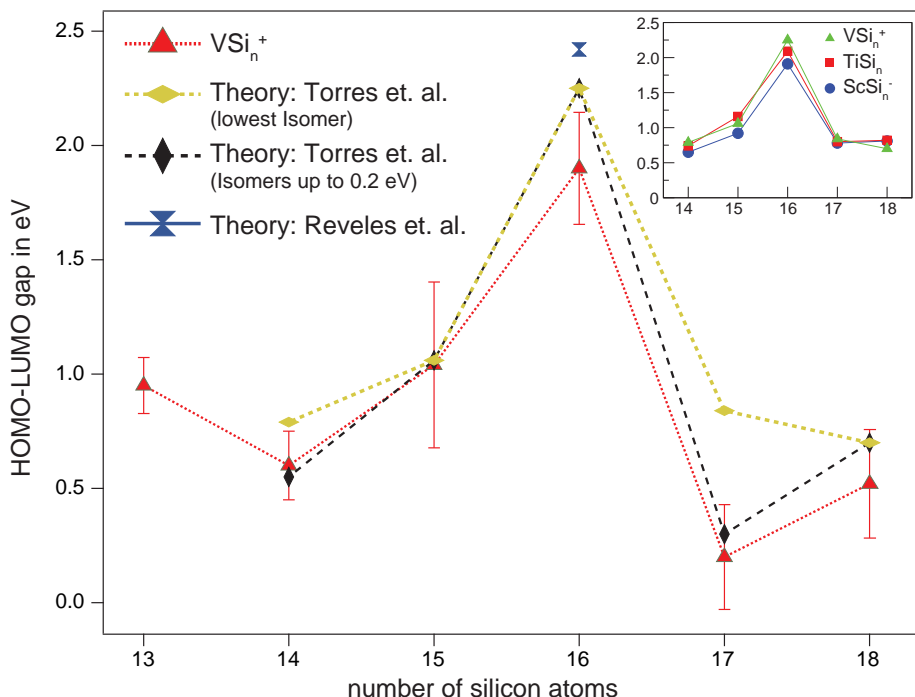had to be mildly adjusted.

Figure 9.3: Experimental HOMO-LUMO gaps of VSi_n^+. The theoretical values [1,31] exhibit an exceptional high HOMO-LUMO gaps in case of VSi_{16}^+, which is higher than the experimentally observed gap. The overall trend of the theoretical data [1] of the lowest VSi_n^+ isomer's HOMO-LUMO gaps (yellow line) deviate slightly from the experimental data. A larger agreement is found, if the lowest HOMO-LUMO gaps of all isomers within 0.11 eV of the energetically lowest Isomer (black line) are considered. The inset shows the theoretical HOMO-LUMO gap of the lowest isomers of the isoelectronic VSi_n^+, $TiSi_n$, and $ScSi_n^-$ [1].

and theoretical data of the energetically lowest isomer's HOMO-LUMO gap deviates between $20\,meV$ (VSi_{15}^+) and $635\,meV$ (VSi_{17}^+), which can be explained by the binding energy of a core exciton in doped silicon clusters. The experimentally determined HOMO-LUMO gap is expected to be lower than the 'real' HOMO-LUMO gap due to the presence of the core hole in resonant x-ray absorption in the final state (cf. sect. 9.1). Therefore a general lower experimental HOMO-LUMO gap than predicted by theory is reasonable. The only deviation from the trend of the calculated gap in dependence of the cluster size is that the succession of the gap magnitude in VSi_{17}^+ and VSi_{18}^+ is reversed. However, if not only the lowest isomer's HOMO-LUMO gaps are considered, but also an isomer of VSi_{14}^+ with an energy of $80\,meV$ above the lowest isomer and an isomer of VSi_{17}^+ with an energy of $110\,meV$ above the lowest isomer (cf. fig. 9.4), agreement of the theoretical calculated HOMO-LUMO gaps and the experimentally determined values increases. The isomers shown in figure 9.4 have different HOMO-LUMO gaps due to the dependence of the electronic structure on the cluster's geometry. If more than one isomer is present in the ion trap, the lowest HOMO-LUMO gap of all
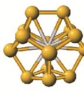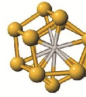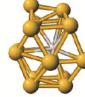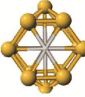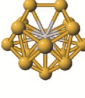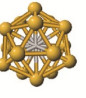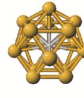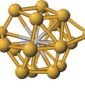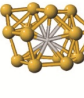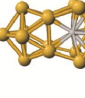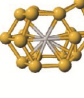
VSi_{14}^{+}					
Energy	0.00 eV	0.08 eV	0.14 eV	0.18 eV	0.19 eV
HOMO-LUMO gap	0.79 eV	0.55 eV	0.77 eV	0.76 eV	1.15 eV
VSi_{15}^{+}					
Energy	0.00 eV				
HOMO-LUMO gap	1.06 eV				
VSi_{16}^{+}					
Energy	0.00 eV	0.01 eV			
HOMO-LUMO gap	2.25 eV	2.25 eV			
VSi_{17}^{+}					
Energy	0.00 eV	0.11 eV			
HOMO-LUMO gap	0.84 eV	0.30 eV			
VSi_{18}^{+}					
Energy	0.00 eV	0.04 eV			
HOMO-LUMO gap	0.70 eV	0.86 eV			

Figure 9.4: Geometric structures, HOMO-LUMO gaps and total energy of VSi_n^+ isomers up to an energy of 0.11 eV above the energetically lowest isomer [1].

isomers is measured provided the isomers are sufficiently abundant. If all isomers of VSi_n^+ up to a total energy difference of 0.11 eV are present in the ion trap, the lowest HOMO-LUMO gap of the respective clusters yield a better agreement between calculated and experimental HOMO-LUMO gaps of VSi_{14}^+ and VSi_{17}^+. In addition the succession of the HOMO-LUMO gap values in case of VSi_{17}^+ to VSi_{18}^+ is in agreement with the calculations. If isomers are in fact present, they have to have their origin in the cluster source, as temperatures in the liquid nitrogen cooled ion trap are far too low for thermal population. They might be generated if during cluster growth the clusters are cooled down by the buffer gas of the cluster source so fast that redistribution of the atoms in the cluster toward the energetic ground state geometry is inhibited. The isomers shown in figure 9.4 are each at a local minimum of the energetic surface with potential walls between them prohibiting further relaxation. Since the cluster is given an internal energy each time a new atom is accumulated by the amount of the binding energy of about 3 eV to 4 eV [1], the height of the potential walls have to be of equivalent magnitude. If one of these isomers is generated and leaves the cluster source, it is

not expected to change its once adopted geometry due to the liquid nitrogen temperature in the experiment later on. However, since this explanation is founded on an increased agreement of the HOMO-LUMO gaps of only one cluster size, VSi_{17}^+, it is no prove of the presence of isomers.

Next to the calculated HOMO-LUMO gaps of VSi_n^+ clusters, the inset in figure 9.3 shows the cluster size dependent HOMO-LUMO gaps of the isoelectronic $ScSi_n^-$, $TiSi_n$ and VSi_n^+ [1]. As can be seen, the interchange of the dopant atom while keeping the number of valence electrons constant yields about the same cluster size dependence of the HOMO-LUMO gap. While cluster sizes n=14-15 have equal geometries for all three dopant atoms, the geometries of the cluster sizes n=16-18 differ slightly between the vanadium and the titanium/scandium doped species [1]. Nevertheless, the resemblance in their geometry seems to be high enough to result in similar values. Similar geometric structures on the other hand seem to be responsible for almost equal configuration of the electronic valence orbitals and therefore for comparable HOMO-LUMO gap values if the number of valence electrons is maintained.

In the following, experimental results are compared to an existing model of the electronic structure for one of these isoelectronic clusters, the highly symmetric VSi_{16}^+. In the second section (sect. 9.3) of this chapter, the spherical shell model, is discussed for VSi_{16}^+, $TiSi_{16}^+$ and $CrSi_{16}^+$, which differ only in their number of valence electrons and by a slight distortion in geometry.

9.2.1 Theoretical Model for the HOMO-LUMO Gap in VSi_{16}^+

The HOMO-LUMO gap of VSi_{16}^+ can be explained within the framework of the spherical shell model [1]. Figure 9.5 shows a schematic view of the valence density of states of the Frank-Kasper polyhedral geometry of VSi_{16}^+. This particular cluster showed a highly symmetric geometry in DFT calculations, which is verified in XAS studies at the transition metal and silicon $L_{3,2}$ edge. Furthermore, calculations predicted an electronic shell closure, leading to a high HOMO-LUMO gap [1, 31]. The quantum numbers next to the DOS correspond to the radial nodes and angular momentum character of the corresponding cluster valence orbital. A detailed discussion of the valence orbital labeling and the spherical shell model is given in section 2. The shell closure is achieved at the clusters 2d valence orbital, which is completely occupied if 68 valence electrons are available ($1s^2\, 1p^6\, 1d^{10}\, 1f^{14}\, 2s^2\, 1g^{18}\, 2p^6\, 2d^{10}$). These electrons are provided by the sixteen
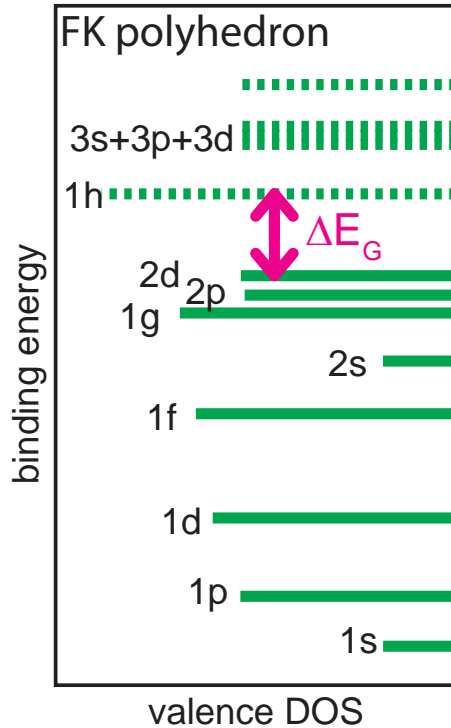
Figure 9.5: Schematic of the calculated DOS of VSi_{16}^+ in the geometry of a perfect Frank-Kaspar polyhedron [1]. The full calculation is shown in fig. 2.5. The calculated HOMO-LUMO gap $\Delta E_G = 2.25\,eV$ between the valence states 2d and 1h, labeled according to the spherical shell model, is marked by the pink arrow.

silicon atom $3s^2 3p^2$ valence electrons ($16 \times 4\,e^-$) and the vanadium atom $3d^3 4s^2$ valence electrons ($5e^-$). The total valence electron count is decreased by one due to the cationic character of the cluster ($16 \times 4\,e^- + 5\,e^- - 1\,e^- = 68e^-$). The LUMO corresponds to the 1h state of the spherical shell model. For VSi_{16}^+, the shell closure of the spherical shell 2d valence state results in a high apparent HOMO-LUMO gap. This is in good agreement with the theoretical predicted value [1,31], when keeping in mind that due to the experimental method the gaps obtained are expected to be systematically lower than the real HOMO-LUMO gap of these systems.

9.2.2 HOMO and LUMO in $TiSi_n^+$ and $CrSi_n^+$

In addition to the HOMO-LUMO gap of VSi_n^+, the energetic distance of the HOMO to the LUMO of $TiSi_n^+$ and $CrSi_n^+$ is determined using the method explained above (cf. sect. 9.1). The results are displayed in figure 9.6. For comparison, the HOMO-LUMO gap of VSi_n^+ is also shown. On the very first glance it can be seen that the values determined for $TiSi_n^+$ and $CrSi_n^+$ differ strongly from

the trend measured for VSi_n^+ clusters. While VSi_n^+ has HOMO-LUMO gaps that show strong size dependences with values between $0.3\,eV$ and $1.9\,eV$, the measured values of $TiSi_n^+$ and $CrSi_n^+$ are arranged near $0\,eV$. Values below $0\,eV$ are due to the influence of the core exciton mentioned before. Consequently, the maximal negative value of $CrSi_n^+$ and $TiSi_n^+$ clusters allows to determine the approximate energy of this core exciton to be in the order of $0.4\,eV$ in the analyzed cluster size regime, which is in the same order of magnitude as the respective energy of $0.9\,eV$ observed for pure silicon clusters [8].

The overall trend observed for $TiSi_n^+$ and $CrSi_n^+$ clusters in figure 9.6 is not
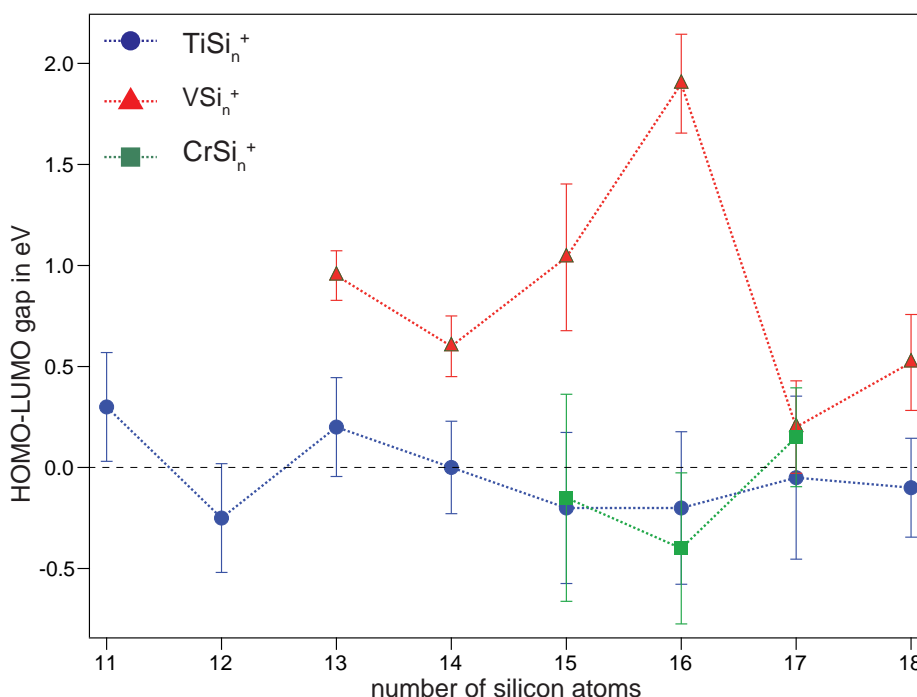
Figure 9.6: Experimentally determined values of the energetic distance between the HOMO and the LUMO of $TiSi_n^+$ (blue circle) and $CrSi_n^+$ (green square). Contrary to the trend observed for VSi_n^+ (red triangle), the overall values for $TiSi_n^+$ and $CrSi_n^+$ are located near $0\,eV$ due to the odd number of valence electrons in the system (see text). Negative values are due to the determination method used.

unexpected, as all of these clusters hold an odd number of valence electrons ($n \times 4e^- + 3e^-$ in case of $TiSi_n^+$ and $n \times 4e^- + 5e^-$ in case of $CrSi_n^+$, cf. fig. 6.2). Since all energy levels can be occupied by a pair of electrons with opposite spin, the odd number of valence electrons situation in the system does not allow each electron to have a partner for spin up spin down occupation of an energy level. Since energy levels holding an spin up and spin down electron are degenerate (Pauli principle), the HOMO and LUMO are degenerate. The direct photoionization threshold energy of valence electrons corresponds to the singly occupied

level. The same energy level can also be reached in resonant excitation at the silicon 2p orbital due to its free space for an additional electron.

In $TiSi_{16}^+$ and $CrSi_{16}^+$ it is possible to describe the states holding the odd number of electrons. Both clusters are Frank-Kaspar polyhedrons with a Jahn-Teller distortion, whose electronic structure is expected to be described by the spherical shell model [1]. Due to the interchange of the transition metal from vanadium to chromium and titanium, the valence occupation is one additional electron in $CrSi_{16}^+$ and one electron less in $TiSi_{16}^+$ in comparison to VSi_{16}^+. In case of $TiSi_{16}^+$, the 67 valence electrons result in a hole in the 2d state of the spherical shell model. Therefore 2d corresponds to the unoccupied state observed in resonant excitations and at the same time to the occupied state determined by direct photoionization of valence states. A similar explanation is present for $CrSi_{16}^+$, since its 69 valence electrons lead to a single electron occupation of the 1h state of the spherical shell model. Therefore, 1h shows as an occupied and unoccupied state in the experimental method used. However, if the spherical shell model for the MSi_{16} clusters in Frank-Kaspar geometry is applicable, the missing electron in the 2d state of $TiSi_{16}^+$ for a complete electronic state closure should be distinguishable from the unoccupied 1h state due to the high sensitivity of XAS on the electronic occupation of valence states. Furthermore, in VUV spectra of $CrSi_{16}^+$ the 1h state of the cluster occupied with a single electron should correspond to a lower intensity in the spectrum than the completely occupied 2d state. Both is observed and presented in the next section 9.3.

9.3 Level Spacing Between Valence Orbitals

In this section, the energetic distance of valence orbitals 2d and 1h of the spherical shell model [1, 57] shown in figure 9.2 is determined. The analysis is based on an observation of the partial ion yield spectrum (PIY) of $TiSi_{16}^+$ at the silicon $L_{3,2}$ edge and a PIY spectrum taken at the VUV energy range of ion $CrSi_{16}^+$. The respective ion yield spectra are shown in figures 9.7 and 9.8.

Level Spacing of 1h and 2d Valence Orbitals in $TiSi_{16}^+$

Due to the high similarity to VSi_{16}^+, the electronic structure of the valence density of states is assumed to be similar. Due to the $2d^9$ configuration, 2d contributes to the unoccupied density of states, which can be probed with x-ray absorption spectroscopy. Figure 9.7 shows the ion yield spectrum of $TiSi_{16}^+$ at the silicon $L_{3,2}$
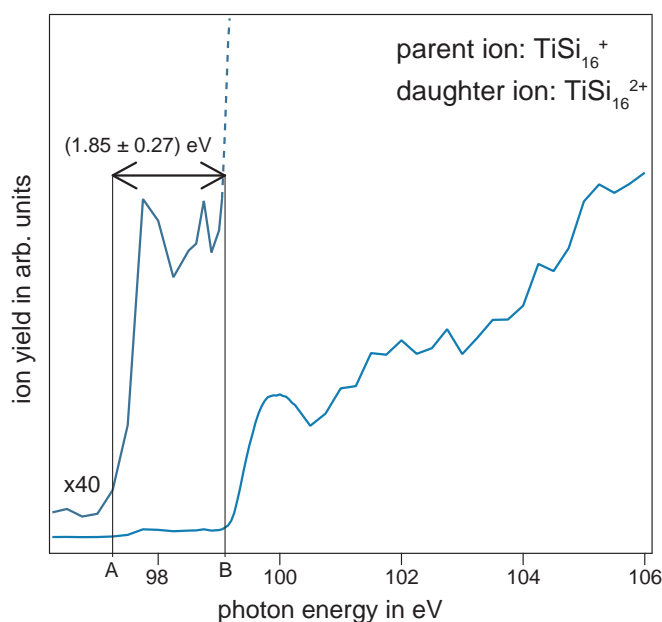
Figure 9.7: Relative position of unoccupied valence orbitals in the ion yield spectrum of $TiSi_{16}^+$. The energetic distance between the threshold energy (A) and (B) corresponds to the energetic level spacing between the 2d and 1h state of the cluster in the notation of the spherical shell model (cf. sect. 9.2 and see text).

edge. The threshold of the resonant absorption is seen in the magnification of the spectrum at the energy marked (A). It can be seen that the ion yield corresponding to the absorption after energy (A) is very low, indicating a corresponding low unoccupied density of states. At the energy marked (B), the resonant absorption increases drastically, which indicates more unoccupied valence states can be reached by the transition of 2p electron. The density of states shown in figure 9.2 and the suggested $2d^9 1h^0$ configuration of $TiSi_{16}^+$ leads to the assumption that threshold (A) corresponds to a resonant transition to the single unoccupied space in the cluster's 2d state. Threshold (B) corresponds consequently to transitions of silicon 2p electrons into the cluster's unoccupied 1h state. If the assumption is correct, the energetic distance of thresholds (A) and (B) in figure 9.7 corresponds to the energetic gap between the 1h and 2d state of the cluster (cf. fig 9.2). The energetic distance of the 2d to 1h state of the cluster is $(1.85 \pm 0.27)\,\text{eV}$ and therefore of the same order of magnitude as the corresponding HOMO-LUMO gap of VSi_{16}^+ of $1.90 \pm 0.24\,\text{eV}$.

Level Spacing of 2d and 1h Valence Orbitals in $CrSi_{16}^+$

$CrSi_{16}^+$ is like $TiSi_{16}^+$ a Frank-Kaspar polyhedron with a Jahn-Teller distortion [94]. Similar to $TiSi_{16}^+$, the valence states should be comparable to the valence struc-

ture found for the VSi_{16}^+ Frank-Kaspar polyhedron, which is also indicated by x-ray absorption studies at the transition metal $L_{3,2}$ edge (cf. sect. 6.3.1). Due to the $2d^{10}1h^1$ configuration a spectroscopic method analyzing the occupied density of states be sensitive on this single electron occupancy of the 1h state and the following completely occupied 2d state at higher binding energies. A similar experiment on $TiSi_{16}^-$ available in literature [83] is introduced before presenting own results. It has been shown for $TiSi_{16}^-$ that an estimate of the HOMO-LUMO gap of neutral $TiSi_{16}$ [51, 83] can be obtained by spectroscopy sensitive on the occupied valence density of states, as already introduced in section 2. $TiSi_{16}$ is shown to hold a very similar geometric structure as VSi_{16}^+ due to its same number of valence electrons [1]. In fact, the spherical shell model was introduced to explain the electronic structure of both cluster alike [1]. The general idea of estimating the HOMO-LUMO gap of $TiSi_{16}$ is using photoelectron spectroscopy on anionic $TiSi_{16}^-$, thus having an occupancy in the 1h state as well as in the 2d state of the cluster. It is presumed that the additional electron in the 1h state does not change the energetic distance of the 2d to 1h state [51,83] and can be described in a one electron picture due to the shell closure of energetically lower lying states. Therefore, the distance can be measured by identifying the 1h and 2d occupancy contribution in the photoelectron spectrum, whose distance corresponds to the HOMO-LUMO gap of the closed shell system $TiSi_{16}$ in the geometry of $TiSi_{16}^-$.

A similar case is present for $CrSi_{16}^+$, which is isoelectronic to $TiSi_{16}^-$. Due to the considerable higher photoionization potential of about $10\,eV$ of the cationic species compared to $3\text{-}4\,eV$ of the anionic species, photoelectron spectroscopy with laser photons is challenging. Using a FEL would solve the problem with respect to the ionization energy, but up to date only one photoelectron study at an FEL is performed on a system with a high absorption cross section in the respective energy regime [101]. Therefore it is unlikely that in the near future PES studies of free size selected MSi_n^+ clusters can be performed at the FEL. However, measurements of the direct photoionization by ion yield spectroscopy in the VUV regime yield comparable data to photoelectron spectroscopy studies, as shown in chapter 8. The results of this ion yield measurements are shown in figure 9.8. For comparison the results of photoelectron spectroscopy studies [51] on the isoelectronic $TiSi_{16}^+$ are shown in the inset of the figure. The partial ion yield of the doubly charged parent cluster $CrSi_{16}^{2+}$ is proportional to the direct photoionization efficiency $h\nu + CrSi_{16}^+ \rightarrow CrSi_{16}^{2+} + e^-$. The photoionization efficiency curve shows clearly a threshold (A) at a photon energy $9.5\,eV$ and after a low intensity plateau a steep rise of the ion yield signal (B) at a photon energy
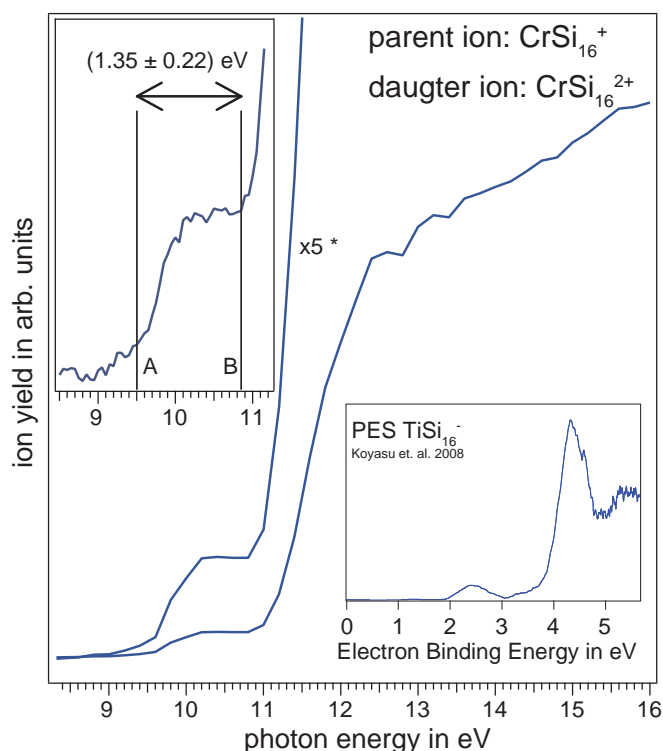
Figure 9.8: Relative position of occupied valence orbitals $2d^{10}$ and $1h^1$ visible in the direct photoionization efficiency curve of $CrSi_{16}^+$. The contribution of the electron in the 1h state of the cluster can be seen as a pre-edge in the photoionization efficiency curve. The top left inset shows a second measurement with a finer energy step size. The energetic distance between (A) and (B) corresponds to the energy gap between the clusters 2d and 1h state (notation of the spherical shell model [1]). For comparison, similar results obtained by PES on the isoelectronic $TiSi_{16}^+$ are shown in the second inset [51,83].

of about $10.9\,\mathrm{eV}$. Comparison with the suggested valence density of states of this cluster (cf. fig. 9.2) leads to the assumption that the threshold (A) corresponds to the photoionization of the $1h^1$ state. The next state at a higher binding energy available for direct photoionization is the completely occupied 2d state, which consequently corresponds to the steep rise in the photoionization efficiency curve (B). Therefore the energetic distance between (A) and (B) corresponds to the energetic gap between the 1h and 2d states (cf. fig. 9.2) of the cluster. The energetic gap is found to be $(1.35 \pm 0.22)\,\mathrm{eV}$, which is less than the equivalent values of VSi_{16}^+ and $TiSi_{16}^+$ but still in the same order of magnitude.

Comparison of 2d-1h Level Spacing in Closed Electronic Shell VSi_{16}^+ and Open Shell $TiSi_{16}^+/CrSi_{16}^+$

The results on the energetic gap between the 2d and 1h (notation of the states cf. fig. 9.2 [1]) in valence states obtained as explained in section 9.2 for VSi_{16}^+
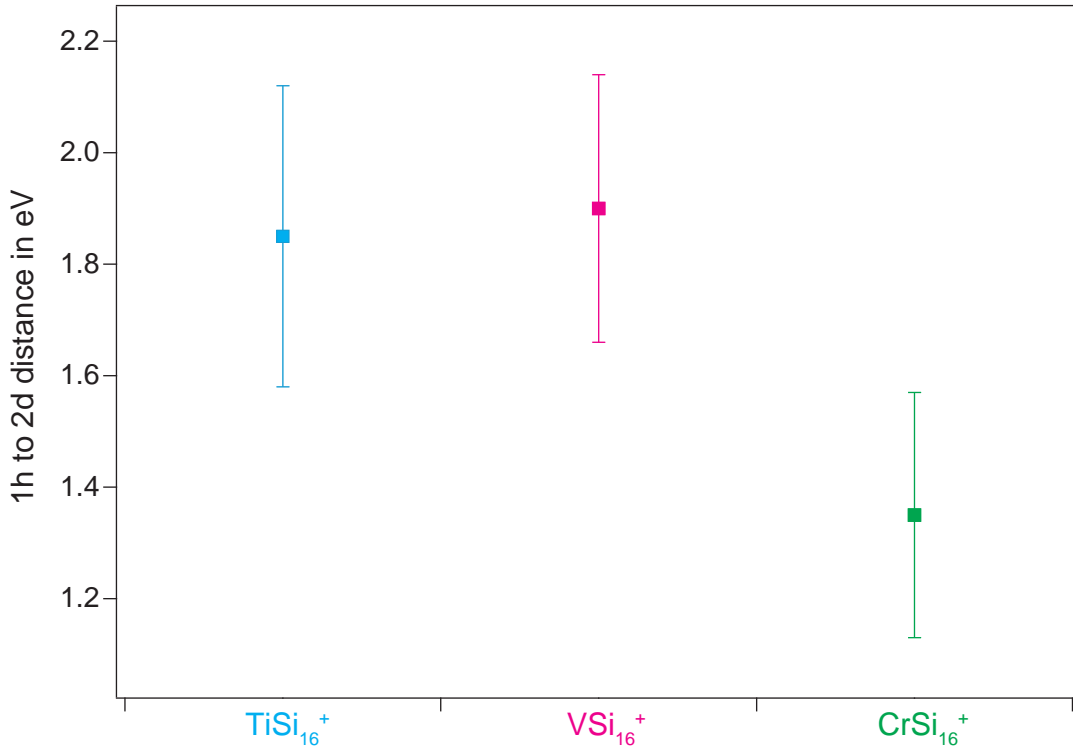
Figure 9.9: Comparison 2d and 1h level spacing of $TiSi_{16}^+$, VSi_{16}^+, and $CrSi_{16}^+$. The level spacing of 2d and 1h is obtained through three different methods due to the differing electronic configuration (see text).It can be seen that the largest energetic gap between the 2d and 1h state shows for the highly symmetric Frank-Kaspar polyhedron VSi_{16}^+, whereas the distances of the respective states are reduced for $TiSi_{16}^+$ and $CrSi_{16}^+$ which have the geometry of a Frank-Kaspar polyhedron with a Jahn-Teller distortion.

and section 9.3 for $TiSi_{16}^+$ and $CrSi_{16}^+$ are compared in figure 9.9. In case of VSi_{16}^+ the energetic gap between the 2d and 1h state of the cluster corresponds to the HOMO-LUMO gap of this cluster size. Due to the different dopant atoms and their electronic configuration (cf. fig. 6.2 and the resulting differing electronic configuration of the clusters valence states, the geometry of an ideal Frank-Kaspar polyhedron [48] is only realized for VSi_{16}^+. $TiSi_{16}^+$ and $CrSi_{16}^+$ show a Frank-Kaspar polyhedron with a Jahn-Teller distortion [94]. The calulated geometries of these clusters are shown in figure 6.10. These differences between the three MSi_{16}^+ clusters result in a different degree of degeneration of the valence states. As is expected due to its highly symmetric structure and electronic shell closure, the largest 2d to 1h gap of $(1.90 \pm 0.24)\,\text{eV}$ is realized for VSi_{16}^+. A similar value is realized for $TiSi_{16}^+$. The level spacing between the 2d and 1h state of this cluster is about $(1.85 \pm 0.27)\,\text{eV}$, which suggests a similar high degeneracy of states as is achieved in VSi_{16}^+. Lower degeneracies would inevitably lead to a wider energetic spread of the valence states, which should lead to a diminished energetic distance

149

between the 2d and 1h state. Theoretical results showed [32] that $TiSi_{16}^+$ has smaller Jahn-Teller distortion than $CrSi_{16}^+$, which might explain this result. In case of heavier Jahn-Teller distorted $CrSi_{16}^+$ [32], the energetic distance between the 2d and 1h state is reduced due to a expected lower degeneracy of states resulting in a wider energetic spread of the 1h and 2d state. This is corroborated by the experimentally obtained energetic distance, which shows a much lower 2d to 1h energy gap of about $(1.35 \pm 0.22)\,eV$ for $CrSi_{16}^+$ than for $TiSi_{16}^+$ or VSi_{16}^+.

Conclusion

The HOMO-LUMO gaps of vanadium doped silicon clusters presented in this chapter showed a good agreement with theoretical calculations [1] as can be seen in figure 9.3. The new method of obtaining the HOMO-LUMO gap by a Born-Haber cycle of resonant transition and direct photoionization energies obtained by ion yield spectroscopy in the x-ray and the VUV energy regime yields satisfying results. The HOMO-LUMO gap of VSi_{16}^+ [1, 31, 32] is found to be $(1.90 \pm 0.24)\,eV$, which is a high value compared to the other cluster sizes of VSi_n^+. It is realized due to the highly symmetric structure and electronic shell closure of VSi_{16}^+ and can be explained according to the spherical shell model introduced in section 2. The cluster size dependence of the HOMO-LUMO gap of VSi_n^+ clusters predicted by theory [1] is also found to be in good agreement with experimental data. This shows that the spherical shell model approach is suited to describe the electronic properties of this particular doped silicon cluster species with a closed electronic shell. Furthermore, it is shown that the spherical shell model can also be applied to open electronic shell MSi_{16}^+ clusters having a Jahn-Teller distorted Frank-Kaspar polyhedral geometry. Figure 9.9 shows the energetic level spacing corresponding to the HOMO-LUMO gap in VSi_{16}^+ as a function of the transition metal dopant. The comparison of the energy gap between valence orbitals of MSi_{16}^+ (M=Ti,V,Cr) is only achieved by the interplay of partial ion yield spectroscopy in the VUV regime and the soft x-ray regime, probing the unoccupied density of states and the occupied density of states respectively. It is suggested that the level spacing of the valence states monitored can be seen as a measure for the degeneracy of states in the respective cluster. In conclusion, it is shown that by the interplay of different measuring techniques new insights on the electronic valence structure of transition metal doped silicon cluster are gained.

Chapter 10

Conclusion

In this thesis the interaction between a silicon cluster and a transition metal dopant is analyzed. The result of this interaction is a complete change of the silicon clusters electronic and geometric structure. It is shown that the electronic configuration of the transition metal atom has a strong influence on the shape of the silicon cage, whereas the silicon cage determines the local electronic configuration at the encapsulated transition metal atom.

The method used is ion yield spectroscopy of product ions generated upon x-ray absorption at the silicon $L_{3,2}$ (chap. 7), the transition metal $L_{3,2}$ (chap. 6) as well as upon VUV spectroscopy at the clusters valence states (chap. 8).
It is shown that this method allows the separate analysis of the resonant silicon 2p excitation and direct silicon 2p photoionization. This way the silicon 2p binding energy and information on the unoccupied density of states at the silicon cage are obtained by only one measurement at the silicon $L_{3,2}$ edge. In addition, valence electron binding energies, previously only known for anionic systems [83] are now determined for cationic transition metal doped silicon clusters, using ion yield spectroscopy in the VUV energy range.
Furthermore, a novel analysis method is introduced to determine the position of occupied and unoccupied valence levels. This method is based on the combination of results obtained at the silicon 2p and valence state absorption edges (chap. 9).

Results obtained by x-ray spectroscopy at the transition metal $L_{3,2}$ edge on VSi_{16}^+ corroborate theoretical predictions [1, 2, 43] on the high symmetry of the silicon shell. A high degree of degeneracy in the local unoccupied density of states at the vanadium atom is observed. In a theoretical approach the high degeneracy is explained in terms of a spherical shell model in tetrahedral symmetry formed

by the empty cage structure [1]. A shell closure present for VSi_{16}^+ leads to the high symmetry of the structure, which is shaped like an ideal Frank-Kaspar polyhedron [2,48]. In case of differing electronic configurations of ± 1 electron as present $CrSi_{16}^+$ and $TiSi_{16}^+$, the calculated structure shows a Jahn-Teller distortion [32,94]. However, $CrSi_{16}^+$ and $TiSi_{16}^+$ show a local electronic structure at the transition metal atom very similar to VSi_{16}^+. Comparison with the local unoccupied density of states probed by x-ray spectroscopy at the silicon $L_{3,2}$ edge also indicates a high degeneracy of states in case of VSi_{16}^+. In contrast to this, the local electronic structure at the Jahn-Teller distorted silicon cages of $TiSi_{16}^+$ and $CrSi_{16}^+$ show spectral signatures of differed degeneracy. Deviation from electronic shell closure seems to affect the silicon cage more strongly than the transition metal dopant.

Information of the position of valence states of MSi_n^+ clusters and the HOMO-LUMO gap is obtained using a novel analysis method mentioned above. The resulting cluster size dependent HOMO-LUMO gap development of VSi_n^+ is in good agreement with theoretical calculations, with an enhanced HOMO-LUMO gap of $(1.90 \pm 0.24)\,eV$ in case of the highly symmetric VSi_{16}^+. The HOMO and the LUMO correspond to states described in the spherical potential model [1]. Corresponding states of $TiSi_{16}^+$ show in signatures in the spectra of the resonant silicon 2p excitation, which probes the unoccupied density of states. The level spacing between the states corresponding to the HOMO and LUMO in VSi_{16}^+ is $(1.85 \pm 0.27)\,eV$. In case of $CrSi_{16}^+$ the corresponding level spacing extracted from signatures in the valence electron photoionization efficiency curve is $(1.35 \pm 0.22)\,eV$. This indicates that the overall electronic valence structure is similar in all three MSi_{16}^+ (M=Ti,V,Cr) clusters. The lower value of $CrSi_{16}^+$ is due to a strong Jahn-Teller distortion resulting in a lower degeneracy of states in comparison to only a slight Jahn-Teller distortion found in the geometry of the cage of $TiSi_{16}^+$ [32].

It is also found that delocalization of valence electrons is enhanced in endohedral transition metal doped silicion clusters regardless of cage symmetry in comparison to exohedral cluster sizes. Upon the exohedral to endohedral transition of a transition metal doped silicon cluster species, the mean weight of partial ion yield spectra taken at the transition metal $L_{3,2}$ edge shifts to higher excitation energies for endohedral clusters. This indicates an abrupt change in the delocalization of valence electrons at this cluster size. This is a result of a lower screening of the metal's core potential due to the higher delocalization of electrons in the initial state leading to a higher excitation energy of resonant

transitions. In addition, the valence density of states rehybridizes upon a total encapsulation of the metal atom, which is represented in a complete change of the spectral fingerprint of partial ion yield spectra. With this result, a second criterion for endohedrality of a transition metal doped silicon cluster is introduced, in addition to the already established method of monitoring the reactivity [34,39].

A further observation of the delocalization of valence electrons is given by analysis of silicon 2p binding energies, extracted from the direct silicon 2p photoionization efficiency curve. It is shown that in the endohedral size regime of MSi_n^+ (M=Ti,V,Cr) clusters, the highest degree of delocalization is reached for the cage with $n = 16$ silicon atoms. Again, this indicates a high symmetry of this structure. In addition, different coordination of silicon atoms in the cage depending on the geometric structure show differing chemical shifts in their respective silicon 2p binding energy. The distribution of 2p binding energies of all silicon atoms in the cage determines the shape of the direct silicon 2p photoionization photoionization efficiency curve. Comparison with quantum chemical calculations on the respective cluster size indirectly yield the information if a calculated geometry of an isomer might correspond to the geometry of the isomer abundant in the experiment.

In summary, element specific spectroscopic studies in the x-ray regime allowed a detailed insight into the electronic and geometric structure of transition metal doped silicon clusters.

Bibliography

[1] M. B. Torres, E. M. Fernandez, and L. C. Balbas. Theoretical Study of Isoelectronic Si_nM Clusters ($M=Sc^-,Ti,V^+$; n=14-18). *Physical Review B*, 75(20):205425, 2007.

[2] V. Kumar and Y. Kawazoe. Metal-Encapsulated Fullerenelike and Cubic Caged Clusters of Silicon. *Physical Rewiew Letters*, 87(4):045503, 2001.

[3] K. Jackson, E. Kaxiras, and M. R. Pederson. Bonding of Endohedral Atoms in Small Carbon Fullerenes. *The Journal of Physical Chemistry*, 98(32):7805, 1994.

[4] S. M. Beck. Studies of Silicon Cluster Metal Atom Compound Formation in a Supersonic Molecular-Beam. *Journal Of Chemical Physics*, 87(7):4233, 1987.

[5] S. M. Beck. Mixed Metal-Silicon Clusters Formed by Chemical-Reaction in a Supersonic Molecular-Beamimplications for Reactions at the Metal Silicon Interface. *Journal Of Chemical Physics*, 90(11):6306, 1989.

[6] V. Kumar. Alchemy at the Nanoscale: Magic Heteroatom Clusters and Assemblies. *Computational Materials Science*, 36(1-2):1, 2006.

[7] A. Einstein. Über einen die Erzeugung und Verwandlung des Lichtes betreffenden heuristischen Gesichtspunkt. *Annalen der Physik*, 322(6):132, 1905.

[8] M. Vogel. *Röntgenspektroskopie an freien größenselektierten Siliziumclustern, dotierten Siliziumclustern und Aluminiumclustern.* Thesis, 2010.

[9] J. J. Yeh and I. Lindau. Atomic Subshell Photoionization Cross Sections and Asymmetry Parameters: $1 \le Z \, leq \, 103$. *Atomic Data and Nuclear Data Tables*, 32(1):1, 1985.

[10] C. Cohen-Tannoudji. *Quantenmechanik*, volume 2. de Gruyter, Berlin - New York, 1999.

[11] M. Martins, K. Godehusen, T. Richter, I. Wolff, and P. Zimmermann. 2p Photoelectron Spectroscopy of the Late 3d Transition Metal Atoms. *Journal of Electron Spectroscopy and Related Phenomena*, 137(Sp. Iss. SI):345, 2004.

[12] J. T. Lau, J. Rittmann, V. Zamudio-Bayer, M. Vogel, K. Hirsch, P. Klar, F. Lofink, T. Moller, and B. von Issendorff. Size Dependence of L-2,L-3 Branching Ratio and 2p Core-Hole Screening in X-Ray Absorption of Metal Clusters. *Physical Review Letters*, 101(15):153401, 2008.

[13] B. T.. Thole and G. van der Laan. Branching Ratio in X-ray Absorption-Spectroscopy. *Physical Review B*, 38(5):3158, 1988.

[14] D. H. Pearson, C. C. Ahn, and B Fultz. White Lines and d-Electron Occupancies for the 3d and 4d Transition-Metals. *Physical Review B*, 47(14):8471, 1993.

[15] M. O. Krause. Atomic Radiative and Radiationless Yields for K-Shells and L-Shells. *Journal Of Physical And Chemical Reference Data*, 8(2):307, 1979.

[16] W. Raith, editor. *Lehrbuch der Experimentalphysik / Bergmann ; Schaefer*, volume 4. de Gruyter, Berlin - New York, 1992.

[17] TURBOMOLE, a development of University of Karlsruhe and Forschungszentrum Karlsruhe GmbH, 1989-2007, TURBOMOLE GmbH, since 2007; available from
`http://www.turbomole.com`.

[18] D. S. Sholl. *Density Functional Theory: A Practical Introduction*, volume 4. John Wiley & Sons, Inc., 2009.

[19] P. Hohenberg and W. Kohn. Inhomogeneous Electron Gas. *Physical Review B*, 136(3B):B864, 1964.

[20] W. Kohn and L. J. Sham. Self-consistent Equations Including Exchange and Correlation Effects. *Physical Review*, 140(4A):1133, 1965.

[21] R. D. Cowan. *The Theory of Atomic Structure and Spectra*. University of California Press, 1981.

[22] F. M. F. deGroot. Multiplet Effects in X-ray Spectroscopy. *Coordination Chemistry Reviews*, 249(1-2):31, 2005.

[23] H. Kroto, J. Heath, S. Obrien, R. Curl, and R. Smalley. C-60 - Buckminsterfullerene. *Nature*, 318(6042):162, 1985.

[24] Z. G. Fthenakis, R. W. A. Havenith, M. Menon, and P. W. Fowler. Structural and Electronic Properties of the Fullerene Isomers of Si-38: A Systematic Theoretical Study. *Physical Review B*, 75(15):155435, 2007.

[25] M. Menon and K. R. Subbaswamy. Structure of Si60 - Cage versus Network Structures. *Chemical Physics Letters*, 219(3-4):219, 1994.

[26] V. T. Ngan, P. Gruene, P. Claes, E. Janssens, A. Fielicke, M. T. Nguyen, and P. Lievens. Disparate Effects of Cu and V on Structures of Exohedral Transition Metal-Doped Silicon Clusters: A Combined Far-Infrared Spectroscopic and Computational Study. *Journal of the American Chemical Society*, 132(44):15589, 2010.

[27] U. Röthlisberger, W. Andreoni, and M. Parrinello. Structure of Nanoscale Silicon Clusters. *Physical Review Letters*, 72(5):665, 1994.

[28] D. Bandyopadhyay. The Study of the Electronic Structures and Properties of Pure and Transition Metal-Doped Silicon Nanoclusters: A Density Functional Theory Approach. *Molecular Simulation*, 35(5):381, 2009.

[29] L. Guo, G. Zhao, Y. Gu, X. Liu, and Z. Zeng. Density-Functional Investigation of Metal-Silicon Cage Clusters MSin (M = Sc, Ti, V, Cr, Mn, Fe, Co, Ni, Cu, Zn; n=8-16). *Physical Review B*, 77(19):195417, 2008.

[30] C. L. Reis and J. M. Pacheco. Bulk Materials Made of Silicon Cage Clusters Doped with Ti, Zr, or Hf. *Journal Of Physics - Condensed Matter*, 22(3):035501, 2010.

[31] J. U. Reveles and S. N. Khanna. Electronic Counting Rules for the Stability of Metal-Silicon Clusters. *Physical Review B*, 74(3):035435, 2006.

[32] M. Gramzow and K. Reuter. Calculations on metal doped semiconductor clusters. Internal report.

[33] M. Ohara, K. Koyasu, A. Nakajima, and K. Kaya. Geometric and Electronic Structures of Metal (M)-Doped Silicon Clusters (M = Ti, Hf, Mo and W). *Chemical Physics Letters*, 371(3-4):490, 2003.

[34] H. Hiura, T. Miyazaki, and T. Kanayama. Formation of Metal-Encapsulating Si Cage Clusters. *Physical Review Letters*, 86(9):1733, 2001.

[35] K. Koyasu, M. Akutsu, M. Mitsui, and A. Nakajima. Selective Formation of MSi16 (M = Sc, Ti, and V). *Journal Of The American Chemical Society*, 127(14):4998, 2005.

[36] J. B. Jaeger, T. D. Jaeger, and M. A. Duncan. Photodissociation of Metal-Silicon Clusters: Encapsulated Versus Surface-Bound Metal. *Journal Of Physical Chemistry A*, 110(30):9310, 2006.

[37] W. Zheng, J. M. Nilles, D. Radisic, and K. H. Bowen. Photoelectron Spectroscopy of Chromium-Doped Silicon Cluster Anions. *Journal Of Chemical Physics*, 122(7):071101, 2005.

[38] P. Gruene, A. Fielicke, G. Meijer, E. Janssens, V.T. Ngan, M.T. Nguyen, and P. Lievens. Tuning the Geometric Structure by Doping Silicon Clusters. *ChemPhysChem*, 9(5):703, 2008.

[39] E. Janssens, P. Gruene, G. Meijer, L. Wöste, P. Lievens, and A. Fielicke. Argon Physisorption as Structural Probe for Endohedrally Doped Silicon Clusters. *Physical Review Letters*, 99(6):063401, 2007.

[40] C. L. Reis, J. L. Martins, and J. M. Pacheco. Stability Analysis of a Bulk Material Built from Silicon Cage Clusters: A First-Principles Approach. *Physical Review B*, 76(23):233406, 2007.

[41] M. W. Radny and Y. Kawazoe. Structure and Stability of the Frank-Kasper W@Si-12, and Ti@Si-15 and Ti@Si-16 Clusters. *Materials Transactions*, 48(4):745, 2007.

[42] J. U. Reveles and S. N. Khanna. Nearly-Free-Electron Gas in a Silicon Cage. *Physical Review B*, 72(16):165413, 2005.

[43] H. Kawamura, V. Kumar, and Y. Kawazoe. Growth Behavior of Metal-Doped Silicon Clusters Si_nM (M = Ti, Zr, Hf; n=8-16). *Physical Review B*, 71(7):075423, 2005.

[44] J. He, K. Wu, C. Liu, and R. Sa. Stabilities of 3d Transition-Metal Doped Si-14 Clusters. *Chemical Physics Letters*, 483(1-3):30, 2009.

[45] J. Han and F. Hagelberg. Recent Progress in the Computational Study of Silicon and Germanium Clusters with Transition Metal Impurities. *Journal Of Computational And Theoretical Nanoscience*, 6(2, Sp. Iss. SI):257, 2009.

[46] M. B. Torres and L. C. Balbas. Relative Stability of Si_n and Si_nSc^- Clusters in the Range n=14-18. *European Physical Journal D*, 43(1-3):217, 2007.

[47] N. Uchida, T. Miyazaki, and T. Kanayama. Stabilization Mechanism of Si_{12} Cage Clusters by Encapsulation of a Transition-Metal Atom: A Density-Functional Theory Study. *Physical Review B*, 74(20):205427, 2006.

[48] F. Frank and J. Kasper. Complex Alloy Structures Regarded as Sphere Packings. 1. Definitions and Basic Principles. *Acta Crystallographica*, 11(3):184, 1958.

[49] K. Koyasu, J. Atobe, M. Akutsu, M. Mitsui, and A. Nakajima. Electronic and Geometric Stabilities of Clusters with Transition Metal Encapsulated by Silicon. *Journal Of Physical Chemistry A*, 111(1):42, 2007.

[50] M. B. Knickelbein and W. J. C. Menezes. Metal Cluster Rare-Gas Van-der-Waals Complexes - Physisorption On A Microscopic Scale. *Journal of Physical Chemistry*, 96(16):6611, 1992.

[51] K. Koyasu, J. Atobe, S. Furuse, and A. Nakajima. Anion Photoelectron Spectroscopy of Transition Metal- and Lanthanide Metal-Silicon Clusters: MSi_n^- (n=6-20). *Journal Of Chemical Physics*, 129(21):214301, 2008.

[52] A. D. Zdetsis, E. N. Koukaras, and C. S. Garoufalis. A Parallel Study of Ni@Si-12 and Cu@Si-12 Nanoclusters. *Journal of Mathematical Chemistry*, 46(3, Sp. Iss. SI):971, 2009.

[53] H. Xu, Z. Zhang, Y. Feng, J. Yuan, Y. Zhao, and W. Zheng. Vanadium-Doped Small Silicon Clusters: Photoelectron Spectroscopy and Density-Functional Calculations. *Chemical Physics Letters*, 487(4-6):204, 2010.

[54] W. D. Knight, K. Clemenger, W. A. deheer, W. A. Saunders, M. Y. Chou, and M. L. Cohen. Electronic Shell Structure and Abundances of Sodium Clusters. *Physical Review Letters*, 52(24):2141, 1984.

[55] W. A. deHeer. The Physics Of Simple Metal-Clustersexperimental Aspects And Simple-Models. *Reviews of Modern Physics*, 65(3):611, 1993.

[56] K. Jackson and B. Nellermoe. Zr@Si20: A Strongly Bound Si Endohedral System. *Chemical Physics Letters*, 254(3-4):249, 1996.

[57] D. Palagin, M. Gramzow, and K. Reuter. On the stability of "'non-magic"' endohedrally doped Si clusters: A first-principles sampling study of MSi_{16}^+ (M =Ti,V,Cr). *submitted*, 2011.

[58] J. T. Lau, K. Hirsch, Ph. Klar, A. Langenberg, F. Lofink, R. Richter, J. Rittmann, M. Vogel, V. Zamudio-Bayer, T. Moeller, and B. von Issendorff. X-ray Spectroscopy Reveals High Symmetry and Electronic Shell Structure of Transition-Metal-Doped Silicon Clusters. *Physical Review A*, 79(5):053201, 2009.

[59] C. L. Reis and J. M. Pacheco. Vibrational Spectra of Silicon Cage Clusters Doped with Ti, Zr, or Hf. *Physical Review B*, 82(15):155440, 2010.

[60] N. Uchida, H. Kintou, Y. Matsushita, T. Tada, and T. Kanayama. Synthesis of New Amorphous Semiconductors Assembled from Transition-Metal-Encapsulating Si Clusters. *Applied Physics Express*, 1(12):121502, 2008.

[61] M. B. Torres, E. M. Fernandez, and L. C. Balbas. Study of the Structural and Electronic Properties of $[Ti@Si_{16}]_n$, $[Sc@Si_{16}K]_n$, and $[V@Si_{16}F]_n$ (n <= 9) Aggregates from First Principles. *Journal of Physical Chemistry C*, 115(2):335, 2011.

[62] B. von Issendorff. Universität Freiburg.

[63] H. Haberland, editor. *Clusters of Atoms and Molecules (Springer Series in Chemical Physics)*, volume 52. Springer Verlag, Berlin - Heidelberg, 1994.

[64] H. Adam, W. Walcher, and M. Wutz. *Handbuch der Vakuumtechnik*. Vieweg, 6. ed. edition, 1997.

[65] W. Paul and M. Raether. Das Elektrische Massenfilter. *Zeitschrift für Physik A*, 140:262, 1955.

[66] F. W. J. Olver, D. W. Lozier, R. F. Boisvert, C. W. National Institute of Standards Clark, Maryland Technology, and University of Maryland, editors. *NIST Handbook of Mathematical Functions*. Cambridge University Press, 2010.

[67] K. Hirsch. *Röntgenabsorptionsspektroskopie an freien, massenselektierten Metallclustern.* Diploma thesis, 2008.

[68] K. Hirsch, J.T. Lau, Ph. Klar, A. Langenberg, J. Probst, J. Rittmann, M. Vogel, V. Zamudio-Bayer, T. Moller, and B. von Issendorff. X-ray Spectroscopy on Size-Selected Clusters in an Ion Trap: From the Molecular Limit to Bulk Properties. *Journal of Physics B: Atomic, Molecular and Optical Physics*, 42(15):154029, 2009.

[69] W. C. Wiley and I. H. McLaren. Time-Of-Flight Mass Spectrometer With Improved Resolution. *Review of Scientific Instruments*, 26(12):1150, 1955.

[70] J. Rittmann. *Elektronische Struktur von 3d-Übergangsmetallclustern.* Diploma thesis, 2007.

[71] J. Rittmann, K. Hirsch, M. Vogel, V. Zamudio-Bayer, T. Möller, B. von Issendorff, and J. T. Lau. Size Dependence in XAS Spectra of Neutral Transition Metal Clusters (V, and Co) in the Gas Phase. *in preparation*, 2011.

[72] B.A. Mamyrin. Time-Of-Slide Mass-Spectrometry and its Applications. *Vestnik Akademii Nauk SSSR*, (8):19, 1979.

[73] B.A. Mamyrin. Time-Of-Flight Mass Spectrometry (Concepts, Achievements, and Prospects). *International Journal Of Mass Spectrometry*, 206(3):251, 2001.

[74] A. Uphoff and J. Grotemeyer. The Secrets of Time-Of-Flight Mass Spectrometry Revealed. *European Journal of Mass Spectrometry*, 9(3):151–164, 2003.

[75] SimIon - Scientific Instrument Services, Inc., USA
`http://simion.com`.

[76] F. Elder, A. Gurewitsch, R. Langmuir, and H. Pollock. Radiation from Electrons in a Synchrotron. *Physical Review*, 71(11):829, 1947.

[77] J.D. Jackson. *Classical Electrodynamics.* New York, Wiley, 1975.

[78] J. Schwinger. On the Classical Radiation of Accelerated Electrons. *Physical Review*, 75(12):1912, 1949.

[79] J. Falta and T. Möller, editors. *Forschung mit Synchrotronstrahlung.* Vieweg+Teubner Verlag, 2010.

[80] A. L. Rockwood and Perttu H. Efficient Calculation of Accurate Masses of Isotopic Peaks. *Journal of the American Society for Mass Spectrometry*, 17(3):415, 2006.

[81] F. Lofink and J. Probst. Front End for Isotopic Pattern Calculator [80], 2009.

[82] J. Probst. *Elektronische Struktur von protonierten Wasserclustern.* Diploma thesis, 2010.

[83] S. Furuse, K. Koyasu, J. Atobe, and A. Nakajima. Experimental and theoretical characterization of MSi16-, MGe16-, MSn16-, and MPb16- (M = Ti, Zr, and Hf): The role of cage aromaticity. *Journal of Chemical Physics*, 129(6):064311, 2008.

[84] J. C. Slater. Atomic Radii in Crystals. *The Journal of Chemical Physics*, 41(10):3199, 1964.

[85] E. Clementi, D. L. Raimondi, and Reinhard W. P. Atomic Screening Constants from Scf Functions. II. Atoms With 37 To 86 Electrons. *Journal Of Chemical Physics*, 47(4):1300, 1967.

[86] Beatriz Cordero, Veronica Gomez, Ana E. Platero-Prats, Marc Reves, Jorge Echeverria, Eduard Cremades, Flavia Barragan, and Santiago Alvarez. Covalent radii revisited. *Dalton Trans.*, 21(21):2832, 2008.

[87] J. A. Bearden and A. F. Burr. Reevaluation of X-ray Atomic Energy Levels. *Reviews Of Modern Physics*, 39(1):125, 1967.

[88] M. Cardona and L. Ley, editors. *Photoemission in Solids I.* Springer-Verlag, 1978.

[89] J. C. Fuggle and N. Martensson. Core-Level Binding-Energies in Metals. *Journal Of Electron Spectroscopy And Related Phenomena*, 21(3):275, 1980.

[90] H. Kawamura, V. Kumar, and Y. Kawazoe. Growth, Magic Behavior, and Electronic and Vibrational Properties of Cr-Doped Si Clusters. *Physical Review B*, 70(24):245433, 2004.

[91] J. T. Lau, M. Vogel, A. Langenberg, K. Hirsch, J. Rittmann, V. Zamudio-Bayer, T. Moller, and B. von Issendorff. Communication: Highest Occupied Molecular Orbital-Lowest Unoccupied Molecular Orbital Gaps of Doped Silicon Clusters from Core Level Spectroscopy. *The Journal of Chemical Physics*, 134(4):041102, 2011.

[92] F. M. F. deGroot. X-ray Absorption and Dichroism of Transition Metals and their Compounds. *Journal of Electron Spectroscopy and Related Phenomena*, 67(4):529, 1994.

[93] F. M. F. deGroot. Utrecht University. personal communication.

[94] H. A. Jahn and E. Teller. Stability of Polyatomic Molecules in Degenerate Electronic States. I. Orbital Degeneracy. *Proceedings of the Royal Society of London. Series A, Mathematical and Physical Sciences*, 161:220, 1937.

[95] M. Vogel, T. Lau, and et al. unpublished.

[96] A. Schafer, C. Huber, and R. Ahlrichs. Fully optimized contracted Gaussian basis sets of triple zeta valence quality for atoms Li to Kr. *The Journal of Chemical Physics*, 100(8):5829, 1994.

[97] C. J.. Karlsson, F. Owman, E. Landemark, Y. C.. Chao, P. Martensson, and R. Uhrberg. Si 2p Core-Level Spectroscopy of the Si(111)-(1 X 1)-H and Si(111)-(1 X 1)-D Surfaces - Vibrational Effects and Phonon Broadening. *Physical Review Letters*, 72(26):4145, 1994.

[98] G. Le Lay, M. Göthelid, T. M. Grehk, M. Björkquist, U. O. Karlsson, and V. Yu. Aristov. Surface Core-Level Shifts of Si(111)7x7: A Fundamental Reassessment. *Physical Review B*, 50(19):14277, 1994.

[99] H. Haberland, B. von Issendorff, Y.F. Ji, and T. Kolar. Transition to Plasmon-like Absorption in Small Hg Clusters. *Physical Review Letters*, 69(22):3212, 1992.

[100] A. Terasaki, T. Majima, C. Kasai, and T. Kondow. Photon-trap spectroscopy of size-selected free cluster ions: "direct" measurement of optical absorption of Ag-9(+). *European Physical Journal D*, 52(1-3):43, 2009.

[101] V. Senz, T. Fischer, P. Oelssner, J. Tiggesbaeumker, J. Stanzel, C. Bostedt, H. Thomas, M. Schoeffler, L. Foucar, M. Martins, J. Neville, M. Neeb, Th.

Moeller, W. Wurth, E. Ruehl, R. Doerner, H. Schmidt-Boecking, W. Eberhardt, G. Gantefoer, R. Treusch, P. Radcliffe, and K. H. Meiwes-Broer. Core-Hole Screening as a Probe for a Metal-to-Nonmetal Transition in Lead Clusters. *Physical Review Letters*, 102(13):138303, 2009.

Appendix A

Supplementary Information

In this chapter of the appendix results of ion yield spectroscopy at the transition metal edge of ScSi_n^+ clusters and the valence states of MSi_n^+ (M=Ti,V,Cr) clusters are shown, which are currently not completely understood. It is discussed if and how they might be explainable in the future.

A.1 Energy Dependent PIY of ScSi_n^+ at the Metal $\text{L}_{3,2}$ Edge

In chapter 6 it is shown that partial ion yields taken at the transition metal $\text{L}_{3,2}$ edge of MSi_n^+ clusters have an equal photo energy dependence, in contrast to energy dependent generation of photo ions in silicon $\text{L}_{3,2}$ edge absorption. This is understood, since the energy deposited in the cluster in x-ray absorption at the metal edge is a few $100\,\text{eV}$ higher than for absorption at the silicon edge. This leads to a fragmentation of all possible excitation channels towards only two or three small fragment ions, which are usually the metal atom M, Si_2^+ and MSi^+. However, in one case non-similar partial ion yield (PIY) spectra are observed, corresponding to different fragment ions. In the fragmentation pattern of ScSi_{16-19}^+, $\text{ScSi}_x\text{O}_y^+$ (x=0-2, y=1,2) fragments appear in addition to the expected ScSi_x^+ (x=0-2) fragments in the mass spectra, as is shown by the detail view of the fragmentation pattern of ScSi_{19}^+ in figure A.1. Partial ion yield spectra of oxidized fragments and pure fragments reveal different spectral fingerprints shown in figure A.3. The PIY of oxidized daughter ions (dashed line) show sharp lines at about $1.3\,\text{eV}$ to $1.8\,\text{eV}$ higher excitation energies than non-oxidized daughter ions.

An oxygen contamination of the endohedral parent cluster ScSi_n^+ (n=16-19)

was not observed, as shown in figure A.2. Pure silicon clusters visible in the mass selection do not disturb the measurement, since for excitation energies at the Sc $L_{3,2}$ edge they do not show distinct features in potentially abundant photo fragments. In addition, contamination is unlikely, since these clusters are endohedral and show a low reactivity towards oxygen, as is described in section 5.2. It should be noted that this behavior of partial ion yields is not found in the analysis of exohedral $ScSi_n^+$ ($n > 16$) clusters measured in a different beam time. A possible explanation might be that although different excitation channels at the metal $L_{3,2}$ edge lead to equally small photo fragments due to the high energy deposited in the cluster, the photo fragment $ScSi_x^+$ is found in either the relaxed ground state or an excited state with a long lifetime, depending on the excitation channel. If the excited state shows a higher reactivity than the ground state, different excitation channels are expected to result in an oxidized or not oxidized fragment ion. The oxygen is present in the residual gas in the ion trap, where fragment ions are stored for at a few $100\,ms$. Exohedral clusters on the other hand did not show dissimilar partial ion yields, which could be due to a lower partial oxygen pressure in the vacuum chamber at the time the spectra were taken, or different final states of fragments are only reached in endohedral $ScSi_n^+$ clusters.

Since dissimilar energy dependences of PIY spectra of different fragment ions do not show for other transition metal doped silicon clusters, it is assumed that distinction of equal sized fragment ions by their final state's excitation is an effect only observable in $ScSi_n^+$.

However, since no oxygen contamination was observed in the parent cluster mass selection and therefore oxidization must have taken place after the photoabsorption of the cluster, the sum of both differing ion yield spectra should show a higher agreement with the x-ray absorption than either one of them alone. The total ion yield shown in chapter 6 therefore corresponds to the sum of the PIY of all measured fragment ions. Despite the fact that an adulteration of the results of the absorption measurements is not assumed, a re-measurement of the spectra is suggested. This re-measurement should at least include the size range the endohedral to exohedral transition takes place in.
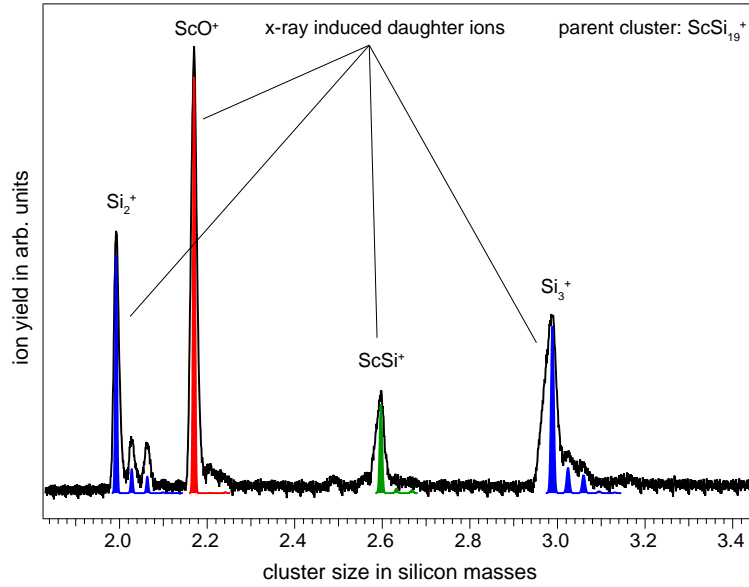
Figure A.1: Section of the mass spectrum of photo fragments of ScSi$_{19}^+$ (black line). The daughter ions show up partially oxidized. For comparison, calculated isotopic patterns of the daughter ions are shown. Pure silicon daughter ions are displayed blue, scandium containing daughter ions without oxygen are displayed green and oxidized daughter ions are shown in red.
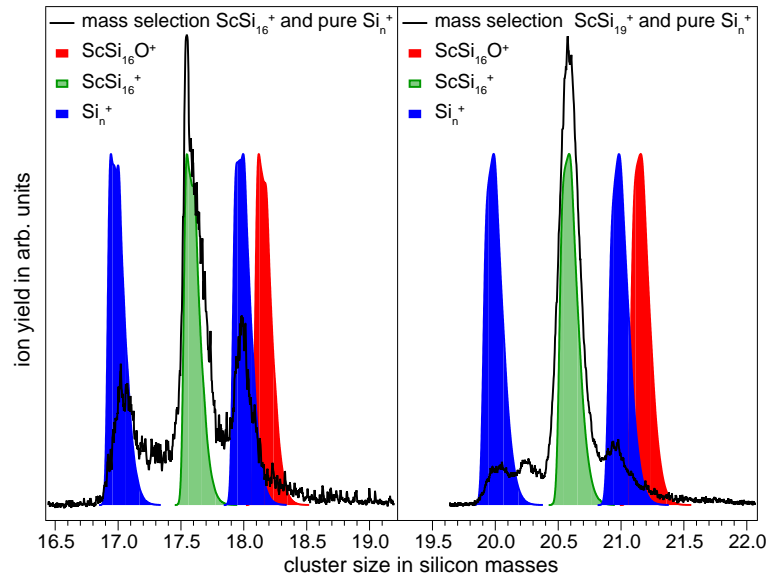

Figure A.2: Mass spectrum of the ScSi$_{16}^+$ and ScSi$_{19}^+$ parent ions. The selected mass range in the experiment shows no oxygen contamination of the parent ions. Pure silicon clusters are present, which do not interfere with the XAS measurement at the scandium L$_{3,2}$ edge (see text).
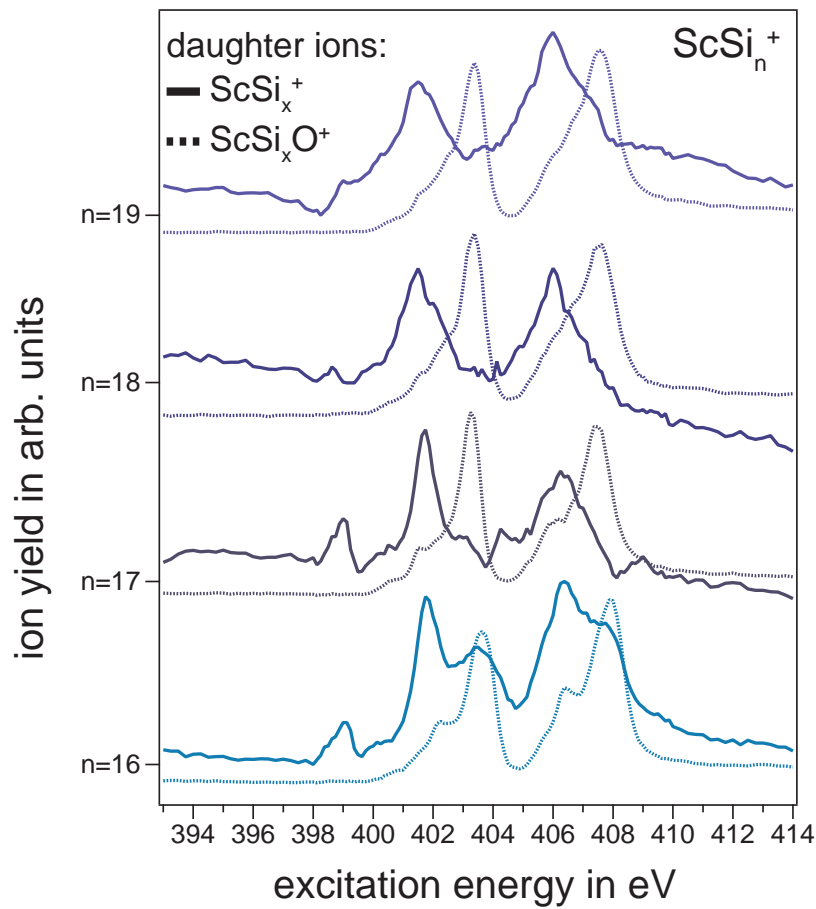
Figure A.3: Partial ion yield spectra of $ScSi_{7-15}^+$ for oxidized $ScSi_xO^+$ (dashed line) and $ScSi_x^+$ daughter ions. The PIY of oxidized ions exhibits $L_{3,2}$ lines shifted by about $1.6\,eV$ with respect to the respective lines obtained from non oxidized daughter ions. The PIY are both normalized, the CIY is shown in figure 6.4. An explanation is given in the text.

A.2 Unidentified Product Ion Generation Channels in the VUV Energy Range

In the past chapters of the thesis it has become obvious that an analysis of partial ion yield (PIY) spectra is essential to gain a profound understanding of the x-ray absorption and subsequent relaxation processes. While the PIY spectra at the transition metal $L_{3,2}$ edge showed almost exclusively (cf. sect. A.1) a minor number of product ions of a parent cluster after x-ray absorption, which are generated by the same excitation and following relaxation channels (cf. sect. 6.1), in the PIY spectra at the $L_{3,2}$ edge generation of a significantly larger number of different product ions is observed. These showed a strong dependence on the excitation process (cf. sect. 7.1), which allowed the distinct examination of resonant x-ray absorption and direct photoionization of MSi_n^+ clusters.

The number of different product ions generated after x-ray absorption at the valence orbitals is even larger and more diversified, as can be seen in figure A.4. Since the main idea of the analysis of MSi_n^+ clusters by ion yield spectroscopy in the VUV range was to determine the direct photoionization threshold energy, for most cluster sizes only the daughter ion whose generation corresponds to this process was recorded. However, for two cluster sizes VSi_{15}^+ and VSi_{16}^+ a larger number of product ions was recorded to allow a profound analysis of the fragmentation pattern. By evaluating the respective PIY spectra excitation channel dependences were expected to show. While the generation channel of two daughter ions, VSi_n^{2+} and VSi_n^{3+} can be directly linked to direct photoionization for energetic reasons explained in section 8.1, generation channels of other product ions are still under discussion. The spectra shown in the following are not normalized to photon flux due to an unknown calibration function of the diode in this energy range. To ensure consistency of PIY spectra even without photon flux normalization, features observed at a certain energy in PIY spectra are compared to the photon flux at the respective photon energy. This allows to select only absorption induced features for further analysis. For comparison, a typical energy dependent photon flux is shown in figure A.5. In addition, the PIY spectra of pure silicon fragments are discarded since paternity can not be definitely affiliated to doped silicon clusters due to the lack of a metal atom (cf. sect. 4.2). Before the PIY spectra of the respective product ions are shown and discussed, the third IP of MSi_n clusters is presented.
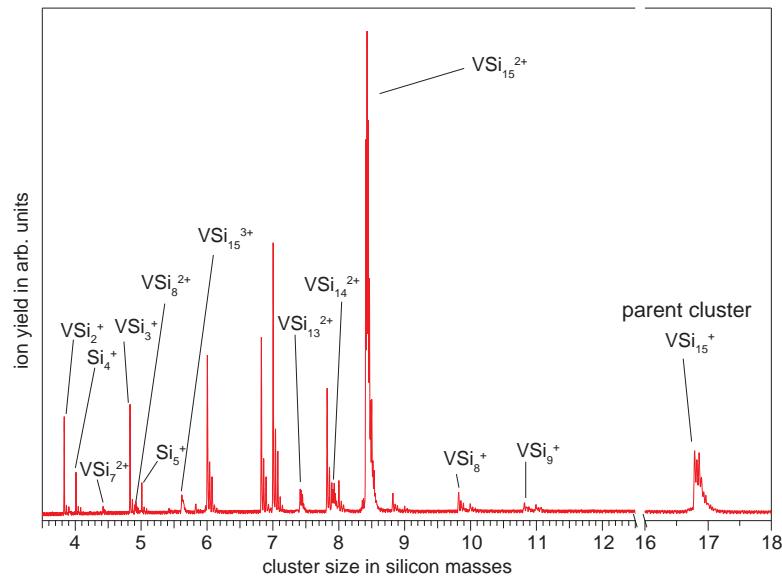
Figure A.4: Mass spectrum of all product ions of VSi_{15}^{+} parent ion that are generated in the energy range between 5 eV to 26 eV. For better visibility, the spectrum is smoothed.
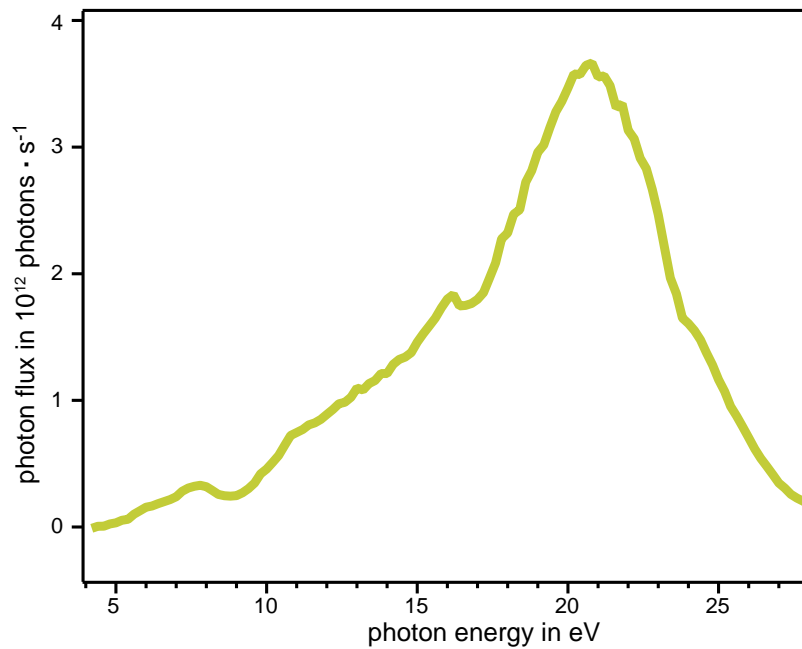

Figure A.5: Approximate photon flux of BESSY II U125-NIM beam line. Although the calibration of the photodiode is found to be inaccurate, strong changes in the photon flux are expected to correspond to real changes in the photon flux.
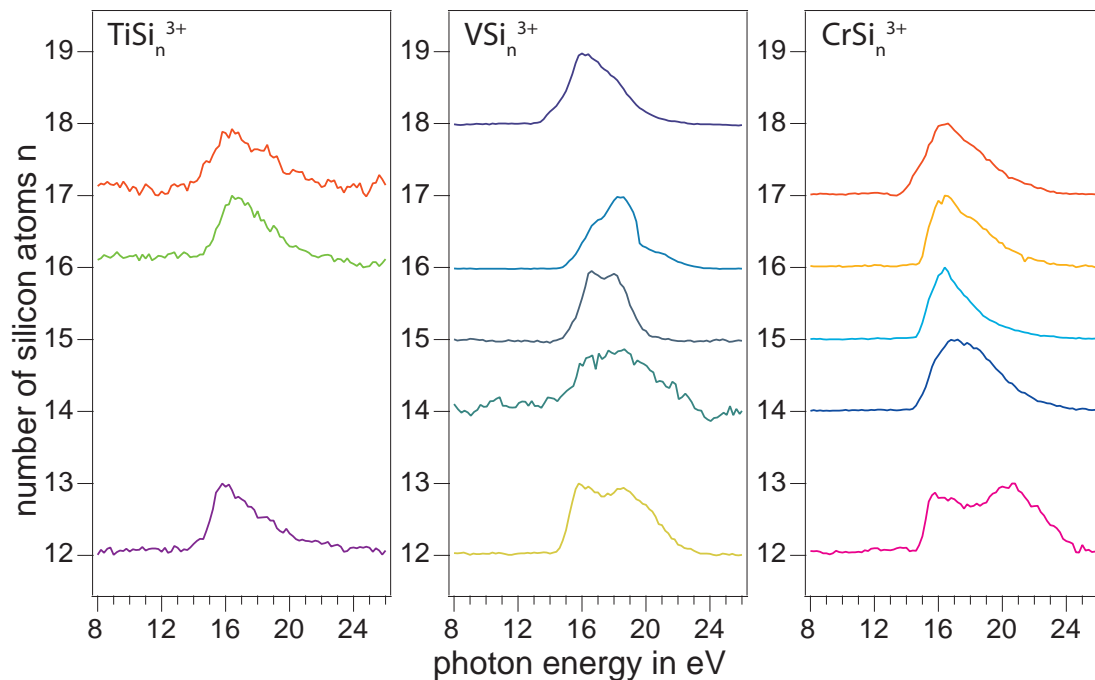
Figure A.6: Photoionization efficiency spectra of MSi_n^+. Two electrons are removed from the system.

Third Ionization Potential of MSi_n Clusters

In addition to the PIY spectra of doubly charged daughter ions, showing the IP of the singly charged parent cluster (second IP with respect to a neutral cluster) as shown in section 8.2, the PIY of MSi_n^{3+} (cf. fig. A.6) is expected to show the third IP with respect to the neutral cluster. It should be noted that despite the IP is denominated 3rd IP of MSi_n that MSi_n^+ is the parent ion in this measurement thus determining the geometric and electronic structure of the initial state cluster. Similar to the explanation for the second IP shown in section 8.2, the third IP is found at the threshold energy of the PIY of MSi_n^{3+}. The respective third IP energies are plotted in figure A.7. Due to a higher charge energy with respect to the doubly charged parent cluster and a lower occupation of valence states, the 3rd IP is found at higher photon energies. In contrast to the 2nd IP, the 3rd IP in figure 8.4 shows the same energy dependencies for all three MSi_n^+ clusters. While for the second IP a possible explanation for different trends of VSi_n^+, $TiSi_n^+$ and $CrSi_n^+$ clusters is given due to the odd (Cr, Ti) or even (V) number of valence electron occupation. When two electrons are removed from a system, one of them is always coming from a system with an odd number of valence electrons and the other from a system with an even number of valence electrons. Therefore the odd or even number of electrons explanation does not

171
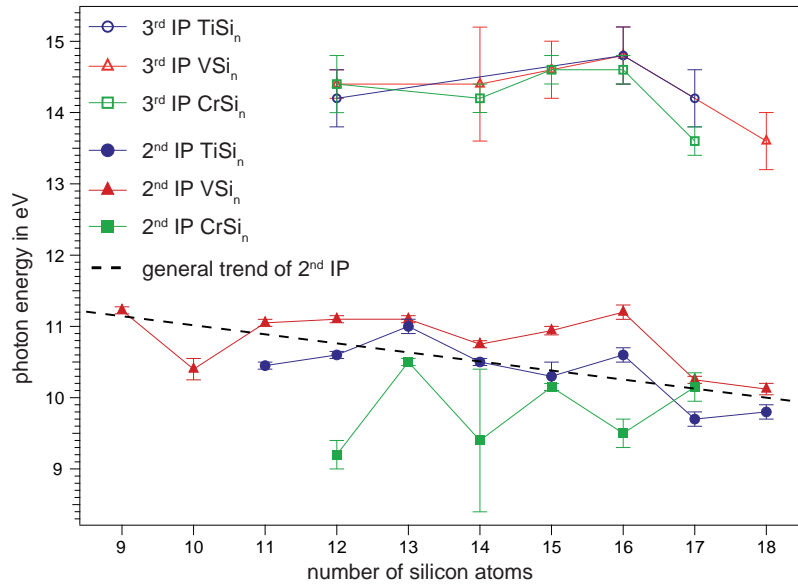
Figure A.7: Third Ionization potential (IP) of MSi_n, M=(Ti,V,Cr), $n \in [9, 18]$ clusters. For comparison, the second IP known from section 8.2 is also shown.

apply for the 3rd IP. Observation of equal size dependencies in the 3rd IP of MSi_n^+ clusters is therefore expected.

Partial Ion Yield Spectra of Doubly Charged Product Ions VSi_x^{2+} of VSi_{15}^+ and VSi_{16}^+

In the mass spectrum of ions generated from the parent clusters VSi_n^+ ($n = 15, 16$) multiple doubly charged product ions show (cf. fig. A.4) in addition to the already known VSi_n^{2+}, from which the direct photoionization threshold is extracted (cf. sect. 8.2).

The product ions appearing upon excitation in the VUV photon energy regime include also many doubly charged fragment clusters MSi_{n-x}^{2+}, whose PIY spectra are presented in figure A.8. The topmost graph in each panel is MSi_n^{2+}, already known from sect. 8.2. From top to bottom of each panel, the product ion size decreases. Although the size range $n = 10 - 12$ was covered by the experimental settings, no fragments were detected in this size range. This indicates that no relaxation channel leading to these daughter ions exists. At smaller cluster sizes, doubly charged daughter ions are observed again.

The threshold energy of the PIY spectrum of VSi_n^{2+} and VSi_{n-1}^{2+} is found at almost equal photon energies, whereas the threshold energy of smaller doubly
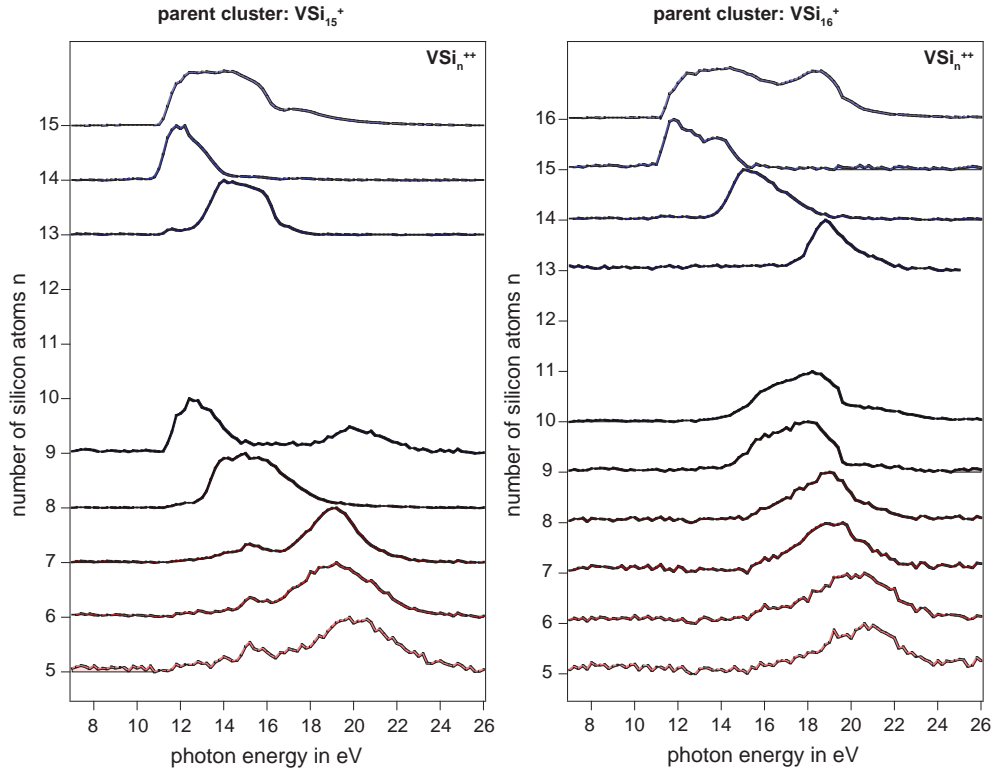
Figure A.8: Partial ion yield of product ions VSi_x^{2+} ($x = n, ..., 5$) of a parent cluster VSi_{15}^+ (right panel) and VSi_{16}^+ (left panel). The daughter ions show a increasing energetic threshold value with decreasing size for $(x) \geq 13$ and $(x) \leq 10$ with a discontinuity between both size regions. The daughter ion sizes missing between the size regions regions are not observed, although the respective mass to charge ratio is analyzed in time of flight spectra (see text). No normalization with respect to photon flux was done (see text).

charged clusters MSi_x^{2+} ($x \geq 13$) are found at higher excitation energies. An increasing threshold energy with decreasing fragment size is observed. Even smaller fragment ions MSi_x^{2+} ($x \leq n-6$) show a similar size dependence of the threshold energy, but the threshold energy of MSi_{13}^{2+} is found at higher excitation energy than MSi_{n-6}^{2+}. As explained in section 8.2 the lowest energy for which MSi_n^{2+} is found has to correspond to the direct photoionization threshold. It would be expected that more energy is needed for generation of a charge on the cluster and simultaneously removal of a silicon atom. Hence equal threshold energies of the PIY of MSi_n^{2+} and MSi_{n-1}^{2+} are not initially expected. In a simple picture, the threshold energy of MSi_{n-1}^{2+} should be found at an energy corresponding to the sum of the direct photoionization threshold and the binding energy of a silicon atom in the cluster. No explanation for this behavior is found. It is suggested that this is an artifact coming from the measurement method. Nonetheless, the spectra are shown for the sake of completeness. It is suggested to remeasure the spectra in order to confirm of disprove this ion yield behavior. If more par-

tial ion yields of a larger number of different MSi_n^+ compositions is available, a explanation of the underlying effect might show.

Partial Ion Yield Spectra of Singly Charged Product Ions VSi_x^{2+} of VSi_{15}^+ and VSi_{16}^+

Partial ion yield spectra of singly charged product ions generated from the parent clusters VSi_n^+ ($n = 15, 16$) are shown in figure A.9. Although in some cases similarities are observed in threshold energy, no certain fragmentation pattern is found. As mentioned above, no calibration with respect to photon flux is done. A certain underlying effect to explain the energy dependence of a fragment ion's yield is still missing. Comparison with a larger data set might make a pattern become more visible. The spectra are only shown for the sake of completeness.
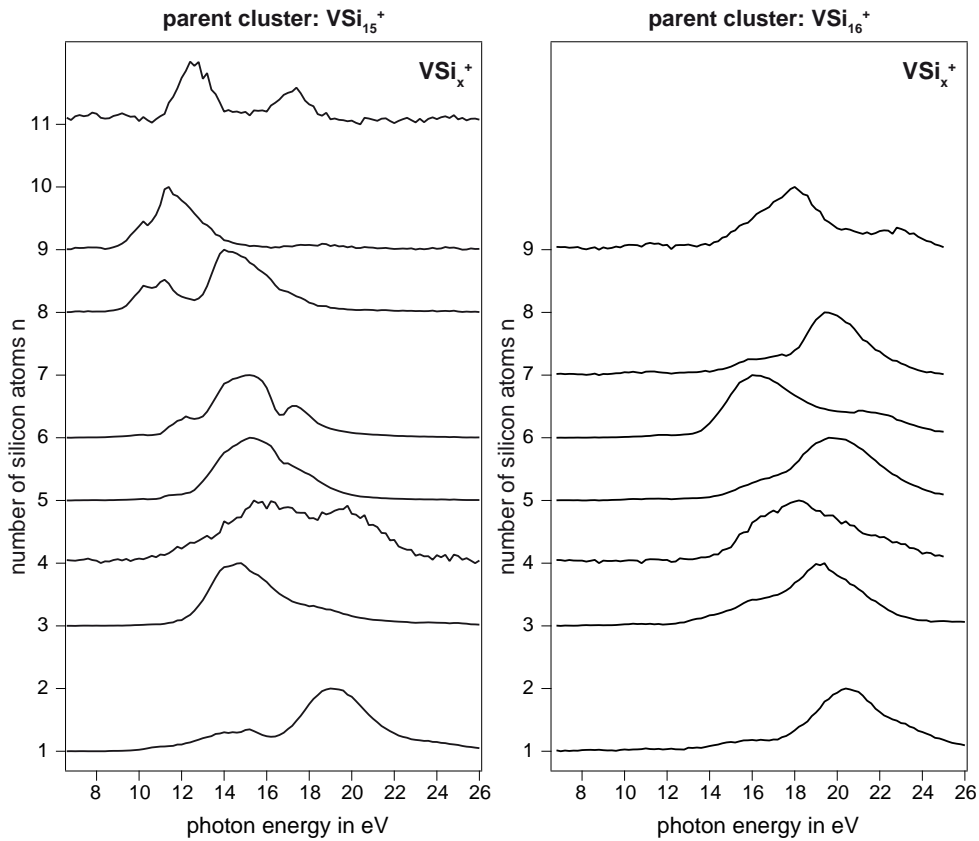
Figure A.9: Partial ion yield of product ions VSi_x^+ of a parent cluster VSi_{15}^+ (right panel) and VSi_{16}^+ (left panel). No normalization with respect to photon flux was done (see text).

Acknowledgment